Measurement of the $B_s \to K^+K^-$ lifetime and extraction of the $\Delta\Gamma_{CP}/\Gamma_{CP}$ at CDF Run II

and

Development of the ATLAS-SCT endcap modules

THÈSE

présentée à la Faculté des sciences de l'Université de Genève
pour obtenir le grade de Docteur ès sciences, mention physique

par

Mauro Donegà

d'Italie

Thèse N° 3766

Ai miei nonni

Abstract

In the first part of the present work we present the first measurement of the B_d and B_s meson lifetimes in charmless decays ($B_d \to K^+\pi^-$, $B_d \to \pi^+\pi^-$, $B_s \to K^+K^-$) based on 360pb^{-1} of $p\bar{p}$ collision taken at the CDF Run II detector and the extraction of $\frac{\Delta\Gamma_{CP}}{\Gamma_{CP}}$ for the B_s-meson.

We find the B_d-meson lifetime (in the $B_d \to K^+\pi^-$ and $B_d \to \pi^+\pi^-$ decay modes) to be:

$$
\begin{aligned}
c\tau(B_d) &= 452 \pm 24 \quad \text{(stat)} \pm 6 \quad \text{(syst)} \ \mu\text{m} \\
\tau(B_d) &= 1.51 \pm 0.08 \quad \text{(stat)} \pm 0.02 \quad \text{(syst)} \ ps
\end{aligned}
$$

and the B_s-meson lifetime (in the $B_s \to K^+K^-$ decay mode) to be:

$$
\begin{aligned}
c\tau(B_s \to K^+K^-) &= 458 \pm 53 \quad \text{(stat)} \pm 6 \quad \text{(syst)} \ \mu\text{m} \\
\tau(B_s \to K^+K^-) &= 1.53 \pm 0.18 \quad \text{(stat)} \pm 0.02 \quad \text{(syst)} \ ps
\end{aligned}
$$

Both measurements are consistent with the world averages.

We calculate the $\frac{\Delta\Gamma_{CP}}{\Gamma_{CP}}$ for the B_s meson combining the measured lifetime in the $B_s \to K^+K^-$ decay with the world average value of the B_s-meson lifetime in the flavour specific decays:

$$
\begin{aligned}
c\tau_{fs} &= 441 \pm 13 \ \mu\text{m} \\
\tau_{fs} &= 1.472 \pm 0.045 \ ps
\end{aligned}
$$

We find:

$$
\Delta\Gamma_{CP}/\Gamma_{CP} = -0.08 \pm 0.23 \ (stat.) \ \pm 0.03 \ (syst.)
$$

that is compatible with the theoretical expectation of $(7.2 \pm 2.4) \times 10^{-2}$.

In the second part of the present work, a few steps of the final R&D of the ATLAS-SCT endcaps modules will be reported.

Two module layouts have been developed on two different electrical hybrids designs. Both layouts have been produced in small prototype series and tested before and after exposing them to a particle fluence equivalent to that expected at the end of the ATLAS data taking.

The modules electrical performance have been tested with a dedicated test-setup and in the test beam. The thermal performance have been studied with finite element analysis and verified with thermal measurements.

The present work has been used to choose the final layout to be used for the final module production.

Résumé

Ce travail de thèse est composé de deux parties. Dans la première partie, je vais présenter la mesure du temps de vie moyen du méson B_s dans la désintégration $B_s \rightarrow K^+K^-$ et l'extraction du paramètre $\Delta\Gamma_s$. La mesure a été faite sur les données collectées dans l'expérience CDF II au près du Tevatron, au laboratoire Fermilab, dans la période entre février 2002 et août 2004.

Dans la deuxième partie, je vais présenter une série de tests sur les modules des bouchons du détecteur de traces au silicium d'ATLAS, qui ont mené à la finalisation du développement. Une attention particulière est portée aux aspects de résistance aux radiations, et leurs performances thermiques et électriques.

Première partie :
Mesure du temps de vie moyen du $B_s \rightarrow K^+K^-$ et extraction du paramètre $\Delta\Gamma_s$ à CDF II

Motivation théorique

La phenoménologie complexe de la physique des hautes énergies est décrite avec une très grande précision dans le cadre d'une théorie de jauge appelée modèle standard (MS). Malgré ses nombreux succès, le modèle standard ne décrit pas certains phénomènes, comme la masse des neutrinos, l'asymétrie matière-antimatière et surtout l'interaction gravitationelle. De nombreuses mesures expérimentales cherchent de nouveaux phénomènes qui s'éloignent des prévisions du MS pour collecter des indices vers sa modification ou son extention.

Un champ de recherche qui a vécu de grands développements ces dernières années est la physique liée au méson B.

La compréhension actuelle de la phénoménologie de la physique du méson B est décrite efficacement par la matrice CKM (d'après les noms de ses découvreurs Cabibbo, Kobayashi et Maskawa). D'un point de vue expérimental, on veut collecter le plus grand nombre de mesures (rapport d'embranchement, temps de vie moyen, etc.), même redondantes, sur les mésons B pour vérifier leur cohérence et l'exactitude de la description théorique fournie par la matrice CKM. La présence éventuelle d'une physique différente du MS apparatrait comme une ou plusieurs mesures non compatibles entre elles ou avec le modèle théorique.

Une phénomène particulièrement intéressant de la physique du méson B porte sur les oscillations entre les états propres de saveur $B - \overline{B}$. D'après la découverte des oscillations du méson K (Fitch et Cronin 1964) et la découverte du même phénomène dans les mésons B_d dans les usines à B (2001), on a essayé de mesurer le phénomène équivalent pour les mésons B_s, qui jusqu'à présent ne peuvent être produits qu'au collisioneur $p - \overline{p}$ Tevatron [1].

L'oscillation des mésons B neutres B_s et B_d est gouverné essentiellement par deux paramètres : la différence en masse Δm entre les deux états propres de masse et la différence entre leurs largeurs de désintégration $\Delta\Gamma$. Les valeurs relatives au méson B_d (Δm_d et $\Delta\Gamma_d$) ont été mesurées avec une très bonne précision dans les usines à B, par contre la mesure des valeurs relatives au méson B_s (Δm_s et $\Delta\Gamma_s$) représente actuellement un secteur de recherche très actif.

La valeur de Δm_s a été récement mesurée par CDF II. Elle est en très bon accord avec les limites imposées par les autres mesures et ne présente aucune déviation par rapport aux prédictions du MS. L'autre paramètre $\Delta\Gamma_s$ est actuellement mesuré avec une moins bonne précision et pourrait encore cacher une nouvelle physique au-delà du MS, dans ses grandes barres d'erreur. On démontre que la manifestation d'une nouvelle physique interviendrait dans le $\Delta\Gamma_s$ en réduisant la valeur prédite dans le modèle standard $(7.4 \pm 2.4) \times 10^{-2}$. Pour cela, il est nécessaire d'effectuer des mesures de haute précision pour mettre une nouvelle physique en évidence.

Dans les détails, le $\Delta\Gamma_s$ est la différence entre la largeur de désintégrasion de l'état propre léger et de l'état propre lourd du B_s. Dans ce travail de thèse, j'ai mesuré le temps de vie moyen de la désintégration $B_s \rightarrow K^+K^-$ qui correspond dans une bonne approximation à la largeur de désintégration de l'état propre léger du méson B_s. En combinant cette mesure avec la valeur existante de la largeur de désintégration de l'état propre lourd, il est donc possible d'extraire le $\Delta\Gamma_s$.

---

[1] Si l'on exclu des tests effectués récemment dans les usines à B

Dispositif expérimental

La mesure présentée a été effectuée sur les données collectées avec le détecteur CDF II placé après d'un des deux points d'interaction du Tevatron. Le Tevatron est un accumulateur $p - \overline{p}$ capable de générer des collisions à une énergie dans le centre de masse de 1.96 TeV, ce qui représente l'énergie la plus grande actuellement atteignable dans des collisions artificielles.

CDF II est un détecteur de particules généraliste composé de plusieurs couches de sous-détecteurs avec des caractéristiques différentes. En partant du point d'interaction et en allant vers l'extérieur, on rencontre d'abord le détecteur interne de traces, composé de 7 couches de détecteurs au silicium (dont l'une est placée sur la ligne de faisceau, à 1.5 cm du point d'interaction), suivit d'une chambre à fils. Le déteceur interne a un diamètre exterieur de 3 mètres. La chambre à fils est entourée par des barres de scintillateurs qui composent le TOF (Time Of flight pour Temps de Vol). Le tout est inséré dans un aimant solénodal capable de générer un champ magnétique de 1.4 Tesla. A l'exterieur de l'aimant on trouve le calorimètre électromagnétique et hadronique et enfin le spectromètre à muons.

Le travail présenté dans cette thèse est la mesure du temps de vie moyen du $B_s \rightarrow K^+K^-$. Cela est fait en mesurant avec une grande précision le temps de vie moyen du méson B_s, c'est à dire la distance entre le point d'interaction et le point de désintégration. Pour faire cela, on exploite en particulier le potentiel du détecteur à silicium pour la mesure précise des vertex primaires et secondaires, et la chambre à fils pour identifier le type de particules générées au vertex secondaire et mesurer leurs impulsions qui permet d'extraire la masse du méson qui s'est désintégré.

Pour obtenir le meilleur pouvoir discriminant de la chambre à fils dans l'identification des différentes particules qui la traversent, j'ai fait l'étalonnage précis de la réponse de ce sous-détecteur.

La mesure du temps de vie moyen du méson B_s exploite la capacité unique du détecteur CDF II de sélectionner (déclenchement) les désintégrations avec des états finaux purement hadroniques. Cela est possible grâce à un système en ligne sophistiqué (SVT) de mesure des paramètres d'impact des traces. Etant donné le temps de vie relativement long du méson B (environ $500 \mu m$), les traces générées dans sa désintégration ont en général un paramètre d'impact élevé. Par contre, les événements de fond dûs aux traces générées par des processus liés à l'interaction forte, sont en

général produits au vertex primaire. En sélectionnant les événements avec des traces avec un grand paramètre d'impact il est possible d'obtenir un échantillon de données contenant une grande concentration de mésons B.

Sélection de l'échantillon de données

Les données brutes provenant du détecteur, malgré la sélection effectuée en ligne par le système de déclenchement et basée sur les paramètres d'impact des traces, contiennent encore un grand taux d'événement non désirés (fond). Pour réduire le nombre de ces événements, j'ai développé une procédure d'optimisation qui exploite la différence de cinématique entre le signal et le fond. En particulier, j'ai identifié des variables (somme des impulsions transverses des deux traces, paramètre d'impact du méson B, paramètre d'impact des traces et qualité du vertex secondaire) pour lesquelles les événements du signal et du fond ont des caractéristiques substentiellement différentes. En sélectionnant seulement des événements qui passent des critères de sélection (coupures) basés sur ces variables, il est possible d'obtenir un échantillon de données avec un niveau de fond petit.

Plus précisément, la sélection s'éffectue en maximisant le rapport $S/\sqrt{S+F}$ où S est le nombre d'événements de signal dans une fenêtre de masse autour du pic du méson B (calculé sur un échantillon de données Monte Carlo) et F est le nombre d'événements de fond dans la même fenêtre (calculé sur les "sideband" des données), par différentes combinaisons de coupures sur les variables définies précédemment.

Mesure du temps de vie moyen du méson B

Les données sélectionnées contiennent 5 catégories d'événements : les quatre principaux modes de désintégration du méson B en deux traces ($B_d \rightarrow K^+\pi^-$, $B_d \rightarrow \pi^+\pi^-$, $B_s \rightarrow K^+K^-$ et $B_s \rightarrow K^-\pi^+$) et les fonds. Le premier pas de l'analyse consiste en la séparation des différentes catégories des événements pour trouver le signal qui nous intéresse $B_s \rightarrow K^+K^-$. Pour séparer ces catégories, j'ai cherché des observables discriminatoires qui seront décrites plus tard. Même si elle est très élevée, la résolution de CDF II sur ces variables ne permet pas une séparation événement par événement pour les 4 catégories de signal. Pour cela on utilise la technique statistique de la vraisemblance pour combiner dans une expression unique l'information

contenue dans les différentes variables. En maximisant la valeur de cette expression (maximum de vraisemblance) et en faisant varier les paramètres représentant les fractions des différentes composantes du signal et du fond, on obtient une estimation des paramètres sur l'échantillon des données sélectionnées.

La discrimination est faite en utilisant des quantités liées à la masse reconstruite de l'événement et à l'identification du type de particules qui composent les états finaux. Plus précisément, on décrit avec une fonction gaussienne la différence en valeur absolue entre la masse reconstruite de l'événement et la masse réelle des mésons B_d et B_s. La probabilité que la désintégration considérée provienne d'un méson B_d (B_s) est d'autant plus grande que la masse reconstruite est proche de la masse réelle du méson B_d (B_s). L'autre caractéristique considérée pour séparer les différentes catégories d'événements est l'identification du type des particules composant les états finaux. Ce type d'information est extrait de l'énergie spécifique déposée dans la chambre à fils par chacune des traces. La description de cette variable est modélisée par des fonctions gaussiennes centrées sur les valeurs de l'énergie déposée attendue par chaque type de trace en fonction de son impulsion. On s'intéresse notamment à la séparation entre Kaons (le seul type de particules dans l'état final $B_s \to K^+K^-$) et les autres types de particules produits dans l'événement (pions, muons, protons et électrons). Avec ces variables on peut extraire statistiquement les fractions des différentes catégories de signal et de fond présents dans l'échantillon de données.

Pour extraire la valeur du temps de vie moyen du $B_s \to K^+K^-$, il est nécéssaire d'inclure dans l'expression de la vraisemblance une variable supplémentaire : la longueur propre de désintégration, c'est à dire la distance entre le vertex primaire et le vertex secondaire.

La maximisation de la nouvelle expression de la vraissemblance sur ces variables, permet d'extraire simultanément les fractions des événements dans les 4 catégories de signal et les temps de vie moyens des mésons B associés à ces catégories. Notons que cette analyse permet aussi d'extraire les temps de vie moyens du méson B_d dans les désintégrations $B_d \to K^+\pi^-$ et $B_d \to \pi^+\pi^-$.

Le point le plus délicat lié à l'introduction de la longueur propre de désintégration dans l'expression de la vraisemblance est le biais introduit par le détecteur. En sélectionnant les événements sur la base des paramètres d'impact des traces on modifie la distribution exponentielle naturelle de la longueur propre de désintégration, en réduisant le nombre d'événements à petite valeur de temps de vie. Pour corriger ce biais, il a été nécéssaire de développer une méthode basée sur les simulations Monte Carlo.

La distribution de longueur propre de désintégration pour chaque canal est décrite par une exponentielle qui dépend du paramètre qui indique le temps de vie moyen de la désintégration, convolué avec une gaussienne qui décrit les effets de résolution du détecteur, le tout multiplié par une fonction d'efficacité qui décrit les effets de la sélection en ligne de l'échantillon et l'optimisation.

La méthode proposée pour corriger le biais provenant des critères de sélection a d'abord été testée sur différents types de données Monte Carlo et a été appliquée avec succès à la mesure du temps de vie moyen des désintégrations $B_d \to D\pi$ et $B_s \to D_s\pi$. Cette méthode a aussi été utilisée comme base pour la mesure des oscillations du méson B_s.

Les résultats de la mesure du temps de vie moyen pour les désintégrations en deux traces des mésons B_d et B_s sont :

$$
\begin{array}{rclclclcl}
c\tau(B_d) &=& 452 &\pm& 24 & \text{(stat)} \pm & 6 & \text{(syst)} & \mu\text{m} \\
\tau(B_d) &=& 1.51 &\pm& 0.08 & \text{(stat)} \pm & 0.02 & \text{(syst)} & ps
\end{array}
$$

$$
\begin{array}{rclclclcl}
c\tau(B_s \to K^+K^-) &=& 458 &\pm& 53 & \text{(stat)} \pm & 6 & \text{(syst)} & \mu\text{m} \\
\tau(B_s \to K^+K^-) &=& 1.53 &\pm& 0.18 & \text{(stat)} \pm & 0.02 & \text{(syst)} & ps
\end{array}
$$

Les résultats sont en accords avec les deux valeurs moyennes mondiales les plus récentes.

L'erreur systématique sur cette mesure est le résultat d'une série d'études pour contrôler de nombreuses quantités utilisées dans l'analyse. Le résultat de ces études montrent que cette erreur est de $6\mu m$, ce qui est beaucoup plus petit que l'erreur statistique.

Discussion des résultats

Les résultats présentés dans la section précédente représentent la première estimation du temps de vie moyen du méson B_s dans la désintégration $B_s \to K^+K^-$ et la mesure du temps de vie moyen du méson B_d dans les désintégrations $B_d \to K^+\pi^-$ et $B_d \to \pi^+\pi^-$.

En supposant que la désintégration $B_s \to K^+K^-$ est entièrement dûe à l'état propre de masse léger du méson B_s, il est possible de combiner la mesure obtenue avec la

valeur connue du temps de vie moyen de l'état propre de masse lourd et d'obtenir le $\frac{\Delta \Gamma_s}{\Gamma_s}$.

La valeur obtenue est :

$$\Delta \Gamma_{CP}/\Gamma_{CP} \quad = \quad -0.08 \pm 0.23 \ (stat.) \ \pm 0.03 \ (syst.)$$

à comparer avec la prévision théorique $(7.4 \pm 2.4) \times 10^{-2}$. La figure 1 représente cette mesure comparée aux autres mesures existantes. Evidemment, l'erreur statistique de
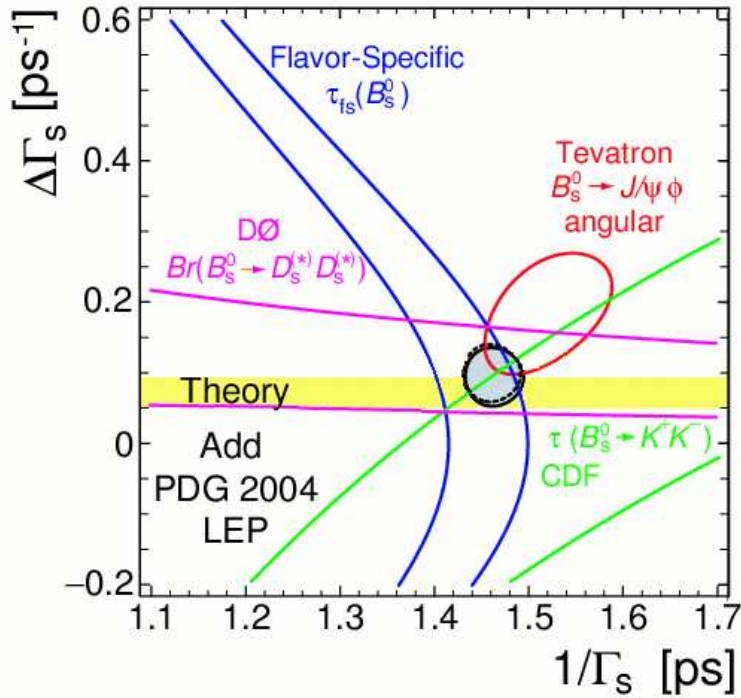

Figure 1: *Résumé des mesures actuelles de $\frac{\Delta \Gamma_s}{\Gamma_s}$.*

cette mesure du DGSGS est encore trop grande pour être significative. Toutefois, comme l'erreur systématique est tres petite, il est possible d'exploiter les méthodes développées dans cette thèse, sur un échantillon de données correspondant à une luminosité intégrée plus grande et d'obtenir une comparaison significative avec la prédiction théorique. En particulier, on estime qu'avec $2fb^{-1}$, on peut obtenir une erreur statistique de l'ordre de 10%. Avec $8fb^{-1}$, l'erreur statistique peut être réduite à environ 5%.

Deuxième partie :
Développement des modules bouchons du détecteur à micro-pistes de silicium, ou SCT, d'ATLAS

Le SCT d'ATLAS

La plus grande énergie dans le centre de masse actuellement atteignable dans des collisions artificielles, de 1.96 TeV, est fournie par le collisionneur $p - \overline{p}$ Tevatron au Fermilab. Le LHC (Large Hadron Collider), au CERN, constitue la prochaine étape dans la physique des hautes énergies, puisqu'il produira des collisions de protons à une énergie de 14 TeV dans le centre de masse. Ce collisonneur délivrera aussi une luminosité 100 fois supérieure à celle fournie par le Tevatron, et sera la machine qui permettra de franchir une étape supplémentaire dans la compréhenson des interactions fondamentales.

Deux faisceaux de protons vont entrer en collision en quatre points où sont situées quatre expériences : Alice, ATLAS, CMS et LHCb. L'expérience Alice va étudier la physique des ions lourds, LHCb va s'intéresser à la physique des particules avec de la beauté, en particulier à la violation de la symétrie CP, ATLAS et CMS vont étudier la physique du modèle standard et au-delà.

Dans cette thèse, je présente le travail fait dans le cadre du développement du détecteur à micro-pistes de silicium d'ATLAS (SCT). Le détecteur ATLAS est un cylindre de 44 mètres de long pour 22 mètres de diamètre, centré autour de l'un des points d'interaction des faisceaux; sa masse totale est de 7000 tonnes. Il est composé de deux types d'aimants et de trois systèmes de détection. En partant du point d'interaction, on trouve successivement : le détecteur interne de traces, l'aimant solénodal ($2T$), les calorimètres (électromagnétique et hadronique), l'aimant torodal (3 à 8 $T.m$) et le spectromètre à muons. Un système de déclenchement complexe, divisé en trois niveaux, permet de réduire la fréquence des événements collectés de 40 MHz, la fréquence des collisions, à 100 Hz, et le taux d'événement enregistrés.

Le détecteur à micro-pistes de silicium d'ATLAS, constitue une des trois techonologies utilisées dans le détecteur interne de traces. Les deux autres étant un détecteur à pixel et un détecteur à radiation de transition (TRT).

Dans ce travail de thèse, j'ai effectué de nombreux tests sur les modules composant les bouchons du SCT. En particulier, j'ai analysé le comportement de ces modules suite à

une exposition à de fortes radiations équivalentes à environ 10 ans de fonctionnement du LHC.

Tenue aux radiation et spécification thermo-électriques

ATLAS doit fonctionner environ 10 ans. Pendant cette période les sous-détecteurs les plus internes seront exposés à de très grandes doses de radiation. Les particules chargées qui traversent les couches du SCT endommagent soit la structure cristaline du sicilicium (qui compose la surface active du détecteur), soit l'électronique de lecture en réduisant ses performances. Pour réduire ces effets, on n'a utilisé dans le projet SCT que des composants "Radiation Hard". Etant donnée, la forte dépendance de ces dommages avec la température, on a développé les modules de manière très précise afin d'avoir le meilleur contrôle possible de la température. Le SCT est composé de trois sous-systèmes : deux bouchons vers l'avant et une partie centrale cylindrique. Ces sous-systèmes ont une structure modulaire, le SCT est composé au total de 4088 modules. Pour garantir la fonctionnalité du SCT pendant la prise de données, chaque module doit respecter de très sévères specifications techniques aussi bien sur les performances electriques que thermiques.

Les spécificités électriques posent des limites sur la quantité de bruit de fond maximum acceptable ainsi que sur l'efficacité de la reconstruction des traces. Les spécificités thermiques fixent la température de fonctionnement des micro-pistes à -7°C et imposent des limites sur le phénomène de "thermal runaway". Ce phénomène est lié à la dépendance du courant de fuite des micro-pistes avec la température. Le courant de fuite des micro-pistes est d'autant plus grand que la température est élevée. La dissipation de chaleur par les courants de fuite dûe à l'effet Joule implique une augmentation de la température et donc du courant lui même et ainsi de suite. Si le système de refroidissement n'est pas capable d'évacuer la chaleur dissipée par le module, leur température augmenterait de manière incontrolée en compromettant irrémédiablement sa fonctionnalité.

Conception thermique des modules

Dans ce travail de thèse, j'ai contribué au développement de la conception finale des modules bouchons du SCT, en étudiant soit les performances électriques soit les

xvi

perfomances thermiques. Suite à des problèmes rencontrés dans la conception des modules "baseline" (K5), on a développé, en parallèle, un module de remplacement de conception différente (KB), en travaillant en particulier à l'étude de sa conception thermo-mécanique.

La première étape consiste à développer un modèle, à l'aide de la technique des éléments finis, pour étudier les meilleurs matériaux utilisables et la meilleur géométrie de module. Quand une conception respectant les spécificités techniques a été trouvée, nous avons commencé la production d'une mini-série de prototypes. Les performances électriques de ces modules ont d'abord été étudiées dans le détail. Ensuite, un des prototypes a été irradié par un faisceau de protons, en simulant la dose de radiation subi par le SCT durant le fonctionnement d'ATLAS. Ces études ont été répétées sur ce module irradié, afin de vérifier qu'il respecte encore les spécifications électriques. Suite à ces tests, nous avons effectué des mesures pour vérifier les performances thermiques prévues par l'analyse avec les les éléments finis. Pour faire cela, on a installé plusieurs senseurs de température sur ce module et on a construit un dispositif pour contrôler soit la température du circuit de refroidissement, soit la température de l'atmosphère dans laquelle le module est placé. Le module étudié a confirmé les excellentes performances predites dans l'analyse avec les éléments finis.

Dans le même temps, le développement en parallèle du module "baseline" a montré qu'il rencontrait lui aussi les spécificités électriques. Pour vérifier que les spécificités thermiques soient aussi respectées, on a utilisé la même technique que précédemment, en modifiant le dispositif pour s'adapter à la géométrie différente du module. Les résultats de ces mesures sont montrés dans la figure 2.
Il est à noter que quand la température de fonctionnement du module est de
-22 °C , la température des micro-pistes est inférieure à -7°C , ce qui rencontre les spécificités thechniques. De plus, le phénomène de "thermal runway" est controlé.

En se basant sur le nombre de modules étudiés, les deux concepts respectent aussi bien les spécificités thermiques que électriques. Le module original, a été privilégié car l'étude d'ingénierie des structures mécaniques des supports était déja bien avancée.

La structure du module (K5) a été jugée positivement par une commission pendant la FDR (Final Design Review), et cette structure a été utilisée pour la construction finale des modules du SCT.
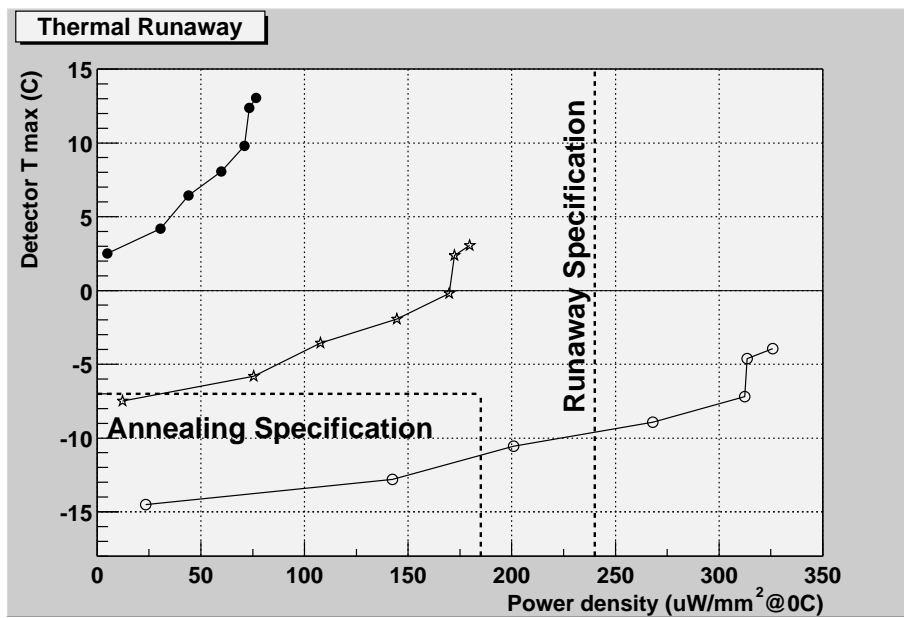
Figure 2: *Thermal runaway normalisé à différentes températures de refroidissement. Les températures du fluide de refroidissement étaient respectivement de -5° C pour les points, -15° C pour les étoiles et -22° C pour les cercles creux.*

Contents

Part I

Measurement of the $B_s \to K^+K^-$ lifetime and extraction of the $\Delta\Gamma_{CP}/\Gamma_{CP}$ at CDF Run II

In the present work, the first measurement of the B-meson lifetime in charmless hadronic decays and the extraction of the $\Delta\Gamma_{CP}/\Gamma_{CP}$ will be presented. The analysis is based on 360pb^{-1} of data collected by the CDF Run II detector at Tevatron between February 2002 and August 2004. The data are collected taking advantage of the unique capability of the CDF Run II detector to select fully hadronic B-meson decays triggering on displaced tracks. The analysed data contains the four main $B^0 \rightarrow h^{\pm}h'^{\mp}$ modes ($B_d \rightarrow K^+\pi^-$, $B_d \rightarrow \pi^+\pi^-$, $B_s \rightarrow K^+K^-$, $B_s \rightarrow K^-\pi^+$) and a fraction of background. A likelihood-based method has been used to disentagle the different signal and background components. The trigger selection on displaced tracks biases the lifetime distribution of the data sample. A Monte Carlo method has been developed to measure the B-meson lifetime on the biased sample. After a successful test on the $B_d \rightarrow D\pi$ and $B_s \rightarrow D_s\pi$ decay modes, the method has been integrated in the previous likelihood-based analysis to fit simultaneously the four main $B^0 \rightarrow h^{\pm}h'^{\mp}$ signal fractions and the lifetimes.

The present work represents the first measurement of the B-meson lifetime in charmless hadronic decays and one of the most precise determination of the $\Delta\Gamma_{CP}$ parameter in the B_s system.

The Monte Carlo method developed to measure the lifetime in trigger biased samples has been also applied successfully to other B-meson decay modes and it has been used in the recently presented B_d and B_s mixing analysis.

The analysis is in the process of being updated on $1fb^{-1}$ of data for the publication.

Chapter 1

Theoretical motivations

The goal of high energy physics is to discover the fundamental building blocks of the matter and understand their interactions. At present physicists have discovered 12 fermions (6 quarks and 6 leptons), are able to describe their interactions using 5 bosons (photon, $W^{\pm}$, Z^0 and the (eight) gluons) and they are searching for the cause of the electroweak symmetry breaking.

Almost the whole phenomenology of particle physics (excluding gravity) spanning many orders of magnitude in energy can be described with astonishing precision in the framework of the Standard Model (SM) [1].

Despite its success, there are a number of observations that do not have a place in the frame of the SM for example the existence of non zero neutrino masses, the matter-antimatter asymmetry and the gravitational interaction. Moreover the SM raises questions that seek for answers outside its realm. For example: what is the origin of unification?; what is the origin of mass?; what is the origin of flavor? (what makes a top-quark a top-quark or a neutrino a neutrino?); what is the origin of CP violation? [2].

Several models have been proposed to describe the present phenomenology and to find the answers to (some of) the previous problems (supersymmetry, extra dimensions, strong dynamics (technicolor, little Higgs) etc..). Despite their different theoretical base, all the SM extensions have a common characteristic: they all predict the presence of new particles and/or interactions. In order to verify which (if any) of the proposed models can describe our knowledge of the fundamental physics to the next energy scale, experimentalists are pursuing two different but complementary paths. The first path seeks new states of matter by direct observation, creating them in high energy collisions. The other path seeks to identify the deviations from SM predictions with precision measurements.

In the present work we follow the second path. The precise measurement of the B_s lifetime to the specific final state K^+K^- may lead, as will be explained in this chapter, to the appearance of new physics (NP) beyond the Standard Model. Unfortunately a direct comparison to the SM prediction of the $B_s \to K^+K^-$ lifetime is not a viable way to infer the presence of NP, because of theoretical uncertainties. In order to observe the presence of NP we will have to compose the result of our measurement with other experimental input and calculate the B_s-meson width difference $\Delta\Gamma$, for which a precise theoretical prediction is available.

We will begin this chapter by showing the roots of the SM description of quark flavour dynamics and how the CKM matrix naturally arises from the Yukawa coupling of the quarks to the Higgs field. We then present a brief description of the theoretical tools used to calculate the B-meson lifetimes to clarify why a direct comparison of our measurement with the SM theoretical prediction is not a viable way to infer the presence of NP. We will then move to the description of the neutral B-meson mixing phenomenon and the effect of CP violation in the B_s width difference. Finally we describe how to obtain the B_s width difference using the measured $B_s \to K^+K^-$ lifetime.

1.1   The weak interaction and the CKM matrix

The Standard Model (SM) of weak interactions [3] is a gauge theory based on the $SU(2)_L \times U(1)_Y$ symmetry group that assumes four massless gauge fields: $\vec{W}_\mu$ and B_μ. The symmetry $SU(2)_L \times U(1)_Y$ is spontaneously broken $SU(2)_L \times U(1)_Y \to U(1)_{em}$ by the Higgs mechanism [4]. The four fields mix, resulting in the three massive intermediate vector bosons $W^\pm$, Z^0, the massless γ and a yet unobserved Higgs boson. The same mechanism is also responsible for the masses of the fermions. Considering only one generation (u,d), the terms of the SM Lagrangian responsible for the quarks masses can be written as:

$$\mathcal{L} = -\lambda_u \left(\bar{Q}\bar{\phi}u_R + \bar{u}_R\bar{\phi}^\dagger Q \right) - \lambda_d \left(\bar{Q}\phi d_R + \bar{d}_R\phi^\dagger Q \right) \tag{1.1}$$

where $\lambda_{u,d}$ are the dimensionless Yukawa coupling that are free parameters in the SM, $Q = [u', d']_L$ is the pair of left handed Dirac quark fields, and ϕ is the scalar Higgs doublet:

$$\phi = \begin{pmatrix} \phi^\dagger \\ \phi^0 \end{pmatrix} \qquad \bar{\phi} = \begin{pmatrix} \bar{\phi}^0 \\ -\phi^- \end{pmatrix} \tag{1.2}$$

Choosing a vacuum expectation value (v) and expanding around it we obtain:

$$m_u = \lambda_u \frac{v}{\sqrt{2}} \qquad m_d = \lambda_d \frac{v}{\sqrt{2}} \tag{1.3}$$

The previous reasoning can be easily generalized to three quarks generations:

$$\begin{pmatrix} u \\ d \end{pmatrix} \qquad \begin{pmatrix} c \\ s \end{pmatrix} \qquad \begin{pmatrix} t \\ b \end{pmatrix} \tag{1.4}$$

obtaining

$$\mathcal{L}_{mass} = \frac{v}{\sqrt{2}} \left[\overline{(u\ c\ t)}'_L \Lambda_U \begin{pmatrix} u \\ c \\ t \end{pmatrix}'_R + \overline{(d\ s\ b)}'_L \Lambda_D \begin{pmatrix} d \\ s \\ b \end{pmatrix}'_R \right] \tag{1.5}$$

In this expression the primed quark field include the quark mixing between the different generations (i.e. the extension to three families of the Cabibbo rotation).

The mass terms for the up and down type quarks are:

$$M_{U,D} = \frac{v}{\sqrt{2}} \Lambda_{U,D} \tag{1.6}$$

In general the matrices $M_{U,D}$ are not diagonal. They can be diagonalized through a bi-unitary transformation $U^\dagger M V = M_{diag}$ where U and D are unitary.

If we consider the primed quark field ψ' we have

$$\bar\psi'_L M \psi'_R = \bar\psi'_L U M_{diag} V^\dagger \psi'_R = \bar\psi_L M_{diag} \psi_R \tag{1.7}$$

where $\psi_R = V^\dagger \psi'_R$ and $\psi_L = U \psi'_L$.

For the quarks there is an observable mixing matrix. Writing the electroweak Lagrangian for the charged current we obtain:

$$\mathcal{L}_W^{c.c.} = \frac{g}{2\sqrt{2}} \left[\overline{(u\ c\ t)}_L \gamma_\mu \begin{pmatrix} d \\ s \\ b \end{pmatrix}'_L W_\mu^\dagger + h.c. \right] = \tag{1.8}$$

$$= \frac{g}{2\sqrt{2}} \left[\overline{(u\ c\ t)}_L \gamma_\mu U_U^\dagger U_D \begin{pmatrix} d \\ s \\ b \end{pmatrix}_L W_\mu^\dagger + h.c. \right] \tag{1.9}$$

where $V_{CKM} := U_U^\dagger U_D$ is a unitary matrix commonly referred to as the CKM (Cabibbo-Kobayashi-Maskawa) matrix [5]. The elements of the CKM matrix are observables and need to be determined experimentally.

1.2 The CKM matrix and the Unitarity Triangle

The CKM matrix determines the strength of the interaction between quarks of different flavor and the W boson. The unitarity of the CKM matrix translates into the absence of flavour changing neutral current (FCNC) processes at tree level in the SM and it represent a generalization of the GIM mechanism [6] to three quarks generations.

The elements of the CKM matrix describe the generic strength of the charged current vertex and are indexed with the flavors of the quarks that participate to that process.

$$V_{CKM} = \begin{pmatrix} V_{ud} & V_{us} & V_{ub} \\ V_{cd} & V_{cs} & V_{cb} \\ V_{td} & V_{ts} & V_{tb} \end{pmatrix}. \tag{1.10}$$

The unitarity of the matrix V implies 6 normalizations

$$\sum_{k=1}^{3} V_{ik} \cdot V_{ik}^* = 1 \qquad \forall i \in 1, 2, 3 \tag{1.11}$$

$$\sum_{k=1}^{3} V_{ki} \cdot V_{ki}^* = 1 \qquad \forall i \in 1, 2, 3 \tag{1.12}$$

and 6 orthogonality relations

$$\sum_{k=1}^{3} V_{ik} \cdot V_{jk}^* = 0 \qquad \forall i, j \in 1, 2, 3 \ (i \neq j) \tag{1.13}$$

$$\sum_{k=1}^{3} V_{ki} \cdot V_{kj}^* = 0 \qquad \forall i, j \in 1, 2, 3 \ (i \neq j) \tag{1.14}$$

The latter can be represented as 6 triangles in the complex plane, all having the same area which can be interpreted as a measure of the CP violation in the SM [7].

The present experimental knowledge of the elements of the CKM matrix are [8]:

$$V_{CKM} = \begin{pmatrix} 0.9739 - 0.9751 & 0.221 - 0.227 & 0.0029 - 0.0045 \\ 0.221 - 0.227 & 0.9730 - 0.9744 & 0.039 - 0.044 \\ 0.0048 - 0.014 & 0.037 - 0.043 & 0.9990 - 0.9992 \end{pmatrix} \tag{1.15}$$

Each $n \times n$ complex unitarity matrix can be parametrized by n^2 real parameters.[1]

---

[1]The complex unitarity matrix has $2n^2$ parameters with n real (diagonal) and $n(n-1)/2$ complex (above or below diagonal) conditions, and therefore $2n^2 - n - n(n-1)/2 = n^2$ free real parameters.

Out of the 9 real parameters describing the CKM matrix only 4 of them (3 angles: $\theta_{12}, \theta_{23}, \theta_{13}$ and a phase δ_{13}) have physical meaning while the remaining 5 can be absorbed by phase redefinitions of the quark fields.

The proposed standard parametrization of the CKM matrix is:

$$V_{CKM} = \begin{pmatrix} c_{12}c_{13} & s_{12}c_{13} & s_{13}e^{-i\delta_{13}} \\ -s_{12}c_{23} - c_{12}s_{23}s_{13}e^{i\delta_{13}} & c_{12}c_{23} - s_{12}s_{23}s_{13}e^{i\delta_{13}} & s_{23}c_{13} \\ s_{12}c_{23} - c_{12}c_{23}s_{13}e^{i\delta_{13}} & -c_{12}s_{23} - s_{12}c_{23}s_{13}e^{i\delta_{13}} & c_{23}c_{13} \end{pmatrix} \quad (1.16)$$

where c_{ij} and s_{ij} represent respectively $\cos\theta_{ij}$ and $\sin\theta_{ij}$. This representation has the advantage that if one of the mixing angles vanishes, the mixing between the corresponding two generations vanishes as well.

For phenomenological application on the other hand it is useful to introduce the Wolfenstein parametrization [9] that reflects the measured hierarchy between the elements of the CKM matrix. Defining

$$s_{12} = \lambda \sim 0.22, \qquad s_{23} = A\lambda^2, \qquad s_{13}e^{-i\delta_{13}} = A\lambda^3(\rho - i\eta) \quad (1.17)$$

we obtain an exact parametrization of the CKM matrix. Expanding each of the matrix elements in λ and neglecting terms of $\mathcal{O}(\lambda^4)$ we can write:

$$V_{CKM} \simeq \begin{pmatrix} 1 - \frac{1}{2}\lambda^2 & \lambda & A\lambda^3(\rho - i\eta) \\ -\lambda & 1 - \frac{1}{2}\lambda^2 & A\lambda^2 \\ A\lambda^3(1 - \rho - i\eta) & -A\lambda^2 & 1 \end{pmatrix} + \mathcal{O}(\lambda^4) \quad (1.18)$$

Using the Wolfenstein parametrization it is straightforward to observe that four of the six triangles implied by the orthogonality relations are squashed (one side much shorter than the other two), while for two of them, all sides have approximately the same length. For these two triangles the orthogonality relations agree with each other at the λ^3 level, corresponding to a very good approximation to the same triangle which is usually referred to as *the* unitarity triangle of the CKM matrix:

$$V_{ud}V_{ub}^* + V_{cd}V_{cb}^* + V_{td}V_{tb}^* = 0 \quad (1.19)$$

In practice it is more convenient to work with the normalized unitarity triangle. The rescaling is performed dividing the previous expression by $V_{cb}V_{cd}^*$ so that one side of the triangle becomes of unit length (see figure 1.1):

$$\frac{V_{ud}V_{ub}^*}{V_{cb}V_{cd}^*} + \frac{V_{td}V_{tb}^*}{V_{cb}V_{cd}^*} + 1 = 0 \quad (1.20)$$
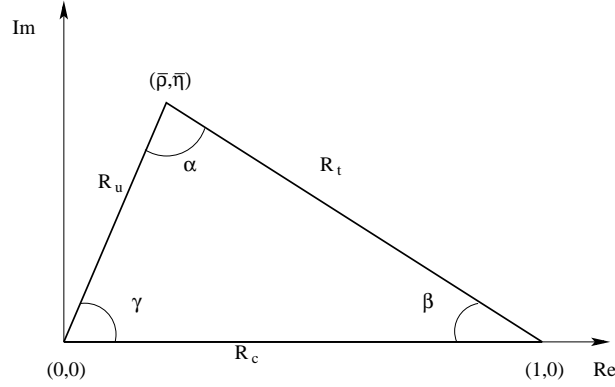
Figure 1.1: *The normalized unitarity triangle.*

The coordinates of the vertex becomes $(0,0)$, $(1,0)$ and $(\bar{\rho}, \bar{\eta})$, where

$$\bar{\rho} = \left(1 - \frac{\lambda^2}{2}\right)\rho \qquad \bar{\eta} = \left(1 - \frac{\lambda^2}{2}\right)\eta \tag{1.21}$$

where ρ and η are the Wolfenstein parameters.

The length of the sides of the normalized triangle are given by:

$$R_c \;=\; 1 \tag{1.22}$$

$$R_u \;=\; \left|\frac{V_{ub}^* V_{ud}}{V_{cb}^* V_{cd}}\right| = \sqrt{\bar{\rho}^2 + \bar{\eta}^2} = \left(1 - \frac{\lambda^2}{2}\right)\frac{1}{\lambda}\left|\frac{V_{ub}}{V_{cb}}\right| \tag{1.23}$$

$$R_t \;=\; \left|\frac{V_{tb}^* V_{td}}{V_{cb}^* V_{cd}}\right| = \sqrt{(1-\bar{\rho})^2 + \bar{\eta}^2} = \frac{1}{\lambda}\left|\frac{V_{td}}{V_{ts}}\right| \tag{1.24}$$

The three angles of the unitarity triangle are given by:

$$\alpha = arg\left(-\frac{V_{td}V_{tb}^*}{V_{ud}V_{ub}^*}\right) \qquad \beta = arg\left(-\frac{V_{cd}V_{cb}^*}{V_{td}V_{tb}^*}\right) \qquad \gamma = arg\left(-\frac{V_{ud}V_{ub}^*}{V_{cd}V_{cb}^*}\right) = \delta \quad (1.25)$$

The triangle corresponding to the B_s meson is:

$$V_{us}V_{ub}^* + V_{cs}V_{cb}^* + V_{ts}V_{tb}^* = 0 \tag{1.26}$$

where we have replaced the d-quark with the s-quark. The first side is much shorter than the other two, Therefore the opposite angle

$$\beta_s = arg\left(-\frac{V_{ts}V_{tb}^*}{V_{cs}V_{cb}^*}\right) = \lambda^2\eta + \mathcal{O}(\lambda^4) \tag{1.27}$$

is of the order of only one degree.

The main goal of the "B-physics" is to experimentally over-constrain the angles and the sides of the B_d and B_s triangles to verify the validity of the CKM picture. The highest precision measurements on the B_d meson have been performed at the B-factories PEP-II by the BaBar[10] collaboration and KEK-B by the Belle[11] collaboration. The highest precision measurements on the B_s meson are performed at the Tevatron by the CDF[12] and D0[13] collaborations.

The B-physics measurements are usually pictured as allowed regions in the $(\bar{\rho}, \bar{\eta})$ plane [14], [15]. The most updated plot is shown in figure 1.2. A measurement not
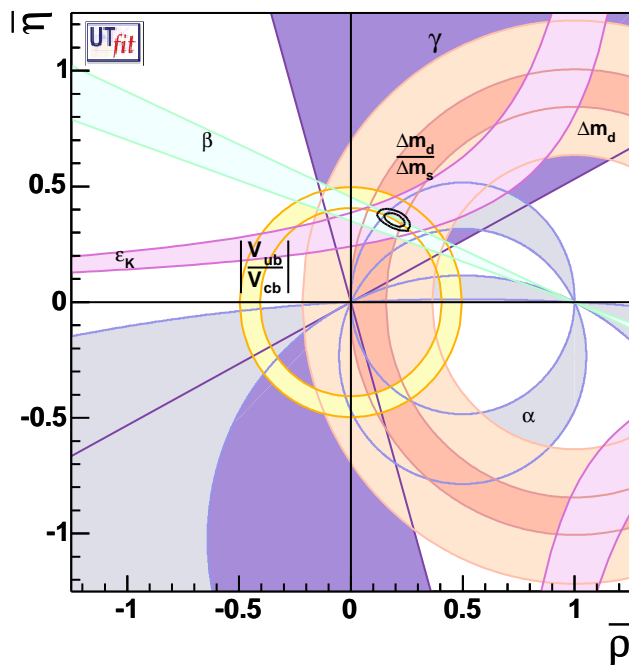
Figure 1.2: *Allowed regions for $(\bar{\rho}, \bar{\eta})$. The closed contours at 68% and 95% probability are shown. The full lines correspond to 95% probability regions for the constraints.*

fitting in the CKM description of the quark sector, would indicate new physics beyond the SM.

1.3 B-meson lifetime

The goal of the present work is to measure the lifetime of the B_s meson through its decays to the K^+K^- final state. The relevance of the measurement resides in its

discovery potential of new physics beyond the SM.

The easiest way to observe the presence of new physics in a process is to compare the results of the experimental measurement with its theoretical prediction in the framework of the SM. As shown in the following, the B_s meson calculation for the specific mode $B_s \rightarrow K^+K^-$ is extremely challenging and it is still affected by large theoretical uncertainties. In order to overcome this limitation and still to be able to challenge the prediction of the SM using the $B_s \rightarrow K^+K^-$ lifetime measurement, we will combine the result of our measurement with other lifetime information reported in literature to calculate the width difference ($\Delta\Gamma$) of the B_s meson, for which theoretical calculation up to NLO QCD corrections exists [16].

In what follows we will present a basic description of the theoretical methods used to calculate the B-mesons lifetime, to understand why the direct comparison with the SM lifetime prediction is not a feasible path toward the observation of NP in the $B_s \rightarrow K^+K^-$ decay.

1.3.1   B-meson Lifetime Calculation

In the framework of the SM it is possible to distinguish three classes of B-meson decays: leptonic, semileptonic and hadronic. In the following we will briefly describe the theoretical challenges behind the widths calculations for the different decay modes [18].
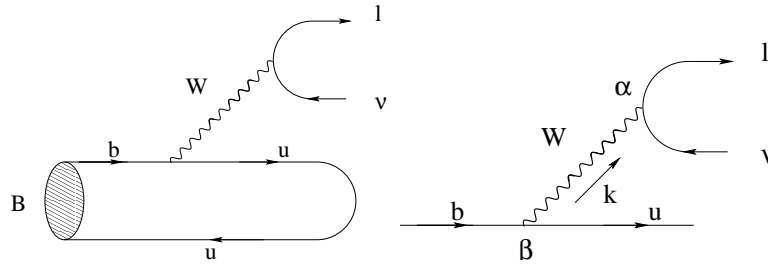
Figure 1.3: *Leptonic B-meson decay.*

The leptonic decay is the simplest to be calculated. Evaluating the Feynman diagram of the $B^- \rightarrow l\bar{\nu}$ in figure 1.3 we obtain

$$T_{fi} = -\frac{g_2^2}{8} V_{ub} \left[\bar{u}_l\gamma^\alpha(1-\gamma_5)v_\nu\right] \left[\frac{g_{\alpha\beta}}{k^2 - M_W^2}\right] \langle 0|\bar{u}\gamma^\beta(1-\gamma_5)b|B^-\rangle \qquad (1.28)$$

where g_2 is the $SU(2)_L$ gauge coupling, V_{ub} is the corresponding CKM element, M_W the mass of the W vector boson and k the four-momentum carried by the W boson.

The hadronic matrix elements can be written as

$$\langle 0|\bar{u}\gamma^\beta(1-\gamma_5)b|B^-(q)\rangle = if_B q^\beta \tag{1.29}$$

where f_B is the B-meson decay constant. The theoretical determination of f_B is very challenging and requires non perturbative techniques as lattice QCD. Performing the appropriate phase space calculation we obtain the decay rate

$$\Gamma(B^- \to l\bar{\nu}) = \frac{G_F^2}{8\pi}|V_{ub}|^2 M_B m_l^2 \left(1 - \frac{m_l^2}{M_B^2}\right)^2 f_B^2 \tag{1.30}$$

where M_B and m_l are the masses of the B-meson and lepton respectively. Because of the small value of $V_{ub} \propto \lambda^3$ (see section 1.2) and the helicity suppression, the typical branching ratio is of the order of $\mathcal{O}(10^{-10})$ and $\mathcal{O}(10^{-7})$ for $l = e$ and $l = \mu$ respectively.

Semileptonic decays have a structure more complicated than leptonic decays. The
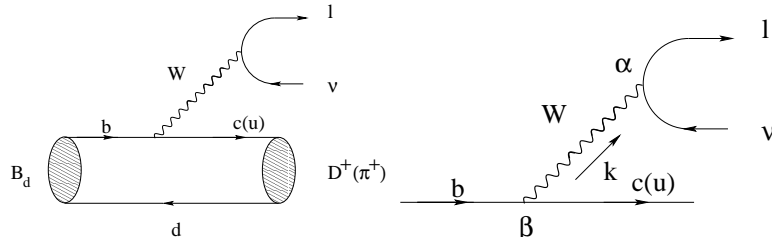
Figure 1.4: *Semileptonic B-meson decay.*

Feynman diagram in figure 1.4 corresponds to the semileptonic decay amplitude:

$$T_{fi} = -\frac{g_2^2}{8}V_{cb}\left[\bar{u}_l\gamma^\alpha(1-\gamma_5)v_\nu\right]\left[\frac{g_{\alpha\beta}}{k^2 - M_W^2}\right]\langle D^+|\bar{c}\gamma^\beta(1-\gamma_5)b|\bar{B}_d^0\rangle \tag{1.31}$$

All the hadronic physics is encoded in the hadronic matrix element:

$$\langle D^+(k)|\bar{c}\gamma^\beta(1-\gamma_5)b|\bar{B}_d^0(p)\rangle = \tag{1.32}$$

$$F_1(q^2)\left[(p+k)_\alpha - \left(\frac{M_B^2 - M_D^2}{q^2}\right)q_\alpha\right] + F_0(q^2)\left(\frac{M_B^2 - M_D^2}{q^2}\right)q_\alpha \tag{1.33}$$

where $q = p - k$ and the $F_{0,1}(q^2)$ denotes the form factors of the $B \to D$ transition. Compared to the leptonic transition we obtain two form factors instead of one, that again will have to be calculated with non perturbative techniques such as lattice QCD.

The most complicated B decays are the fully hadronic transitions, which are mediated by $b \rightarrow q_1 q_2 d(s)$ quark level processes, with $q_1, q_2 \in u, d, c, s$. There are two kind of diagram topologies contributing to these decays (see figure 1.5): tree diagrams and penguin diagrams. The latter consist of gluonic (QCD) penguin and electroweak (EW) penguins. Depending on the flavor content of the final states we can classify
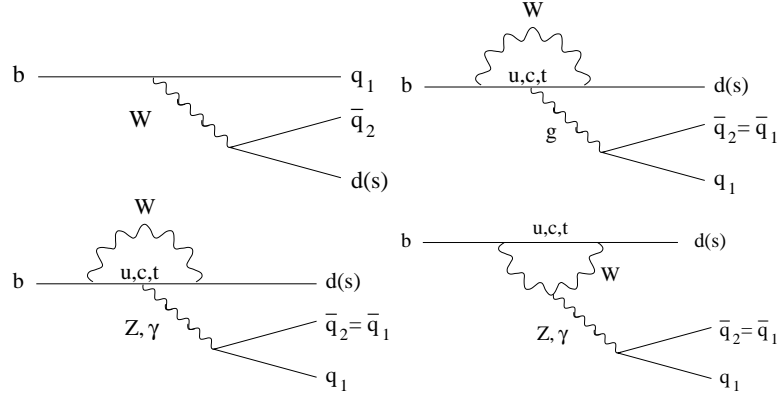
Figure 1.5: *Hadronic B-meson decay: (top-left) tree diagram; (top-right) QCD penguin; (bottom) EW penguins.*

the decays as follows:

- $q_1 \neq q_2 \in u, c$: only tree diagram contributes

- $q_1 = q_2 \in u, c$: tree and penguin diagrams contribute

- $q_1 = q_2 \in d, s$: only penguin diagrams contribute

The technique to analyse the hadronic B decays is based on the low-energy effective Hamiltonians, calculated using the operator product expansion (OPE), giving a transition matrix as follows:

$$\langle f | \mathcal{H}_{eff} | i \rangle = \frac{G_F}{\sqrt{2}} \lambda_{CKM} \sum_k C_k(\mu) \langle f | Q_k(\mu) | i \rangle \tag{1.34}$$

where G_F is the Fermi constant, λ_{CKM} is the CKM factor and μ is an appropriate renormalization scale. The OPE technique allows to separate the long-distance contributions described by the hadronic matrix elements $\langle f | Q_k(\mu) | i \rangle$ calculated with non-perturbative techniques from the short-distance contributions which are described by perturbative quantities $C_k(\mu)$ called Wilson coefficient functions. The Q_k are operators, generated by electroweak and QCD interactions and which describe the

"effective" decay. Unfortunately, the evaluation of the hadronic matrix elements is associated with large uncertainties and it still represent a very challenging theoretical task.

The $B_s \to K^+K^-$ lifetime belongs to the latter class of decay and because of the large theoretical uncertainties it is not yet possible to observe the presence of NP contributions through the direct comparison to the SM predictions.

1.4   Neutral B-meson mixing

The width difference $\Delta\Gamma$ plays an important role in the neutral B_s-meson mixing phenomenon [19].

$B_s - \bar{B}_s$ mixing refers to the transition between the two flavor eigenstates of the neutral B_s-meson $|B_s\rangle$ and $|\bar{B}_s\rangle$[2]. In the SM the $B_s - \bar{B}_s$ mixing is caused (at the lowest order) by the fourth order flavor changing weak interaction described by the box diagrams shown in figure 1.6. These transitions are usually called $|\Delta b| = 2$ amplitudes because they change the b-quark quantum number by two units. A
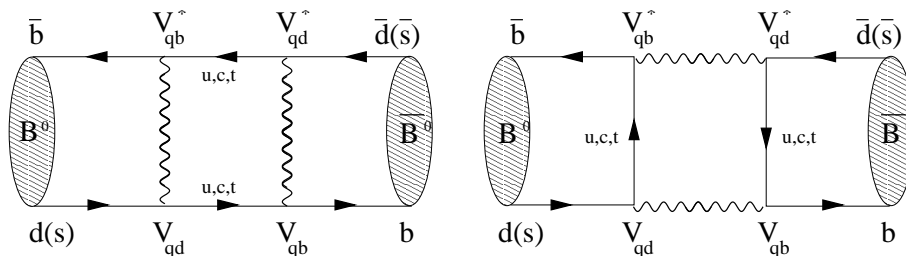
Figure 1.6: *Lowest order diagrams leading to the neutral B_s-mesons mixing*

B_s-meson generated at time $t = 0$ as a flavor eigenstate $|B_s\rangle$ evolves in a time-dependent quantum superposition of the two flavor eigenstates: $|B_s(t)\rangle$, $|\bar{B}_s(t)\rangle$. The time evolution of the $B_s - \bar{B}_s$ system is governed by the Schrödinger equation:

$$i\frac{d}{dt}\left(\begin{array}{c} |B_s(t)\rangle \\ |\bar{B}_s(t)\rangle \end{array}\right) = \left(M - \frac{i}{2}\Gamma\right)\left(\begin{array}{c} |B_s(t)\rangle \\ |\bar{B}_s(t)\rangle \end{array}\right) \tag{1.35}$$

where M and Γ are the 2×2 mass and decay hermitian matrices. $|B_s(t)\rangle$ denotes the state at time t of a meson produced as a B_s at time $t = 0$ (an analogous definition holds for $|\bar{B}_s(t)\rangle$).

---

[2]We will denote the neutral B-meson as B_s but the formalism we are developing can be applied to the B_d-meson as well

The off-diagonal elements M_{12} and Γ_{12} are responsible for the $B_s - \bar{B}_s$ mixing. In case of $M_{12} = \Gamma_{12} = 0$ (i.e. diagonal matrices) the B_s-meson created in a specific flavor eigenstate would remain indefinitely in that state.

Γ_{12} originates from the final states common to both B_s and $\bar{B}_s$. Since Γ_{12} is dominated by tree-level CKM-favoured decays, it is practically insensitive to any new physics contribution.

M_{12} is dominated by the box diagram in figure 1.6. This contribution is suppressed by four powers of the weak coupling constant and two powers of $|V_{ts}| \sim 0.04$ and so new physics could easily compete with the SM.

The mass eigenstates (Light-$|B_L\rangle$ and Heavy-$|B_H\rangle$) at time $t = 0$ are defined as the linear combination of $|B_s\rangle$ and $|\bar{B}_s\rangle$

$$|B_L\rangle = p|B_s\rangle + q|\bar{B}_s\rangle \tag{1.36}$$

$$|B_H\rangle = p|B_s\rangle - q|\bar{B}_s\rangle \tag{1.37}$$

with $|p|^2 + |q|^2 = 1$.

Denoting the masses and widths of the two mass eigenstates as $M_{L,H}$ and $\Gamma_{L,H}$, we define:

$$\Gamma = \frac{1}{B_s} = \frac{\Gamma_H + \Gamma_L}{2} \qquad \Delta m = M_H - M_L \qquad \Delta\Gamma = \Gamma_L - \Gamma_H \tag{1.38}$$

where $\Delta m > 0$ by definition and $\Delta\Gamma$ can be either signs but it is positive in the SM.

Solving the eigenvalue problem of $M - i\Gamma/2$ we find[3]:

$$\Delta m = 2|M_{12}| \qquad \Delta\Gamma = 2|\Gamma_{12}|\cos\phi \qquad \frac{q}{p} = -e^{-i\phi_M} \tag{1.39}$$

where $\phi_M = \arg(M_{12})$ is the phase of the mass matrix off diagonal element and the phase ϕ is the relative phase between the off-diagonal mass and the decay matrix elements:

$$\frac{M_{12}}{\Gamma_{12}} = -\left|\frac{M_{12}}{\Gamma_{12}}\right|e^{i\phi} \tag{1.40}$$

The phase ϕ is physical, i.e. it cannot be eliminated by rephasing. With this convention we ca write:

$$|B_L\rangle = \frac{1 + e^{i\phi}}{2}|B_s^{even}\rangle - \frac{1 - e^{i\phi}}{2}|B_s^{odd}\rangle \tag{1.41}$$

$$|B_H\rangle = -\frac{1 - e^{i\phi}}{2}|B_s^{even}\rangle + \frac{1 + e^{i\phi}}{2}|B_s^{odd}\rangle \tag{1.42}$$

---

[3]The experimental information $\Delta m \gg \Gamma$ model independently implies $|\Gamma_{12}| \ll |M_{12}|$

In the SM $\phi = \phi_M - \arg(-\Gamma_{12})$ and it is predicted to be of the order of 0.01, that translates in a tiny difference between mass eigenstates and flavor eigenstates.

The key quantity that we will encounter in the time evolution formulae and the CP violation effects for the B_s-meson is:

$$\lambda_f = \frac{q}{p}\frac{\bar{A}_f}{A_f} = \eta_f e^{-i\phi_M} \tag{1.43}$$

where $A_f = \langle f|B_s\rangle$, $\bar{A}_f = \langle f|\bar{B}_s\rangle$ and η_f is the CP parity of f: $CP|f\rangle = \eta_f|f\rangle$.

The time evolution of the B_s states will make use of the following definitions [19]:

$$\mathcal{A}_{CP}^{dir} = \frac{1-|\lambda_f|^2}{1+|\lambda_f|^2} \qquad \mathcal{A}_{CP}^{mix} = -\frac{2\Im(\lambda_f)}{1+|\lambda_f|^2} \qquad \mathcal{A}_{\Delta\Gamma} = -\frac{2\Re(\lambda_f)}{1+|\lambda_f|^2} \tag{1.44}$$

$\mathcal{A}_{CP}^{dir}$ describes the direct CP violation and stems from $|A_f| \neq |A_{\bar{f}}|$. $\mathcal{A}_{CP}^{mix}$ describes the CP asymmetry in mixing and stems from the interference of the decay amplitudes of the mixed and unmixed B-meson, i.e. $\bar{B}^0 \to f$ and $B^0 \to f$. These three quantities are not independent and obey the relation

$$\mathcal{A}_{CP}^{dir} + \mathcal{A}_{CP}^{mix} + \mathcal{A}_{\Delta\Gamma} = 1. \tag{1.45}$$

Time evolution of the tagged B^0 mesons

Integrating the Schrodinger equation, we obtain the following decay rates for the tagged B_s and $\bar{B}_s$ states:

$$\Gamma(B_s(t) \to f) = N_f|A_f|^2 \frac{1+|\lambda_f|^2}{2} e^{-\Gamma t}$$

$$\left[\cosh\frac{\Delta\Gamma t}{2} + \mathcal{A}_{CP}^{dir}\cos(\Delta mt) + \mathcal{A}_{\Delta\Gamma}\sinh\frac{\Delta\Gamma t}{2} + \mathcal{A}_{CP}^{mix}\sin(\Delta mt)\right] \tag{1.46}$$

$$\Gamma(\bar{B}_s(t) \to f) = N_f|A_f|^2 \frac{1+|\lambda_f|^2}{2} e^{-\Gamma t}$$

$$\left[\cosh\frac{\Delta\Gamma t}{2} - \mathcal{A}_{CP}^{dir}\cos(\Delta mt) + \mathcal{A}_{\Delta\Gamma}\sinh\frac{\Delta\Gamma t}{2} - \mathcal{A}_{CP}^{mix}\sin(\Delta mt)\right] \tag{1.47}$$

where N_f is a time-independent normalization factor.

Time evolution of the untagged B^0 mesons

Since B_s and $\bar{B}_s$ are produced in equal numbers, the untagged decay rate for the process $B_s \to f$, with f the general final state can be written as:

$$\Gamma[f, t] = \Gamma(B_s(t) \to f) + \Gamma(\bar{B}_s(t) \to f) = \tag{1.48}$$

$$N_f \left[e^{-\Gamma_L t}|\langle f|B_L\rangle|^2 + e^{-\Gamma_H t}|\langle f|B_H\rangle|^2 \right] \sim \tag{1.49}$$

$$N_f|A_f|^2 \left[1 + |\lambda_f|^2 \right] e^{-\Gamma t} \left\{ \cosh\frac{\Delta\Gamma t}{2} + \sinh\frac{\Delta\Gamma t}{2}\mathcal{A}_{\Delta\Gamma} \right\} \tag{1.50}$$

The expression in eq.1.49 explicitly shows how the decay is governed by two exponentials associated to the heavy and light eigenstates. Choosing the normalization such that $BR[all] = 1$, we can relate the overall normalization to the branching ratio:

$$BR[f] = \frac{1}{2}\int_0^\infty dt\Gamma[f, t] \sim \frac{N_f}{2}|A_f|^2 \left[1 + |\lambda_f^2| \right] \frac{\Gamma + \mathcal{A}_{\Delta\Gamma}\Delta\Gamma/2}{\Gamma^2 - (\Delta\Gamma/2)^2} \tag{1.51}$$

and write 1.50, the time evolution of the decay of an untagged B_s sample, as:

$$\Gamma[f, t] = 2BR[f]\frac{\Gamma^2 - (\Delta\Gamma/2)^2}{\Gamma + \mathcal{A}_{\Delta\Gamma}\Delta\Gamma/2}e^{-\Gamma t} \left[\cosh\frac{\Delta\Gamma t}{2} + \sinh\frac{\Delta\Gamma t}{2}\mathcal{A}_{\Delta\Gamma} \right] \tag{1.52}$$

In this way if $\Gamma = (\Gamma_L + \Gamma_H)/2$ is known, one could perform a two parameters fit of the decay distribution and determine $\Delta\Gamma$ and $\mathcal{A}_{\Delta\Gamma}$.

This expression shows that with a sizable $\Delta\Gamma$ it should be possible to extract information on the CP violation ($\mathcal{A}_{\Delta\Gamma}$) even from untagged B_s decays.

In the B_d system the the world average mass difference indicates [20]:

$$\Delta m_d = 0.511 \pm 0.003(stat) \pm 0.005(syst) \tag{1.53}$$

The fractional width difference is calculated to be very small $(2.42 \pm 0.59) \times 10^{-3}$ [21] and a recent measurement [22] has obtained

$$\frac{\Delta\Gamma_d}{\Gamma_d} = -0.008 \pm 0.037(stat) \pm 0.018(syst) \tag{1.54}$$

compatible with the prediction.

The experimental knowledge of the B_s sector is rapidly evolving following the improved performance of the Tevatron accelerator complex. A redundant set of measurements on the B_s meson triangle allows to bound the presence of NP in the B_s sector. The measurement of Δm_s and Δm_d allow to extract the magnitude of the

ratio of the CKM elements $|V_{td}/V_{ts}|$ and so to constrain one side of the unitarity triangle R_t in eq.1.24. The CDF collaboration recently produced the first measurement of Δm_s [23]:

$$\Delta m_s = 17.33 \pm^{+0.42}_{-0.21} (stat.) \pm 0.07 (syst.) \tag{1.55}$$

(which is compatible with the SM expectation) supplanting the previous double bound [24]. The measurements of $\Delta \Gamma_s$ and A_{SL} (the semileptonic charge asymmetry, measuring the CP violation in mixing) allow for the first time to bound the phase β_s of the total mixing amplitude. The fractional width difference is predicted to be large $(7.4 \pm 2.4) \times 10^{-2}$ [16], and the recently updated world average indicates [14]:

$$\frac{\Delta \Gamma_s}{\Gamma_s} = +0.25 \pm 0.09 \tag{1.56}$$

The average of A_{SL}, compatible with zero, is [17]:

$$A_{SL} = -0.013 \pm 0.015 \tag{1.57}$$

The constraints on the mixing phase are still too weak to draw any conclusion on the presence of NP[17]. To improve these constrain, smaller experimental uncertainties on $\Delta \Gamma_s$ and A_{SL} are of primary importance.

In the next section we will show how the measurement of the $B_s \to K^+K^-$ life leads to the determination of $\Delta \Gamma_s$.

1.5 B_s width difference and the $B_s \to K^+K^-$ lifetime

The width difference $\Delta \Gamma$ can be measured from the time evolution of the untagged B_s sample. As shown in eq.1.49, the general expression for the $B(\bar{B}) \to f$ decay formula is governed by a two exponential formula that can be rewritten, using eq.1.37 and eq.1.43, as:

$$\Gamma[f,t] = 2BR(B_s \to f)\Gamma e^{-\Gamma t} \left[(1 - \mathcal{A}_{\Delta\Gamma}) e^{-\Gamma_L t} + (1 + \mathcal{A}_{\Delta\Gamma}) e^{-\Gamma_H t} \right] \tag{1.58}$$

In principle one could measure $\Delta \Gamma$ by fitting the decay distribution of any decay $|\mathcal{A}_{\Delta\Gamma}| \neq 1$ to the previous expression of $\Gamma[f,t]$. In practice, however, one will at best be able to measure the deviation from a single exponential up to terms linear in $\Delta\Gamma t$. Expanding the previous expression in $\Delta\Gamma t$ one finds:

$$\Gamma[f,t] = 2BR(B_s \to f)\Gamma e^{-\Gamma t} \left[1 + \frac{\Delta\Gamma}{2} \mathcal{A}^f_{\Delta\Gamma} \left(t - \frac{1}{\Gamma} \right) \right] + \mathcal{O}\left((\Delta\Gamma t)^2\right) \tag{1.59}$$

Unless one is able to resolve the quadratic terms $\mathcal{O}\left((\Delta\Gamma t)^2\right)$, one can only determine the product $\Delta\Gamma\mathcal{A}_{\Delta\Gamma}^f$.

Flavour specific modes, on the other hand, are characterized by $\lambda_f = 0$ and so $\mathcal{A}_{\Delta\Gamma}^f = 0$. Thus the term involving $\Delta\Gamma$ vanishes and therefore they determine Γ up to $(\Delta\Gamma)^2$.

In order to gain information on $\Delta\Gamma$ from eq 1.58 one must consider decays with $\lambda_f \neq 0$. But λ_f and $\mathcal{A}_{\Delta\Gamma}^f$ depend on the mixing phase ϕ_M and therefore change in the presence of new physics in M_{12}. Within the SM we can calculate ϕ_M and $\mathcal{A}_{\Delta\Gamma}^f$ and then extract $\Delta\Gamma$ from the measured product $\Delta\Gamma\mathcal{A}_{\Delta\Gamma}^f$. In the presence of new physics one needs additional information. This can be accomplished, for example, measuring both Γ_L and Γ_H.

In the SM the B_s phase $\phi = \beta_s$ is small (see section 1.2) and can be neglected in the discussion of $\Delta\Gamma$. Doing so, the mass eigenstates coincide with the CP eigenstates (eq.1.42) defined as:

$$|B_s^{even}\rangle = \frac{1}{\sqrt{2}}\left(|B_s\rangle - |\bar{B}_s\rangle\right) = |B_L\rangle$$

$$|B_s^{odd}\rangle = \frac{1}{\sqrt{2}}\left(|B_s\rangle + |\bar{B}_s\rangle\right) = |B_H\rangle \qquad (1.60)$$

Being dominated by the phase of the tree diagram, the $b \to c\bar{c}s$ transition can be used as an example to illustrate how to measure the two exponential Γ_L and Γ_H. Any $b \to c\bar{c}s$ decay into a CP-even final state (like $B_s \to D_s^+ D_s^-$) stems only from the $|B_L\rangle$ component of the untagged B_s sample. Hence a lifetime fit to this decay determines Γ_L. Any $b \to c\bar{c}s$ decay into a CP-odd final state, on the other hand, (like the $L = 1$ angular state of the $B_s \to J/\psi\phi$ decay) determines Γ_H.

These are easy to demonstrate from eq.1.58 using the value of $\mathcal{A}_{\Delta\Gamma}^f$. From eq. 1.39 $q/p = -1$ and the CP parity is $\bar{A}_f/A_f = -\eta_f$. Hence for any $b \to c\bar{c}s$ decay the coefficient of $\exp(-\Gamma_H t)$ vanishes for a CP-even eigenstate ($\eta_f = +1$) while the $\exp(-\Gamma_L t)$ vanishes for a CP-odd final state ($\eta_f = -1$).

The decay examined in the present work $B_s \to K^+ K^-$ has a less straightforward theoretical interpretation.

The $B_s \to K^+ K^-$ is a CKM-suppressed decay mode, where the weak phase of the decay is not known. This complication stems from the not yet understood relative contribution of the penguin diagrams with respect to the tree [25]. However by vertex counting in the diagrams in figure 1.5 it is possible to observe that the $b \to u\bar{u}s$ tree diagram is suppressed, with respect to the penguin diagram, by $\mathcal{O}(\lambda)$. It is therefore expected that the examined transition receives its dominant contribution from penguin decays.

Another "complication" comes from NP contribution in the penguin loops. The presence of CP violating NP could significantly modify the phase of the decay and so

$\lambda_{K^+K^-}$ could be significantly different from $+1$ so that $\mathcal{A}_{\Delta\Gamma}^{K^+K^-} \neq -1$.

In both cases (tree contribution or NP) a contribution from $B_s^{odd} \to K^+K^-$ would arise and so spoiling the single exponential distribution of the $B_s \to K^+K^-$ proper decay time.

If we assume the $b \to u\bar{u}s$ to be dominated by penguin loops and that new physics does not contribute significantly to the penguin loops, $\lambda_{K^+K^-}$ would indeed be equal to $+1$ and the coefficient $\left(1 + \mathcal{A}_{\Delta\Gamma}^{K^+K^-}\right)$ would vanish, eliminating the contribution of $\exp(-\Gamma_H t)$ from the decay width in eq. 1.58.

The analysis of the $B_s \to K^+K^-$ lifetime has been performed fitting the proper decay time distribution to a single exponential, assuming the decay dominated by the CP-even component and assuming no contributions coming from NP [4].

As shown in section 1.3, due to the large theoretical uncertainties on the SM prediction of the $B_s \to K^+K^-$ lifetime, it is not possible to gain direct information on NP comparing the present measurement with the theoretical estimate. It is however possible to compose the $B_s \to K^+K^-$ lifetime with other lifetime information in literature to extract $\Delta\Gamma_s$, a quantity calculated up to NLO QCD corrections [5].

In the SM the mass eigenstates coincide with the CP eigenstates (eq. 1.60) and $\Delta\Gamma_{SM} = \Delta\Gamma_{CP} = \Gamma_L - \Gamma_H$. The effect of CP violating phases in NP would reduce $\Delta\Gamma$ [26]:

$$\Delta\Gamma = \Delta\Gamma_{CP}\cos\phi \qquad (1.61)$$

while $\Delta\Gamma_{CP} = 2|\Gamma_{12}|$ is not sensitive to new physics.

In the SM $\phi = \beta_s = arg(-(V_{cs}V_{cb}^*)/(V_{ts}V_{tb}^*)) \sim 0$, so $\cos\phi \sim 1$. With CP violating NP β_s could be larger, leading to $\cos\phi < 1$ and so reducing $\Delta\Gamma$.

The reduction of $\Delta\Gamma$ can be also intuitively understood as follows. In absence of CP violation, the two mass eigenstates are also CP eigenstates. The large $\Delta\Gamma$ is an indication that most of the B_s decays are into CP even final states. With CP violation the mass eigenstates are no longer approximate CP eigenstates. Then both mass eigenstates can decay into CP even final states. Consequently $\Delta\Gamma$ is reduced.

Experimentally, the estimate of $\Delta\Gamma_s$ is however challenging. Even if the SM prediction of $\Delta\Gamma/\Gamma$ for the B_s-meson is of the order of 10% a measurement of a non zero $\Delta\Gamma/\Gamma$ would require to achieve an absolute uncertainty of about 3%. In presence of NP the measured $\Delta\Gamma/\Gamma$ would be further reduced requiring even higher precision.

---

[4]The attempt to fit the proper decay time distribution to the complete formula in eq. 1.58, due to the still low statistics of the analyzed sample, lead to non conclusive results on the presence of a CP-odd component.

[5]This procedure will be followed in the results discussion in Chapter 5

Chapter 2

Experimental apparatus

"Misura ció che é misurabile, e rendi misurabile ció che non lo é."
Galileo Galilei

The Fermilab accelerator complex is a chain of machines used to produce, accelerate and store particles at high energy. Generally, particles with known properties are used as a tool to investigate new characteristics of matter. An example are α particles first discovered and studied with radioactive substances and then used as projectile to explore the nucleus of the atom. Today at Fermilab, almost a hundred years later, well known particles (protons) and their also well known anti-particles (anti-protons) are brought to collide at high energy to create and study new (unstable) forms of matter. Because of the large mass of the particle we are interested in (the b-quark is heavier than the helium nucleus, the top quark is as heavy as the Ytterbium nucleus) we need to go to high energy collisions. Since the production of heavy particles, even at the energy reachable at Fermilab, is a rare process, we do not collide protons and anti-protons one by one. Instead we produce dense fluxes of particles (beams) and make them to collide. The Fermilab accelerator complex is at present the facility that creates the highest energy artificial collision: $1.96\ TeV$. In nature much higher energies are reached through many, mostly not yet understood, processes. One TeV is about 10^{12} times the energy of the visible light. If to see the light we can use our eyes as detectors, in order to "see" the usually short lived particles created in high energy collisions it is necessary to use very specialized devices such as CDF (Collider Detector at Fermilab) to collect the data analysed in the present measurement. The high energy physics detectors collect the "debris" originating from the decay of the particles produced in the collisions and allow physicists to reconstruct their original characteristics. High energy physics detectors are divided in sub-detectors with characteristics related to way the "debris" interact with matter. Close to the collision point there is the tracker, a group of sub-detectors that are almost transparent to all the particles. These sub-detectors are designed in layers, each of which records

the point where the particles have passed. Connecting the points together we obtain their trajectories (tracks). After the tracker there are the calorimeters, which are based on a very different principle. Most particles enter the calorimeters and initiate a particle shower, depositing the energy that will be measured. For this reason these detectors are usually very thick and made of materials like steel. The last layer of the typical high energy physics detector is usually the muon detector. Muons are in fact very penetrating particles and the only ones that are able to pass undisturbed through the calorimeters (aside from neutrinos that are not detected at all in collider experiments).

In this chapter we will describe the Fermilab accelerator complex and give details of the structure of the CDF sub-detectors used in the present measurement.

CDF collected data in the years 1992 - 1996, the so called Run I period. Between 1996 and 2001 both the accelerator complex and the detector underwent major upgrades and from 2001 to the present it has been collecting the Run II data. With the structure of the detector greatly improved during the upgrades, we refer to the present detector as CDF II.

Here and in the following we will omit the "II" part of "CDF II", unless explicitly stated.

2.1   The Accelerator complex

The Fermilab accelerator complex [27] is presented in figure 2.1. It is a chain of accelerators ending in what today is the highest energy proton-antiproton collider, the "Tevatron". The main goals of the accelerator complex are proton-antiprotons collisions at the center of mass energy of 1.96 TeV, and high intensity proton beams used for neutrino physics and fixed target experiments. In this section we describe how the protons and anti-protons beams are produced and brought to collide.

Protons are taken from hydrogen. The neutral hydrogen atoms are first ionized to H^- (stripping an electron from a cesium surface) and then accelerated with a Cockcroft-Walton accelerator, which is a 750 kV DC voltage source. The 750 keV H^- ions are sent to a linac [28] that brings their energy to 400 MeV. The ions are then injected in the Booster [29], a synchrotron. Passing through a thin carbon foil, the two electrons are stripped off turning the H^- ions into bare protons that are accelerated to 8 GeV and transferred to the Main Injector [30]. The Main Injector is another synchrotron that can operate in different modes. It can accelerates the protons up to 150 GeV and inject them in the Tevatron, or it can accelerate protons to 120 GeV to be used to produce anti-protons. Moreover it is also designed to receive the anti-protons left over from the collisions in the Tevatron, decelerate them to 8 GeV and transfer them to the Recycler [32]. This mode of operation is still under development.
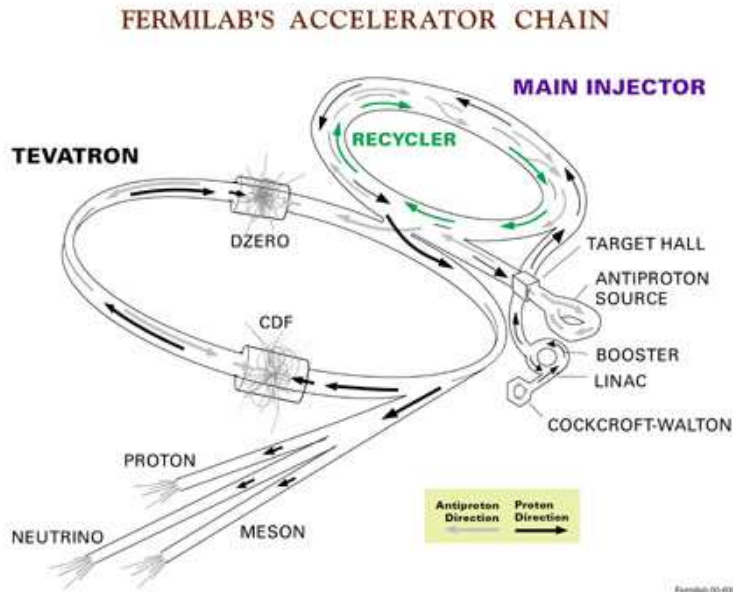
Figure 2.1: *Fermilab accelerator complex.*

The anti-protons are produced directing 120 GeV protons on a nickel target [31]. The particles produced at the target are focused with a lithium lens and passed through a dipole magnet that selects the anti-protons with an average energy of 8 GeV. At this stage the anti-protons have a wide energy spectrum. In order to collect them in the accumulator ring, it is necessary to cool the beam. This is performed with the stochastic cooling technique. The basic principle is to sample the average motion of the anti-protons in the beam with a pickup sensor and send the information to a kicker magnet to correct their trajectory.

Out of one million protons on target only about 20 anti-protons will survive at the Accumulator.

The anti-protons stacked in the Accumulator in 36 bunches of about 3×10^{10} particles are then injected back to the Main Injector, where they are accelerated to 150 GeV with the corresponding 36 proton bunches of about 3×10^{11} particles. Finally protons and anti-protons are injected in the Tevatron [33] that accelerates them to 980 GeV before initiating the collisions at the two collision points: B0 hosting the CDF detector and D0 hosting the homonymous detector.

The instantaneous luminosity at the collision points can be approximated to:

$$\mathscr{L} = \frac{f \cdot N_B \cdot N_p \cdot N_{\bar{p}}}{2\pi \left(\sigma_p^2 + \sigma_{\bar{p}}^2 \right)}$$

where f is the revolution frequency, N_B is the number of bunches in the collider, N_p, $N_{\bar{p}}$ are the number of protons and anti-protons per bunch and σ_p, $\sigma_{\bar{p}}$ are the r.m.s. beam size at the collision points. Table 2.1 list some collider parameters. The typical instantaneous luminosity at the beginning of the store routinely exceeds

Parameter	
number of bunches (N_B)	36
bunch length [cm]	18
bunch spacing [ns]	396
σ_p [μm]	20
$\sigma_{\bar{p}}$ [μm]	20
protons/bunch (N_p)	3.3×10^{11}
anti-protons/bunch (N_p)	3.6×10^{10}
interaction/crossing	5.3
typical luminosity [$cm^{-2}s^{-1}$]	0.9×10^{32}

Table 2.1: *Run II Tevatron parameters.*

1.0×10^{32} $cm^{-2}s^{-1}$. Figure 2.2 shows the instantaneous and integrated luminosities plots at the moment of writing.

2.2   The CDF detector

CDF [34] is a general purpose detector which combines precision tracking with fast projective calorimetry and fine grained muon detection. A sketch of the detector is shown in figure 2.3. The tracking systems are contained in a superconducting solenoid 4.8 m long and 1.5 m in radius, with a 1.4 T magnetic field parallel to the beam axis. The calorimetry and the muon detectors are all located outside the magnet. CDF uses a cylindrical coordinate system (r, ϕ, z) with the origin located at the center of the detector, the z axis along the nominal direction of the proton beam and the $\phi = 0$ or "y axis" pointing upward. Charged particles moving in an homogeneous solenoidal magnetic field follow helical trajectories. Reconstructed trajectories are referred to as "tracks".
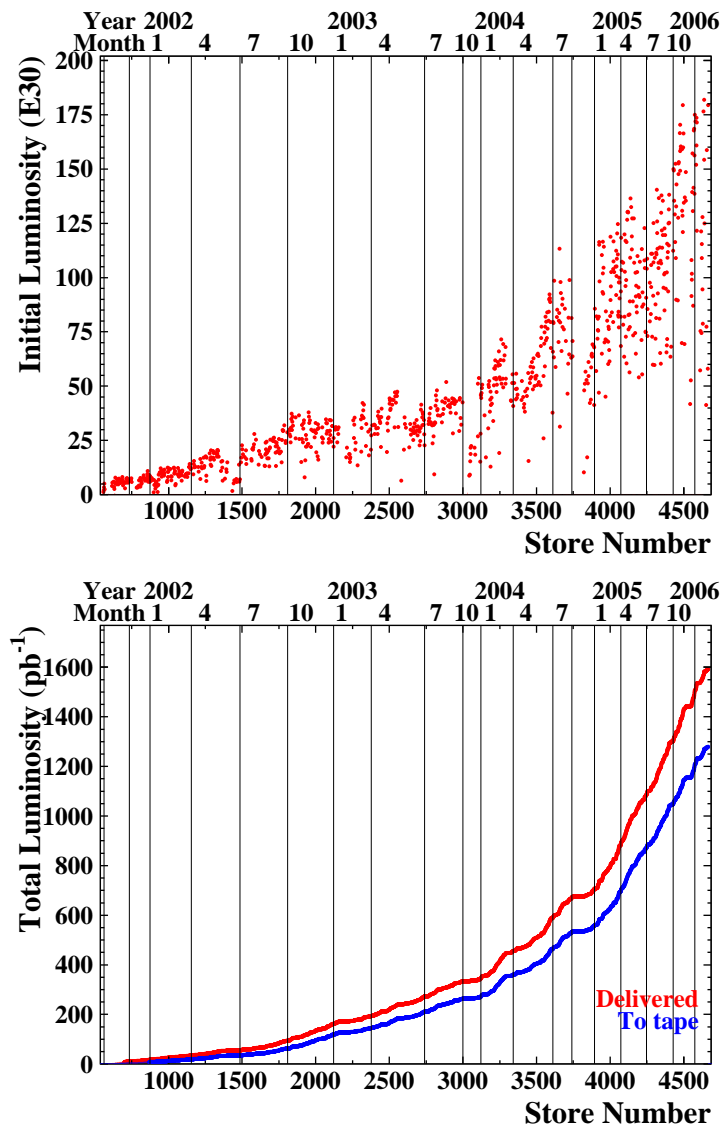
Figure 2.2: *(top) Peak instantaneous luminosities. (bottom) Integrated luminosity, (red) delivered and (blue) recorded.*
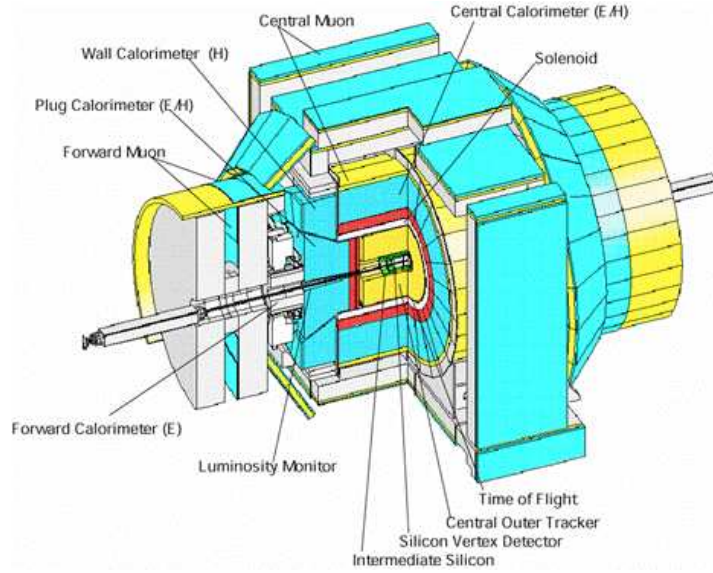
Figure 2.3: *The CDF detector.*

The helix is defined by five parameters. Three of them describe the position in cylindric coordinates of the point of closest approach of the helix to the beam axis: d_0, ϕ_0, z_0. The other two describe the momentum vector: C the curvature and $\cot\theta$ the pitch of the helix. From these quantities it is possible to extract the transverse and longitudinal momenta of the track.

The plane perpendicular to the beam axis is referred to as "transverse plane". Quantities defined in the transverse plane are conserved.[1]

We define the rapidity as:

$$\zeta := \frac{1}{2} \log \frac{E + p_z}{E - p_z}$$

where E is the energy of the particle and p_z is the longitudinal momentum. Under a boost β along the z-axis it transforms as $\zeta' = \zeta + \tanh^{-1}\beta$, which means that rapidity intervals are invariant under such a transformation. In the ultra-relativistic approximation we can define the "pseudo-rapidity":

$$\eta := -\log\tan\frac{\theta}{2}$$

---

[1]In a hadron-hadron collision not all of the centre of mass energy is absorbed in the collision. The partons carry only a fraction of the kinetic energy of the proton, as a result the centre of mass of the colliding partons is boosted along the beamline by a variable amount.

where θ is measured from the z axis. The pseudorapidity has a pure geometrical meaning. This variable is often used to indicate the angle between the y-axis and a track. All sub-detectors (whenever appropriate) are uniformly segmented in (η, ϕ) which simplifies the data interpretation.

The Run II Tevatron upgrade brought higher luminosity and a finer spaced beam structure (36 bunches with a bunch spacing of 396 ns to be compared with the 6 bunched at 3.5 μs of the Run I). This led to issues of occupancy and pile-up that required a series of major upgrades in the CDF detector, resulting it in what we know today as CDF II.

- Silicon detector: the SVX II has a larger surface and η coverage than its predecessor SVX.

- A new drift chamber "Central Outer Tracker" (COT), has replaced the Run I CTC, with a faster charge collection time.

- Extensions have been made of the electromagnetic and hadronic calorimeters for a coverage up to $\eta = 3$.

- Extension of the muon chambers for a coverage up to $\eta = 1.5$ have been made.

- Improved particle identification is achieved through the dE/dx measurement in the drift chamber and the newly installed Time of Flight (TOF) detector.

- A new data acquisition is capable of sustaining the 396 ns bunch spacing.

- There is an innovative trigger capability.

In the following we will describe the sub-detectors most relevant to the present analysis.

2.3 Vertexing and Tracking

Efficient and precise charged particle vertexing and tracking for both high and low momentum tracks is required in many physics analyses. This is achieved in CDF with silicon detectors and a drift chamber. In figure 2.4 a schematic view of a quarter of the tracker system shows its position with respect to the solenoid and the plug calorimeters. Table 2.2 describes the main tracker parameters.

CDF   Tracking   Volume
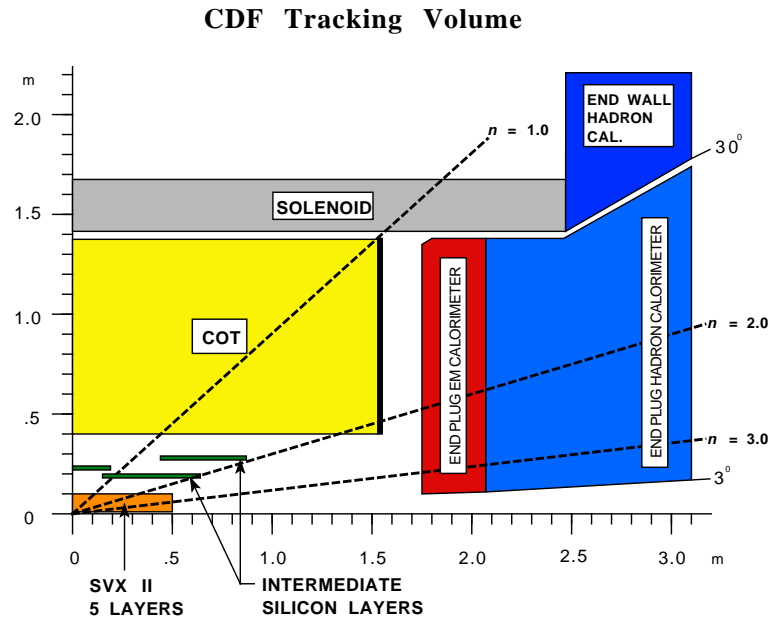
Figure 2.4: *A schematic view of the CDF tracker.*
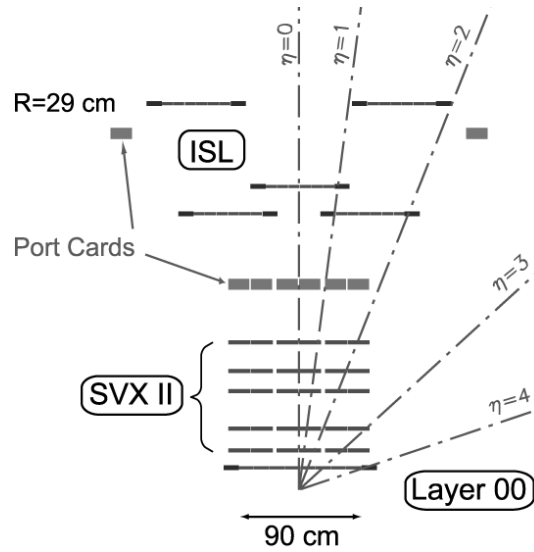
Figure 2.5: *η coverage of the silicon layers.*

2.3.1 Silicon Detectors

The innermost tracking device is a silicon micro-strip vertex detector, which consist of three sub-detectors: "Layer 00", "SVX II" and "ISL", see figure 2.5. Layer 00 (L00) [35] is a single sided silicon assembly, installed on the beryllium vacuum pipe at a radius 1.5 cm from the beam. Though L00 has only $r - \phi$ information, thanks to its proximity to the collision point it allows when combined with the SVX II information to measure a mean d_0 resolution of 25 μm.

The Silicon VerteX detector (SVX II) [36] is mechanically divided in three barrels with a total length of 98 cm and a η coverage $|\eta| < 2$. Each barrel supports 5 layers of double sided silicon micro-strip detectors located at radii between 2.4 and 10.7 cm. The layers are numbered inside out from 0 to 4. Layers 0, 1 and 3 combine $r - \phi$ measurement on one side with a 90° stereo measurement in the other. Layers 2 and 4 combine the $r - \phi$ measurement with a small stereo angle $20mrad$. The fundamental mechanical unit, called "ladder", is made by 4 silicon crystals aligned along the z direction. The crystals are mounted on a boron-carbon structure to minimize the thermal stress. Twelve ladders make a layer and the 60 ladders in each barrel are mounted between beryllium bulkheads that also support the read out electronics and the cooling pipes. The readout chips are mounted on an electrical hybrid on the surface of the silicon, for a faster data acquisition. The entire SVX II can be readout in 10 μs. The high speed readout allows, as it will be shown, to include the silicon information already at the second level of trigger.

The Intermediate Silicon Layer (ISL) [37] consists of one silicon layer at a radius of 22 cm in the central region and two silicon layers at radii 20 and 28 cm in the forward region. ISL increases the number of silicon layers available to reconstruct the tracks. In particular, although most of the track reconstruction algorithms start from the COT information, the ISL layers provide a curvature measurement sufficient for the stand-alone use of the silicon tracker in $|\eta| < 2$.

2.3.2 Drift Chamber

The Central Outer Tracker (COT) [38] is an open cell drift chamber with a cylindrical symmetry around beam pipe. Radially, the COT contains 96 sense wires layers, grouped in eight "superlayers" (see figure 2.6). Each superlayer is divided in ϕ is supercells each of which contains 12 sense wires, the maximum drift distance being approximately the same for all superlayers. The entire COT contains 30,240 sense wires, half of which are aligned along the z-axis while the remaining half is tilted of a small angle (2°). The active radius of the COT extends from 44 cm to 138 cm and it is 310 cm in length. This means that trajectories at $|\eta| < 1$ pass through all eight superlayers. The COT is filled with a Argon-Ethane-CF4 (50:35:15) gas mixture. This gas mixture has been chosen to have a maximum electron drift time of

COT	
Radial coverage	from 44 to 132 cm
Pseudorapidity coverage	$\|\eta\| < 1$
Number of superlayers	8
Maximum drift distance	0.88 cm
Resolution	180 μm
Number of channels	30,240
Material radiation length	1.3% X_0
ISL	
Radial coverage	from 20 to 28 cm
Pseudorapidity coverage	$\|\eta\| < 1.9$
Number of layers	1 at $\|\eta\| < 1$ and 2 at $1 < \|\eta\| < 2$
Resolution	20 μm (axial)
Number of channels	268,800
Material radiation length	2% X_0
SVX II	
Radial coverage	from 2.4 to 10.7 cm
Pseudorapidity coverage	$\|\eta\| < 2$
Number of layers	5
Resolution	16 μm (axial)
Number of channels	423,936
Material radiation length	3.5% X_0
L00	
Radial coverage	from 1.35 to 1.65 cm
Number of layers	1
Resolution	9 μm (axial)
Number of channels	13,824

Table 2.2: Main characteristics of the tracking system.
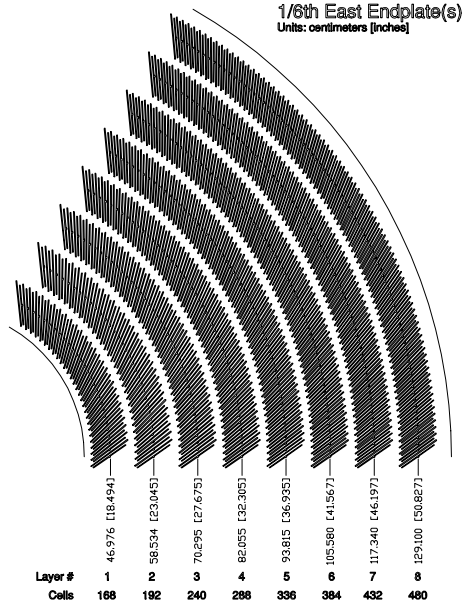
Figure 2.6: *One sixth of the superlayers structure of the COT.*

about 100 ns. Given the 1.4 T solenoidal magnetic field and the cell's electric field, the Lorentz angle is approximately 35°. Since the maximum resolution on the hit is obtained when the electron drift direction is perpendicular to that of the track, to compensate the Lorentz angle the cells are tilted by 35° away from the radial position. The single hit position resolution of the COT has been measured to be about 140 μm, that translates into a transverse momentum resolution $\frac{\delta p_T}{p_T} \sim 0.15\% \frac{p_T}{GeV/c}$.

2.3.3 Time of Flight

Between the magnetic coil and the COT the Time of Flight detector (TOF) [39] is installed. This system is composed of scintillator bars 3 m long and 4 cm thick. The bars are read out at each end by a photomultiplier tube. The timing and amplitude of the pulses allow an average resolution of about 130 ps. As will be shown in the next section, this performance makes the TOF a good particle identification detector for low momentum tracks.

2.4 Particle identification

Particle identification is obtained in CDF by measuring the tracks' specific energy deposition in the COT and by measuring the time of arrival in the bars of the TOF.
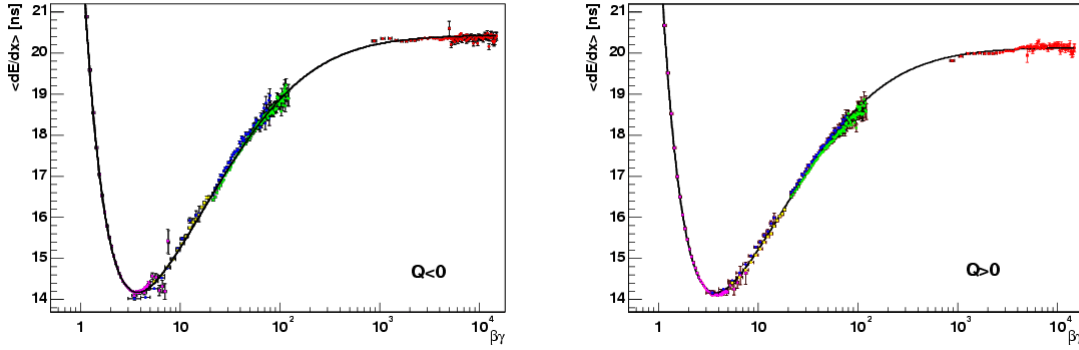
Figure 2.7: *Specific ionization universal curves as a function of $\beta\gamma$, left are negative charged particles, right positive charged particles: (pink) protons, (yellow) kaons, (blue) pions, (green) muons, (red) electrons.*

Signals on the sense wire of the COT are processed by the ASDQ (Amplifier, Shaper, Discriminator with charge encoding) chips. The time over threshold of the signal is related to the amount of charge collected by the wire. The width of the signals is calibrated to correct for the intrinsic spread due to the COT geometry, the path length of the particle, the electronics pedestals etc. Once calibrated the pulse width will be related to the specific energy loss of the charged particles in the chamber (dE/dx). After these "wire-by-wire" calibrations [40], chamber inefficiencies and other global effects leave residual non-uniformities in the (η, ϕ) dE/dx distribution. To remove this dependences a set of track based calibrations [41] have been produced with different particle species (protons, pions, kaons, muons and electrons) covering a $\beta\gamma$ range between 1 and 10^4. The result of the calibrations is shown in figure 2.7. Figure 2.8 shows the separation between pions and respectively kaons, electrons and protons. The separation between pions and kaons is about 1.6 σ at 3 GeV/c, the separation between pions and electrons is about 2 σ at 3 GeV and the separation between pions and protons is about 2 σ at 5 GeV/c. The particle identification performance of the COT does not allow an event by event separation of the particle species. Nevertheless, the attained separation is a crucial ingredient for many statistical analysis.

The time of flight t, is defined as the time interval between the collision and the arrival of the particle at the TOF bars. Similarly, the path length L of the particle is calculated as the distance between the beam collision and the point where the particle crosses the scintillator bars. Using the momentum information and the speed $(\beta\gamma)$ of
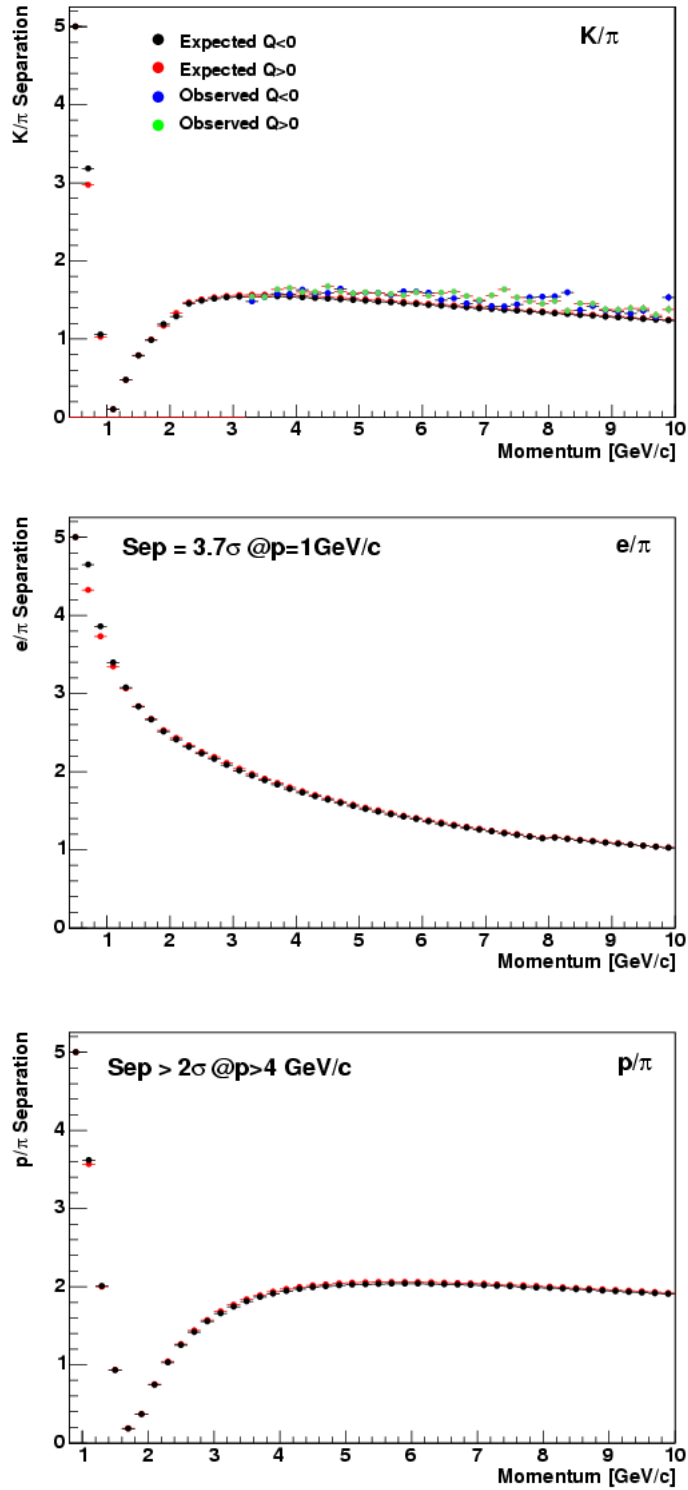
Figure 2.8: *Expected particle separation performance as a function of the particles momentum using the COT dE/dx information for $\pi - K$ (top left), $e - \pi$ (top right), $p - \pi$ (bottom). In all plots black dots are the negative charges, red the positive. The top left plot shows also the measured separation between kaons and protons, in blue (negative) and green (positive) charges.*
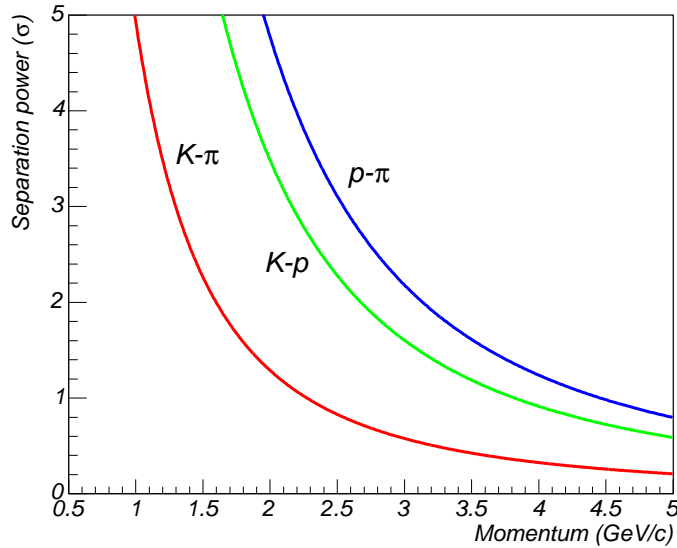
Figure 2.9: *TOF separation power: (red) kaon-pion, (green) kaon-proton, (blue) pion-proton.*

the particle it is possible to estimate its mass:

$$m = \frac{p}{c}\sqrt{\left(\frac{ct}{L}\right)^2 - 1}$$

The particle identification obtained with this method is particularly powerful at low momenta (see figure 2.9). For track momenta below 1.6 GeV/c the kaon pion separation is above 2 σ [42].

2.5   Other Sub-detectors

Beside the tracker, CDF contains other sub-detectors. Because they are not relevant for the present analysis, only a brief description of them will be given here.

2.5.1   Calorimetry

The CDF calorimetry has a projective geometry, which means that the segmentation in η, ϕ towers is pointing towards the interaction region. The coverage is 2π in ϕ and $|\eta| < 4.2$. The calorimeter is divided in three regions: central, plug and

forward. Each tower covers $\Delta\phi = 7.5°$ and $\Delta\eta = 0.1$ in the central region while in the forward region the ϕ segmentation is 15°. Each calorimeter tower consists of an electromagnetic shower counter followed by an hadronic calorimeter. This allows a comparison of the electromagnetic and hadronic energy deposited in each tower and thus the identification of electrons and photons from hadrons.

The electromagnetic calorimeter is subdivided in three sub-detectors: central (CEM), plug (PEM) and forward (FEM). The CEM uses lead sheets interspersed with scintillator as the active material. The PEM and FEM are proportional chambers. Both CEM and PEM are equipped with shower maximum detectors, named CES (central) and PES (plug), embedded at a depth of about 6 radiation lengths. These position detectors allow for track matching thus contributing to the electron photon identification. They also provide transverse shower profile information to improve the γ/π^0 separation. Just before the CEM there is a set of multiwire proportional chambers called Central Pre-showeR (CPR) that samples the electromagnetic showers beginning in the solenoid material in front of them, enhancing the photon and soft electrons identification.

The central (CHA)and endwall (WHA) hadron calorimeters are composed of alternating layers of iron and scintillator. The plug (PHA) and forward (FHA) detectors are made of alternating layers of iron and gas proportional chambers.

2.5.2 Muon Systems

The muon systems are hosted in the outer part of CDF behind the calorimetry and, in some cases, additional steel absorber. The muon system is composed of scintillator counters and proportional drift chambers: CMU (Central MUon detector), CMP (Central Muon uPgrade), CMX (Central Muon eXtension), IMU (intermediate MUon detector). The first two detectors cover the region $|\eta| < 0.6$ while the CMX extends the coverage to $|\eta| < 1$. The IMU, covering the region $1 < |\eta| < 2$ with fine granularity, is motivated by the ability of the CDF silicon tracker to reconstruct track with $|\eta| > 1.0$ and so to provide momentum measurements in the forward region.

2.6 Trigger system

At the Tevatron there is an average of one collision every 396 ns, with a typical event size of about 100 kB. The data rate is much larger than can be stored and even if stored, it would be too large to be analysed. For this reason an on-line selection of the potentially interesting events is made. The choice of the selection criteria dictates the kind of physics the experimentalist wants to study.

The CDF has a three level trigger architecture [43], with each level performing a partial reconstruction of the event, enough to be able to judge whether or not it is
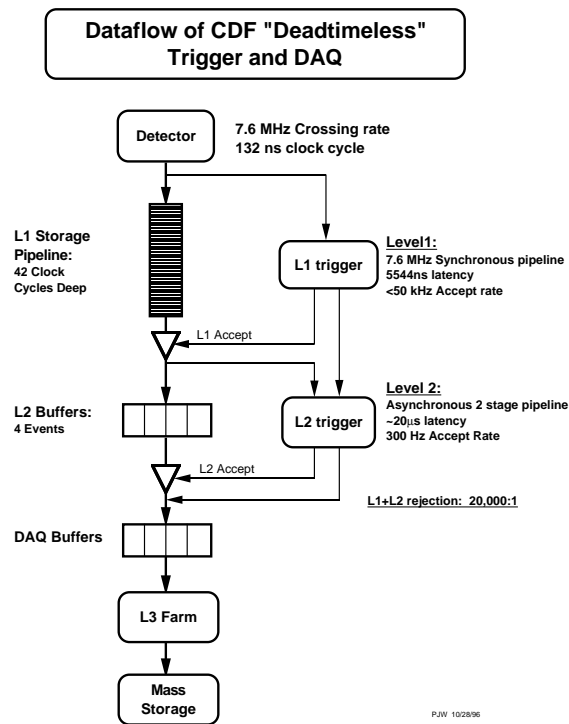
Figure 2.10: *CDF trigger flow chart.*

interesting to be handed to the next level. In this way each level reduces the data rate to be analysed, and so the higher levels will have more time (accuracy) to screen the event and perform more precise selections. A schematic of the trigger system is shown in figure 2.10. At Level 1 and 2 only very quick and rough pattern recognition and filtering algorithms are used. The delay necessary to make a trigger decision is achieved by storing the event information in a pipeline. At Level 1, for each Tevatron clock cycle the event is moved up one position in the pipeline. By the time it reaches the last position in the pipeline the Level 1 trigger will have decided whether to accept the event, and pass it to the next trigger level, or to reject it. The Level 1 pipeline has 42 slots, corresponding to a decision time of 5 μs. The rejection factor at Level 1 is about 150, the accept rate is below 50 kHz. At Level 2 a four-event buffer allows for a decision time of 20 μs. The Level 2 rejection factor is, as for the Level 1, about 150 and the accept rate is about 300 Hz. At the third level, nearly one second is given to each CPU to analyse the event. As a result almost off-line quality algorithms can be applied to reconstruct the event. The Level 3 rejection factor is about 4.

A collection of requirements at the three trigger levels is called "trigger path". The trigger path used in this analysis is called "Two Track Trigger". This trigger

path is optimized to find c-mesons and b-mesons that decay in fully hadronic final states.

The strategy followed to achieve this goal is as follows. At Level 1, rough measurements of track momenta and opening angle, allow the rejection of low momentum tracks mainly coming from soft $p - \bar{p}$ interactions. At Level 2 given the longer time available, SVX II information are used in order to get the impact parameter measurement of the tracks; tuning the request on the impact parameters of the tracks it is possible to select only those tracks coming from long lived particles such as the b-mesons.

2.6.1   Level 1

The Level 1 trigger acquires information coming from the calorimeters, the tracking system, and the muon chambers. For the purpose of the present analysis only the information from the tracker is used. In order to quickly analyse the information coming from the tracker, a device called eXtremely Fast Tracker (XFT) [44] has been developed on custom made electronics. This device examines the hit information of the COT in ϕ wedges of 15°. Based on pre-loaded patterns of COT hits, the XFT is capable of recognizing track segments of $p_T > 1.5 \ GeV/c$. Combining the hit information from the COT with the beamline position a rough measurement of the p_T and the ϕ_6 (the angle in the transverse plane measured at superlayer 6) of the tracks is made.

2.6.2   Level 2

At Level 2, rough tracking information from the XFT is combined with the SVX II cluster information by the Silicon Vertex Tracker (SVT) [45] as shown in figure 2.11. The XFT p_T and ϕ_6 track parameters are used as a starting point to reconstruct the silicon tracks requiring a hit for each of the five silicon layers (ISL and L00 excluded). The information coming from the 12 wedges of SVX II are digitized in parallel by the front-end electronics mounted directly on the silicon sensors. The signals are then passed to a system called "Hit Finder" that excludes noisy strips and calculates the centroid of the charge deposited. The map of the hits is then passed to the "Associative Memory" (produced by the University of Geneva). An SVT track starts with an XFT "seed" which is extrapolated in the SVX and compared with a group of possible patterns stored in the associative memory, called "roads". The identified roads are stored in the "Hit Buffer" and represent a particular "tube" inside which is possible to reconstruct the track with better precision. This is done by the "Track Fitter", implemented with a series of commercial processors that makes an interpolation of the data obtaining three parameters that identify the track in the
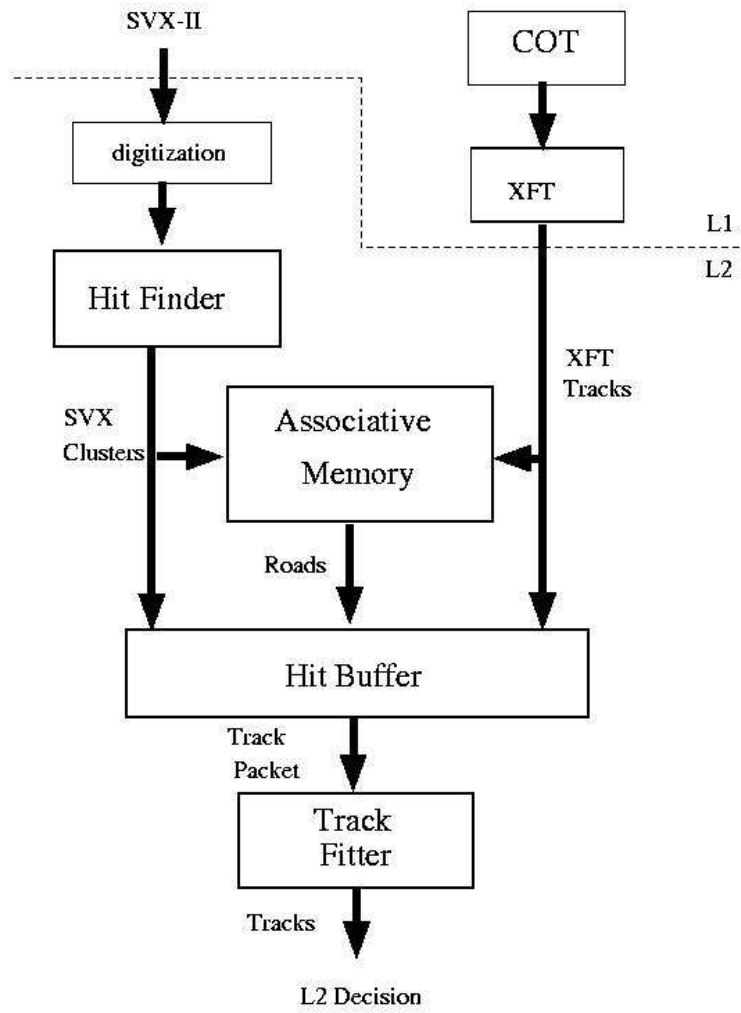
Figure 2.11: *Architecture of the Silicon Vertex Tracker.*

transverse plane: the impact parameter, the transverse momentum and the angle ϕ_0. The interpolation procedure is made in a linear approximation to reduce the calculation time. Though only the p_T, ϕ and d_0 of the track are reconstructed, the resolution obtained on the track fit, is comparable with that obtained off-line. This means that even confirming the Level 1 requirements implies rejecting events. The resolutions achieved by the SVT are:

- $p_T : \sigma(p_T)/p_T^2 = 0.003 \ GeV^{-1}$

- $\phi : \sigma(\phi_0) = 1 \ mrad$

- $\sigma(d_0) = 35 \ \mu m$

At hadron colliders the most studied B-meson decay modes are those including one or two leptons in the final state (respectively semileptonic and leptonic decays), because the leptons, typically muons, are easy to detect in the high multiplicity environment of the hadron-hadron collision. Thanks to the SVT, CDF is the only experiment able to trigger on fully hadronic B-meson decays in an hadron collider environment. This gives the unique opportunity to study several decay modes (such those of the present analysis) that are otherwise inaccessible at Tevatron.

2.6.3 Level 3

The Level 3 [46] trigger is implemented as a PC farm with roughly 300 CPUs. Analyzing one event per CPU every second the Level 3 farm sustains an accept trigger rate of about 300 Hz. The algorithms used to reconstruct the events are very similar to those used off-line, therefore achieving a very accurate level of selection.

Chapter 3

Dataset and Candidate Selection

The aim of the present analysis is to measure the lifetime of the B_d and B_s mesons decaying in two light hadrons (pions and kaons). The total cross section for $p - \bar{p}$ collisions at the centre of mass energy $\sqrt{s} = 1.96 \ TeV$ is about $100 \ mb$[1]. This means that, considering a typical Tevatron store with an averaged instantaneous luminosity of $10^{32} \ cm^{-2}s^{-1}$, there are 10^7 collision per second. Out of those only about 0.1% (cross section of $100 \ \mu b$) are collision where a b-quark is created. About 10 % of those b-quarks hadronize in b-flavored baryons and 90 % in b-flavored mesons. The b-flavoured mesons might hadronize taking from the vacuum a light quark ($B_u \sim B_d \sim 45\%$) an s-quark ($B_s \sim 10$) or a c-quark ($\ll 1\%$). Finally the typical branching ratio for the decay in two light hadrons is about 10^{-6}. This means that out of 10^7 events produced per second only about 10^{-3} per second are used in this analysis.

It is for this reason that strict criteria are applied during data taking to select the interesting "signal" events and reject the remaining "background" events. The first selection is implemented at the trigger level and then, once the data are recorded, it is possible to use more time consuming criteria and further eliminate the undesired events.

In this section the online and offline selection procedures are detailed.

3.1 Trigger Paths

The data analysed have been collected by the CDF detector with the Two Track Trigger (TTT), from February 2002 until August 2004. The total integrated luminosity of the dataset correspond to $355 \ pb^{-1}$.

---

[1]$1 \ barn \ = \ 10^{-24} cm^2$.

The two track trigger is composed by several trigger paths. A trigger path is a well defined sequence of Level 1, Level 2 and Level 3 triggers. The ones used in this analysis are the B_PIPI and B_PIPI_HIGH_PT.

During the period of data taking some of the triggers underwent modifications and improvements. In particular, as the Tevatron instantaneous luminosity increased thanks to the improving accelerator complex performance, it has been necessary to reduce some trigger rates by applying a prescale. Prescaling a trigger by a factor N means taking 1 event every N. To better use the trigger bandwidth, a dynamic prescale (DPS) has been added to few particularly high rate triggers. The dynamic prescale adjusts the prescale factor N according to the instantaneous luminosity. Since the instantaneous luminosity of the store decreases with time due to the various interactions between the colliding beams, the dynamic prescale factor decreases along the store to keep the trigger band width fully occupied.

3.1.1   The B_PIPI Trigger Path

At Level 1 the B_PIPI trigger path requires a pair of XFT tracks with opposite charge and $p_T > 2.04~GeV/c$. The track pair is required to have the scalar sum of the transverse momenta, $\Sigma p_T > 5.5~GeV/c$ and opening angle calculated at the radial distance corresponding to the super-layer 6 of the COT , $\Delta\phi_6 < 135°$. The Level 1 trigger has been dynamically prescaled. The prescale factors are in the range from 1 to 10.

The Level 2 trigger requires two SVT tracks. Each track is required to have an SVT fit $\chi^2 < 25$, an impact parameter as measured in the SVT between 100 μm and 1 mm and $p_T > 2~GeV/c$. The two tracks are requested to have opposite charge, an opening angle which satisfies $20° < \Delta\phi_6 < 135°$, a scalar sum of the transverse momenta $\Sigma p_T > 5.5~GeV/c$, a minimum decay length of the reconstructed B candidate $|L_{xy}| > 200~\mu m$ and an impact parameter of the reconstructed B candidate $|d_0(B)| < 140~\mu m$.

The Level 3 executable builds "hybrid tracks" setting the impact parameter d_0 to the SVT measured value and the other four track parameters (ϕ_0, z_0, C, $\cot\theta$) to the ones measured by the COT. The Level 3 operates the confirmation of the Level 1 and Level 2 requirements on the hybrid tracks and selects those candidates for which the pseudorapidity of the tracks is $|\eta| < 1.2$ and the invariant mass of the B candidate calculated assigning the pion mass to both tracks is between 4.0 GeV/c^2 and 7.0 GeV/c^2.

3.1.2 The B_PIPI_HIGH_PT Trigger Path

The B_PIPI_HIGH_PT trigger path applies the same requirements of the B_PIPI, but tightening few of them.

At Level 1 it requires both tracks to have $p_T > 2.46 \ GeV/c$ and scalar sum of the transverse momenta $\Sigma p_T > 6.5 \ GeV/c$. At Level 2 it confirms, on SVT tracks, the scalar sum of the transverse momenta $\Sigma p_T > 6.5 \ GeV/c$ and tighten the transverse momentum cut to $p_T > 2.5 \ GeV/c$. At Level 3 has exactly the same requirements as for the B_PIPI.

The B_PIPI_HIGHPT trigger has been run unprescaled for a large fraction of data and with a fixed prescale factor of 2 for the latest data.

Averaged over the whole dataset, 7% of the events has been triggered exclusively by the B_PIPI_HIGHPT trigger.

3.2 Offline Event Selection

The generic decay topology for the $B^0 \rightarrow h^{\pm} h'^{\mp}$ decay is shown in figure 3.1. It
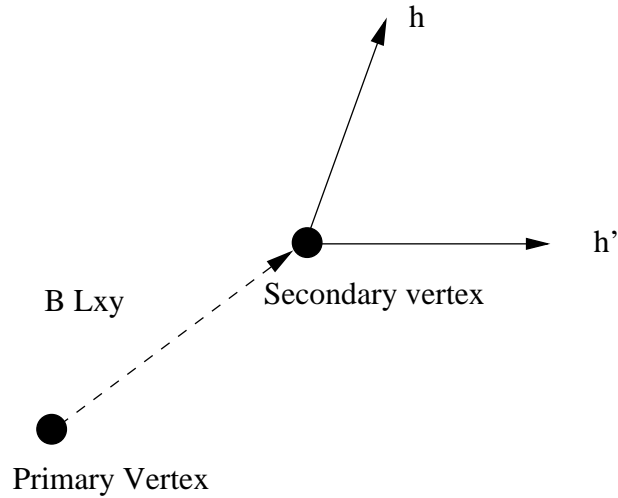

Figure 3.1: *Topology of a $B^0 \rightarrow h^{\pm} h'^{\mp}$ decay.*

consists in a displaced vertex with two tracks attached to it. At trigger level the B-meson candidate selection is performed only on quantities projected onto the transverse plane. Since each pair of tracks intersects in the transverse plane (unless parallel but this is a very improbable occurrence) few of them will make their way through the trigger selection. Also, candidates coming from B-meson decays with more complex decay topologies, where one or more tracks are not reconstructed, might pass the

trigger chain. For this reason more stringent requirements than at trigger level are requested offline in order to enhance the purity of the signal.

3.2.1   Track Selection

The event reconstruction is entirely track based, hence special care is devoted to select only the tracks with the highest quality and to minimize fake tracks coming from noise hits and mismeasured tracks caused by misalignment of the tracking system. The easiest way to reduce the number of these tracks is to require a minimum number of hits in the COT and in the silicon detectors. Each track is required to have at least 3 SVX $r - \phi$ hits and at least 5 hits in two axial and two stereo COT super-layers. The silicon hits requirements assure a good vertex determination, while the COT hits assures a good momentum measurement.

The tracks are first fitted without taking into account the multiple scattering of the charged particles through the COT materials. Hence the error matrix of this first track fit underestimates the uncertainties on the track parameters. To properly correct for this effect, tracks are refitted with a rescaled covariance matrix [47]. The scaling factors are the following:

$$
\begin{aligned}
s(\lambda) &= \sqrt{1 + p_\lambda(1 + \lambda^2)^{1.5}/p_T^2} & \text{with} \quad p_\lambda &= \quad 1.544 \\
s(c) &= \sqrt{1 + p_c/p_T^2} & \text{with} \quad p_c &= \quad 21.72 \\
s(z_0) &= \sqrt{1 + p_{z_0}(1 + \lambda^2)^{1.5}/p_T^2} & \text{with} \quad p_{z_0} &= \quad 1.71 \\
s(d_0) &= \sqrt{1 + p_{d_0}/p_T^2} & \text{with} \quad p_{d_0} &= \quad 11.57 \\
s(\phi_0) &= \sqrt{1 + p_{\phi_0}/p_T^2} & \text{with} \quad p_{\phi_0} &= \quad 14.64
\end{aligned}
$$

The rescaled COT track is then used as a starting point for final refit where the SVX hits are added.

The refit procedure is also necessary to correct for the energy loss in the material, that depends on the particle mass hypothesis; the model for the material description [47] is based on the Kalman track refitting package [48]. Specific alignment tables are used in the track refit to calculate the relative position of all subdetectors with respect to the CDF global reference frame.

3.3   Reconstruction

To reconstruct the $B^0 \rightarrow h^\pm h'^\mp$ candidates, the collected events have been run through the `CharmMods` [49] reconstruction package. Final $B^0 \rightarrow h^\pm h'^\mp$ candidates

are reconstructed by vertexing opposite charged tracks (using the `CTVMFT` package [50]), assigning the pion mass to each track, and confirming the `B_PIPI` trigger on each candidate as preselection requirements.

Candidates can be formed from two random tracks that, even if far apart on the longitudinal axis, once projected onto the transverse plane, pass all the trigger requirements. In order to reduce these candidates we apply the cut $\Delta z < 3\ cm$ as a pre-requisite. The primary vertex position is obtained by averaging the beam position over the run.

The preselection cuts used to reconstruct the $B^0 \to h^\pm h'^\mp$ candidates are listed in table 3.1.

Variable	Cut
Track # hits COT (Axial)	≥ 5 hits in ≥ 2 SL
Track # hits COT (Stereo)	≥ 5 hits in ≥ 2 SL
Track # hits R-ϕ SVX	≥ 3 hits in 4 different layers
Track p_T	$\geq 1.9\ GeV/c$
Track $|\eta|$	< 2
$\Delta_{z_0}(\pi^+, \pi^-)$	$< 3cm$

Table 3.1: *Preselection cuts used to reconstruct $B^0 \to h^\pm h'^\mp$ candidates.*

3.4 Monte Carlo Simulation

Monte Carlo simulations of the signals are used at several points of the analysis. A sample of pure Monte Carlo signal is useful in particular to tune the selection requirements to isolate the signal from the background and, as will be explained in the next chapter, it is a fundamental ingredient of the method we have used to measure the lifetimes. In the present analysis there is no need to describe the generic background with Monte Carlo simulations. The background description is usually extracted from opportune choice of signal sidebands. The only source of background studied with Monte Carlo simulations is that coming from the few mis-reconstructed B-meson decay modes that, appearing in the proximity of the $B^0 \to h^\pm h'^\mp$ mass peak, might bias the lifetime measurement.

The Monte Carlo simulations are performed following the sequence: quark production, quark fragmentation, B-meson decay, simulation of the detector response and simulation of the trigger.

The particle generation is performed with `BGen` [51], a Monte Carlo package based on NLO cross section calculations. `BGen` produces a single b-quark. The fragmentation is implemented using the Peterson fragmentation functions [52]. To simulate the B-meson decay we used `EvtGen` [53] a package tuned at the b-factories over the past years. The simulation of the detector is performed with `Geant` [54]. This package follows each generated particle through the various materials of the detector simulating their energy deposition. This information is then passed to the simulation of the electronics readout. In this way the simulation output can be used as input to the same reconstruction program used for data.

The detector simulation represents the detector in its ideal behaviour. Real data includes many more effects related to time dependent inefficiencies, electronic noise and the malfunctioning of isolated subdetectors components. The trigger has also undergone several modifications during the data taking period. To account for all this effects a "realistic simulation" has been developed. Over the data taking periods several runs have been taken as representative for short data sections where detector and trigger conditions were stable. The realistic simulation produces the required integrated luminosity using those representative runs (with the real detector configuration) and weighting them to the integrated luminosity of the corresponding data section so that the final product of the simulation closely represents the data.

The Monte Carlo samples have been generated using the standard procedure and scripts approved by the CDF-B Monte Carlo group using generation 5.3.4 of the CDF simulation software [55]. For each signal we generated a number of events, after trigger requirements, equivalent to about 40 times the statistics available on data. We generated decay samples for the four signal modes:
$B_d \to K^+\pi^-$, $B_d \to \pi^+\pi^-$, $B_s \to K^+K^-$, $B_s \to K^-\pi^+$ (and charge conjugates).

3.4.1   Monte Carlo validation

In order to evaluate whether the Monte Carlo simulations correctly represented the data, a comparison between sideband subtracted data and Monte Carlo was performed. The sideband subtraction used symmetric sidebands $4\,\sigma$ away from the signal peak and $3\,\sigma$ wide. The Monte Carlo signal was created assuming a $B^0 \to h^\pm h'^\mp$ mass peak composed of 60 % $B_d \to K^+\pi^-$, 26 % $B_s \to K^+K^-$, and 14 % $B_d \to \pi^+\pi^-$ (and charge conjugates) [56]. We observe a small discrepancy at low values of the B-meson p_T spectrum between the Monte Carlo and the sideband subtracted signal (see figure 3.2). To correct for this effect we re-weighted the Monte Carlo with weights derived from the comparison of the p_T spectrum of Monte Carlo signal events and sideband subtracted data. Figures 3.3 and 3.4 shows the comparison between p_T re-weighted Monte Carlo and sideband subtracted data for few variables. The agreement is generally good.
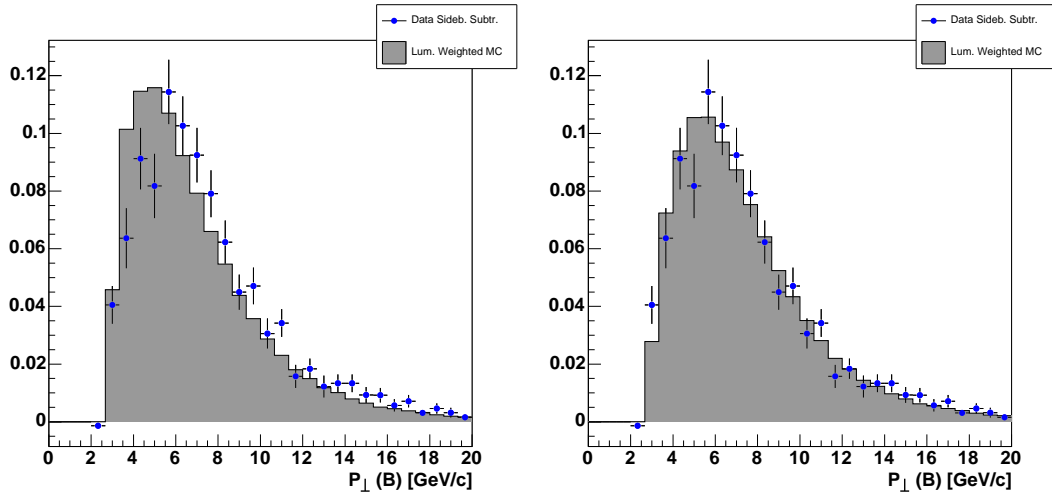
Figure 3.2: *B-meson p_T re-weighting. In both plots the blue dots are the sideband subtracted data while the shaded histogram is the Monte Carlo. The plot on the left compares the B-meson p_T distribution as obtained from Monte Carlo with the sideband subtracted data. The plot on the right shows the same distribution re-weighted to obtain the necessary agreement between Monte Carlo and sideband subtracted data.*
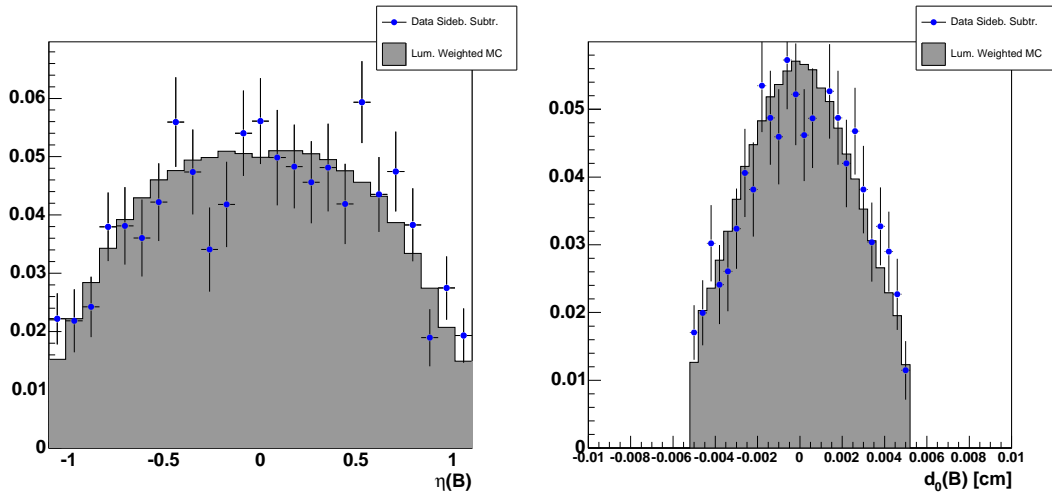

Figure 3.3: *In both plots the blue dots are the sideband subtracted data while the shaded histogram is the re-weighted Monte Carlo. The plotted variables are: B-meson pseudorapidity and B-meson impact parameter.*
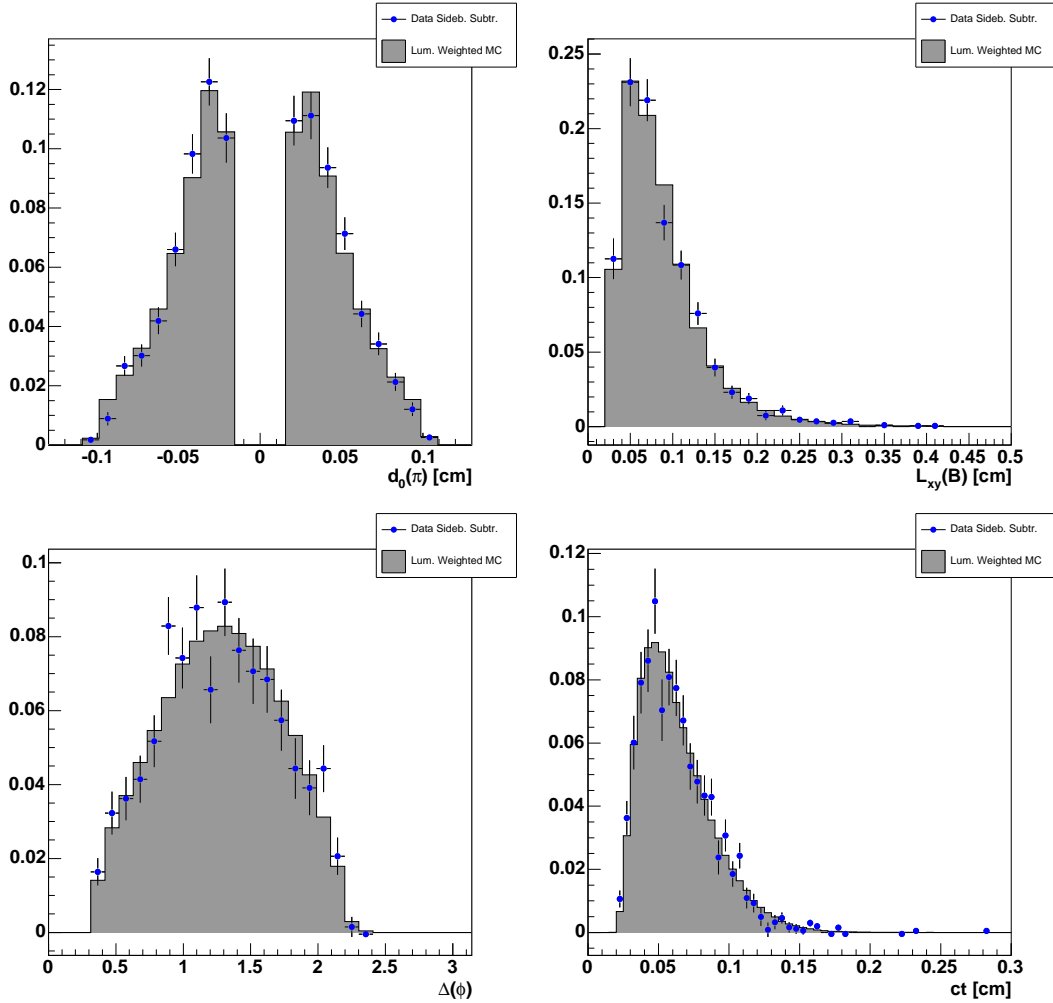
Figure 3.4: *In all the plots the blue dots are the sideband subtracted data while the shaded histogram is the re-weighted Monte Carlo. The plotted variables are: track impact parameters, B-meson transverse decay path (L_{xy}); two-track $\Delta\phi$; B-meson proper decay length.*

3.5 Optimization of the Signal Selection Requirements

The goal of the present analysis is to measure the B_d lifetime in $B_d \to K^+\pi^-$ and $B_d \to \pi^+\pi^-$ decays, and the B_s lifetime in $B_s \to K^+K^-$ and $B_s \to K^-\pi^+$ decays.

While the B_d lifetime has already been measured with high precision at the "B factories", the present measurement of the $B_s \to K^+K^-$ lifetime is the first estimation of this observable. From previous analyses [56] we know that the number of $B_s \to K^-\pi^+$ events we might expect with the present statistics on data is too small to obtain a precise measurement of $B_s \to K^-\pi^+$ lifetime.

Given our interest in the $B_s \to K^+K^-$ lifetime measurement relative to the lifetimes of the other decay modes, we have optimized our selection criteria in order to maximize our sensitivity to that observable. Thus we optimized our analysis selection criteria by maximizing the signal significance $S/\sqrt{S+B}$, where S is the number of $B_s \to K^+K^-$ events in a mass window of $\pm 3\sigma$ around the $B^0 \to h^\pm h'^\mp$ mass peak and B is the number of background events in the same mass window. The maximum of the signal significance depends on the correct estimation of the number of signal events in the sample, i.e. the number of $B_s \to K^+K^-$ events in the $B^0 \to h^\pm h'^\mp$ mass peak. It is easy to verify that considering just the total number of $B^0 \to h^\pm h'^\mp$ events would lead to a sub-optimal choice of the cuts. We assume the fraction of $B_s \to K^+K^-$ events in the mass peak to be 26 % as measured by previous analyses [56].

To optimize the signal significance we studied a number of possible kinematics selection criteria, or cuts. The variables we chose to cut on in order to maximize the signal significance are the sum of the transverse momenta of the two tracks $p_T(\pi_1) + p_T(\pi_2)$, the minimum between the absolute value of the impact parameters of the two tracks $min(|d_0(\pi_1)|, |d_0(\pi_2)|)$, and the impact parameter of the B-meson $d_0(B)$. Many other variables have been studied but none of them considerably improved the significance of the $B_s \to K^+K^-$ signal.

The optimization procedure takes as input the reconstructed candidates which pass the preselection cuts listed in table 3.1, with the additional requirement of a B-meson isolation $I > 0.5$, where the isolation is defined as $I = \frac{p_T(B)}{p_T(B)+\Sigma p_T}$ in a (η, ϕ) cone of radius 1.0. The isolation is a measure of how many tracks appear in a given cone around the B-meson trajectory and thus it is closely related to the way the b-quarks hadronize. Cutting on the isolation reduces considerably the combinatorial background, i.e. the background where two random tracks in the event form a track pair that passes all the trigger requirements, even if those tracks do not belong to a real B-meson decay.[2]

---

[2]The isolation cut efficiency has been studied in [57] on a $B \to J/\psi K$ sample. The B_d and B_s

The mass spectrum resulting from this set of preliminary cuts is fitted with a superimposed gaussian and exponential function to describe respectively the signal and the background. From the parameters of the gaussian fit, the initial number of $B_s \rightarrow K^+K^-$ signal events is extracted.

To apply the different combinations of cuts, we span a discrete space where the number of dimensions is given by the number of cuts and the granularity in each dimension is given by the the number of steps we use to describe the cut:

- $P_t(\pi_1)$+$P_t(\pi_2)$ from 5.5 GeV/c up to 7.0 GeV/c in 10 steps

- B-meson impact parameter from 30 μm up to 100 μm in 10 steps

- $min(|d_0(\pi_1)|, |d_0(\pi2)|)$ from 100 μm up to 300 μm in 10 steps

The number of $B_s \rightarrow K^+K^-$ events at each combination of cuts is obtained multiplying the initial number of $B_s \rightarrow K^+K^-$ events in the signal peak by the efficiencies for the single cuts as obtained from Monte Carlo. In doing this (instead of simply calculating the number of events from a fit to the data), we reduce the sensitivity to the sample statistical fluctuations.

The number of background events at each combination of cuts in the selected mass window is calculated fitting the background spectrum with an exponential, counting the number of events in the sidebands and rescaling it (using the exponential distribution) to the number of events underneath the signal peak.

In figure 3.5 we show the signal significance and the efficiency for each of the analysed cuts. To produce these plots all the cuts are fixed to their optimal value and only that plotted is left floating.

The optimization procedure lead to the list of cuts showed in the first column of table 3.2.

Another powerful way to distinguish signal from background is to look at the quality of the vertex. A real B-meson decay will have a high three dimensional χ^2 probability, a candidate faked by a couple of random tracks, on the other hand, will have a small probability. Since the Monte Carlo simulation does not correctly describe the three dimensional χ^2 probability, this variable has not been included in the optimization process. Instead we compared sideband subtracted signal and sideband (see figure 3.6) and we required a 3D χ^2 vertex fit probability greater than 1% which reduces the background by 37.2%, with only a 6.6% loss on the signal, hence enhancing the signal significance, as shown in the second column of 3.2. The effect on the mass spectrum of this additional cut is shown in figure 3.7

---

mesons have different fragmentation and so we expect a slightly different isolation distribution. The effect of this on the lifetimes measurement is analysed in the cross check section 4.7.

$\Sigma P\perp$ (GeV/c)	>	5.95	5.95
$d_0(B)$ (μm)	<	50	50
$\min(|d_0(\pi_1)|, |d_0(\pi_2)|)$ (μm)	>	180	180
Prob($3D\chi^2$)	>	-	0.01
$S/\sqrt{S+B}$		35.9	37.4
Signal events		2264	2215
Background events		1713	1076
S/N		1.3	1.97

Table 3.2: *List of the optimized cuts. The effect of the additional Prob(3Dχ^2) cut is shown in the last column. The number of signal and background events are calculated in the signal region defined as $\pm 3\sigma$ of the mass peak.*

Applying the optimized cut listed in table 3.2 we are left with about 2200 signal events on a background of about 1000 events, giving a signal to background ratio of about 2.
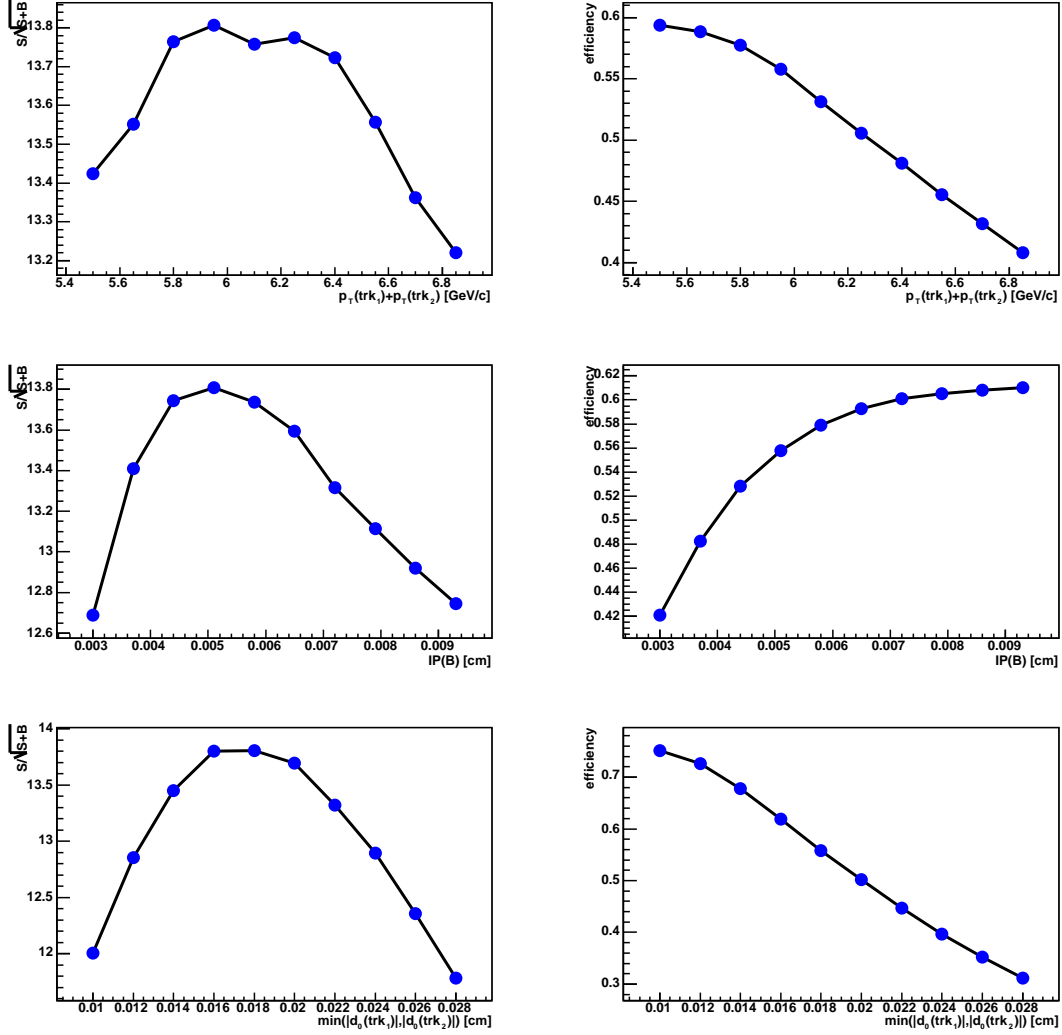
Figure 3.5: *"N-1 plots": in all the plots the cuts are fixed to their optimal value and only the plotted one is allowed to float. The left plots show the signal significance $S/\sqrt{S+B}$ for the the selected cut; the right plots show the efficiency of the same cut on $B_s \to K^+ K^-$ Monte Carlo; first row: shows the $P_t(\pi_1) + P_t(\pi_2)$ cut in GeV/c^2; second row: impact parameter of the B-meson in cm; third row: $min(|d_0(\pi_1)|, |d_0(\pi2)|)$ in cm.*
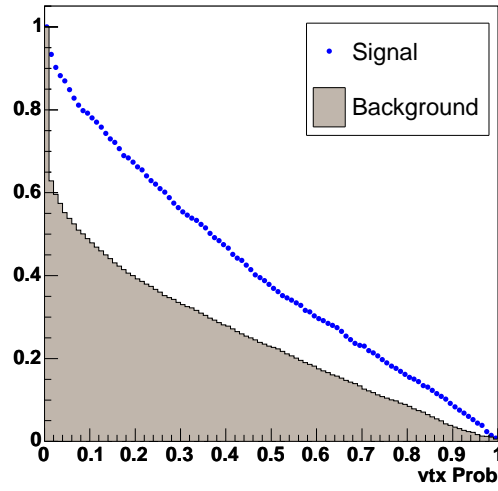
Figure 3.6: *Cumulative function of the three dimensional vertex χ^2 probability. The bin x contains the fraction of signal (blue) and background (grey) events that pass the cut Prob(3D χ^2) > x.*
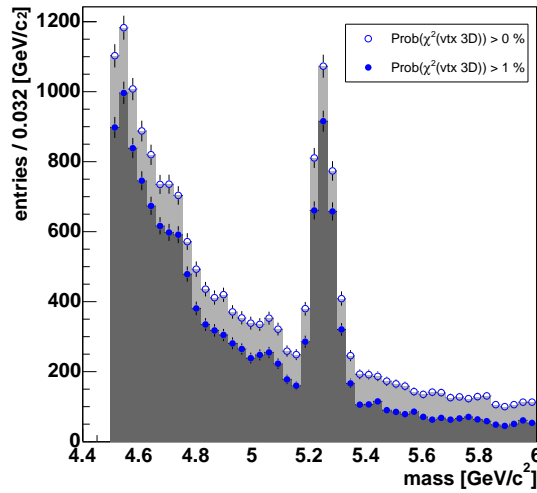

Figure 3.7: *Effect of 3D vertex fit probability cut. Mass spectrum without the 3D vertex fit probability cut (empty dots) and requiring a 3D vertex fit probability cut greater than 1% (filled dots).*

Chapter 4

Lifetime Analysis

"La théorie des probabilités n'est que le bon sense reduit au calcul"
Pierre Simon Laplace

"If your result needs a statistician then you should design a better experiment."
Ernest Rutherfod

The decay of an unstable particle is a quantum effect with no analogs in classical physics. The proper decay time, i.e. the period of time between the particle production and the decay, is distributed according to an exponential probability distribution. The measurement of a particle lifetime consists in extracting the time constant of the decay from an exponential fit of the proper decay time distribution of the data. Unfortunately this easy task is often complicated by experimental limitations.

In this chapter we will describe how from the $B^0 \to h^\pm h'^\mp$ data sample we will extract the four main signals fraction ($B_d \to K^+\pi^-$, $B_d \to \pi^+\pi^-$, $B_s \to K^+K^-$, $B_s \to K^-\pi^+$) and their lifetimes. Given the negligible $\Delta\Gamma_d$ the $B_d \to K^+\pi^-$ and $B_d \to \pi^+\pi^-$ decays will be assigned the same lifetime. The $B_s \to K^+K^-$ lifetime measurement will be our main goal as this work represents its first determination and because it allows the determination of $\Delta\Gamma_{CP}$ if combined with other lifetime measurements.

The measurement of the $B_s \to K^+K^-$ lifetime presents two main complications. The first is that the collected signal is mixed with the other $B^0 \to h^\pm h'^\mp$ decay modes $B_d \to K^+\pi^-$, $B_d \to \pi^+\pi^-$, $B_s \to K^-\pi^+$ and with the background. The CDF mass resolution and particle identification capability do not allow for an event by event separation of the $B_s \to K^+K^-$ from the other decays. The second complication is that the effect of the detector resolution on the proper decay time measurement and the two tracks trigger (TTT) used to collect the data bias the proper decay time distribution of the sample.

In order to measure the $B_s \rightarrow K^+K^-$ lifetime it is first necessary to find a way to disentangle the different contributions of the $B^0 \rightarrow h^\pm h'^\mp$ signal and background, and then correct for the sculpting effects of the detector and the trigger on the proper decay time distribution.

The four $B^0 \rightarrow h^\pm h'^\mp$ decay modes and the background have few distinctive characteristics. The kinematics of these decays is slightly different due to the mass difference between the B_d and B_s mesons and to the different masses of the decay products (π, K). Moreover, the measurement of the energy loss in the drift chamber of the decay products can be used to disentangle kaons from pions.

None of these elements alone is sufficient to separate the different contributions. For this reason it has been decided to gather all these pieces of information in a likelihood function [58]. The separation in a likelihood fit is purely statistical: given a candidate the likelihood function estimates the *probability* of it being background or one of the signal components; given a sample of candidates, the fit output will be the *fractions* of background and of the different signal components.

The sculpting of the proper decay time operated by the TTT and by the detector resolution has been modeled using Monte Carlo simulations. An acceptance (or efficiency) function has been calculated and used opportunely to weight in the likelihood function the term describing the proper decay time distribution of the sample.

The complete likelihood fit is then performed using the kinematics, particle identification, and proper decay time information of the B-meson candidates. The estimation of the fractions of background and each of the four signal components, and the corresponding lifetimes is obtained simultaneously, by maximizing the likelihood function on the selected sample of B-meson candidates that we described in chapter 3.

4.1 Mass Spectrum

The invariant mass spectrum of the data sample has been plotted in figure 4.1 in the mass range $[4.9, 6.0]$ GeV/c^2.

The candidates' invariant mass has been calculated assigning the pion mass to the two tracks attached to the secondary vertex. This choice is completely arbitrary, any other mass assignment would be equivalent. The reason behind this is that we don't know what is the true mass of the particles originated at the secondary vertex, because the particle identification is not sufficiently discriminating. Assigning the same mass value to all the tracks leads to a wrong estimation of the invariant mass of the B candidate and distorts the mass spectrum. In particular, since the final states of the $B^0 \rightarrow h^\pm h'^\mp$ decays are pions and kaons and the kaon has higher mass than the pion, the invariant mass will be underestimated in all the decays involving a kaon shifting the $B^0 \rightarrow h^\pm h'^\mp$ mass peak towards lower mass values. In section 4.2.1 we
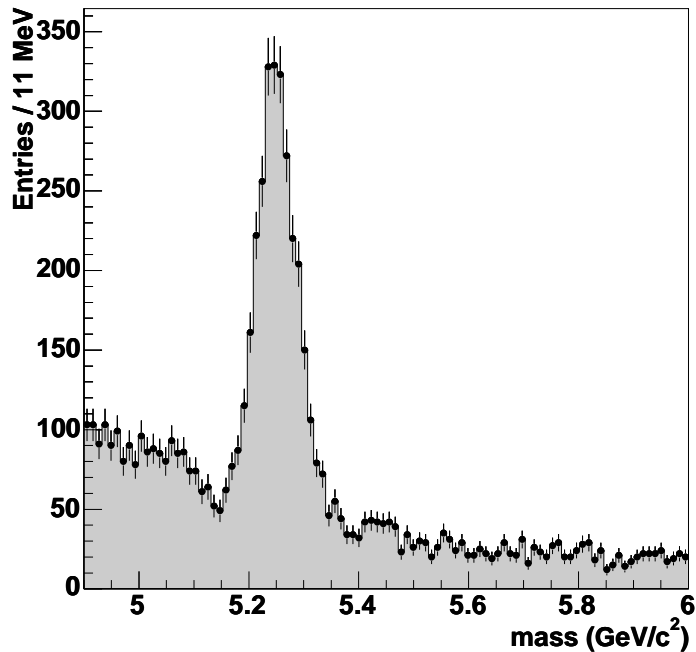
Figure 4.1: *Invariant Mass spectrum of the optimized data sample*

will describe a method to correct for the wrong tracks mass assignment during the development of the likelihood.

The mass spectrum in figure 4.1 shows the typical structures of the fully hadronic B-mesons decay: the B-meson peak, the combinatorial background having an exponentially decreasing shape that spans the whole mass window and the partially reconstructed B decays appearing as a bump on the left of the B-meson peak. The combinatorial background is composed by tracks pairs produced in the collision, that pass all the trigger and offline selection requirements, though they do not result from the decay of a B-meson. The partially reconstructed decays instead are B-meson decays with a more complicated topology where one or more final states escaped detection.

To avoid that partially reconstructed B_d decays bias the measurement of the lifetime of the $B_s \rightarrow K^+K^-$ mode, or that partially reconstructed B_s decays bias the lifetime of the B_d modes, it is necessary to estimate the fraction of the different background sources in the signal mass window and eventually to include those contributions, with appropriate templates, in the lifetime fit.

To identify the partially reconstructed decay modes producing the structure around

5.05 GeV/c^2, we looked, with purely kinematical simulations, for B-meson decay modes having three or more decay products, that can produce a two pions invariant mass event in that region. We found the following decay modes involving a ρ meson plus a pion or a kaon:

- $B^0 \to \rho^\pm \pi^\mp$; $B^\pm \to \rho^0 \pi^\pm$

- $B^0 \to \rho^\pm K^\mp$; $B^\pm \to \rho^0 K^\pm$

- $B_s \to \rho^\pm K^\mp$

We have performed a realistic simulation for these decay modes, with the same framework used to produce the $B^0 \to h^\pm h'^\mp$ components. The mass distribution is shown in figure 4.2. The end point of the mass distribution is different for the different decay modes. In particular the $B^0 \to \rho^\pm K^\mp$ $B^\pm \to \rho^0 K^\pm$ are shifted to lower invariant mass values compared with the $B^0 \to \rho^\pm \pi^\mp$ $B^\pm \to \rho^0 \pi^\pm$ that are shifted towards lower values with respect to the $B_s \to \rho^\pm K^\mp$.
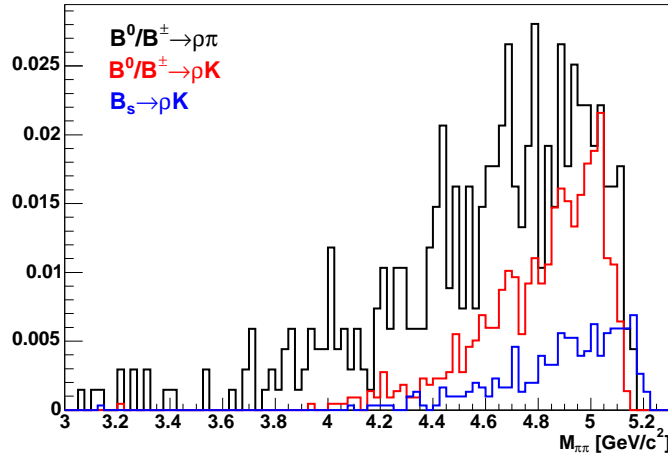

Figure 4.2: *Mass distribution of the partially reconstructed $B^0 \to \rho^\pm \pi^\mp$ - $B^\pm \to \rho^0 \pi^\pm$ (black), $B^0 \to \rho^\pm K^\mp$ - $B^\pm \to \rho^0 K^\pm$ (red), $B_s \to \rho^\pm K^\mp$ (blue).*

To evaluate the fraction of those events underneath the $B^0 \to h^\pm h'^\mp$ signal peak we performed an unbinned maximum likelihood fit on the mass variable only. Each category of events composing the data sample (signal, partially reconstructed B-meson decays and combinatorial background) has to be described in the fit with a template representing its mass distribution.

We parametrize the $B^0 \rightarrow h^{\pm}h'^{\mp}$ peak with a single gaussian. We checked on Monte Carlo simulations that this model is indeed adequate for the scope.

To parametrize the partially reconstructed decays, we summed the identified contributions according to their relative branching ratios and f_s/f_d (f_s and f_d are the b-quark fragmentation fractions). For the B_u and B_d modes we took the values from the Particle Data Book [8], for the yet unmeasured B_s modes we used the theoretical predictions [59] and for f_s/f_d we used the latest Heavy Flavor Averaging Group (HFAG) estimation [20]: (the reported uncertainties are the sum in quadrature of the statistical and the systematic uncertainties)

- $\mathrm{BR}(B^+ \rightarrow \rho^0\pi^+)\times 10^6 = 8.1^{+1.0}_{-1.1}$

- $\mathrm{BR}(B^+ \rightarrow \rho^0 K^+)\times 10^6 = 4.27^{+0.54}_{-0.56}$

- $\mathrm{BR}(B^0 \rightarrow \rho^{\pm}\pi^{\mp})\times 10^6 = 24.0 \pm 2.5$

- $\mathrm{BR}(B^0 \rightarrow \rho^{\pm}K^{\mp})\times 10^6 = 9.9^{+1.6}_{-1.5}$

- $\mathrm{BR}(B_s \rightarrow \rho^{\pm}K^{\mp})\times 10^6 = 19.2 \div 24.6$

- $f_s/f_d = 0.2613 \pm 0.005$

The function we chose to parametrize the template describing the partially reconstructed decays is an argus function [60] convoluted with a gaussian. The invariant mass template is shown in figure 4.3.

The combinatorial background has been parametrized with an exponential distribution. We performed the fit to our candidates in the invariant mass window [4.9,6.0] GeV/c^2. The projection of the fit on the data is plotted in figure 4.4.

Using the relative branching fractions mentioned above we estimate a total contamination of the partially reconstructed decays equal to 1.1% relative to the $B_d \rightarrow K^+\pi^-$ signal fraction above 5.15 GeV/c^2.

For the fractions and lifetimes fit, we decided to use 5.15 GeV/c^2 as the lower limit on the invariant mass window, and 5.38 GeV/c^2 as upper limit to fully contain the $B^0 \rightarrow h^{\pm}h'^{\mp}$ mass peak.

Given the small contamination of the partially reconstructed B-meson decays in the selected mass window, we do not include their description in the fraction and lifetime fit. Their contamination to the $B^0 \rightarrow h^{\pm}h'^{\mp}$ lifetimes will be treated as a systematic uncertainty (see section 4.6.5).

4.2 Disentangling the $B^0 \rightarrow h^{\pm}h'^{\mp}$ contributions

The separation of the different $B^0 \rightarrow h^{\pm}h'^{\mp}$ components in the signal peak of figure 4.4 is performed using kinematics and particle identification information.
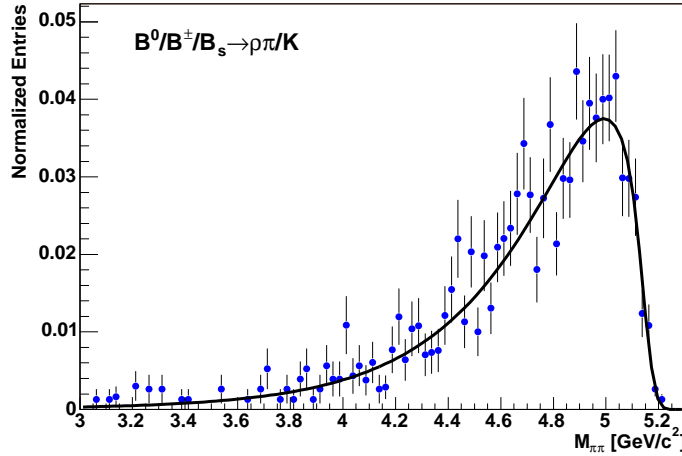
Figure 4.3: *Mass templates of the sum of the partially reconstructed B decays: $B^0 \to \rho^{\pm}\pi^{\mp}$ - $B^{\pm} \to \rho^0\pi^{\pm}$, $B^0 \to \rho^{\pm}K^{\mp}$ - $B^{\pm} \to \rho^0 K^{\pm}$, $B_s \to \rho^{\pm}K^{\mp}$.*

4.2.1 Kinematics

As already noted, the pions mass has been assigned to both tracks attached to the secondary vertex. This implies that only in the case of the $B_d \to \pi^+\pi^-$ both tracks will have the correct mass assignment. For all other decays at least one mass assignment will be wrong. In figure 4.5 we show the Monte Carlo simulation of the invariant mass for the four main decay modes reconstructed with the pion mass hypothesis. The relative normalizations of the four signals in this plot have been set for the sake of demonstration to: $B_d \to K^+\pi^-$ 60%, $B_d \to \pi^+\pi^-$ 15%, $B_s \to K^+K^-$ 22% and $B_s \to K^-\pi^+$ 3%.

The $B_d \to \pi^+\pi^-$ is centered at the correct B_d mass. The $B_s \to K^+K^-$ is centered at an invariant mass lower than the true B_s one because both decay product are kaons (which are heavier than the pion). By accident, the difference in invariant mass of the B_d and B_s mesons is compensated by the mass difference between kaon and pion and so the $B_s \to K^+K^-$ overlaps almost perfectly with the $B_d \to \pi^+\pi^-$. The $B_d \to K^+\pi^-$ and the $B_s \to K^-\pi^+$ (with only one kaon in the final states) are centered at values lower than respectively the B_d and B_s true masses.

From the spectrum in figure 4.5 we observe that with purely kinematical considerations we have some separation power to distinguish $B_d \to K^+\pi^-$ from $B_s \to K^-\pi^+$ but not the $B_d \to \pi^+\pi^-$ and $B_s \to K^+K^-$. This will be done using the particle identification.

The mass shift due to the wrong mass assignment can be quantified. Consider a
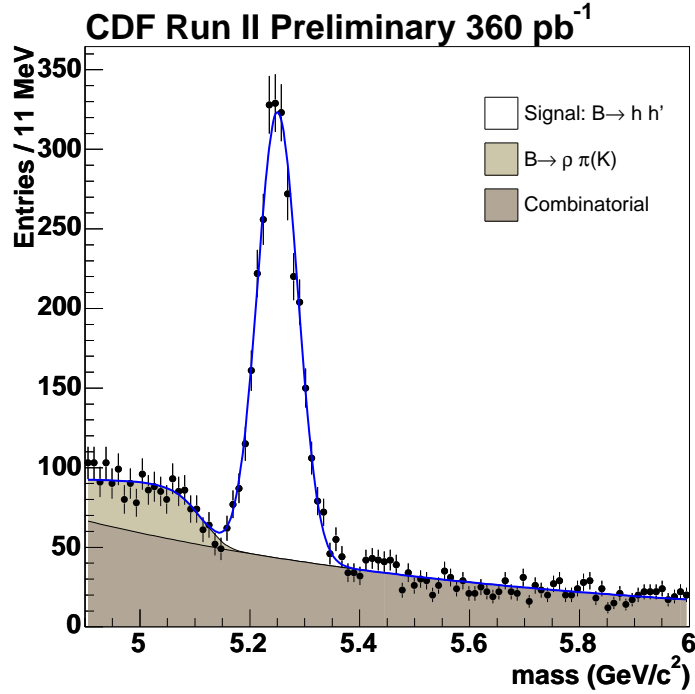
Figure 4.4: *Unbinned likelihood mass fit. Projection of the likelihood function on data. In light grey the partially reconstructed $B^+ \rightarrow \rho\pi(k)$, $B^0 \rightarrow \rho\pi(k)$ decays, in dark grey the combinatorial background, in white the signal*

two body decay $B \rightarrow h_1 h_2$. The squared invariant mass of the system is:

$$M^2_{h_1 h_2} = \left(\sqrt{m^2_{h_1} + p^2_{h_1}} + \sqrt{m^2_{h_2} + p^2_{h_2}} \right)^2 - (\vec{p}_{h_1} + \vec{p}_{h_2})^2$$

Since the tracks pairs triggered by the TTT have $p_T > 2$ GeV/c and the pion and kaon masses are respectively 0.140 MeV/c^2 and 0.494 MeV/c^2 we can approximate the squared invariant mass expression at first order in $O((m_{h_{1(2)}}/p_{h_{1(2)}})^2)$. With this approximation the difference between the squared invariant mass $M^2_{h_1 h_2}$ and the squared invariant mass reconstructed with a different mass assignment $M^2_{h'_1 h'_2}$ is:

$$M^2_{h_1 h_2} - M^2_{h'_1 h'_2} \sim \left(1 + \frac{p_{h_1}}{p_{h_2}} \right) \left(m^2_{h_2} - m^2_{h'_2} \right) + \left(1 + \frac{p_{h_2}}{p_{h_1}} \right) \left(m^2_{h_1} - m^2_{h'_1} \right)$$
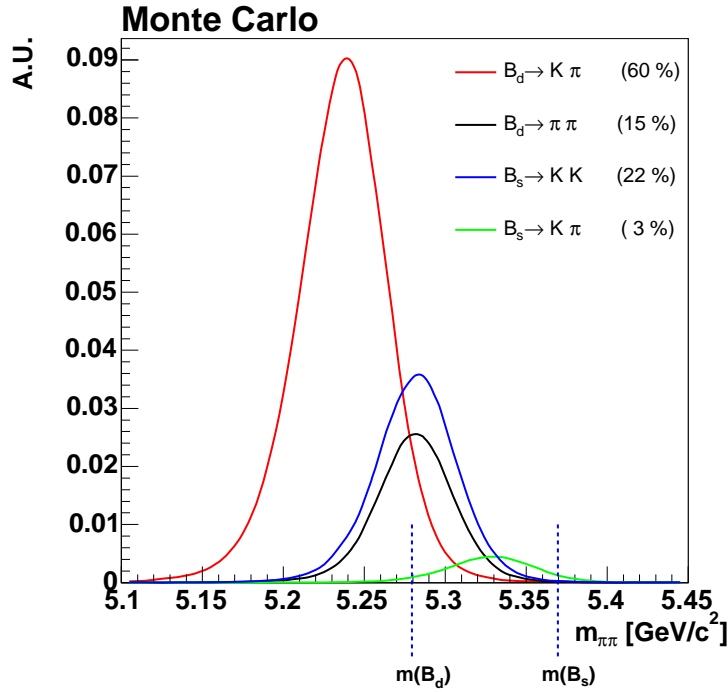
Figure 4.5: *Monte Carlo simulations: the four main contributing modes of the $B^0 \rightarrow h^{\pm}h'^{\mp}$ signal, reconstructed assigning the pion mass hypothesis to both the decay tracks.*

This expression shows that given the mass reconstructed with a particular mass assignment to the final states $M^2_{h_1 h_2}$, the mass reconstructed with any other mass assignment $M^2_{h'_1 h'_2}$ can be expressed as a function of the quantity p_{h_1}/p_{h_2}.

In our case we always assign the pion mass to the final states, so we can write:

$$M^2_{h'_1 h'_2} \sim M^2_{\pi\pi} - \left(1 + \frac{p_1}{p_2}\right)\left(m^2_\pi - m^2_{h'_2}\right) - \left(1 + \frac{p_2}{p_1}\right)\left(m^2_\pi - m^2_{h'_1}\right)$$

where p_1 and p_2 are the two tracks momenta. The variables $M_{\pi\pi}$ and p_1/p_2 contain all the information contained in the four possible mass assignments ($\pi\pi$, $K\pi$, πK, KK).

If $M_{h'_1 h'_2}$ is the invariant mass obtained using the correct mass assignment $m_{h_{1(2)}}$ to the final states, the mass calculated using the π mass assignment to both final states

is given by the following kinematics function:

$$\mathcal{M}^2\left(\frac{p_1}{p_2}\right) \sim M_{h'_1 h'_2}^2 + \left(1 + \frac{p_1}{p_2}\right)\left(m_\pi^2 - m_{h_2}^2\right) + \left(1 + \frac{p_2}{p_1}\right)\left(m_\pi^2 - m_{h_1}^2\right)$$

In the case of the $B_d \to K^+\pi^-$ and $B_s \to K^-\pi^+$ events, the πK or the $K\pi$ assignment leads to different forms of $\mathcal{M}(p_1/p_2)$. It is possible to take advantage of this including the charge of the final products in this description to tag the flavour of the B-meson. To do this we define the variable:

$$\alpha = q_1\left(1 - \frac{p_1}{p_2}\right)$$

where p_1, p_2 are now the three momenta of the two tracks and p_1 is chosen to be the lowest momentum track and q_1 its charge. The kinematics functions written in terms of the α-variable for the different $B^0 \to h^{\pm}h'^{\mp}$ modes are listed in table 4.1.

At a given α, $\mathcal{M}(\alpha)$ represents the expectation value for $M_{\pi\pi}$. In case of wrong mass assignment it gives an α dependent offset to the mass distribution. This behaviour is shown in figures 4.6 and 4.7 where we plot the $M_{\pi\pi}$ mass distribution as a function of α and the profile of that distribution $\langle M_{\pi\pi}\rangle$ for the different $B^0 \to h^{\pm}h'^{\mp}$ decay modes. The $\mathcal{M}(\alpha)$ are overlaid to the Monte Carlo data to show that the first order expansion is accurate enough to describe the α dependence.

For the $B_d \to \pi^+\pi^-$ decay (correct mass assignment to both final states) there is no dependence of the $M_{\pi\pi}$ distribution on the α variable. For the $B_s \to K^+K^-$ decay (wrong mass assignment for both final states) the $M_{\pi\pi}$ distribution is even in the α variable. For the $B_d \to K^+\pi^-$ and $B_s \to K^-\pi^+$ decays (wrong mass assignment only to one of the final states), the α dependence is monotonic and the slope for a B decay is opposite to the slope of a $\bar{B}$ decay.

These functions can be used as "templates" of the expected reconstructed mass as a function of α in a likelihood fit to disentangle the different $B^0 \to h^{\pm}h'^{\mp}$ components.

Decay mode	$\mathscr{M}^2(\alpha) : (\alpha < 0)$
$B_d \to \pi^+\pi^-$	$M_{B_d}^2$
$B_d \to K^+\pi^-$	$M_{B_d}^2 + (2+\alpha)(m_\pi^2 - m_K^2)$
$\bar{B}_d \to K^-\pi^+$	$M_{B_d}^2 + (1 + \frac{1}{1+\alpha})(m_\pi^2 - m_K^2)$
$B_s \to K^+K^-$	$M_{B_s}^2 + (3 + \alpha + \frac{1}{1+\alpha})(m_\pi^2 - m_K^2)$
$B_s \to K^-\pi^+$	$M_{B_s}^2 + (1 + \frac{1}{1+\alpha})(m_\pi^2 - m_K^2)$
$\bar{B}_s \to K^+\pi^-$	$M_{B_s}^2 + (2+\alpha)(m_\pi^2 - m_K^2)$

Decay mode	$\mathscr{M}^2(\alpha) : (\alpha > 0)$
$B_d \to \pi^+\pi^-$	$M_{B_d}^2$
$B_d \to K^+\pi^-$	$M_{B_d}^2 + (2-\alpha)(m_\pi^2 - m_K^2)$
$\bar{B}_d \to K^-\pi^+$	$M_{B_d}^2 + (1 + \frac{1}{1-\alpha})(m_\pi^2 - m_K^2)$
$B_s \to K^+K^-$	$M_{B_s}^2 + (3 - \alpha + \frac{1}{1-\alpha})(m_\pi^2 - m_K^2)$
$B_s \to K^-\pi^+$	$M_{B_s}^2 + (1 + \frac{1}{1-\alpha})(m_\pi^2 - m_K^2)$
$\bar{B}_s \to K^+\pi^-$	$M_{B_s}^2 + (2-\alpha)(m_\pi^2 - m_K^2)$

Table 4.1: *Explicit expression of the $\mathscr{M}(\alpha)$ for the different $B^0 \to h^\pm h'^\mp$ modes*
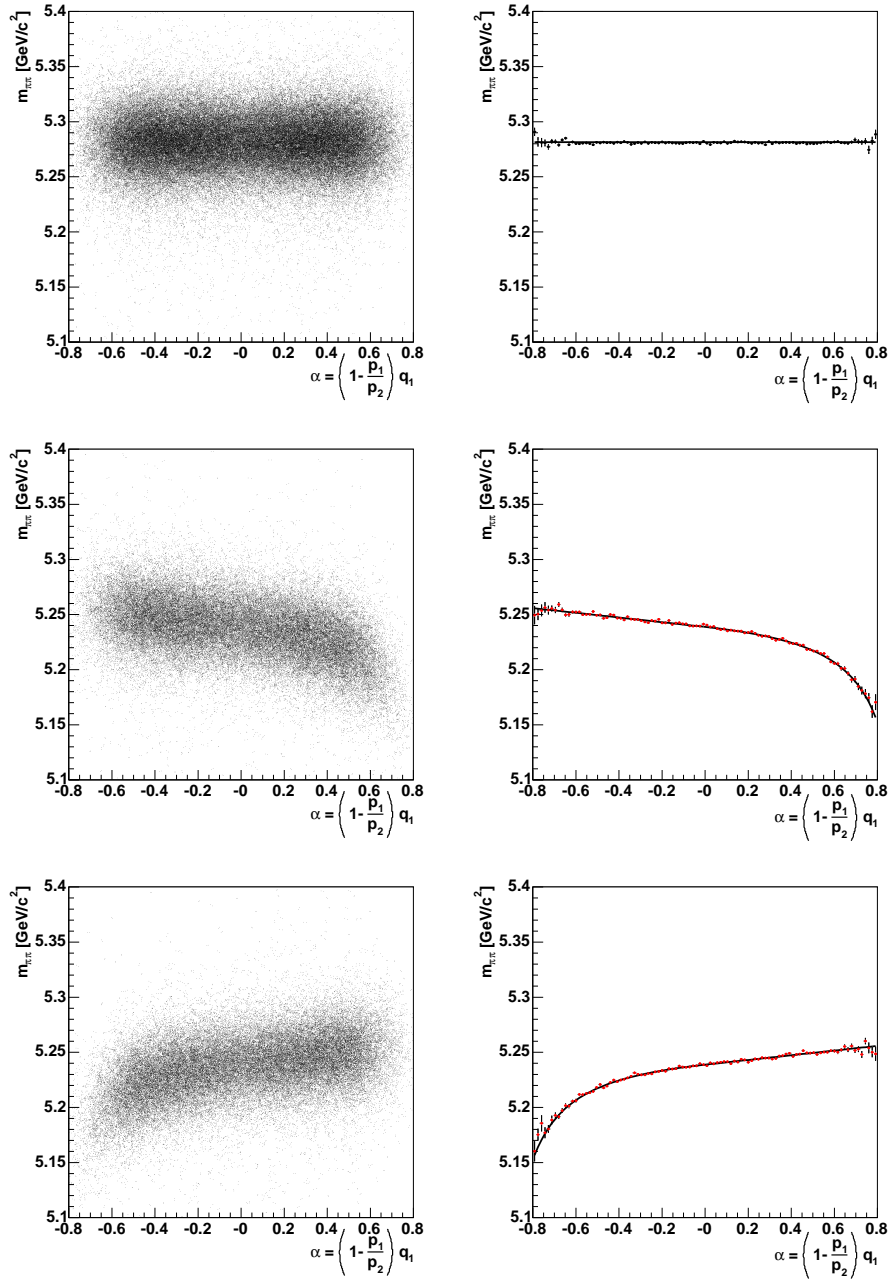
Figure 4.6: *Monte Carlo $M_{\pi\pi}$ distribution as a function of α. On the left the scatter plots, on the right the profiles of those plots overlaid to the formulas derived for $\mathscr{M}(\alpha)$ The plotted decays are: $B_d \rightarrow \pi^+\pi^-$ (top), $B_d \rightarrow K^+\pi^-$ (centre) and $\bar{B}_d \rightarrow K^-\pi^+$ (bottom).*
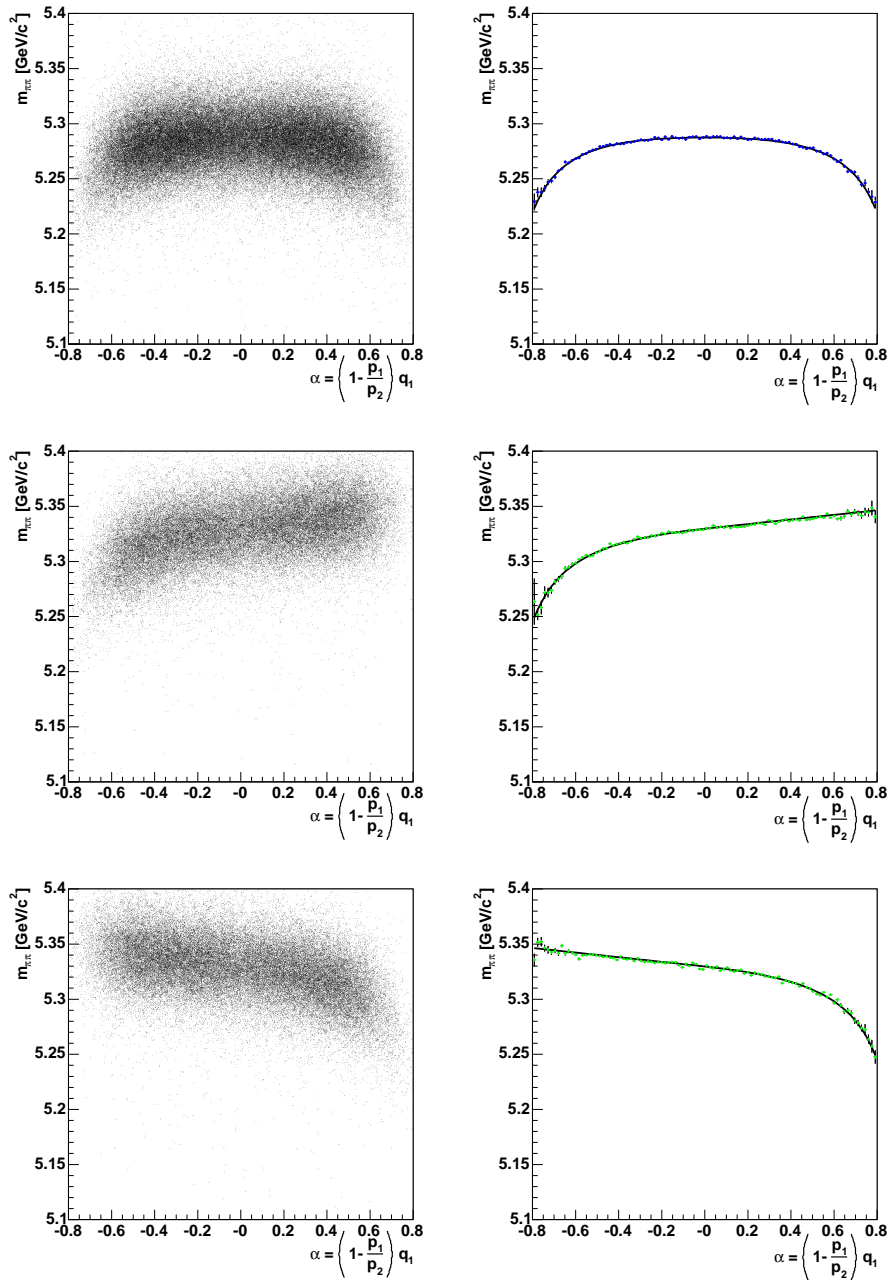
Figure 4.7: *Monte Carlo $M_{\pi\pi}$ distribution as a function of α. On the left the scatter plots, on the right the profiles of those plots overlaid to the formulas derived for $\mathscr{M}(\alpha)$ The plotted decays are: $B_s \to K^+K^-$ (top), $B_s \to K^-\pi^+$ (centre) and $\bar{B}_s \to K^+\pi^-$ (bottom).*

4.2.2 Particle identification

The reconstructed $M_{\pi\pi}$ distribution of the $B_d \to \pi^+\pi^-$ and $B_s \to K^+K^-$ decays almost perfectly overlap, indicating that the two contributions cannot be separated using only the kinematics information. On the other hand being the final states of respectively two pions and two kaons, we can take advantage of the particle identification to disentangle them. The particle identification does not add any separation power for the $B_d \to K^+\pi^-$ and $B_s \to K^-\pi^+$ decays, because they both have one pion and one kaon in their final states.

    The particle identification is obtained from the specific ionization (dE/dx) of the tracks in the COT. The additional information coming from the TOF, does not add much separating power in the range of momenta of our data sample, for this reason it has not been used. More details on this will be given in the cross checks section (see 4.6.6 and 4.6.7).

    It has been observed that the dE/dx residual distribution (defined as the difference between the measured and the expected dE/dx for a given particle species obtained from the calibrated universal curve) deviates from the gaussian shape showing a tail towards high values of dE/dx. In figure 4.8 we show as an example the residual distribution of the positive pions.[1] The dE/dx information will be used in a likelihood
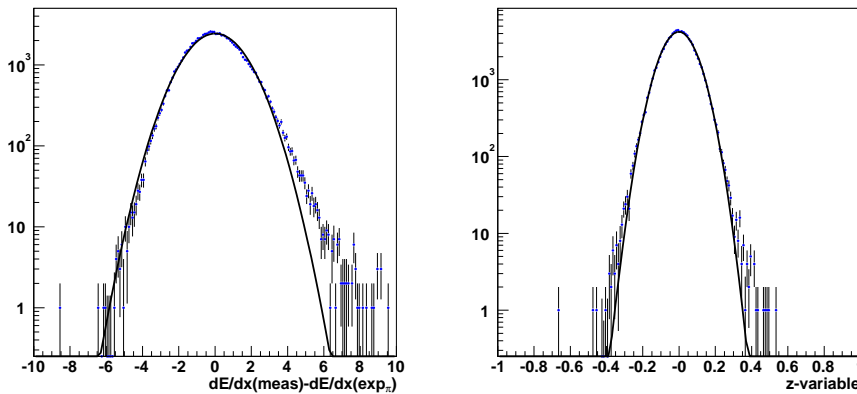

Figure 4.8: *(Left) dE/dx positive pions residual distribution fitted with a gaussian function; (right) the corresponding z variable distribution fitted with a gaussian function.*

function, so we would need to correctly describe the tail of this distribution. Instead

---

[1]The pion sample is taken from the $\overset{(-)}{D}{}^* \to \overset{(-)}{D} \pi^\pm$ and $\overset{(-)}{D} \to \pi^\pm K^\mp$. The charge of the pion coming from the D^* decay is used to identify the $D(\bar{D})$ and so from the charge of the tracks we identify which track is the pion and which is the kaon

of using the residuals in the dE/dx variable, we define the variable z:

$$z(p) = \log\left(\left.\frac{dE}{dx}\right|_m (p)\right) - \log\left(\left.\frac{dE}{dx}\right|_\pi (p)\right) = \log\left(\frac{\left.\frac{dE}{dx}\right|_m (p)}{\left.\frac{dE}{dx}\right|_\pi (p)}\right)$$

where p is the momentum of the track, $\left.\frac{dE}{dx}\right|_m (p)$ is the measured dE/dx and $\left.\frac{dE}{dx}\right|_\pi (p)$ is the dE/dx value predicted on the calibrated universal curve, assuming the pion mass. Thus the z variable distribution is equivalent to the residual distribution of the logarithms of the measured and expected dE/dx. The advantage in using the z variable is that it follows to an excellent approximation a gaussian distribution, and for this reason it will be very easy to introduce it in a likelihood.

4.3   Lifetime extraction

In the absence of any kind of trigger bias and resolution effects, the decay time distribution of an unstable particle follows an exponential distribution:

$$f(t) = \frac{1}{\tau}e^{-\frac{t}{\tau}}$$

where t is the proper decay time of the candidate and τ is the lifetime. With an abuse of notation we will call ct the proper decay time where, more correctly, we should talk about proper decay length. Since we will never use directly the proper decay time t, we will keep referring to ct as the proper decay time without creating any ambiguity. The proper decay time is defined as:

$$ct = L\frac{1}{\beta\gamma} = L\frac{m}{p} = L_{xy}\frac{m}{p_T}$$

where L is the three dimensional flight distance of the B-meson, i.e. the distance between the production position (primary vertex) and the decay position (secondary vertex) and m, p are respectively its mass and its momentum. Since the detector has the higher accuracy in the transverse plane, in practice we always use the above quantities projected onto it: L_{xy} and p_T.

Detector resolution effects introduce a smearing of the time measurement in such a way that the actual decay time distribution is described by the convolution:

$$f(ct) = \frac{1}{c\tau}e^{-\frac{ct}{c\tau}} \otimes R(ct; ct')$$

where $R(ct; ct')$ is an appropriate resolution function, ct is the reconstructed proper time (the measured quantity), while ct' is the true proper time (unknown).

The Two-Track Trigger (TTT) requirements on the track impact parameters, on the track pair opening angle and transverse decay length modify the proper decay time distribution, so that the distribution is no longer described by the previous equation.

The method we developed to extract the lifetime from a TTT biased sample, consists in parameterizing all the trigger and off line selection effects, into a single acceptance (efficiency) function of the reconstructed (measured) lifetime ($\epsilon(ct)$), so that the final proper decay time distribution is represented by:

$$f(ct) = \frac{1}{c\tau} e^{-\frac{ct}{c\tau}} \otimes R(ct; ct') \cdot \epsilon(ct)$$

A drawback of this approach is that the method relies on the correct description of the trigger effects and, most important, of the resolution models used in the simulation of the CDF II detector. Indeed the accuracy of the simulations is sufficient for the aim of the measurement, as shown in the following.

A general feature of the data sample collected selecting the events on their impact parameters is the reduction of the statistical power of the sample. As has been shown in [61], the statistical power of N signal events can be expressed as

$$\mathscr{P} = 1 - \left\langle \left(\frac{\frac{1}{2}\frac{\Delta t}{\tau}}{\sinh\left(\frac{1}{2}\frac{\Delta t}{\tau}\right)} \right)^2 \right\rangle$$

where Δt is the width of the time window defined by the lifetime cuts and τ is the lifetime of the data sample. $\mathscr{P}$ is the statistical power of the sample, i.e. N biased events have the same statistical power as $\mathscr{P} \cdot N$ unbiased events. Notice that as far as the statistical power is concerned, a cut on the minimum of the track impact parameter has to be considered on the same foot as an upper cut on the impact parameter, and more generally as all the cuts that reduce the proper time window. Given the typical proper decay time window of this analysis and the lifetime of the B-mesons, the reduction in statistical power is about 3.

4.3.1 Measurement of the efficiency functions

The easiest way to measure the efficiency function is to produce a Monte Carlo sample of the signal under investigation and take the bin by bin ratio of the proper decay time distribution of the events that pass the TTT ($H^{TTT}(ct)$) and the distribution before applying the TTT requirements ($H(ct)$)

$$\epsilon(ct) = \frac{H^{TTT}(ct)}{H(ct)}$$

This naive attempt does not give the correct efficiency function. The detector resolution applies a smearing on the data that modifies the turn on of the proper decay time distribution with respect to the ideal exponential case. The error on the proper decay time is calculated from the error propagation on the proper decay time formula:

$$\sigma_{ct} = \sigma_{L_{xy}} \frac{m}{p_T}$$

where we neglected the error on p_T.

The pitfall of this definition of efficiency function is that the σ_{ct} of the candidates has a different distribution for the events before and after the TTT selection. The reason is that the TTT selects a specific region of the kinematics phase space and in general a better track quality with respect to the remaining tracks in the sample. A possible extension of the method in two dimensions, parameterizing the efficiency function in (ct, σ_{ct}), would require a huge Monte Carlo statistics, making the method impractical.

An easier way to correctly define the efficiency function, that we will use in the following, is to take the ratio of the proper decay time distribution of the triggered sample and the distribution that the same sample would have had in absence of any selection cuts:

$$\epsilon(ct) = \frac{H^{TTT}(ct)}{\sum_i \exp(-ct/c\tau^{MC}) \otimes G(\sigma_{ct}^i)}.$$

The numerator has the same meaning as before, the denominator is the sum over all the events that *pass* the TTT of the lifetime distribution convoluted with the detector resolution function. In our description the resolution function is a gaussian centered at zero and width equal to σ_{ct}. This approach by construction takes into account the correct σ_{ct} distributions and requires to generate a Monte Carlo sample only of events triggered by the TTT.

It is worth noting that the τ used in the definition of the efficiency function is that used to produce the Monte Carlo sample. However the shape of the $\epsilon(ct)$ for a given decay depends only on its topology and in particular does not depend on the value of τ used to generate the Monte Carlo sample. The test to confirm this is reported in Appendix A.

The efficiency curve will appear in the maximum likelihood fit in a term like:

$$T(ct, \sigma_{ct}; c\tau) = (\exp(-ct/c\tau) \otimes G(0, \sigma_{ct})) \cdot \epsilon(ct)$$

where ct, σ_{ct} are the candidate proper decay length, τ is the lifetime parameter we want to fit and G is a gaussian representing the detector smearing. As all the terms in the likelihood function this term is a probability density function, hence it has to be normalized on the range of definition. The gaussian describing the detector

resolution depends event by event on σ_{ct}, and the whole term has to be normalized accordingly. This computational requirement guided the choice of the efficiency function parametrization. Given that the number of events in the data sample is of the order of a few thousand, we cannot afford in the likelihood maximization a numerical integration for each of them, so we have looked for a function that multiplied by an exponential convoluted with a gaussian would result in an analytically integrable (hence computationally light) expression. The parametrization we chose is:

$$\epsilon(ct) = \sum_{i=0}^{3} N_i (ct - \beta_i)^2 \cdot e^{-\frac{ct}{c\tau_i}} \cdot H(ct - \beta_i)$$

which is the sum of three terms with the same functional form but different input parameters $(N_i, \beta_i, c\tau_i)$. The number of terms we added has been chosen to better model the efficiency distributions. The systematic associated to the specific choice of the parametrization will be evaluated in 4.6.12. For each of the terms, H is the Heaviside function that determine the starting point of the distribution. The second order polynomial describes the turn on at low ct values and the exponential accounts for the high ct tail.

A series of tests performed on the efficiency functions to prove the correctness of the method are reported in Appendix A.

4.4 Likelihood of the Combined Fractions and Lifetime Fit

The simultaneous fit of the fractions and lifetimes on the $B^0 \to h^{\pm} h'^{\mp}$ sample merges in one likelihood function the information about the kinematics of the decay, the particle identification information about the two tracks, and the proper decay time of the B-meson candidate.

The likelihood function is written as:

$$\mathscr{L} = \prod_{i=1}^{N} \mathscr{L}_i$$

where N is the number of B-meson candidates in the data sample and $\mathscr{L}_i$ is the likelihood function calculated on the i-candidate:

$$\mathscr{L}_i = (1 - b) \cdot \mathscr{L}_{Signal} + b \cdot \mathscr{L}_{Background}$$

where b is the background fraction, $\mathscr{L}_{Signal}$ is the likelihood term for the signal and $\mathscr{L}_{Background}$ is the likelihood term for the background.
The signal likelihood is written as:

$$\mathscr{L}_{Signal} = \sum_{j=modes} f_j \cdot \mathscr{L}_j^{kin} \cdot \mathscr{L}_j^{PID} \cdot \mathscr{L}_j^{time}.$$

The index j runs over the four main $B^0 \rightarrow h^{\pm}h'^{\mp}$ decay modes ($B_d \rightarrow K^+\pi^-$, $B_d \rightarrow \pi^+\pi^-$, $B_s \rightarrow K^+K^-$, $B_s \rightarrow K^-\pi^+$ and charge conjugated) and the parameters f_j are their relative fractions to be determined by the fit. $\mathscr{L}^{kin}$, $\mathscr{L}^{PID}$, $\mathscr{L}^{time}$ are respectively the likelihood terms containing the information about the kinematics, the particle identification and the proper decay time of the signal.

The likelihood term describing the background has an analogous form:

$$\mathscr{L}_{Background} = \mathscr{L}_{bkg}^{kin} \cdot \mathscr{L}_{bkg}^{PID} \cdot \mathscr{L}_{bkg}^{time}$$

where again $\mathscr{L}_{bkg}^{kin}$, $\mathscr{L}_{bkg}^{PID}$, $\mathscr{L}_{bkg}^{time}$ are the likelihood terms containing respectively the information about the kinematics, the particle identification and the proper decay time of the background.

4.4.1   Signal Likelihood

Kinematics Term

The signal likelihood term containing the information about the kinematics of the decay is written as the product of a PDF (probability density function) for the invariant mass of the candidate $m_{\pi\pi}$ and α and a second PDF of the variables α and p ($p = p_1 + p_2$ sum of the three-momenta of the tracks). For each of the four main $B^0 \rightarrow h^{\pm}h'^{\mp}$ decay modes (j $= B_d \rightarrow K^+\pi^-$, $B_d \rightarrow \pi^+\pi^-$, $B_s \rightarrow K^+K^-$, $B_s \rightarrow K^-\pi^+$) the kinematics likelihood term is:

$$\mathscr{L}_j^{kin} = PDF_j^{kin}(m_{\pi\pi}, \alpha, p; \sigma_j, M_j(\alpha))$$

$$= PDF_j(\alpha, p) \cdot PDF_j(m_{\pi\pi}, \alpha; \sigma_j, M_j(\alpha))$$

$$= P(\alpha, p) \cdot \left(f_n \cdot \frac{1}{\sigma_n\sqrt{2\pi}} e^{-\left(\frac{m_{\pi\pi} - M_j(\alpha)}{\sqrt{2}\sigma_n}\right)^2} + (1-f_n) \cdot \frac{1}{\sigma_w\sqrt{2\pi}} e^{-\left(\frac{m_{\pi\pi} - M_j(\alpha)}{\sqrt{2}\sigma_w}\right)^2} \right)$$

The chosen PDF of the $m_{\pi\pi}$ variable (the mass term) is the sum of two gaussians both centered at $M_j(\alpha)$ and widths σ_n for the narrow one, σ_w for the wide one. f_n is the relative weight of the narrow gaussian. $M_j(\alpha)$ are the analytic functions that determine the expected $m_{\pi\pi}$ mass as a function of α for the decay mode j. For the

explicit functional form of the $M_j(\alpha)$ functions see table 4.1.

Figure 4.9 shows the mass distributions of the four main $B^0 \to h^{\pm}h'^{\mp}$ decay modes. The width of the narrow gaussian is $\sigma_n = 22 MeV/c^2$, the width of the wide gaussian is $\sigma_w = 50\ MeV/c^2$ and the relative weight of the narrow gaussian is $f_n = 0.05$. The widths of the double gaussian are extracted from Monte Carlo and rescaled to
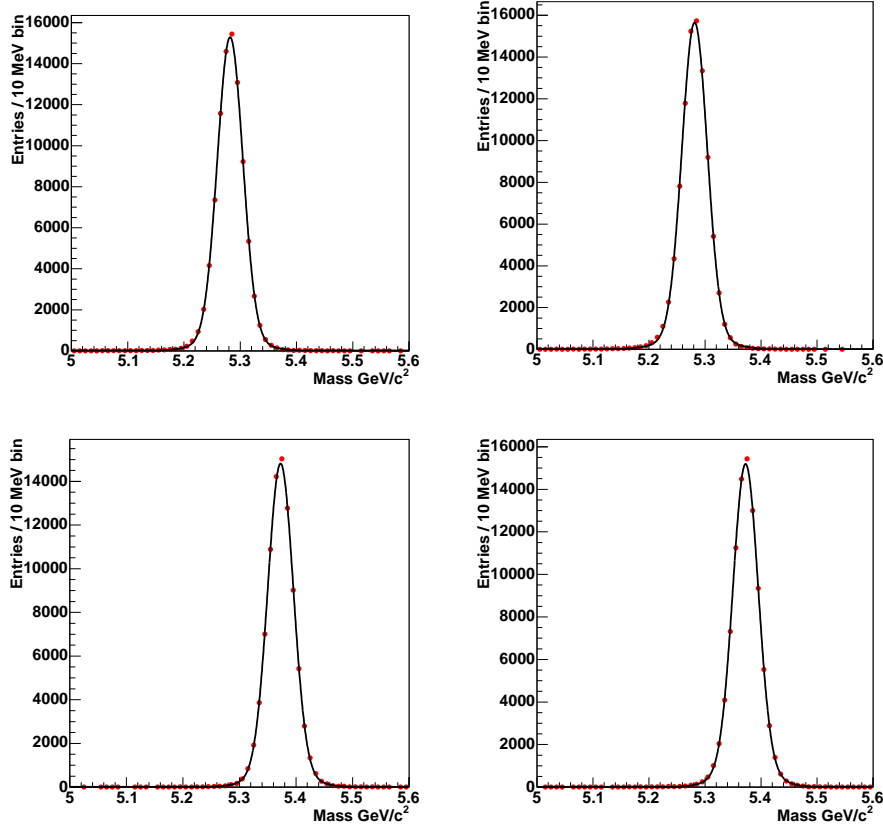

Figure 4.9: *Mass templates: top left $B_d \to K\pi$; top right $B_d \to \pi\pi$; bottom left $B_s \to KK$; bottom right $B_s \to K\pi$*

data, using a scaling factor of 1.17, obtained comparing Monte Carlo and data on the $B^{\pm} \to J/\psi K^{\pm}$ decay mode. A detailed study of the mass resolution scaling factor will be performed in the systematic uncertainties section.

The mass term contains information about the absolute mass scale of the detector, through the values of the B-meson masses in the expressions $M_j(\alpha)$. We used the values of the B_d and B_s meson masses measured in CDF Run II [62]:

- $m(B^0) = 5279.63 \pm 0.53_{(stat.)} \pm 0.33_{(syst.)} MeV/c^2$

- $m(B_s^0) = 5366.01 \pm 0.73_{(stat.)} \pm 0.33_{(syst.)} MeV/c^2$

The $P_j(\alpha, p)$ term has been written with the kinematics term even if its presence will be necessary only when the PID information is added. Since both kinematics and PID are functions of the variables (α, p), the combined probability is $P(Kin(\alpha, p), PID(a, p))$. This can be written in terms of the conditional probabilities:

$$P(Kin(\alpha, p), PID(a, p)) = P(Kin(\alpha, p)|PID(\alpha, p)) \cdot P(\alpha, p) =$$
$$P(Kin(\alpha, p)) \cdot P(PID(\alpha, p)) \cdot P(\alpha, p)$$

that can be read as, the probability of having certain kinematics and PID values, given (α, p) is the product of the probabilities of having a given value for the kinematics, a given value of the PID and a given value of the (α, p) variables.

This function could have been written in terms of α and one of the momenta p_1 or p_2. We chose $p = p_1 + p_2$ because the resulting distribution is easier to model.

The $P(\alpha, p)$ distribution is obtained for each of the four main $B^0 \rightarrow h^{\pm} h'^{\mp}$ decays from Monte Carlo simulations. It is fitted simultaneously in α and p with the following functional form:

$$P(\alpha, p) = \frac{1}{norm} e^{a_5\, p} \sum_{i=0}^{4} (a_i, p_i) \sum_{j=0}^{6} b_j \left(\alpha\, \frac{p-2}{p-4} \right)^j$$

where the a_i, b_j coefficients depend on the specific decay mode. The odd b_j terms are set to zero for the modes that are symmetric in the α variable, $B_d \rightarrow \pi^+ \pi^-$, $B_s \rightarrow K^+ K^-$.

The templates used for the different decay modes are collected in Appendix B.

Particle Identification Term

The likelihood term containing the information about the particle identification is written as:

$$\mathcal{L}_j^{PID} = PDF_{h,h'}^{PID}(z(1), z(2); \hat{z}_h(1), \hat{z}_{h'}(2), \sigma_h, \sigma_{h'})$$

$$= \frac{1}{\sigma_h \sqrt{2\pi}} e^{-\left(\frac{z(1) - \hat{z}_h(1)}{\sqrt{2}\, \sigma_h} \right)^2} \cdot \frac{1}{\sigma_{h'} \sqrt{2\pi}} e^{-\left(\frac{z(2) - \hat{z}_{h'}(2)}{\sqrt{2}\, \sigma_{h'}} \right)^2}$$

where $h(h')$ represent the mass hypothesis of the track ($h = \pi, K$, $h' = \pi, K$), and $1(2)$ represent the lower(higher) three momentum of the track. This ranking is inherited from the definition of α in the kinematics term.

As already shown, the variable z (function of the track momentum) is defined as the logarithm of the ratio between the measured dE/dx of the track and its expected

dE/dx in the pion mass hypothesis:

$$z(p) = \log\left(\frac{\frac{dE}{dx}\big|_m (p)}{\frac{dE}{dx}\big|_\pi (p)}\right)$$

where p is the momentum of the track.

The variable $\hat{z}$ (function of the track momentum) is the logarithm of the ratio between the expected dE/dx of the track in the $h = \pi, K$ mass hypothesis and the expected dE/dx of the track in the pion mass hypothesis.

$$\hat{z}(p) = \log\left(\frac{\frac{dE}{dx}\big|_h (p)}{\frac{dE}{dx}\big|_\pi (p)}\right)$$

The variable $\sigma_{h(h')}$ is the resolution on the z variable in the $h(h')$ mass hypothesis.

With these definitions the gaussian describing the PID of a pion track will be centered at zero and the gaussian of a kaon track will be centered (depending on its momentum) at a negative value.

The width $\sigma_{h(h')}$ of the gaussian describing the z variable distribution of a track is derived from the resolution of the dE/dx measurement in the COT as from the dE/dx calibrations. The resolution obtained from the COT calibrations are: $\sigma_{\pi^+} = 0.089$, $\sigma_{\pi^-} = 0.092$, $\sigma_{K^+} = 0.097$, $\sigma_{K^-} = 0.100$.

Proper Decay Time Term

The likelihood term containing the proper decay time information is written as:

$$\mathcal{L}_j^{time}(ct, \sigma_{ct}; c\tau_j) = \left(e^{-\frac{ct}{c\tau_j}} \otimes G(ct; 0, \sigma_{ct})\right) \cdot \epsilon_j(ct).$$

The first term is the convolution of the exponential decay law with a resolution function chosen to be a gaussian centered at zero and width equal to the ct uncertainty of the event. The second term, $\epsilon_j(ct)$, is the Monte Carlo based efficiency function describing the sculpting effect of both the TTT and the selection cuts. The efficiency curves for the B_d ($B_d \to K^+\pi^-$ and $B_d \to \pi^+\pi^-$) and B_s ($B_s \to K^+K^-$ and $B_s \to K^-\pi^+$) are very similar, because of the identical topology of the decays and the very similar masses involved.

The data have been collected with the two trigger paths `B_PIPI` and `B_PIPI_HIGH_PT`, the second having tighter kinematics requirements on the track pair. The efficiency curves calculated on the Monte Carlo events selected with the kinematics requirements of the two trigger paths are different. Hence, the efficiency curve for both B_d decay
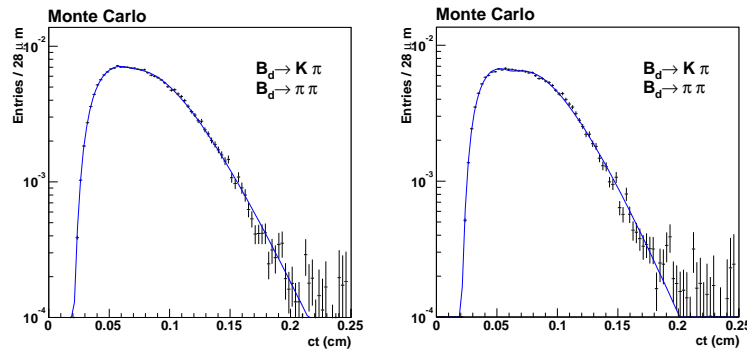
Figure 4.10: *Efficiency curves for the B_d meson: (left)* B_PIPI *trigger confirmation, (right)* B_PIPI_HIGH_PT *trigger confirmation.*
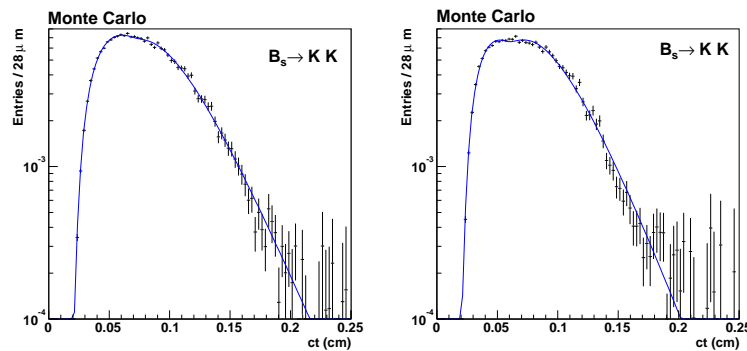

Figure 4.11: *Efficiency curves for the B_s meson: (left)* B_PIPI *trigger confirmation, (right)* B_PIPI_HIGH_PT *trigger confirmation.*

modes and B_s decay modes has been written as the sum of two efficiency curves calculated requiring the B_PIPI or B_PIPI_HIGH_PT trigger confirmation, weighted on the relative fractions of the two trigger paths. The events triggered by the B_PIPI_HIGH_PT represent the 7% of the total (see 3.1) . The curves obtained are plotted in figure 4.10 and 4.11. The parameters used in the description of the efficiency functions are listed in tables B.2 and 4.3.

Parameter	B_PIPI	B_PIPI_HIGH_PT
N_1	$4.121 \cdot 10^2$	$5.680 \cdot 10^2$
β_1	$1.932 \cdot 10^{-2}$	$1.940 \cdot 10^{-2}$
$c\tau_1$	$7.906 \cdot 10^{-3}$	$8.019 \cdot 10^{-3}$
N_2	$3.052 \cdot 10^2$	$4.052 \cdot 10^2$
β_2	$6.529 \cdot 10^{-2}$	$5.815 \cdot 10^{-2}$
$c\tau_2$	$1.744 \cdot 10^{-2}$	$1.712 \cdot 10^2$
N_3	$1.054 \cdot 10^2$	$1.445 \cdot 10^2$
β_3	$2.319 \cdot 10^{-2}$	$2.267 \cdot 10^{-2}$
$c\tau_3$	$1.952 \cdot 10^{-2}$	$1.729 \cdot 10^{-2}$

Table 4.2: *Parameters used to describe the efficiency functions of the B_d meson decays ($B_d \rightarrow K^+\pi^-$, $B_d \rightarrow \pi^+\pi^-$), for the two trigger paths:* B_PIPI *and* B_PIPI_HIGH_PT. β_i *and* $c\tau_i$ *units are* μm

Parameter	B_PIPI	B_PIPI_HIGH_PT
N_1	$1.175 \cdot 10^3$	$2.122 \cdot 10^3$
β_1	$2.085 \cdot 10^{-2}$	$2.110 \cdot 10^{-2}$
$c\tau_1$	$7.199 \cdot 10^{-3}$	$6.943 \cdot 10^{-3}$
N_2	$6.953 \cdot 10^2$	$2.226 \cdot 10^3$
β_2	$6.970 \cdot 10^{-2}$	$6.705 \cdot 10^{-2}$
$c\tau_2$	$1.566 \cdot 10^{-2}$	$1.350 \cdot 10^{-2}$
N_3	$1.158 \cdot 10^2$	$1.332 \cdot 10^2$
β_3	$2.543 \cdot 10^{-2}$	$2.522 \cdot 10^{-2}$
$c\tau_3$	$1.985 \cdot 10^{-2}$	$1.883 \cdot 10^{-2}$

Table 4.3: *Parameters used to describe the efficiency functions of the B_s meson decays ($B_s \rightarrow K^+K^-$, $B_s \rightarrow K^-\pi^+$), for the two trigger paths:* B_PIPI *and* B_PIPI_HIGH_PT. β_i *and* $c\tau_i$ *units are* μm

4.4.2   Background Likelihood

The likelihood term describing the background has the same structure as that used for the signal:

$$\mathscr{L}_{Background} = \mathscr{L}_{bkg}^{kin} \cdot \mathscr{L}_{bkg}^{PID} \cdot \mathscr{L}_{bkg}^{time}$$

but it differs from it for the functional forms used to write the single terms. The kinematics term is written as:

$$\mathscr{L}_{bkg}^{kin} = PDF_{bkg}^{kin}(m_{\pi\pi}, \alpha, p) = P'(\alpha, p) \cdot \frac{1}{Norm} \left(e^{c_0 + c_1 \cdot m_{\pi\pi}} + c_2 \right)$$

The mass distribution of the background is determined by the parameters c_0, c_1, c_2 that are extracted from the unbinned fit to the mass only variable (see figure 4.4). The used values are $c_0 = 27745.9$, $c_1 = -1.24$ and $c_2 = 4.57$. $P'(\alpha, p)$ is the probability density function of the variables (α, p) for the background which is obtained by fitting the bidimensional distribution of the variables (α, p) from data using the $B^0 \to h^{\pm}h'^{\mp}$ sidebands (chosen symmetrically around the $B^0 \to h^{\pm}h'^{\mp}$ mass peak at $[-7, -4] \cup [+4, +7]$ standard deviations). The functional form used to fit the (α, p) distribution is:

$$P'(\alpha, p) = \frac{1}{norm} \left[1 + \left(\frac{p - \lambda}{a} \right)^2 \right]^{-m} \exp \left[-\nu \tan^{-1} \left(\frac{p - \lambda}{a} \right) \right] \sum_{j=0}^{6} b_j \left(\alpha \, \frac{p - 2}{p - 4} \right)^j$$

The results of the fit are reported in Appendix B.

The PID term is written as:

$$\mathscr{L}_{bkg}^{PID} = PDF^{PID}(z(1), z(2); \hat{z}_h(1), \hat{z}_{h'}(2)), \sigma_h, \sigma_{h'})$$

$$= \left(f_{\pi} \cdot \frac{1}{\sigma_{\pi}\sqrt{2\pi}} e^{-\left(\frac{z(1) - \hat{z}_{\pi}(1)}{\sqrt{2} \, \sigma_{\pi}} \right)^2} + (1 - f_{\pi}) \cdot \frac{1}{\sigma_K\sqrt{2\pi}} e^{-\left(\frac{z(1) - \hat{z}_K(1)}{\sqrt{2} \, \sigma_K} \right)^2} \right) \times$$

$$\left(f_{\pi} \cdot \frac{1}{\sigma_{\pi}\sqrt{2\pi}} e^{-\left(\frac{z(2) - \hat{z}_{\pi}(2)}{\sqrt{2} \, \sigma_{\pi}} \right)^2} + (1 - f_{\pi}) \cdot \frac{1}{\sigma_K\sqrt{2\pi}} e^{-\left(\frac{z(2) - \hat{z}_K(2)}{\sqrt{2} \, \sigma_K} \right)^2} \right)$$

where we have kept the same notation used in the signal likelihood and we have added the parameter f_{π} that describes the fraction of pions in the background. In this term we are considering a background composed by pions and kaons only. In reality the tracks in the background might be generated by any of the stable or long lived particle species as pions, kaons, protons, muons and electrons. As pointed out in section 2.4, the COT has a limited separation power. Electrons have more
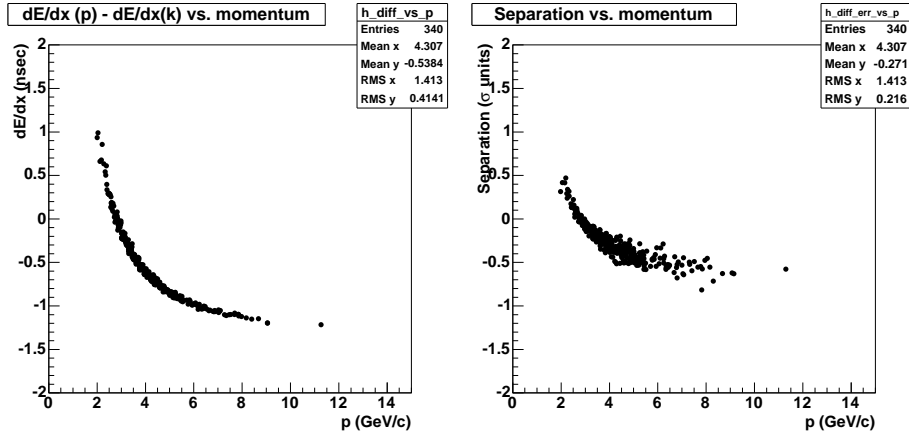
Figure 4.12: *(left) difference in the predicted dE/dx for proton and kaon hypothesis* $(\frac{dE}{dx}(proton) - \frac{dE}{dx}(kaon))$ *as a function of the track momentum; (right) proton kaon separation* $\frac{\frac{dE}{dx}(p) - \frac{dE}{dx}(k)}{\sqrt{\sigma(p)^2 + \sigma(k)^2}}$ *as a function of the track momentum*

than 2 σ separation from pions in the momentum range of interest, while muons and pions have practically the same specific ionization. Kaons and protons have the same specific ionization at about 3 GeV/c. In figure 4.12 we show the difference in specific ionization calculated using the momentum spectrum of the background in the mass region [5.4, 5.6] GeV/c^2, assigning to the tracks successively the proton and the kaon mass hypothesis In the same figure is also shown the separation between protons and kaons defined as $\frac{\frac{dE}{dx}(p) - \frac{dE}{dx}(k)}{\sqrt{\sigma(p)^2 + \sigma(k)^2}}$. The average separation is $\sim 0.26\sigma$. The maximum separation is 0.6 σ for tracks above 5 GeV/c^2 but those tracks account for only $\sim 25\%$ of the entire background spectrum.

In the present analysis we have decided to approximate the background description with only two particle categories: "pions" that will describe the tracks generated by pions and muons, and "kaons", that will describe the tracks generated by kaons and protons. Electrons are expected to represent a small fraction of the background tracks [63] and so, even if they have a relatively large separation from pions, they will be omitted from the background likelihood. The bias caused by these approximations is treated as a systematic uncertainty in section 4.6.8.

The likelihood term containing the proper decay time information is written as:

$$\mathscr{L}^{time}(ct; \sigma, c\tau') = \frac{1}{c\tau'} e^{-\frac{ct}{c\tau'}} \otimes \frac{1}{\sigma\sqrt{2\pi}} e^{-\left(\frac{ct-\mu}{\sqrt{2}\,\sigma}\right)^2}$$
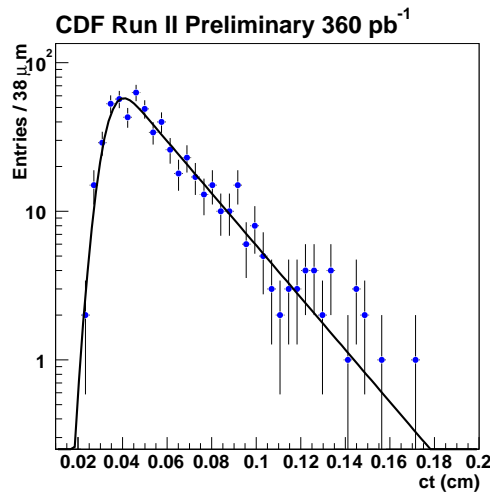
Figure 4.13: *Lifetime template of the mass sideband [5.4,5.6] GeV/c^2*

This term is the convolution of a lifetime distribution of time constant τ' (which represent the effective lifetime of the background), with a gaussian centered at μ and width σ. Both parameters are extracted from the data using the sideband [5.4,5.6] GeV/c^2, The background proper decay time distribution is plotted in figure 4.13 and the template parameters are listed in table 4.4.

Parameter	Value (μm)
$c\tau'$	$2.47 \cdot 10^{-2}$
μ	$3.3 \cdot 10^{-2}$
σ	$5.3 \cdot 10^{-3}$

Table 4.4: *Parameters used to describe the background lifetime template*

4.4.3 Tests on a toy Monte Carlo

The likelihood has been encoded in a "fitter" in the ROOT data analysis framework, and maximized using the MINUIT package.[2] The validity of the fitter has been verified in several ways. Here we report some tests performed on a toy Monte Carlo and on realistic Monte Carlo simulations.

In a toy Monte Carlo, the events to be fitted are generated on the likelihood function itself, i.e. each variable ($m_{\pi\pi}$, α, p, z_1, z_2, ct) is generated randomly from the corresponding term in the likelihood function. The first aim of this test is to verify that the fitter actually finds the correct likelihood maximum, but it is also used to understand how the different terms of the likelihood allow to separate the signal and background components and to predict the uncertainties we expect on the parameters we fit, assuming a given statistics and the signal and background fractions.

The first toy Monte Carlo test is performed using only the kinematics terms of the likelihood. The input to this fit are templates described above, the fractions for the four $B^0 \to h^{\pm}h'^{\mp}$ main decay modes and the fraction of background. We used as input fractions for the signal modes the one obtained in the study [56], and we assume 30% of background calculated from the study of the mass spectrum in fig 4.4. The results of the fit on 3219 events (2318 signal events and 901 background events, corresponding to the number of events expected in the final fit) are reported in table 4.5. The fit converged to the correct input values for the $B_d \to K^+\pi^-$ and $B_s \to K^-\pi^+$ but not for the $B_s \to K^+K^-$ and $B_d \to \pi^+\pi^-$. This is expected because the former can be separated with kinematics information only, while the latter are indistinguishable without using particle identification. The relative errors for the fractions are smaller for the $B_d \to K^+\pi^-$ and $B_s \to K^-\pi^+$ than for the $B_s \to K^+K^-$ and $B_d \to \pi^+\pi^-$. Also this effect can be explained as before with the absence of particle identification.

A second test has been performed adding the particle identification terms to the kinematics ones. The input to the fitter are the same as in the previous test. The results are reported in table 4.5. The fitter converged to the correct input values. The relative errors on the signals fractions are now very similar as a results of the particle identification information that allows to disentangle the $B_s \to K^+K^-$ from the $B_d \to \pi^+\pi^-$.

Finally we added the proper decay time information to the likelihood. We kept the same input fractions as before and we used as input lifetimes the values from the PDG: $c\tau(B_d) = 460\mu m$, $c\tau(B_s \to K^+K^-) = c\tau(B_s \to K^-\pi^+)438\mu m$. The fitter converged to the correct input values as reported in table 4.5.

---

[2]The MINUIT package includes a tool to find the relative minima of any user defined function. So, instead of maximizing the likelihood $\mathscr{L}$ we minimize $-\log\mathscr{L}$.

The projections of the fitted likelihood function on the toy MC data is plotted in figures 4.14 - 4.19.

It is worth notice here that the proper decay time information does not add much separating power, as demonstrates the almost unchanged statistical error on the fractions. This because the lifetimes of the different decay modes have very similar values.

Parameter	Input value	Kinematics	Kinematics PID	Kinematics PID Decay time	Units
$f(B_d \to K\pi)$	60	59.8 ± 1.9	59.8 ± 1.8	59.8 ± 1.7	%
$f(B_d \to \pi\pi)$	13	9.2 ± 6.6	13.4 ± 1.4	13.4 ± 1.4	%
$f(B_s \to KK)$	26	30.8 ± 6.8	26.0 ± 1.6	26.0 ± 1.6	%
$f(B_s \to K\pi)$	0	0.3 ± 1.6	0.3 ± 1.5	0.3 ± 1.5	%
$f(Background)$	30	30.8 ± 6.8	30.3 ± 1.8	30.3 ± 1.8	%
$c\tau(B_d)$	464	-	-	480.8 ± 29.6	μm
$c\tau(B_s \to KK)$	438	-	-	417.6 ± 54.0	μm

Table 4.5: *Results of the toy Monte Carlo tests.*

The last test performed using toy Monte Carlo data is the study of the pulls distributions. The pull of a quantity q is defined as $(q_m - q_g)/\sigma_m$ where q_m, q_g are the values of the measured (fitted) and generated (the toy Monte Carlo input) quantity, and σ_m is the statistical uncertainty on the measured value.

The pull distribution for a given quantity should be a standard gaussian. A distribution not centered at zero reveals a bias of the fitter, a distribution larger(narrower) than one, shows that the error on the corresponding quantity is under(over)-estimated. We repeated 100 pseudo-experiments, i.e. we generated and fitted 500 statistically independent samples of toy events (with the same characteristics of the preceding tests). The results of the pulls tests are reported in figure 4.20 and are indeed normally distributed.
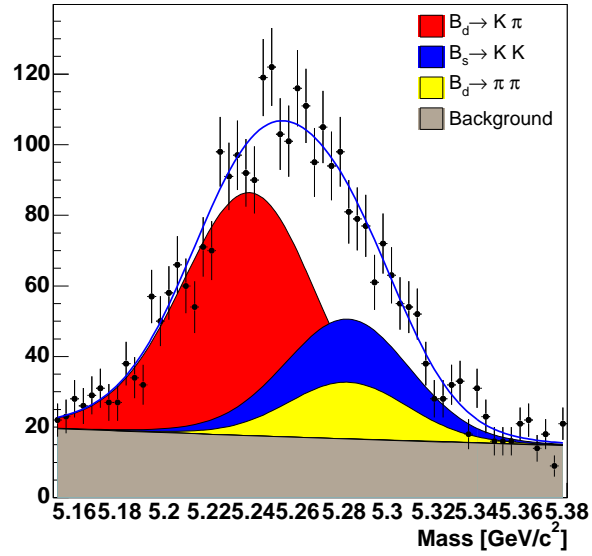
Figure 4.14: *Projection on the $m_{\pi\pi}$ variable of the likelihood fitted on toy Monte Carlo events.*
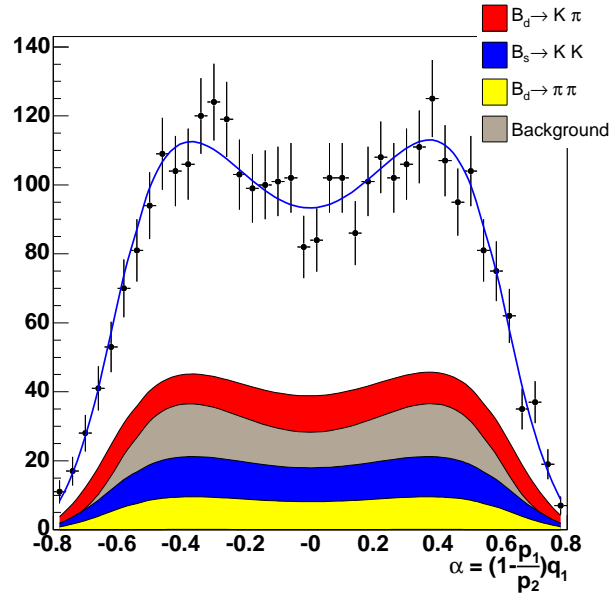

Figure 4.15: *Projection on the α variable of the likelihood fitted on toy Monte Carlo events.*
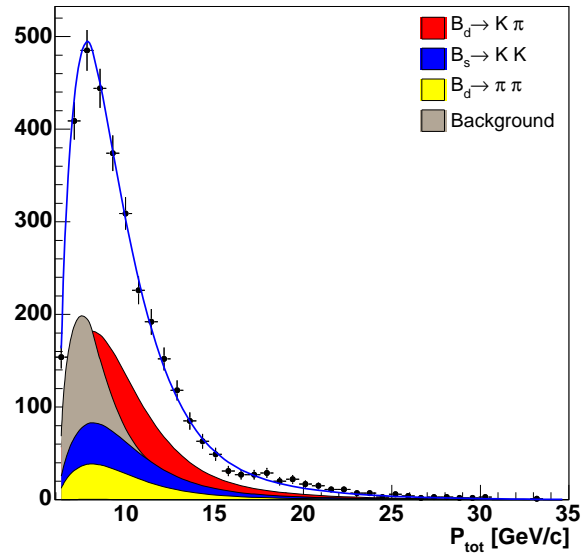
Figure 4.16: *Projection on the p variable of the likelihood fitted on toy Monte Carlo events.*
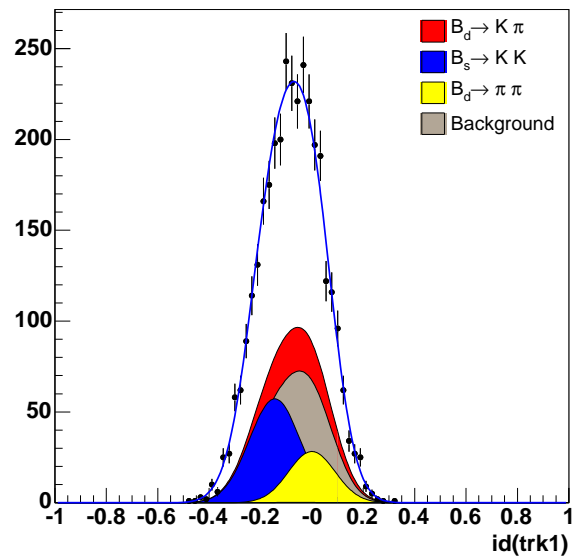
Figure 4.17: *Projection on the z_1 variable of the likelihood fitted on toy Monte Carlo events.*
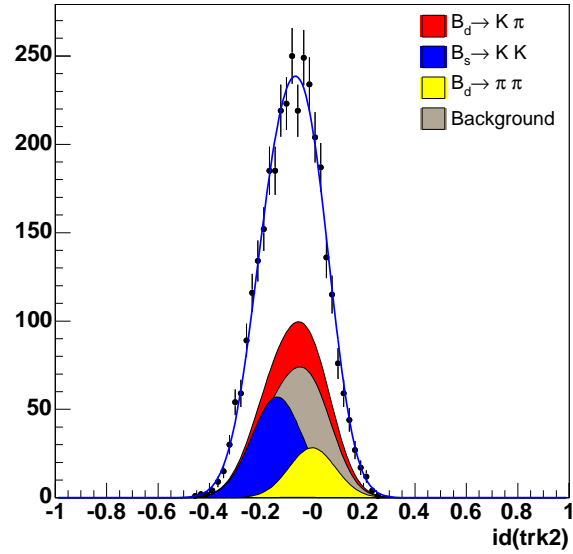
Figure 4.18: *Projection on the z_2 variable of the likelihood fitted on toy Monte Carlo events.*
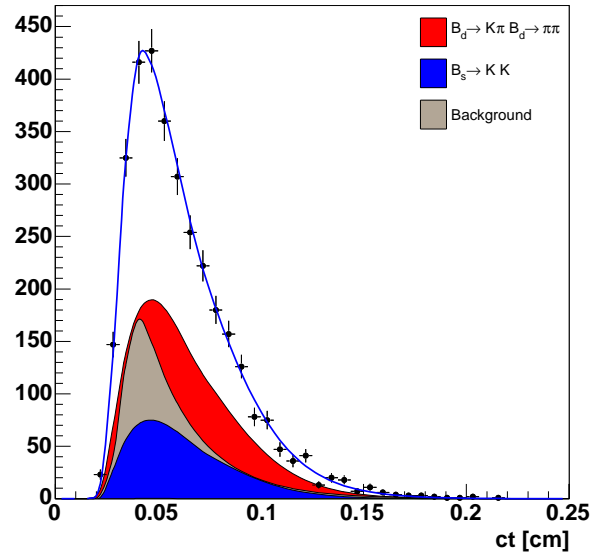
Figure 4.19: *Projection on the ct variable of the likelihood fitted on toy Monte Carlo events.*
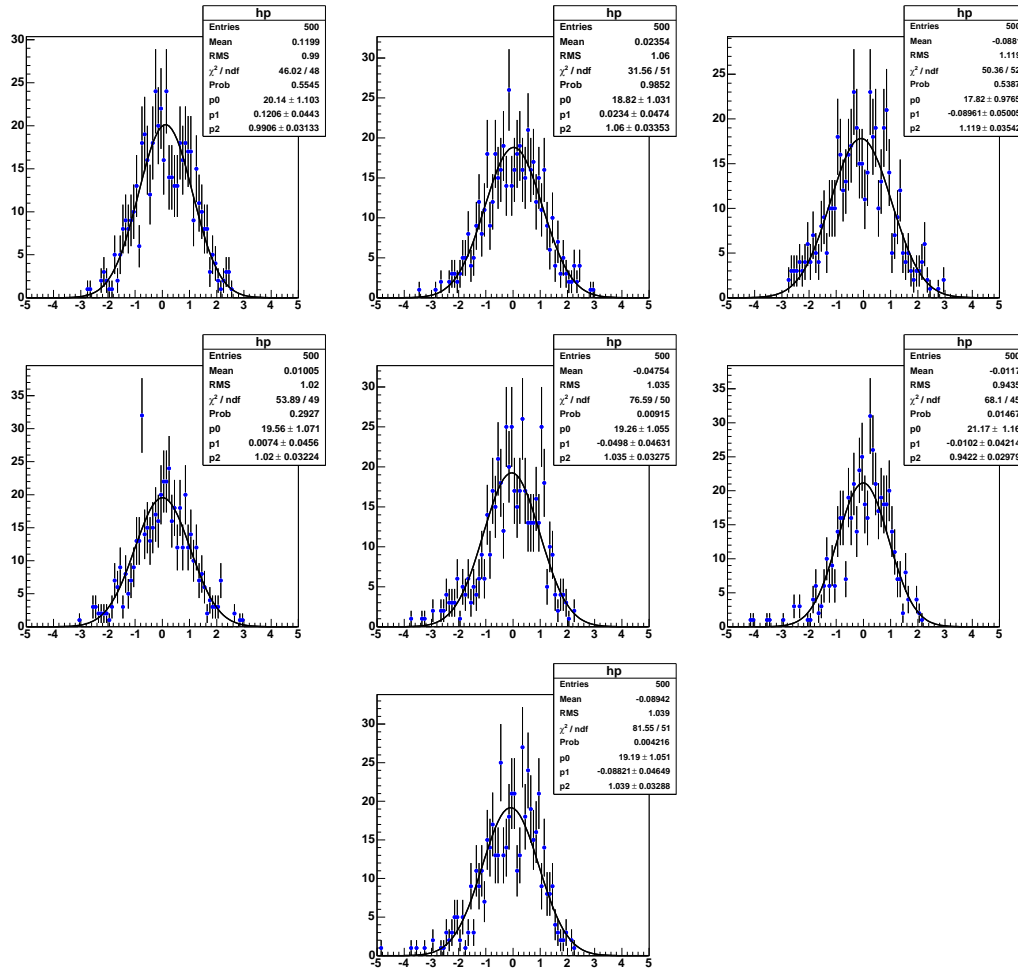
Figure 4.20: *Pulls distributions for the fitted quantities. $B_d \to K^+\pi^-$ fraction (top left); $B_d \to \pi^+\pi^-$ fraction (top centre); $B_s \to K^+K^-$ fraction (top right); background fraction (middle left); B_d lifetime (middle centre); $B_s \to K^+K^-$ lifetime (middle right); $B_s \to K^-\pi^+$ lifetime (bottom).*

4.4.4 Tests on Realistic Monte Carlo

The toy Monte Carlo tests allow to verify that the maximization of the likelihood converges indeed to the input values used to generate the toy events. On the other hand it doesn't reveal if the templates and the efficiency curves used in the description of the signal are correct. To check their correctness, we performed a fit on a realistic Monte Carlo sample. To avoid possible pitfalls due to the difference in the relative fractions of the four main $B^0 \to h^\pm h'^\mp$ modes, we decided to generate a Monte Carlo sample where those fractions are all artificially set to 25%. The generated statistics is about 10 times higher than the one available at present on data. The results of the fit are reported in table 4.6. We observe that the fitted values all agree with the input ones within the statistical uncertainty, demonstrating that the templates and efficiency functions used correctly describe the signal components.

Parameter	Input value	Fitted value	Units
$f(B_d \to K\pi)$	25	24.6 ± 0.3	%
$f(B_d \to \pi\pi)$	25	25.6 ± 0.3	%
$f(B_s \to KK)$	25	25.0 ± 0.4	%
$f(B_s \to K\pi)$	25	24.8 ± 0.4	%
$c\tau(B_d)$	464	468.3 ± 7.2	μm
$c\tau(B_s \to KK)$	438	429.7 ± 9.1	μm
$c\tau(B_s \to K\pi)$	438	449.4 ± 12.0	μm

Table 4.6: *Results on a high statistics Monte Carlo sample.*

4.5   Combined fractions and lifetime fit results

The fitter we developed has been challenged in several ways in the previous sections, where it proved its reliability. In this section we will finally perform the measurement applying the fitter on data.

The measurement is performed on the events that pass the optimized set of analysis cuts and that lies in the volume of the input variables defined by:

- invariant mass of the B candidates: $m_{\pi\pi} \in [5.15, 5.38]\ GeV/c^2$

- α variable: $\alpha \in [-0.8, 0.8]$

- scalar sum of the tracks momenta: $p \in [5.95, 35.0]GeV/c$

- proper decay time of the B candidate: $ct \in [0.0, 0.25]$ cm

The invariant mass range has been sized following the results of background analysis with the mass only fit performed in section 4.1. The other boundaries are set not to reject any event. The total number of event with this requirements is 3219.

The $B_s \to K^+K^-$ lifetime measurement is pursued in two steps.

1: B_d lifetime unconstrained

In the first step we fit the four $B^0 \to h^{\pm}h'^{\mp}$ fractions, the lifetimes of the B_d and $B_s \to K^+K^-$, and the fraction of pions in the background. All the parameters describing the signal templates and background are fixed. We apply a gaussian constraint to the background fraction and slope, obtained in the mass spectrum study in figure 4.4. We apply a gaussian constrain to the background lifetime to the value obtained for the proper decay time template and we constrained the $B_s \to K^-\pi^+$ lifetime to the PDG world average. This last requirement has been applied because with the present integrated luminosity we expect a very small number of $B_s \to K^-\pi^+$ events.

The results of the fit are reported in table 4.7. The fitted signal relative fractions and the fractions of pions in the background are in agreement with previous CDF Run II $B^0 \to h^{\pm}h'^{\mp}$ analysis [56]. The B_d lifetime is measured to be $452 \pm 24\mu m$ and the $B_s \to K^+K^-$ lifetime $463 \pm 55\mu m$, where the error is statistical only. The lifetime of the B_d meson is in good agreement with the PDG world average of $460 \pm 4\mu m$ [8], where the error is statistical only.

Figure 4.21, reports the likelihood scans for the fractions and lifetimes, showing an almost perfectly parabolic minimum.

The correlation matrix is reported in tables 4.22. The largest correlation are, as expected, between the fractions of pion in the background and the parameter containing the information about the $B_d \to \pi^+\pi^-$ signal fraction (-0.472); between

Parametes	value			
$f(B_d \to K\pi)$	62.7	$\pm$	1.7	%
$f(B_d \to \pi\pi)$	15.3	$\pm$	1.5	%
$f(B_s \to KK)$	22.3	$\pm$	1.7	%
$f(B_s \to K\pi)$	-0.3	$\pm$	1.0	%
$f(\text{background})$	27.8	$\pm$	1.4	%
f_π in the background	51.7	$\pm$	3.0	%
$c\tau(B_d)$	452	$\pm$	24	μm
$c\tau(B_s \to K^+K^-)$	463	$\pm$	55	μm

Table 4.7: *Results of the combined fractions and lifetimes fit (uncertainties are statistical only)*

the lifetime of the $B_s \to K^+K^-$ and the B_d (-0.270); between the lifetime of the $B_s \to K^+K^-$ and the background (-0.101); between the lifetime of the B_d and the background (-0.282).

2: B_d constrained

Since the value fitted for the B_d lifetime is compatible with the world average, in the second step of our fitting procedure we also apply a gaussian constraint to the B_d lifetime to the PDG value to take advantage of the world average precision. The results of the fitted quantities are reported in table 4.8. The $B_s \to K^+K^-$ lifetime is measured to be $458 \pm 53\mu m$ where the error is statistical only. The constraint on the B_d lifetime does not change the values of the fitted fractions, but it does shift the $B_s \to K^+K^-$ fitted lifetime by 5 μm .

The fit projections on data are plotted in figures 4.23-4.28.

Parametes	value			
$f(B_d \rightarrow K\pi)$	62.7	$\pm$	1.7	%
$f(B_d \rightarrow \pi\pi)$	15.3	$\pm$	1.5	%
$f(B_s \rightarrow KK)$	22.3	$\pm$	1.7	%
$f(B_s \rightarrow K\pi)$	-0.3	$\pm$	1.0	%
f(background)	27.8	$\pm$	1.4	%
f_π in the background	51.8	$\pm$	3.0	%
$c\tau(B_d)$ constrained to PDG	460	$\pm$	4	μm
$c\tau(B_s \rightarrow K^+K^-)$	458	$\pm$	53	μm

Table 4.8: *Results of the combined fractions and lifetimes fit with B_d lifetime constrained to the PDG value (uncertainties are statistical only)*
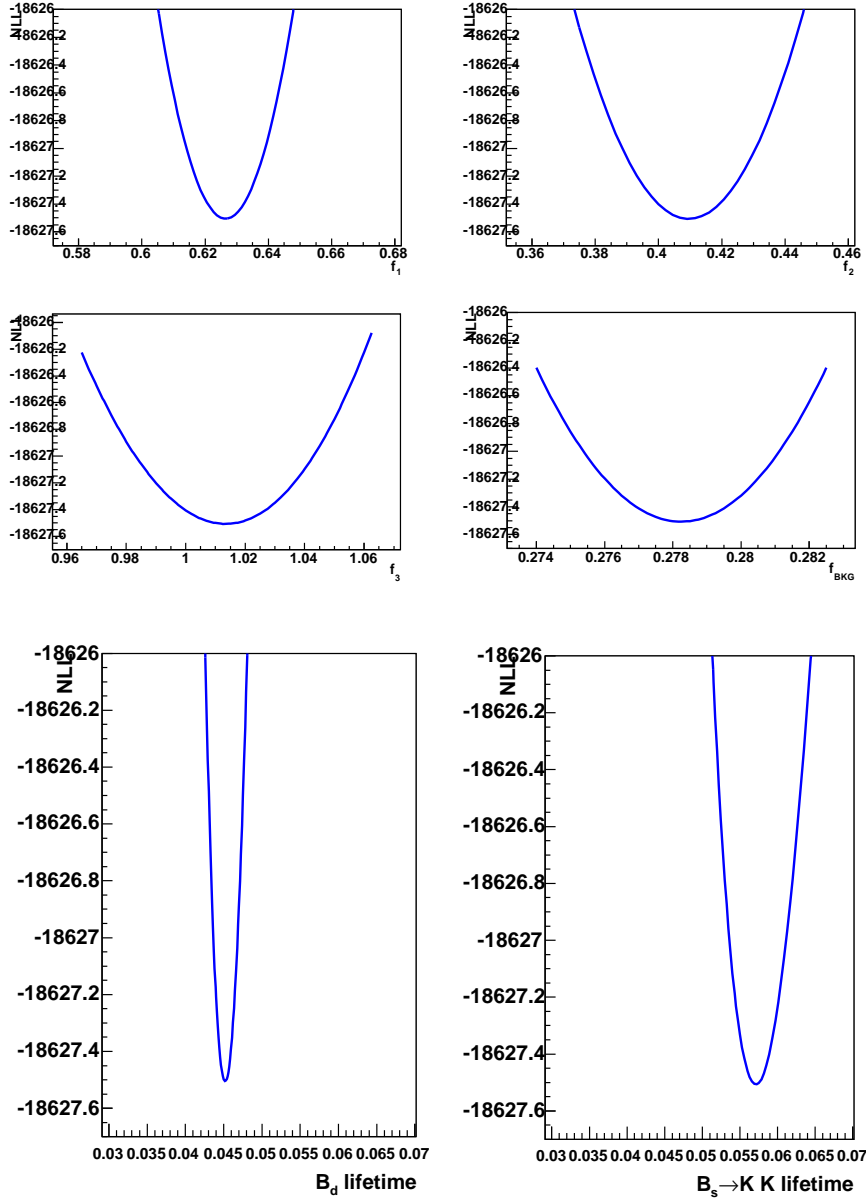
Figure 4.21: *Likelihood scans: (top) fitted fractions, (bottom) fitted lifetimes*

```
PARAMETER  CORRELATION COEFFICIENTS
   NO.   GLOBAL     1       2       3       6       9      13      14      15      18      19
    1   0.07362   1.000  -0.032  -0.005   0.026   0.003   0.008   0.000   0.014   0.056  -0.013
    2   0.47610  -0.032   1.000  -0.044  -0.015  -0.472  -0.072   0.000   0.039  -0.011   0.049
    3   0.05230  -0.005  -0.044   1.000  -0.017   0.004   0.003  -0.001   0.001  -0.010  -0.005
    6   0.04979   0.026  -0.015  -0.017   1.000  -0.012   0.014   0.000   0.005  -0.005   0.017
    9   0.47757   0.003  -0.472   0.004  -0.012   1.000   0.091  -0.000  -0.051   0.008  -0.068
   13   0.41607   0.008  -0.072   0.003   0.014   0.091   1.000  -0.000  -0.270   0.001  -0.282
   14   0.00098   0.000   0.000  -0.001   0.000  -0.000  -0.000   1.000  -0.000   0.000   0.000
   15   0.32933   0.014   0.039   0.001   0.005  -0.051  -0.270  -0.000   1.000   0.003  -0.101
   18   0.05880   0.056  -0.011  -0.010  -0.005   0.008   0.001   0.000   0.003   1.000  -0.005
   19   0.34083  -0.013   0.049  -0.005   0.017  -0.068  -0.282   0.000  -0.101  -0.005   1.000

 1: F_B0_kpi
 2: F_B0_pipi/(1-F_B0_kpi)
 3: F_Bs_kk/(1-F_B0_kpi)/(1-F_B0_pipi)
 6: F_BG (Background Fraction)
 9: Fraction of pi in the background
13: B0 lifetime
14: Bs->Kpi lifetime
15: Bs->KK lifetime
18: slope of the background
19: Background average lifetime
```

Figure 4.22: *Correlation matrix of the combined fractions and lifetimes fit*
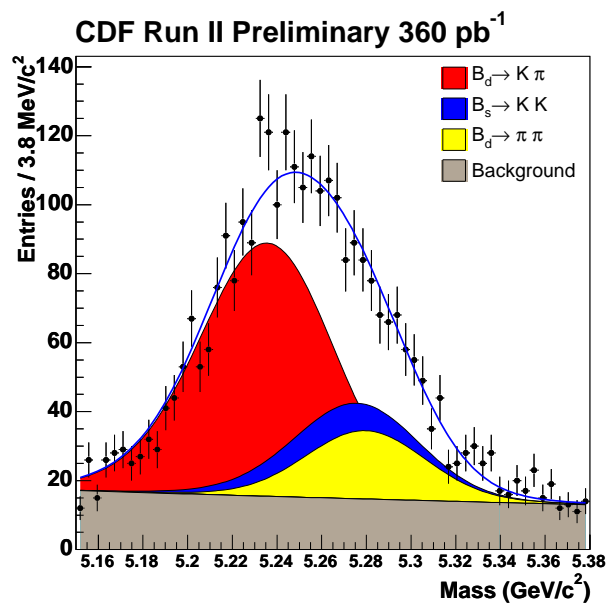
Figure 4.23: *Projection of the likelihood on data: $m_{\pi\pi}$ variable*
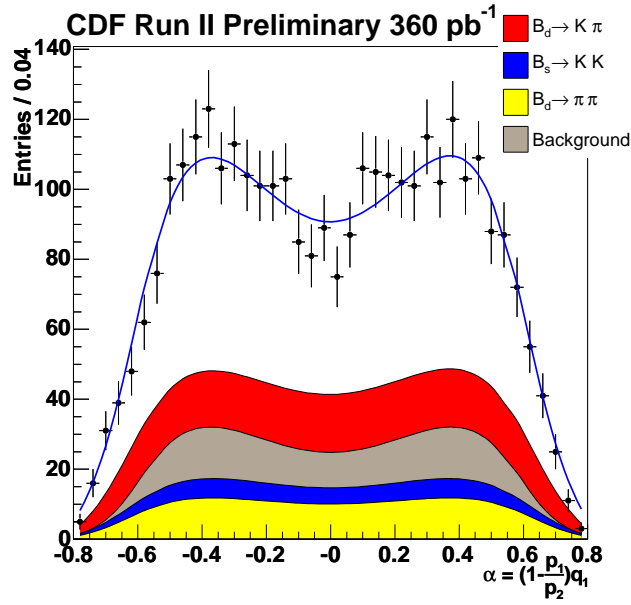
Figure 4.24: *Projection of the likelihood on data: α variable*
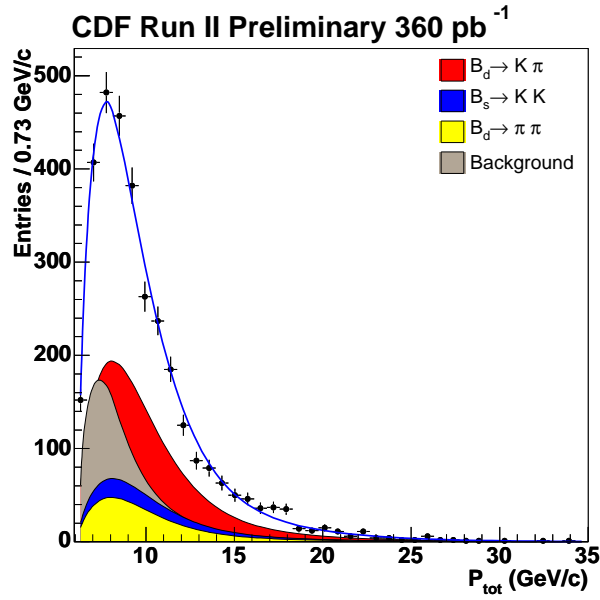
Figure 4.25: *Projection of the likelihood on data: p variable*
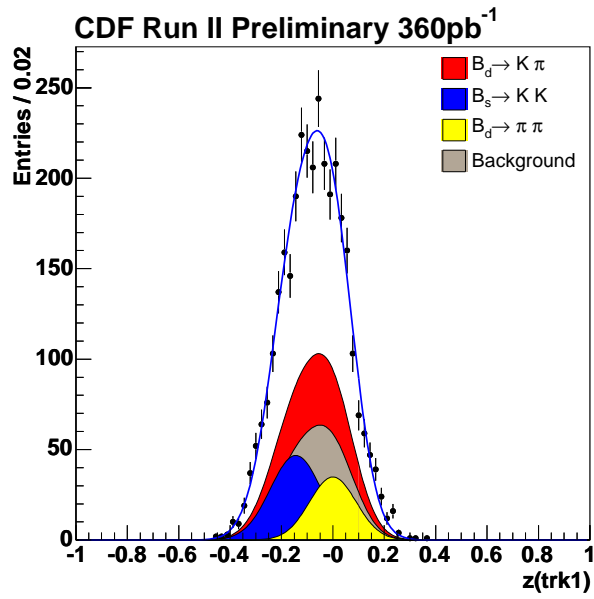
Figure 4.26: *Projection of the likelihood on data: z_1 variable*
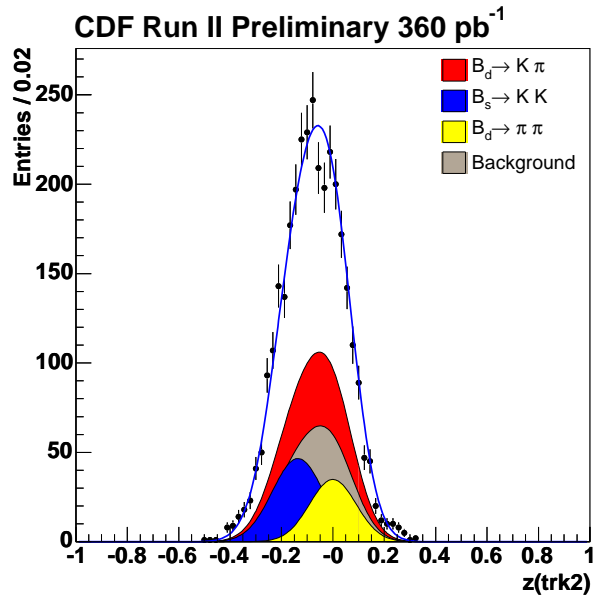

Figure 4.27: *Projection of the likelihood on data: z_2 variable*
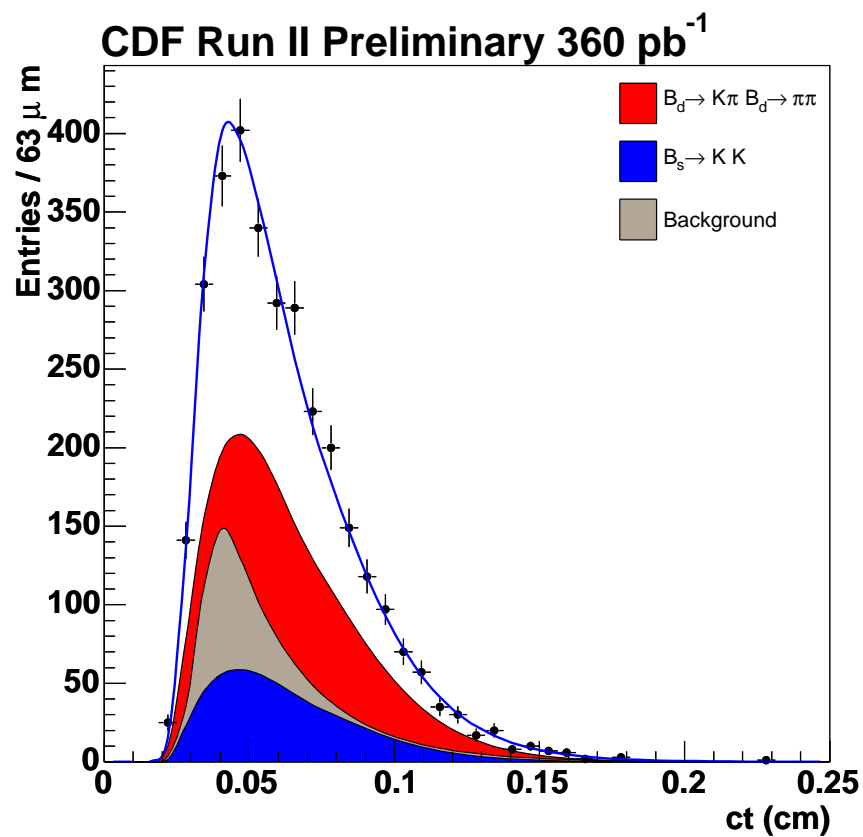
Figure 4.28: *Projection of the likelihood on data: ct variable*

4.6   Systematic Uncertainties

In this section we discuss the main sources of systematic uncertainties of the B_s and B_d lifetime measurements. A few sources of systematic uncertainty are common to all CDF lifetimes measurements being affected by the TTT and the selection cuts bias. We will refer to the results of the studies performed in [65], [66] and [67], to quantify the systematic uncertainties related to the alignment of the silicon detectors and to the proper decay time resolution model.

In this section we report on those specific systematic effects affecting our measurement of the B_s and B_d meson lifetimes in the $B^0 \to h^\pm h'^\mp$ sample.

4.6.1   Absolute Mass Scale

The combined fractions and lifetime fit is performed assuming a known absolute mass scale, introduced through the B_d and B_s masses. The values used in the fit are the published values measured by CDF Run II [62]. Since the mass is an information used to disentangle the different signal contributions, we can expect a systematic uncertainty in the relative signal fractions and consequently on the B_d and B_s lifetimes. To asses this systematic uncertainty we varied the absolute mass scale by (± 0.6 MeV/c^2), a value that is obtained in the analysis described in [68], and which is estimated by comparing $B^+ \to J/\psi K^+$ event-by-event mass differences (in the sample reconstructed with the same software release and calibrations used in our analysis), with those used in the published CDF Run II results.
We obtain a systematic uncertainty of ± 0.6 μm .

4.6.2   Mass Resolution Scale Factor

In our double gaussian model for the signal mass distribution, we use the resolution obtained in the realistic simulations, multiplied by a scaling factor obtained by comparing the resolution of the invariant mass measured in $B^+ \to J/\psi K^+$ data and the corresponding realistic simulation. With this procedure we obtained a scaling factor of 1.17. This determination of the scaling factor assumes that the ratio between the mass resolution of the data and the Monte Carlo, is the same for the $B^0 \to h^\pm h'^\mp$ and $B \to J/\psi K$ decays.

In order to evaluate the systematic uncertainty resulting from this assumption we have measured the scaling factor (again comparing the resolution on data with the one obtained from realistic simulation) on two other samples: $D^+ \to K^+\pi^-\pi^+$ and $D^0 \to K^+\pi^-$. For the three body decay $D^+ \to K^+\pi^-\pi^+$ we obtain a scaling factor of 1.07. For the calculation of the scaling factor in the $D^0 \to K^+\pi^-$, which is a two body
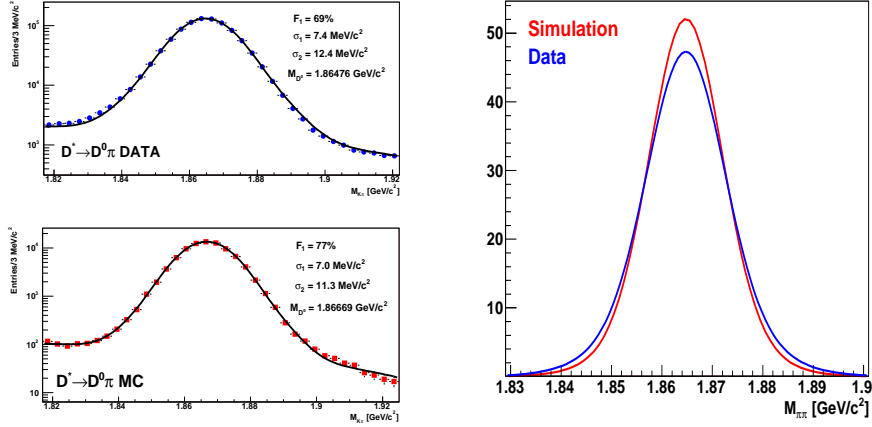
Figure 4.29: *Comparison of the D^0 mass spectrum between data and MC. (left) top: data mass spectrum, peak fit with two gaussian plus a second order polynomial for the background; bottom: MC mass spectrum, peak fit with two gaussian plus a second order polynomial for the background; (right) the double gaussian fits of data and MC overlaid*

decay as the $B^0 \rightarrow h^{\pm} h'^{\mp}$, we performed a more detailed study comparing widths and fractions of the two gaussians building our resolution model. We performed a generic $D^* \rightarrow D^0 \pi$ Monte Carlo allowing the D^0 to decay to all possible modes. The comparison between data and Monte Carlo (figure 4.29), shows a very good agreement between the two. The scaling factor obtained from the $D^0 \rightarrow K^+ \pi^-$ is 1.12.

In order to estimate the systematic uncertainty coming from the mass scaling factor we re-performed our fit varying it conservatively from 1.07 to 1.24.
We obtain a systematic uncertainty of ± 0.5 μm . We also varied the relative fractions between the two gaussians, by enlarging the wide one by 50%, obtaining a systematic effect of $\pm 0.3 \mu m$.

4.6.3 B Meson Input Masses

The B-meson masses are an input parameter to the fit through the analytical expression of $M(\alpha)$. In order to estimate the systematic uncertainty due to the finite precision on the determination of the input masses we varied the B_d and B_s masses by ± 1 standard deviation of the CDF Run II published values [62].
We obtain a systematic uncertainty of ± 0.4 μm .

4.6.4   Model for the (α, p) Parametrization

The (α, p) parameterization for the background has been extracted from a binned fit to the histogram built on the signal sidebands [5.0,5.1] U [5.4,5.5] GeV/c^2 (see Appendix B). We considered the systematic effect of the low background statistics varying one by one the parameters of the model within $\pm 1\sigma$. We also considered the effect of the $B \to \rho\pi(K)$ partially reconstructed decays, subtracting their contribution from the left sideband and extracting a new template. To asses this effect a toy study has been performed with 100 pseudo-experiments each with the same statistics as that of the data. The results gave a negligible systematic uncertainty.

4.6.5   Partially Reconstructed $B \to \rho\pi$ Decay Contamination

In section 4.1, we observed a contamination from $B \to \rho K/\pi$ partially reconstructed decays of 1.1% relative to the $B \to K\pi$ signal and in the standard fit we neglect this contamination. To quantify the possible bias coming from those decays, we included them in the fit with the appropriate templates, keeping their fraction fixed. The bias given by this contamination is $\pm 0.02\mu m$.

4.6.6   dE/dx Calibrations

We have evaluated the systematic effect associated to the uncertainties relative to the dE/dx calibrations. The calibrations were performed fitting the universal curve (Bethe-Bloch) to the dE/dx distribution obtained with different particle species (see section 2.4). The additive correction factor is evaluated as the offset of the pull distribution of the measured dE/dx with respect to the universal curve. To evaluate the systematic effect on the lifetimes, we added to the calibration an overall shift equal to the uncertainty of the pull fit and we varied the dE/dx resolutions, again by the uncertainty of the pull fit.

   We estimate a systematic uncertainty due to the dE/dx calibrations of ± 2.0 μm .

4.6.7   dE/dx Track Correlations

In [64] a small correlation was observed between the measurement of the dE/dx for the two tracks. The study in [64] measures the branching ratio for the various $B^0 \to h^{\pm}h'^{\mp}$ modes and is based on the same data sample and the same likelihood structure of the present analysis with the addition of a dE/dx correlation term. We estimate the effect on B_d and $B_s \to K^+K^-$ lifetimes of neglecting the dE/dx correlation term, performing the fit with the four main $B^0 \to h^{\pm}h'^{\mp}$ decay modes fractions fixed to the values obtained in [64] We obtain an systematic effect of $\pm 1\mu m$.

4.6.8 Background Composition Model

As described in section 4.4.2 we assume that our background is composed of pions and kaons. This assumption is based on the observation that protons and kaons and also pions and muons are practically indistinguishable in the momentum range of our sample's background. Electrons, on the other hand, have a separation larger than 2.0 σ from pions in the whole momentum range. Since the fraction of electrons in the background has been measured in [64] to be about 2%, we neglected this contribution in the standard fit.
We estimate the systematic uncertainty that we get from this simplification, by comparing the results of the standard fit with a modified version that includes a 2% fixed fraction of electrons in the background composition model. We obtain a systematic uncertainty of $\pm 1.4 \mu m$.

4.6.9 Monte Carlo Input p_T Spectrum

Realistic Monte Carlo samples have been generated with `BGen` using the default p_T spectrum that is known not to reproduce perfectly data at low momenta (figure 4.30 left). This effect is understood because the p_T spectrum used in the Monte Carlo simulations has been obtained from multibody decays of the B-meson, that have an harder p_T spectrum compared to the $B^0 \rightarrow h^{\pm} h'^{\mp}$ one. As a results, the low momentum region is not accurately described. A re-weighting procedure was applied to our signal Monte Carlo samples to minimize such a discrepancy. The re-weighting curve has been calculated as the ratio between the data and the Monte Carlo p_T spectra. We asses the systematic uncertainty due to the parametrization of the re-weighting curve fitting the ratio of the p_T spectra with different functional forms (see figure 4.30 right) and then extracting the efficiency curves and the (p_{tot}, α) templates on the Monte Carlo re-weighted with these functions. We quote as systematic uncertainty the largest variation observed on the B_d and B_s meson lifetimes performing the fit with the re-weighted templates and efficiency curves. The systematic effect we observe is 2.3 μm .

4.6.10 B_d, B_s Differences in p_T Spectrum

The B_d and B_s mesons are expected to have a slightly different p_T spectrum. The latter is expected to have a slightly softer spectrum compared to the B_d because, naively, it takes an heavier quark from the vacuum to hadronize. To asses the effect of this difference, we generated a new p_T spectrum for the B_s meson by shifting each entry of the standard re-weighted spectrum by -2%[69]. We used the re-weighted events to recalculate all the templates and proper decay time efficiency curves for
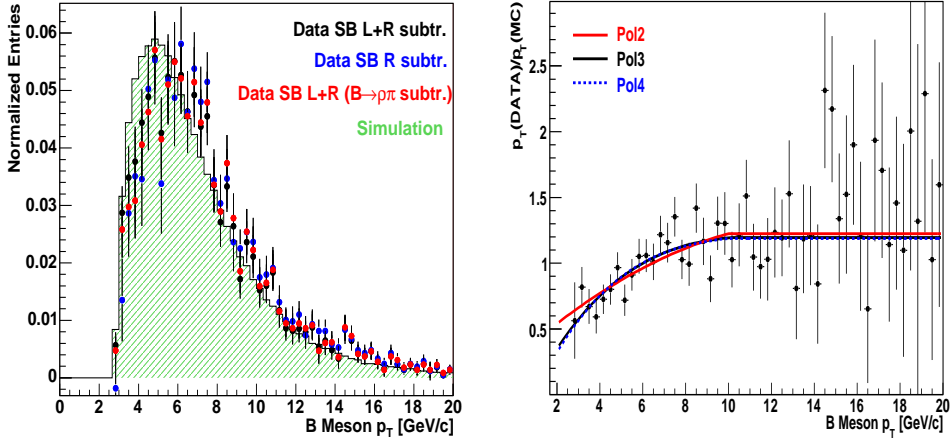
Figure 4.30: *Left: The B-meson transverse momentum spectrum distribution from sideband subtracted signal data, and from Monte Carlo simulation. The simulations are plotted in green, while the data are plotted with different sideband definitions, showing little dependence on the particular choice. We plotted the sideband subtractions performed with: (black) two symmetric sidebands ($[-7, -4] \cup [4, 7]\ \sigma$) around the $B^0 \to h^{\pm}h'^{\mp}$ peak; (blue) only the right sideband; (red) we first subtracted the $B \to \rho\pi(K)$ contribution from the left sideband and then we performed the sideband subtraction using this and the right sideband. Right: Ratio of data over Monte Carlo as a function of the B-meson transverse momentum fitted with different functional forms*

the $B_s \to KK/K\pi$ decay modes and repeated the full fit, obtaining a systematic uncertainty below $\pm 0.5\ \mu$m .

4.6.11   XFT-Trigger Efficiency

Due to the different specific ionization of pions and kaons, the XFT efficiency is different for the two species (see figure 4.31). A different turn on of the XFT efficiency as a function of the transverse momentum may result in differences in the B-meson p_T spectrum for the $B_s \to KK$ with respect to the $B_d \to K^+\pi^-$ and $B_d \to \pi^+\pi^-$ and so result in different efficiency curves. The effect, small above 2 GeV/c^2, it is not modelled in the MC. In order to asses the effect of this source of systematic uncertainty we re-weighted the p_T spectrum for the different $B^0 \to h^{\pm}h'^{\mp}$ decays with the XFT relative efficiencies for kaons and pions as measured on a high statistics D^+ sample. We obtain a systematic effect smaller than 0.5 μm .
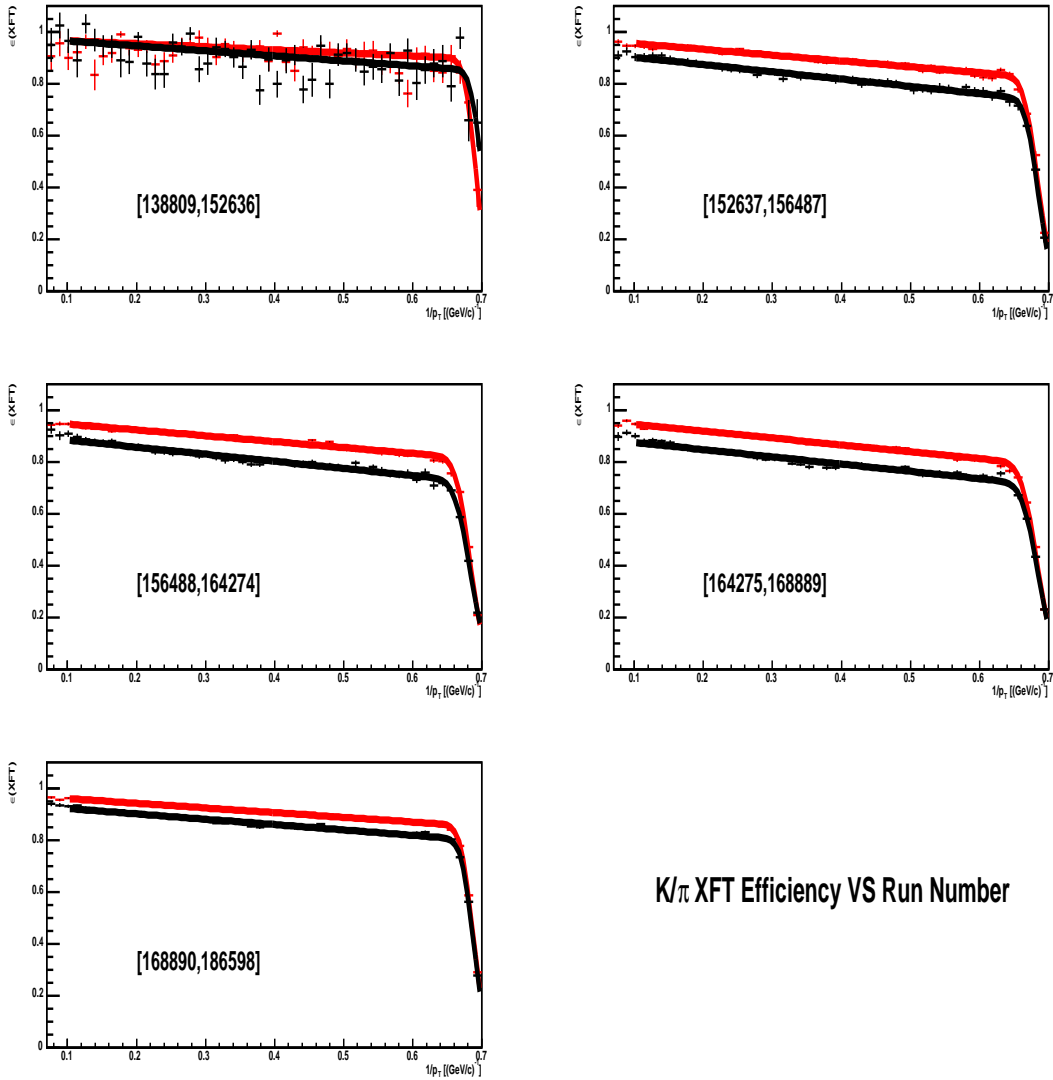
Figure 4.31: *XFT efficiency for (red) pions and (black) kaons as a function of* $1/p_T$ *in different run ranges*

4.6.12 Model for ct Efficiency Functions

The lifetime fit method relies on the correct extraction of the efficiency curves and on the correct parameterization. Those curves are fitted on Monte Carlo and therefore have associated errors. A way to evaluate the bias introduced by the parameterization would be to vary the parameters between their errors to obtain new curves and compare the obtained results. Unfortunately those parameters are strongly correlated and this procedure would easily lead to an overestimate of the effect. Instead, to asses this source of systematic uncertainty we proceeded in two different ways:

- As described in section 4.3.1 the parametrization of the efficiency functions used in the analyses is the sum of three functions or "building blocks":

$$\epsilon(ct) = \sum_{i=0}^{3} N_i (ct - \beta_i)^2 \cdot e^{-\frac{ct}{c\tau}} \cdot H(ct - \beta_i)$$

  The more "building blocks" that we add to the description, the more accurate it becomes. On the other hand the fit to extract those curves becomes extremely unstable because of the excessive number of parameters involved. We performed the fit of the efficiency curves with up to five building blocks, varying also the fit range.

- We changed the functional form to describe the efficiency curve using a ratio of polynomials, which gives an accurate description of the distributions obtained in the realistic simulation:

$$\epsilon(ct) = \frac{(a_0 \cdot ct + a \cdot ct^2 + a_1 \cdot ct^3)^2}{(a_2 + a_3 \cdot ct + a_4 \cdot ct^2 + a_5 \cdot ct^3 + a_6 \cdot ct^4)^2}$$

  Here, the numerator describes the initial rise, while the denominator takes care of the decreasing behavior at high ct values. This parametrization is computationally heavy because the involved integrals have to be solved numerically. For this reason we decided to use the analytically integrable parametrization for our fit.

We quote a systematic uncertainty of $\pm 1.9 \mu m$ as the largest variation we observed with the different parameterizations.

4.6.13 ct Resolution Scale Factor

CDF B-meson lifetime analyses are quite insensitive to relatively large variations of the overall scale of the proper decay time resolution, because the typical ct resolution

is one order of magnitude smaller than the typical B meson lifetimes. Since the realistic simulation does not perfectly describe the time resolution of the detector, in our nominal fit we used a scale factor of 1.4, as evaluated [65]. In order to quantify the systematic uncertainty associated to this effect we varied the ct scaling factor from 1.1 to 1.7, obtaining as expected negligible variations on the fitted lifetimes.

4.6.14 SVT - Offline Resolutions

One of the main effects that can bias a lifetime measurement affected by the impact parameter selections is due to the correlation between SVT (online) and offline impact parameter resolutions. In order to understand the total bias coming from this effect, in the analysis described in [65], the lifetime measurements have been performed using different configurations of impact parameter cuts between on-line and off-line confirmation, obtaining a systematic uncertainty of $\pm 1\mu m$. In our analysis we apply much tighter cuts on the impact parameter of the offline tracks ($> 180\ \mu m$) so that we expect a much smaller effect on the lifetimes.
We assume conservatively the same systematic of $\pm 1.0\ \mu$m .

4.6.15 ct Model for the Combinatorial Background

In our fit we derived the parameters of the template for the proper decay time distribution of the combinatorial background from the high mass sideband
($[5.4, 5.6]\ GeV/c^2$). To fit the template we use an exponential convoluted with a gaussian. In the full fit we allow the lifetime of the exponential to float but we gaussian constrain its value to the value obtained in the fit to the sideband.

To check a possible dependence of the template from the choice of the side-band we made different templates using different definitions of the signal side-bands. We split the sideband in two different regions, $[5.4, 5.5]\ GeV/c^2$ and $[5.5, 5.6]\ GeV/c^2$, and we recalculate the parameters of the templates in the two regions. We quote, as the systematic uncertainty associated to the description of the background proper time distribution, the maximum variation on the B_d and B_s meson lifetimes measured by performing the fit with the different templates. We obtain a systematic effect of ± 2.0 μm .

4.6.16 Trigger Composition

The $B \rightarrow hh$ candidates are collected by two different trigger paths B_PIPI and B_PIPI_HIGH_PT with different requirements on the transverse momentum of each track and on the scalar sum of the transverse momenta (see section 3.1). As a result, the two trigger paths select events with different B momentum spectra, and

so characterized by a different bias in the proper decay time. The efficiency curves for both B_d and B_s mesons have been calculated using a realistic simulation for both trigger scenarios. The efficiency curves used in the fit have been weighted according to relative composition of our data in terms of the two trigger paths. Uncertainties on the knowledge of the relative composition may systematically affect the measurement of the B-meson lifetimes. In order to evaluate the residual systematic we repeated our combined fit by changing the relative fraction of `B_PIPI_HIGH_PT` to `B_PIPI` by $\pm 10\%$.

We obtain a systematic effect of ± 1.0 μm .

4.6.17   SVX-Alignments and Proper Time Resolution Model

Effects of the alignments and of the proper time resolution model have been the subject of many detailed studies. We refer to the results in [65] (and in the references therein) to quantify these systematic uncertainties: ± 2.4 μm .

4.6.18   Systematic Uncertainties Summary

Table 4.9 summarize the values of the studied sources of systematic uncertainties. The sum in quadrature of all the systematic uncertainties leads to a global effect of 5.6 μm .

Effect	Uncertainty (μm)
Absolute Mass scale	± 0.6
Mass resolution scale factor	± 0.5
Mass resolution model	± 0.3
B-meson input masses	± 0.4
Partially reconstructed $B \to \rho^{\pm} K^{\mp}$ decays contamination	± 0.02
dE/dx calibrations	± 2.0
dE/dx tracks correlations	± 1.0
Background Composition Model	± 1.4
Monte Carlo input p_T spectrum	± 2.3
XFT-trigger efficiency	< 0.5
Model for ct efficiency functions	± 1.9
ct resolution scale factor	negligible
SVT - Offline resolution	± 1.0
ct model for the combinatorial background	± 2.0
Trigger composition	± 1.0
SVX-alignments and proper time resolution model	± 2.4
Effect of the variable proper decay time resolution in the likelihood	± 0.4
Correlation between kinematics and PID terms with the lifetime term in the likelihood	± 1.4
Total	± 5.6

Table 4.9: *Summary table of systematic uncertainties. The effect of the variable proper decay time resolution in the likelihood and the effect of the correlation between kinematics and PID terms with the lifetime term will be described in sections 4.7.2, 4.7.3.*

4.7   Cross checks

In this section we report some cross checks performed on various items of the analysis. Those effects, not considered as systematic uncertainties, have been studied in order to prove the robustness of the measurement with respect to particular procedures that we adopted in the analysis of the data.

4.7.1   Optimization procedure

In order to check the validity of the cuts optimization procedure we have performed a second optimization based on a multivariate likelihood ratio discriminant. We used binned histograms to estimate the probability distributions of the variables we intend to use in the optimization.

We construct a relative likelihood using as observables the scalar sum of the two track transverse momentum, the proper decay length projected in the transverse plane, the B-meson impact parameter, the minimum impact parameter of the two tracks. In the standard (cut based) optimization we did not use the three dimensional probability of the two track vertex fit as the discriminating observable, because that quantity is not very well reproduced by the Monte Carlo simulations. As a cross check of its influence on the optimization, we included this quantity in the relative likelihood.

We used half (even) signal Monte Carlo events and half (even) data sideband events to construct the likelihood ratio histograms and the remaining half to optimize the cut on the likelihood ratio variable. Figure 4.32 shows the distribution of the likelihood ratio discriminant (LH) for signal and background events. Signal events tend by construction to have a LH close to 1, while background events tend to have a LH close to 0.

We optimized the cut on the likelihood ratio against $S/\sqrt{(S+B)}$ with the same definition of S and B used in our standard (cut based) optimization. Figure 4.32 shows the distribution of $S/\sqrt{(S+B)}$ as a function of the likelihood ratio cut, and the value at which the maximum of the score function is reached. The maximum appears as a short plateau instead of a sharp peak.

In Figure 4.33 the two-pion invariant mass distribution of the $B \to hh$ candidates obtained using the standard optimization and the likelihood ratio optimization (using a tighter and looser choice for the LH cut among all the plateau values that maximize the score function), and the L_{xy} distribution of the candidates in the signal region obtained applying the standard selection and the likelihood ratio discriminant, are shown.

With this method (including the three dimensional vertex fit probability) we obtained similar results in terms of $S/\sqrt{(S+B)}$ and S/B with respect to the standard
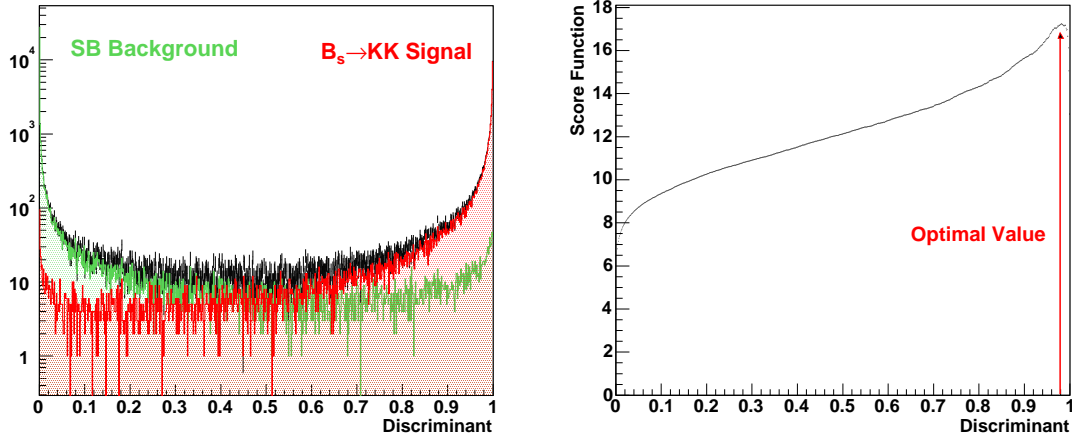
Figure 4.32: *(Left) Distribution of the likelihood ratio discriminant (LH) for signal and background events. (Right) Distribution of $S/\sqrt{(S+B)}$ as a function of the likelihood ratio cut, and the value at which the maximum of the score function is reached*

optimization, with gains variable between about $+3\%$ and about $+10\%$ in favour of the likelihood ratio based optimization. We decided not to use this optimization procedure for the analysis. because of the harder resulting cut on the L_{xy} observable as shown in figure 4.33
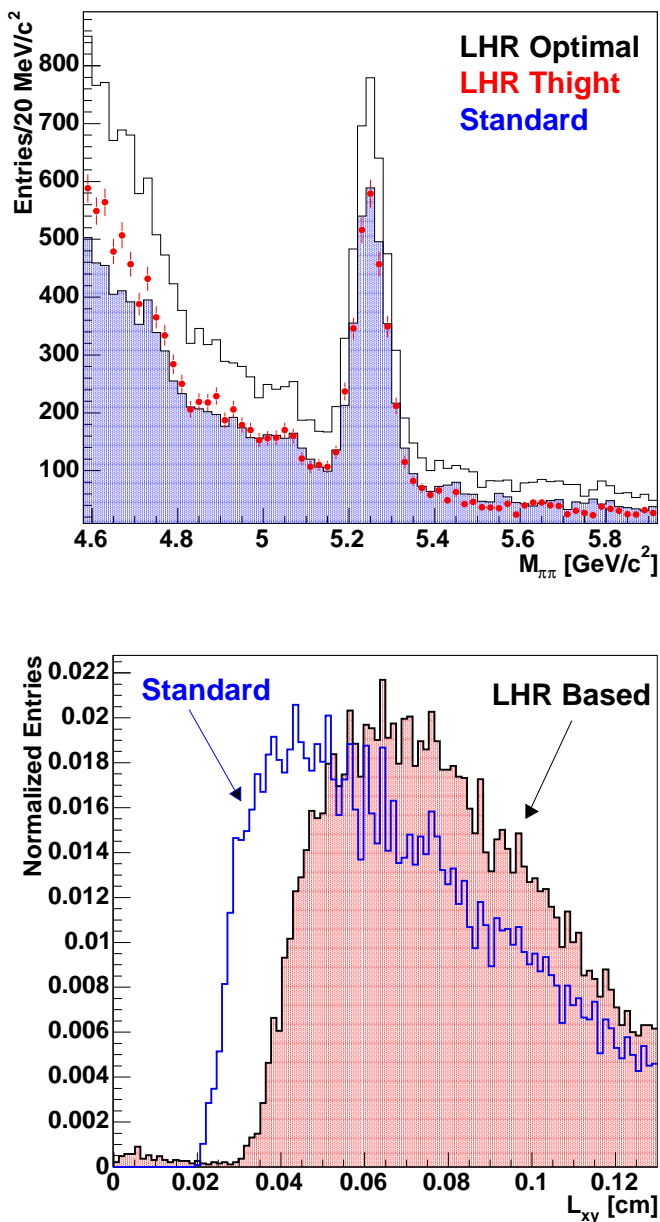
Figure 4.33: *(Left) Two pion invariant mass distribution of the $B \to hh$ candidates obtained using the standard optimization (blue shaded histogram) and the likelihood ratio optimization (using a tighter (red dots) and looser (black histogram) choice for the LH cut among all the plateau values that maximize the score function). (Right) L_{xy} distribution of the candidates in the signal region obtained applying the standard selection and the likelihood ratio discriminant*

.

4.7.2 Effect of the Variable Proper Decay Time Resolution in the Likelihood

The typical likelihood function used to describe the proper decay time has the form:

$$\mathscr{L} = \prod_i (1 - b) \cdot p(ct_i, \sigma_{ct}|sig) + b \cdot p(ct_i, \sigma_{ct}|bkg)$$

where b is the background fraction. For simplicity we consider here only one signal, but the reasoning is easily extended to more than one. The proper decay time ct enters this expression event by event, while the proper decay time resolution σ_{ct} is a fixed parameter. The generalization of the likelihood to include the event by event proper decay time resolution σ_{ct}^i can be written as:

$$\mathscr{L} = \prod_i (1 - b) \cdot p(ct_i, \sigma_{ct}^i|sig) + b \cdot p(ct_i, \sigma_{ct}^i|bkg)$$

The likelihood written in this way is incomplete[70]. Remembering the conditional probability $p(x_i, \sigma_{ct}^i|X) = p(x_i|\sigma_{ct}^i, X)p(\sigma_{ct}^i|X)$ we should have written:

$$\mathscr{L} = \prod_i (1 - b) \cdot p(ct_i|\sigma_{ct}^i, sig)p(\sigma_i|sig) + b \cdot p(ct_i|\sigma_{ct}^i, bkg)p(\sigma_i|bkg)$$

The incomplete likelihood expression is nevertheless valid if $p(\sigma_{ct}^i|sig) = p(\sigma_{ct}^i|bkg)$; in this case, the terms being equal for both signal and background, they can be factored out.

In the present analysis we assumed identical σ_{ct} distributions for the signal and background. This approach greatly simplifies the computation of the likelihood. In fact considering different σ_{ct} distributions for signal and background would require an event by event normalization of the likelihood in the two variables ct, σ_{ct}, to be performed numerically.

In order to verify a possible bias on the lifetime measurements coming from the assumption of identical σ_{ct} distributions for signal and background, we performed a toy study which included the parametrization of the σ_{ct} distributions as measured from sideband subtracted signal and mass sidebands. We parametrized the proper decay time uncertainty distributions with bifurcated gaussians, whose parameters are listed in Table 4.10. The results of the toy Monte Carlo study indicates a bias of $0.4\mu m$, which has been accounted as systematic uncertainty.

	mean (μm)	σ_L (μm)	σ_R (μm)
Signal	32.2 μm	6.0	12.0
BG	36.0 μm	11.0	16.0

Table 4.10: *Parameters of the bifurcated gaussians used to parametrize the distributions of the proper decay time uncertainty of the B-meson for the signal and background samples.*

4.7.3   Correlation Between Kinematics and PID Terms with the Lifetime Term

The kinematics and PID terms of the likelihood are functions of several variables including the sum of the three momenta of the tracks, p; the lifetime term in the likelihood is a function of (ct, σ_{ct}), which depends on the transverse momentum (p_T) of the B-meson. Since the sum of the momenta of the two tracks (p) is correlated with the transverse momentum of the B-meson ($p_T(B)$), there is a correlation between the kinematics-PID terms and the lifetime term. The effect of the correlation has been studied using a toy Monte Carlo. We divided the p spectrum of the signal in three bins of equal statistics. For each of those bins we fitted an efficiency curve. We also fitted an efficiency curve using all the events regardless of their momenta (p independent). In the toy study we generated the proper decay time of the events on the efficiency curve corresponding to their p (hence introducing an explicit dependence from p), and we fitted the sample obtained with the efficiency curve that does not depend on the p.

The result of this study indicates a bias of 1.4 μm . Since the effect is small and a proper treatment of this correlation would require a delicate parametrization of the efficiency curves, adding the p information, we chose to include this effect in the systematic uncertainties.

4.7.4   Isolation cut

We used the isolation as a quantity to discriminate the $B^0 \to h^{\pm} h'^{\mp}$ signal from the background in the sample optimization. The isolation is correlated to the transverse momentum (p_T) of the B-meson. Since the proper decay time of the B-meson is a function of its p_T, we verified the sensitivity of the present measurement to the particular choice of the isolation cut. In order to do this we changed the isolation cut by $\pm 10\%$ and re-performed the whole analysis.

We observed a shift in the $B_s \to K^+ K^-$ lifetime of $+3 \mu m$ when we used reduced

the isolation cut by -10% and a shift of $+2\mu m$ when we tighten the cut by $+10\%$. These values are consistent with statistical fluctuations of the sample, confirming a negligible bias on the lifetimes due to the particular choice of the isolation cut.

4.7.5 Use of the Time of Flight Detector in Particle Identification

We checked the reduction on the uncertainty on the $B_s \rightarrow K^+K^-$ lifetime measurement adding the time of flight (TOF) information in our particle identification likelihood term. We weighted the combined TOF and dE/dx K/π separation curves, with the track momentum spectrum of the data sample that pass the analysis cuts. As observed in section 2.4, the TOF adds significant separation between kaons and pions only below 3 GeV/c. The analysis cut on the sum of the momenta of the two tracks at 5.95 GeV/c severely reduces the fraction of tracks with momentum below 3 GeV/c.

However, since the separation between $B_s \rightarrow K^+K^-$ and $B_d \rightarrow \pi^+\pi^-$ signals is entirely PID based, even a small gain in separation power might sizably reduce the uncertainty on the lifetime estimates. To quantify this effect, we performed a toy study generating events with pion-kaon separation equal to that obtained using the TOF information. The statistical uncertainty reduction on the lifetime estimation is estimated to be below 1μm for both B_d and B_s. Since the systematic uncertainty introduced by the use of the TOF, through its calibration uncertainty, is of the same order of magnitude, we decided not to use the TOF information in the fit.

Chapter 5

Results Discussion

> *"There are two possible outcomes: if the result confirms*
> *the hypothesis, then you've made a measurement.*
> *If the result is contrary to the hypothesis,*
> *then you've made a discovery."*
> *Enrico Fermi*

In the previous chapters we described the procedure used to measure the lifetimes of the B-mesons in charmless decays : $B_d \rightarrow K^+\pi^-$, $B_d \rightarrow \pi^+\pi^-$, $B_s \rightarrow K^+K^-$, $B_s \rightarrow K^-\pi^+$ (the analysed sample showed a negligible fraction of $B_s \rightarrow K^-\pi^+$ decays and so no useful information could be extracted on its lifetime).

We characterized the $B_d \rightarrow K^+\pi^-$ and $B_d \rightarrow \pi^+\pi^-$ by the same lifetime. The choice of measuring only one value instead of two separated lifetimes for the two decays is supported by the actual knowledge of $\Delta\Gamma_d = -0.008 \pm 0.037(stat) \pm 0.018(syst)$ [22]. That is, independently of the CP content of the specific decays, they will all have the same lifetime. The measured lifetime is:

$$
\begin{array}{rcllllll}
c\tau(B_d) & = & 452 & \pm & 24 & (\text{stat}) \pm & 6 & (\text{syst}) \ \mu\text{m} \\
\tau(B_d) & = & 1.51 & \pm & 0.08 & (\text{stat}) \pm & 0.02 & (\text{syst}) \ ps
\end{array}
$$

The B_d measured lifetime is in good agreement with the world average $1.537 \pm 0.015(ps)$ and it is compared with the values in literature in figure 5.1.

The most important result obtained with the present analysis is the first measurement of the $B_s \rightarrow K^+K^-$ lifetime:

$$
\begin{array}{rcllllll}
c\tau(B_s \rightarrow K^+K^-) & = & 458 & \pm & 53 & (\text{stat}) \pm & 6 & (\text{syst}) \ \mu\text{m} \\
\tau(B_s \rightarrow K^+K^-) & = & 1.53 & \pm & 0.18 & (\text{stat}) \pm & 0.02 & (\text{syst}) \ ps
\end{array}
$$

The B_s lifetime is compared with the values in literature in figure 5.2.

As shown in section 1.5, the CP content of the $B_s \rightarrow K^+K^-$ decay is not known, hence the interpretation of this result need some special care.

115

Measurements of B_d lifetime

OPAL 1995		$1.53 \pm 0.12 \pm 0.08$
DELPHI 1995		$1.63 \pm 0.14 \pm 0.13$
DELPHI 1995		$1.62^{+0.14}_{-0.13} \pm 0.08$
ALEPH 1996		$1.49^{+0.17}_{-0.15} {}^{+0.08}_{-0.06}$
ALEPH 1996		$1.25^{+0.15}_{-0.13} \pm 0.05$
DELPHI 1997		$1.532 \pm 0.041 \pm 0.040$
SLD 1997		$1.64 \pm 0.08 \pm 0.08$
L3 1998		$1.52 \pm 0.06 \pm 0.04$
CDF 1998		$1.474 \pm 0.039^{+0.052}_{-0.051}$
OPAL 1999		$1.523 \pm 0.057 \pm 0.053$
ALEPH 2000		$1.518 \pm 0.053 \pm 0.034$
OPAL 2000		$1.541 \pm 0.028 \pm 0.023$
BABAR 2001		$1.546 \pm 0.032 \pm 0.022$
BABAR 2002		$1.529 \pm 0.012 \pm 0.029$
CDF 2002		$1.497 \pm 0.073 \pm 0.032$
BELLE 2002		$1.554 \pm 0.030 \pm 0.019$
BABAR 2003		$1.52^{+0.024}_{-0.023} \pm 0.02$
2004 World Average		1.537 ± 0.015
This measurement		$1.51 \pm 0.08 \pm 0.02$

Figure 5.1: *Measurements of the B_d meson lifetime.*

Although the $B_s \rightarrow K^+K^-$ is dominated by the CP-even component $B_s^{even} \rightarrow K^+K^-$, the CP-odd component could still contribute allowing the decay $B_s^{odd} \rightarrow K^+K^-$.

The reason for this, as shown in section 1.5, is twofold. On one side the the $B_s \rightarrow K^+K^-$ happens through the $b \rightarrow u\bar{u}s$ transition which is not completely dominated by a single phase. Even if the decay is dominated by the penguin diagrams, a contribution from the tree diagram could introduce a different phase that would also allow the $B_s^{odd} \rightarrow K^+K^-$ decay. On the other hand, the presence of CP violating NP would introduce an additional phase in the decay that would again allow for the $B_s^{odd} \rightarrow K^+K^-$ to contribute.

The lifetime of the $B_s \rightarrow K^+K^-$ decay has been extracted using a single exponential description for its proper decay time distribution. This procedure assumes that the decay is dominated by a single phase and so the analysed process is simply 100% $B_s^{even} \rightarrow K^+K^-$, with no contribution from $B_s^{odd} \rightarrow K^+K^-$.

We have also attempted to perform the fit to the complete expression in eq.1.58, to extract the lifetime of both CP components as well as $\mathcal{A}_{\Delta\Gamma}$, but due to the small
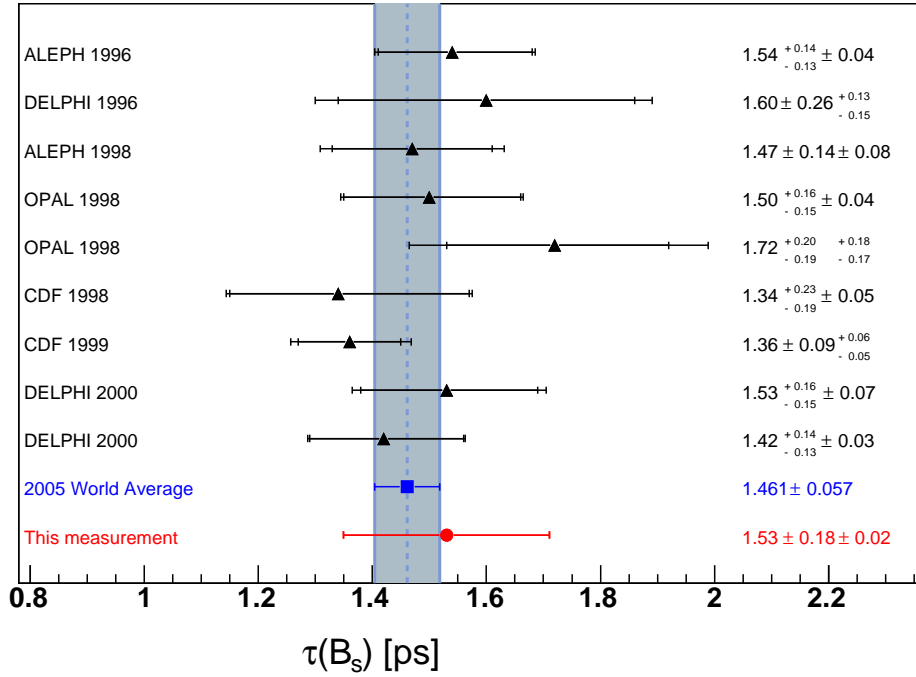
Figure 5.2: *Measurements of the B_s meson lifetime.*

statistics of the analysed sample we did not obtain a conclusive result on the presence of a second CP component.

Assuming the $B_s \to K^+K^-$ 100% CP-even and assigning, as shown in the first chapter, the CP-even component to the "Light" eigenstate, the measured $B_s \to K^+K^-$ lifetime is simply the inverse of Γ_L. Combining the measured Γ_L with either the Γ_H (Heavy eigenstate assigned to the CP-odd) or the Γ_{fs} (obtained from lifetime of the flavour specific decays) it is possible to extract $\Delta\Gamma_{CP}$.

Since the uncertainty on Γ_H is higher than the one of Γ_{fs} (reflecting the fact that the B_s decays are dominated by the CP-even final states) we calculate $\Delta\Gamma_{CP}$ from the lifetime information of the flavour specific decays.

The world average of the flavour specific decays is:

$$c\tau_{fs} = 441 \pm 13 \; \mu\text{m}$$
$$\tau_{fs} = 1.472 \pm 0.045 \; ps$$

The expression that relates the τ_{fs} to τ_L and τ_H can be derived by writing eq.1.58

as:

$$\Gamma[f,t] = Ae^{-\Gamma_L t} + Be^{-\Gamma_H t} = e^{\Gamma_s t}\left[(A+B)\cosh\frac{\Delta\Gamma_s t}{2} + (B-A)\sinh\frac{\Delta\Gamma_s t}{2}\right] \quad (5.1)$$

where $A = A(t)$ and $B = B(t)$ can be read off from eq.1.58.

If one uses a maximum likelihood fit of eq.5.1 to a single exponential

$$\Gamma[f,t] = \Gamma_f e^{\Gamma_f t} \quad (5.2)$$

it will yield the following result [71]:

$$\Gamma_f = \frac{A/\Gamma_L + B/\Gamma_H}{A/\Gamma_L^2 + B/\Gamma_H^2} \quad (5.3)$$

In flavor-specific decays we have $A = B$ (see eq.1.43) and so we obtain:

$$\tau_{fs} = \frac{\tau_L^2 + \tau_H^2}{\tau_L + \tau_H} \quad (5.4)$$

Solving the previous equation for τ_H, we obtain $\tau_H = 422.58$. Knowing Γ_L and Γ_H it is now possible to compute the $\frac{\Delta\Gamma_{CP}}{\Gamma_{CP}}$:

$$\frac{\Delta\Gamma_{CP}}{\Gamma_{CP}} = 2\frac{\tau_H - \tau_L}{\tau_H + \tau_L} = -0.08 \quad (5.5)$$

The uncertainty on the $\frac{\Delta\Gamma_{CP}}{\Gamma_{CP}}$ value is calculated using:

$$\sigma\left(\frac{\Delta\Gamma_{CP}}{\Gamma_{CP}}\right) = 2\frac{\tau_{fs}}{\tau_L}\sqrt{\left(\frac{\sigma_{\tau_L}}{\tau_L}\right)^2 + \left(\frac{\sigma_{\tau_{fs}}}{\tau_{fs}}\right)^2} \quad (5.6)$$

leading to the final result:

$$\Delta\Gamma_{CP}/\Gamma_{CP} = -0.08 \pm 0.23 \ (stat.) \ \pm 0.03 \ (syst.)$$

which is compatible with the current theoretical prediction $(7.4 \pm 2.4)\cdot 10^{-2}$[16].

Two measurements of the $\frac{\Delta\Gamma_{CP}}{\Gamma_{CP}}$ have been recently presented by the D0 collaboration analysing $1fb^{-1}$ of data .

The first measurement performs the angular analysis of the $B_s \to J/\psi\phi$ decay to estimate the CP-even and CP-odd components lifetimes, obtaining [72]

$$\Delta\Gamma_{CP}/\Gamma_{CP} = 0.15 \pm 0.10 \ (stat.)^{+0.03}_{-0.04} \ (syst.)ps^{-1}.$$

The second measurement extracts the $\frac{\Delta\Gamma_{CP}}{\Gamma_{CP}}$ from the measurement of the $\text{BR}(B_s \to D_s^{(*)}D_s^{(*)})$, under the assumption that the decay is predominantly CP-even, obtaining [73]

$$\Delta\Gamma_{CP}/\Gamma_{CP} = 0.142 \pm 0.064 \; (stat.)^{+0.058}_{-0.050} \; (syst.).$$

The combination of all the measurements is shown in figure 5.3 [74]. The updated
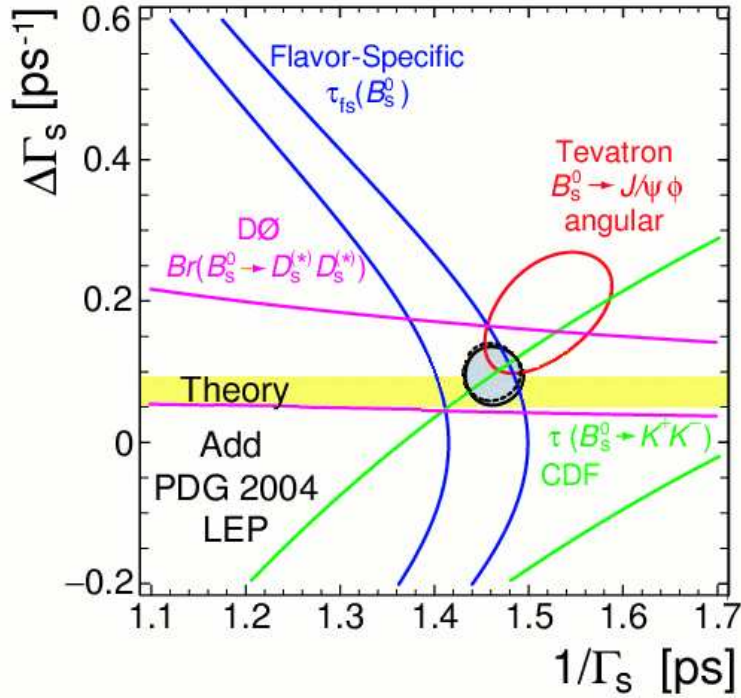
Figure 5.3: *Current measurements of $\frac{\Delta\Gamma_s}{\Gamma_s}$ in the ($\Delta\Gamma_s$,Γ_s) plane.*

current world average including the present measurement is [14]:

$$\frac{\Delta\Gamma_s}{\Gamma_s} = +0.25 \pm 0.09.$$

The small systematic uncertainty of the present method will allow to successfully apply it to a larger data sample. In figure 5.4 we show the extrapolation of the statistical uncertainty on the lifetimes estimates and the $\Delta\Gamma_{CP}/\Gamma_{CP}$ up to 8 fb^{-1}. The present method will allow a measurement with a statistical uncertainty of 10% with a data sample from an integrated luminosity of 2 fb^{-1}. With 8 fb^{-1}, reachable at the end of the Tevatron Run II, it will be possible to reduce the statistical uncertainty to 5%.
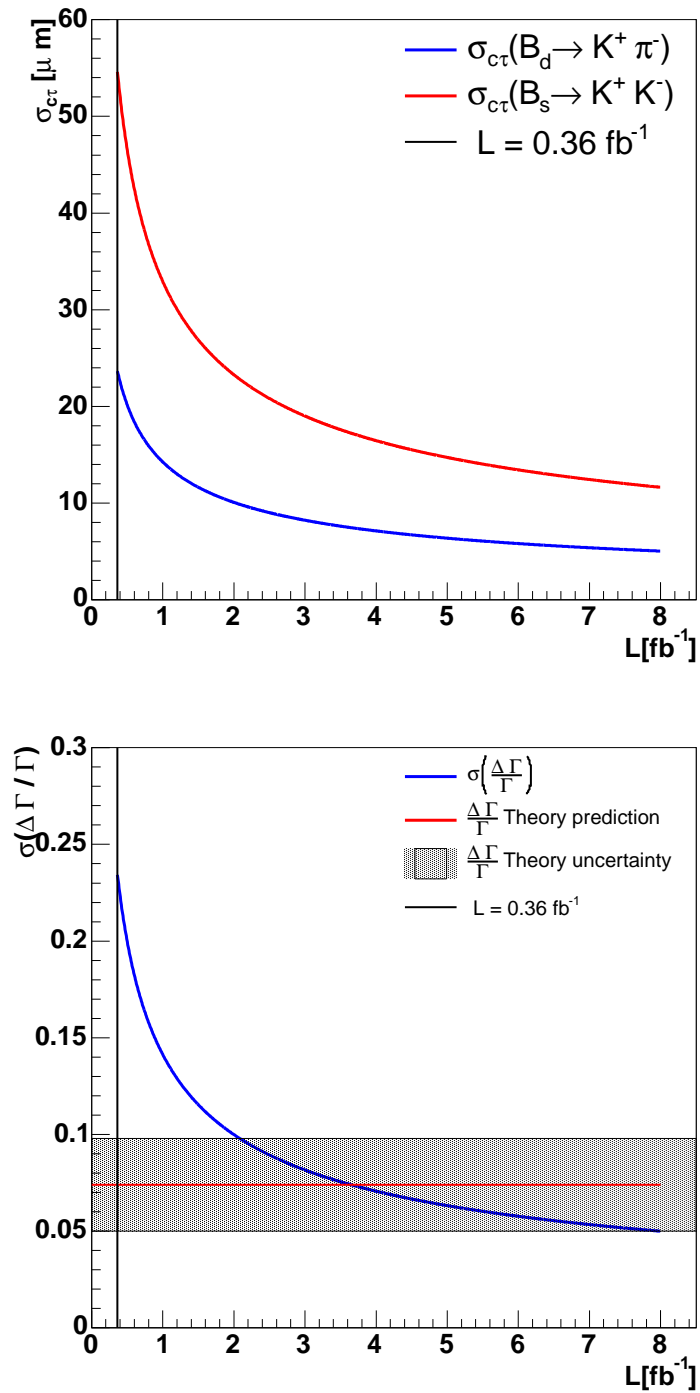
Figure 5.4: *Statistical uncertainty on the lifetime estimates (left) and the $\Delta\Gamma_{CP}/\Gamma_{CP}$ (right) up to 8 fb^{-1}. The black line shows the present integrated luminosity.*

Part II

Development of the ATLAS-SCT endcap modules

In this second part, a few steps of the final R&D of the ATLAS-SCT endcaps modules will be reported. After a brief description of the Large Hadron Collider (LHC) and the ATLAS detector, few details about the ATLAS-SCT will be given.

In chapter 7, the description of the radiation damage in silicon detectors will bring us to the problem of managing high leakage currents and to the modules thermal specification. The effects of the radiation on the electrical performance will also be shown.

In chapter 8 the description of the endcap modules design is presented with particular attention to their thermal performance.

The work exposed in this chapter has been used as supporting documentation for the Final Design Review (FDR) of the endcap modules [75]. The developed design, considered satisfactory by the reviewers, has been used for the final modules production.

The presented results have been partially published in the journal "Nuclear Instruments and Methods in Physics Research" [76], [77], [78].

Chapter 6

The ATLAS Silicon Tracker (SCT)

"The interesting thing about doing new experiments
is that you never know what the answer is going to be!"
Raymond Davies

The Standard Model, still leaves unanswered many questions on the nature of particles and forces. Experiments as well as theory consistency bounds strongly suggest that signs of new physics should appear around the TeV energy scale.

The highest energy accelerator at present is the Tevatron at FNAL briefly described in chapter 2. The next frontier in collider physics is the Large Hadron Collider (LHC) at CERN.

The detectors that are being mounted at the LHC represent a new generation of particle detectors. They have to be faster, because of the high luminosity of the LHC, more discriminating, in order to extract the few hunted events from the many orders of magnitude higher background and especially more resistant, to survive the high radiation level around the collision points.

6.1   LHC and ATLAS

The Large Hadron Collider (LHC) [79], being built at CERN, is going to produce proton-proton collisions at a centre of mass energy of $\sqrt{s} = 14\,TeV$, and instantaneous luminosity $\mathscr{L} = 10^{34}\ cm^{-2}s^{-1}$. It differs from the Tevatron, the actual highest energy hadron collider ($\sqrt{s} = 1.96\,TeV$, $\mathscr{L} = 10^{32}\ cm^{-2}s^{-1}$), in that it collides two beams of protons instead of protons-antiprotons. This choice has the advantage of overcoming the anti-proton production, which represent one of the limitation factors of the Tevatron luminosity, at the cost of a much more difficult design. In fact, while protons and antiprotons can be stored using the same magnetic field and so the same beam pipe, the two proton beams have to travel in opposite magnetic fields, and so

in two separated beam pipes. Compared to the Tevatron, the LHC has a centre of
mass energy larger by a factor of seven and an instantaneous luminosity roughly two
orders of magnitude higher. The beam parameters showed for the Tevatron in table
2.1 are reported for the LHC in table 6.1.

Parameter	Value
number of bunches (N_B)	2808
bunch length [cm]	7.55
bunch spacing [ns]	25
σ_p [μm]	16.7
protons/bunch (N_p)	1.15×10^{11}
interaction/crossing	20
peak luminosity [$cm^{-2}s^{-1}$]	1.0×10^{34}

Table 6.1: *LHC basic beams parameters.*

The LHC intersects the two proton beams at four interaction regions where the
high energy physics detectors will be installed. Two of them, ATLAS and CMS,
are general purpose detectors aiming at the observation of new physics. The ALICE
detector will study the new states of matter generated in heavy ions collisions taking
advantage of the capability of the LHC to accelerate also heavy ions beams. The
LHCb detector will seek the sign of new physics through the detailed study of the
b-quark properties.

The overall ATLAS detector design [80], shown in figure 6.1, is driven by the
choice of its magnetic fields configuration. The subdetectors composing the tracker
(or inner detector), which is closer to the interaction point will be immersed in a
solenoidal field of 2 T along the symmetry axis of the detector, bending the tracks
in the transversal plane. The outer part of the detector, the muon spectrometer, will
be immersed in a toroidal magnetic field with a field-integral of 3 to 8 $T \cdot m$, bending
the tracks in the plane defined by the track and the symmetry axis of the detector.

The inner detector covers the region in $|\eta| < 2.5$ and it is composed by three
sub-detectors (see figure 6.2: the pixel detector, the silicon tracker (SCT) and the
transition radiation detector (TRT). The pixel detector [81] is the closest to the
interaction region. It's composed by three concentric barrels, with radii from 4.8 to
16 cm and three disks per side. The pixels will provide excellent vertexing information,
allowing high performance b-tagging. The SCT is composed by silicon micro-strip
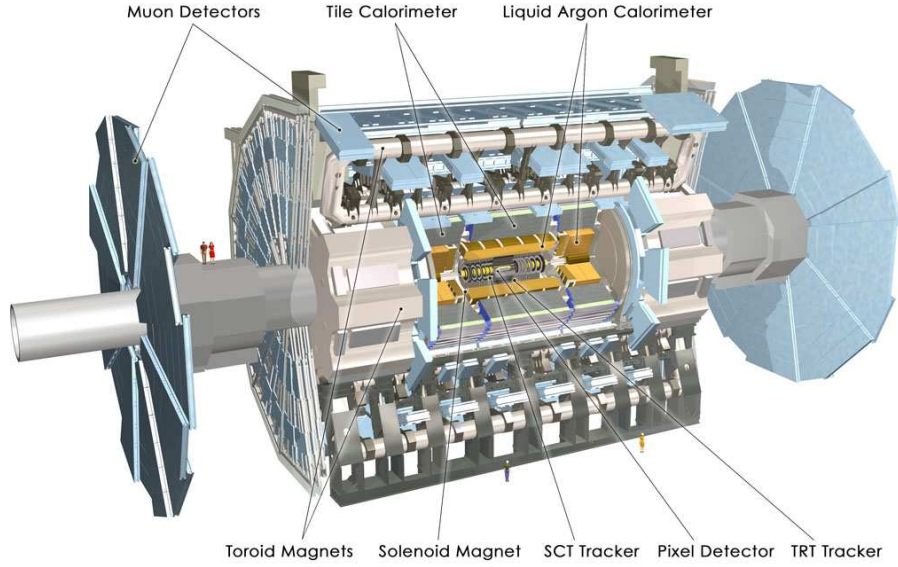
Figure 6.1: *ATLAS: A Toroidal LHC ApparatuS*

detectors disposed on four concentric barrels from 30 up to 52 cm and nine disks per side. The SCT will be described in more detail in the following section. The TRT [82] uses straw detectors to give a large number of points on every track (typically 36). The TRT barrel is built in modules with radii from 56 up to 107 *cm*. The two end-caps have 18 wheels each. The fourteen wheels closer to the interaction point have an inner diameter of 64 *cm* and an outer radius of 103 *cm* while the last four have the smaller inner radius of 48 cm.

The magnetic field for the inner detector is provided by a solenoid, whose coil integrated in the cryostat of the electromagnetic calorimeter. The electromagnetic calorimeter [83] is divided into two portions, the barrel and end-cap calorimeters, covering respectively the regions between $|\eta| < 1.475$ and $1.375 < |\eta| < 3.2$. The electromagnetic calorimeter is a sampling calorimeter with liquid argon as active material and lead as absorber. To have an azimuthal coverage without cracks, the calorimeter has an accordion geometry. The hadronic calorimeter [83] covers the region up to $|\eta| < 5$ (see figure 6.3). It is built with different design solution in the different $|\eta|$ intervals to cope with the different particle densities and radiation doses. Within $|\eta| < 1.6$, the barrel region, it is built with iron-scintillator tiles. Between $1.5 < |\eta| < 4.9$ it uses liquid argon technology. This region is divided in the end-cap region instrumented with copper plates interleaved with liquid argon, and the forward region, built as a metal matrix with equally spaced holes filled with rods. The liquid argon is again used as active material and it fills the thin gap between the rods and
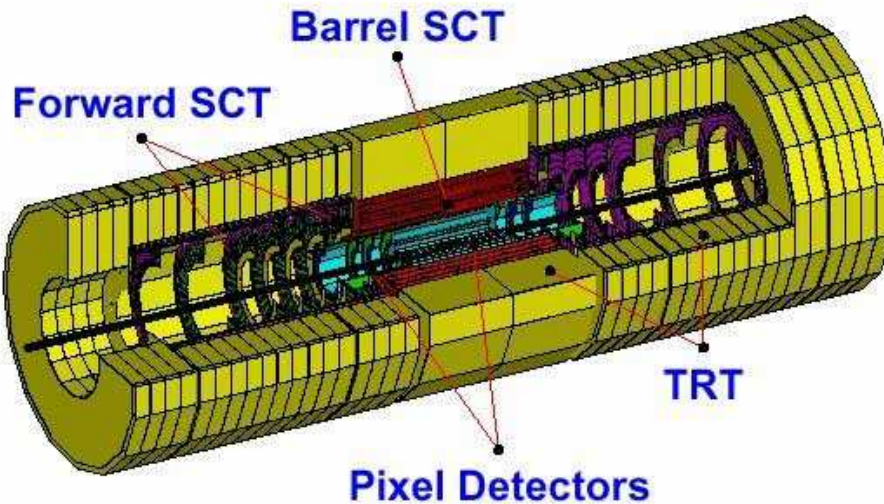
Figure 6.2: *Inner detector schematics*

the metal matrix. The muon chambers [84] immersed in the toroidal field compose the muon spectrometer (see figure 6.4). In the barrel region the spectrometer inner diameter is 9.4 m and the outer 19.5 m. The muon spectrometer is composed by different types of detectors. In the barrel region there are three measurement stations built with monitored drift tubes (MDT). For the end-cap region the three stations are built with proportional chambers (Cathode Strip Chambers).

The ATLAS trigger [85] is designed in three levels. The Level 1 uses information from the calorimetry and muon detectors, its input rate is the LHC bunch crossing frequency of 40 MHz. The latency necessary to decide whether accept or reject an event is 2 μs and it is obtained with pipelines at the sub-detectors level. The acceptance rate of the Level 1 trigger is 100 kHz. The Level 1 trigger identifies regions of interest for the event, and passes the information coming from all the interested sub-detectors, to the Level 2. The Level 2 is built with farms of PCs, and its acceptance rate is about 1 kHz with a latency of 10 ms. The events accepted by the Level 2 are built and passed to the Event Filter representing the Level 3 trigger which, with an average treatment time of 1 second, can apply more sophisticated algorithms and calibrations adapted from the offline, to decide is the events has to be rejected or passed on to the final mass storage. The final ATLAS acceptance rate is about 100 Hz.
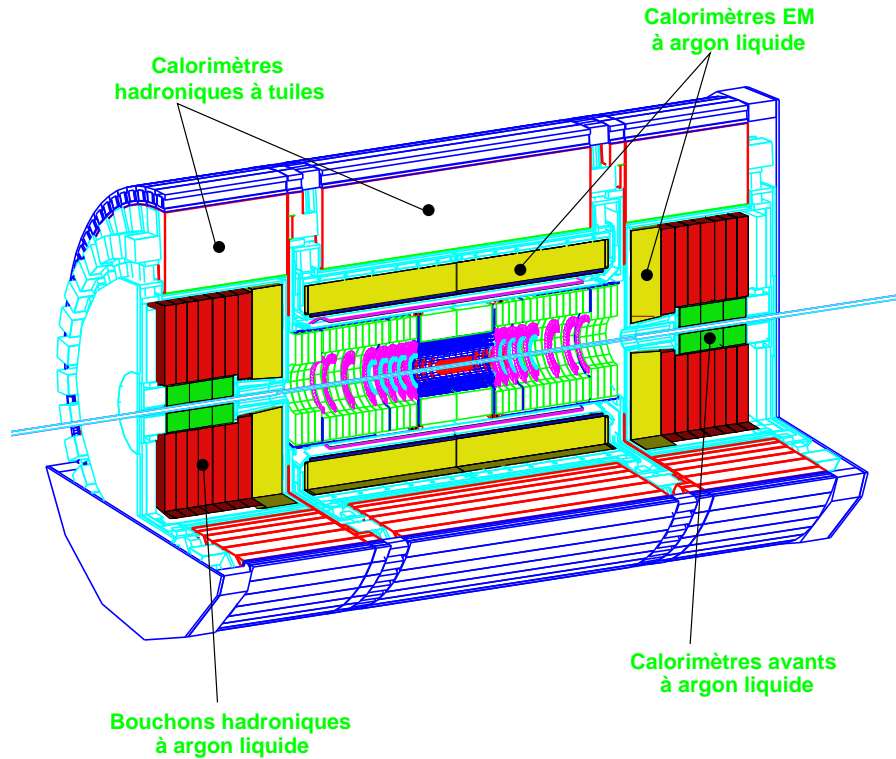
Figure 6.3: *ATLAS calorimeters layout.*

6.2   Silicon Diode

Before describing the ATLAS SiliCon Tracker (SCT) we will recall the basic operating principles of a microstrip silicon detector.

The silicon strip detectors are based on the operational principle of the p-n junction diode [90].

The electrical characteristics of pure silicon can be modified introducing known amounts of impurities in its lattice. This process is called doping.

The silicon atom has valence four. The "n-type" doped silicon is produced adding pentavalent atoms (like phosphorus) called donors because they can very easily release an electron (accept a hole). The "p-type" doped silicon is produced with trivalent atoms (like boron) called acceptors, because they can very easily accept an electron (release a hole).

To understand the p-n junction we can imagine to bring together two initially separated p-type and n-type pieces of silicon, forming the so called abrupt junction. Through thermal motion, the electrons and holes will migrate across the junction
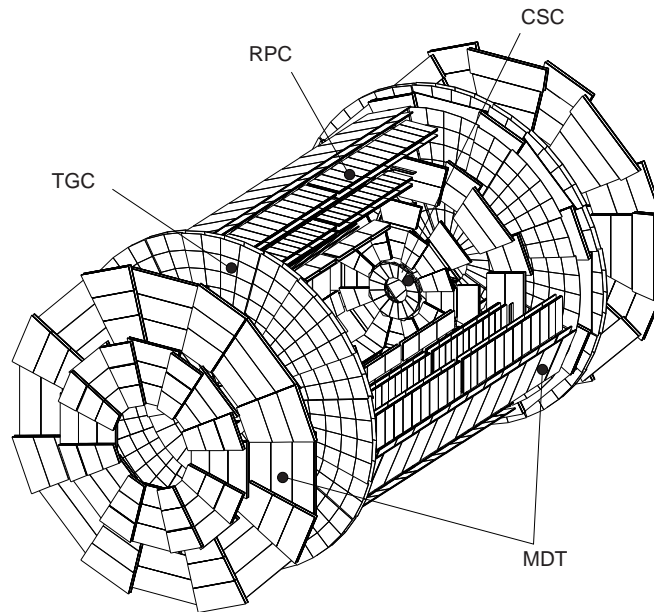
Figure 6.4: *Muon spectrometer layout*

where they will combine. This migration leaves a net negative charge in the p-type side and a net positive charge in the n-type side. This region called "space charge" or "depletion" region has no free carriers. The "built-in potential" created by the net charges around the depletion region will prevent further electron-hole migration.

In the case of the ATLAS SCT strips the diode is build with a p^+-n junction, meaning that the p-side is more heavily doped than the n-side. For this reason the depletion region extends more in the less doped n-side. Applying an external bias to the junction, with same sign of the built-in potential, we can increase the dimensions of the depletion region up to the whole thickness of the n-type layer.

If a charged particle (figure 6.6)traverse the depleted region it will ionize the silicon creating electron-hole couples that will drift respectively towards the positive and negative potentials, inducing the electric fields that will be read out to detect the position where the particle had passed.

The background in this simplified detector would be produced by electron-hole pairs created by thermal excitation (minority carriers). In absence of electric field the created electron-hole pairs would recombine, but in the electric field across the
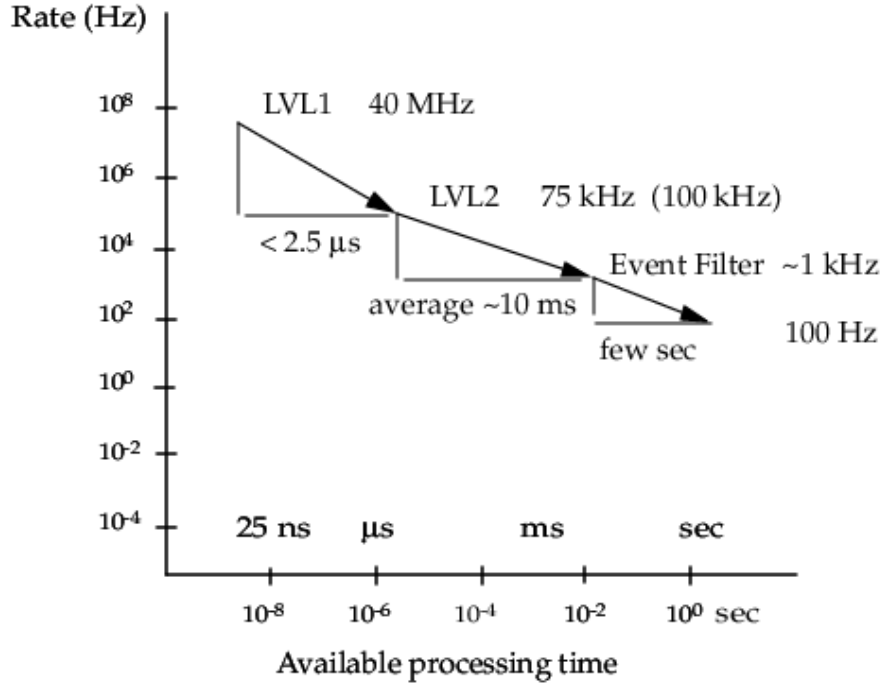
Figure 6.5: *Trigger reduction scheme.*

junction, the pairs will give rise to a net current known as "leakage current":

$$I \propto \sqrt{V} \cdot e^{\frac{-E_g}{2kT}}$$

where V is the voltage applied across the junction, E_g is the effective charge carrier activation energy ~ 1.2 eV, T is the temperature and k is the Boltzmann constant. The leakage current is temperature dependent; a useful approximation of the leakage current temperature dependence is that it doubles for each temperature increase of seven degrees.

6.3 The SCT

The silicon tracker (SCT) [82] (located between the pixel and the transition radiation detector) is composed by four concentric barrels and nine disks for each of the two end-caps, all tiled with silicon micro-strip modules. The layout of the SCT is shown in figure 6.8. The 4088 SCT modules (2112 barrel modules and 1976 endcap modules) are equivalent to a total silicon surface of about $61m^2$ and more than six millions
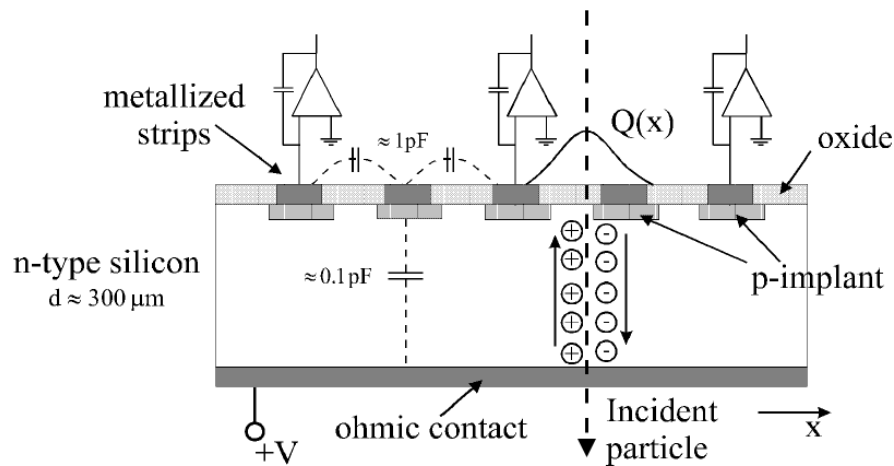
Figure 6.6: *Schematic cross section of a silicon microstrip detector.*

readout channels. This represents about an order of magnitude increase with respect to the CDF-SVX II detector with a surface of about $11m^2$ and 750,000 channels. Each silicon detector in the SCT is made of 768 p^+-n strips. A brief description of the functioning principles of silicon strip detectors will be given in the next section.

The goal of the SCT is to provide four (one for each barrel) precision measurements on the track trajectory. These, combined with the information from the rest of the inner detector will be used to measure the momentum of the tracks (p), their impact parameter (d_0) and their vertex position. The design resolutions are summarized in figure 6.7

The whole design of the SCT, structures and modules, aims at minimizing the amount of material of the tracker, to reduce the multiple scattering. The modules are mounted on carbon fibres support structures and are biased through low mass power tapes. The data transmission from the SCT to the outside world is performed with optical links.

The functionality of the modules in the SCT are the same for both the barrel and the end-cap modules. Only the geometry of the modules is different. The barrel modules have rectangular detectors to cover the surface of the barrels, while the end-cap modules have a wedge shape to cover the disks. Only one type of module is used for the barrel; the end-cap modules instead, come in four different geometries depending on their radial position on the disks: inner, middle and outer. The middle modules come into two arrangements, long and short.

The details about the end-cap module design, which represent the main subject of the present work, will be given in chapter 8.
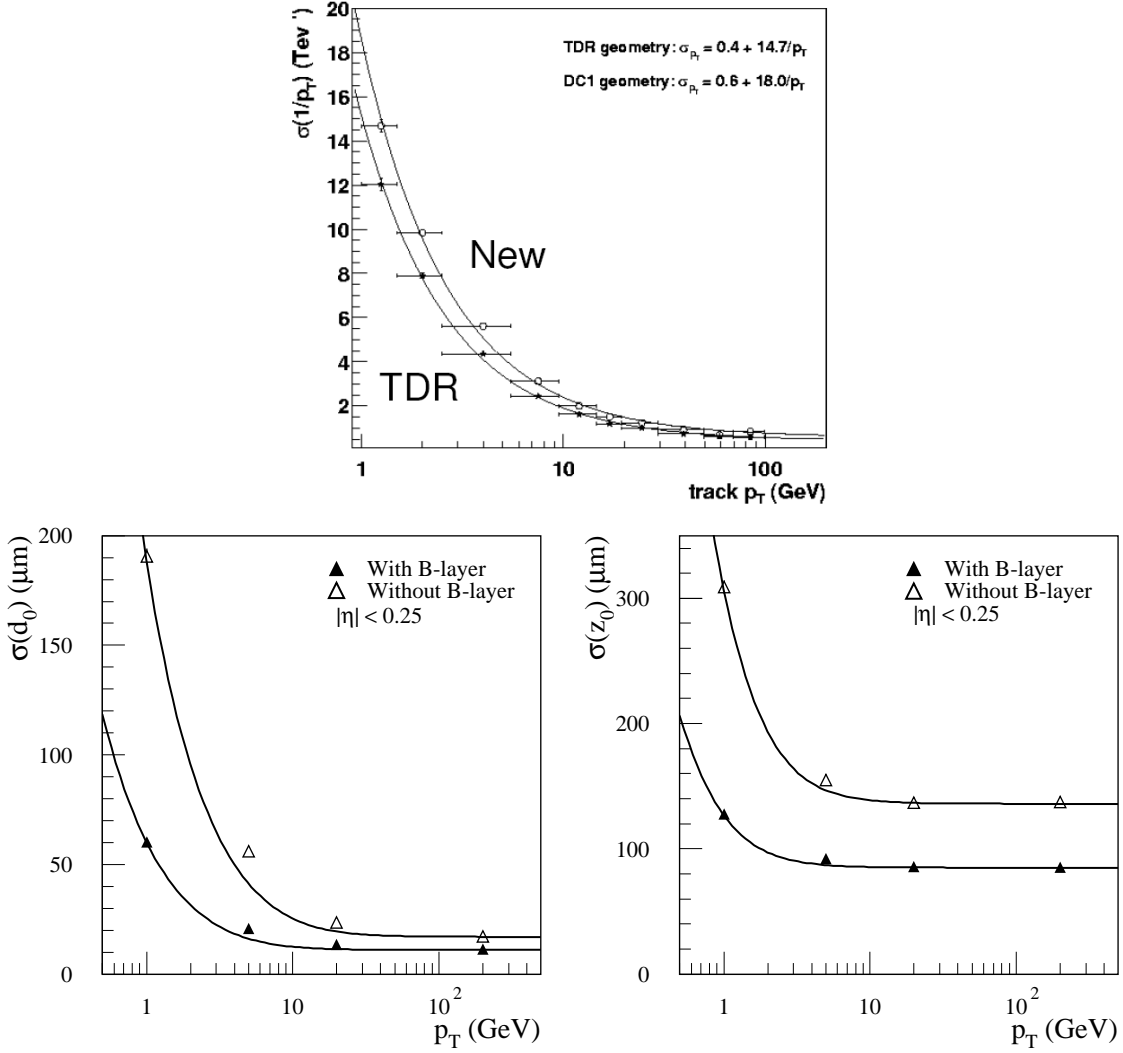
Figure 6.7: *Design resolutions as a function of the transverse momentum: (left) transverse momentum, (centre) impact parameter, (right) longitudinal impact parameter resolution.*
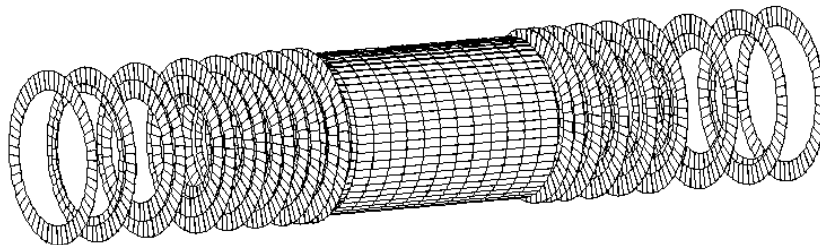
Figure 6.8: *The SCT layout.*

Each SCT module (belonging to the barrel or to the endcap) has the same basic structure: a mechanical support structure, the silicon microstrip detectors acting as sensing elements glued on both sides of the support structure and the hybrid which is an electric circuit mounted on a kapton support. The hybrid houses the readout chips and distributes the detectors bias and the chips low voltages. Each module of the SCT communicate with the rest of the ATLAS data acquisition system through optical fibers. The electric signals coming from the readout chips are converted to optical pulses with specific chips called "opto-links". The end-cap module opto-links are mounted on the hybrid, while the barrel modules ones are mounted on a secondary flex circuit.

The detectors are glued on both sides of the modules with a little (40 $mrad$) tilt angle. This allows two have the two-dimensional position of the intersection point between the track and the module. The third coordinate is given by the position of the detector plane. The strip pitch is 80μm giving a standard deviation (assuming a rectangular distribution) of $\sigma_{strip} = 80/\sqrt{12} = 23\mu m$. This resolution, combined with the tilt angle, gives a final resolution of $\sigma_y = 16\mu m$ and $\sigma_x = 580\mu m$, where (x, y) is the detector plane, x is oriented along the symmetry axis of the module and y orthogonal to it.

6.3.1   The ABCD3T Readout Chip

The SCT modules will have to operate at the high frequency dictated by the LHC bunch crossing and be able to sustain the high radiation levels of the LHC. Each SCT (barrel and endcap) module has 1536 microstrip readout with twelve ASICs (Application Specific Integrates Circuits), named ABCD3T built in radiation hard DMILL technology [86]. The layout of the ASIC is shown in figure 6.9. It has an analog front-end and a digital part with several functionalities.

The analog front-end is an amplifier-shaper-discriminator sequence replicated for each channel. The discriminator gives a binary information on the channel. If the
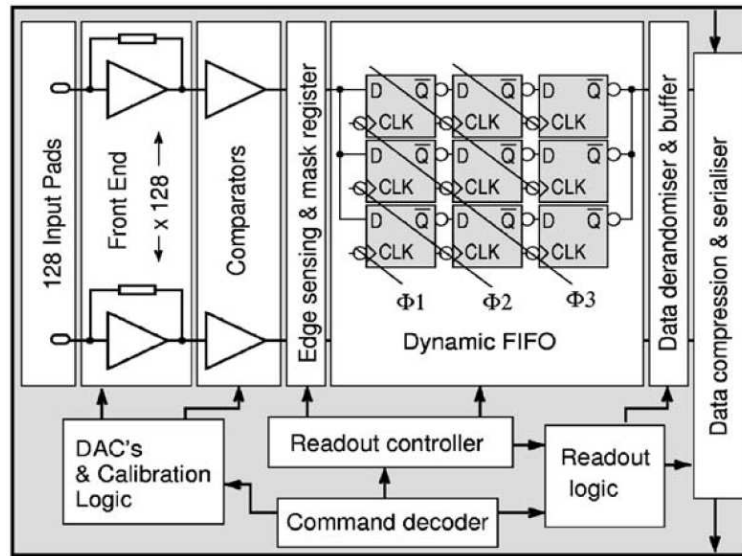
Figure 6.9: *Block diagram of the ABCD3T chip*

charge released by the traversing particle is above a certain threshold, the channel will give a logical state one and zero otherwise. The choice of a binary read-out has been made to reduce the amount of information to be handled by the data acquisition. The discriminator threshold can be set at the chip level and then, to correct the unavoidable channel by channel offsets discrepancies, a programmable offset correction circuit is implemented for each channel with the DAC's (digital to analog converters). The digital part of the ASIC operates at the bunch crossing frequency of the LHC, 40 MHz. The latency required by the Level 1 trigger decision time, is obtained with a 132 cell long digital FIFO pipeline. Between the analog front-end and the digital part, a mask register allows to mask noisy or damaged channels, to avoid reading them out. The ASIC also implements the zero suppression and the encoding of the event to be read out at the Level 1 accept signal. The first ASIC on each side of the module is connected to the optical link; at the Level 1 accept signal the other five ASICs on each side of the module send their data to the master, through a token-ring network, and the master passes the data to the optical link. In case of failure of a single ASIC it is possible to bypass it, without interrupting the readout chain. In case of failure of one of the two master ASICs, it is possible to read out the whole module with the other one. This arrangement has been designed to avoid that the failure of a single chip might translate in loosing an entire module of the SCT. Finally each chip has a charge injection internal circuitry used in the calibrations of the modules. Further details about the ABCD3T architecture can be found in [76].

Chapter 7

Radiation Hardness and Thermal-Electrical Specifications

Charged particles passing through the silicon detectors create a *temporary* damage to its microscopic structure, through the production of electron-hole pairs. The electric field induced by the electron-hole pairs allows to identify with high resolution the position where the particle had passed. The same particles that we want to measure might modify *permanently* the microscopic properties of the silicon, compromising their functionality as detectors. In order to limit the effects of the radiation damage, it is possible to improve the intrinsic radiation hardness of the materials used to build the detectors. At macroscopic level, the temperature at which the silicon operates influence substantially the evolution of the radiation damages. For this reason a careful design of the of the SCT modules, especially for what concerns their thermal performance is of primary importance.

In the following sections we will present a brief description of the most relevant silicon radiation damages and the thermal and electrical specifications that each module has to cope with in order to grant acceptable thermal-electrical performance even if heavily irradiated.

7.1 Radiation Damage

The radiation passing through a silicon detector can damage its microscopic structure leading to several macroscopic effects that in general worsen the performance of the detector. The radiation damages in silicon can be divided into two main categories: surface and bulk damages [91].

The surface of the silicon detectors is partially covered by silicon oxide (SiO_2) which is an insulator. Even before irradiation, there are strong electric fields at the boundaries between the strongly doped region and the insulator. Since the oxide is

not a ordered lattice, the radiation damages of to its bulk can be ignored. Instead, the electron-hole pairs created by ionization in the oxide are of primary importance. The mobility of the electrons in the insulator is several orders of magnitude higher than the mobility of the holes. Hence the generated electrons can drift out of the insulator rather quickly, while the generated holes will remain trapped in the oxide building up a positive charged region, increasing the risk of electrical breakdown and also increasing the leakage current.

The bulk damages are created by the interaction of the incident radiation with the lattice of the silicon. The incident radiation can displace atoms from their original location in the lattice causing two types of "primary defects": interstitials (atoms between lattice locations) and vacancies (empty lattice locations). Depending on their recoil energy, dislocated atoms in the lattice can produce "defects complexes", where groups of atoms (clusters) are displaced from their initial positions in the lattice.

The lattice defects have usually complicated electrical properties. They can capture and emit electrons and holes, increasing the detector leakage current. They can trap electrons and holes and re-emit them with some time delay, reducing the charge collection efficiency and so effectively reducing the generated signal. Or they can change the charge density in the depletion region requiring a higher voltage to fully deplete the detector.

Here we will concentrate on the effect of the radiation damages on the leakage current.

The radiation damage at first increases the leakage current in the detectors, but it has been observed that at the end of the irradiation the leakage current diminishes with time. The rate at which the leakage current diminishes strongly depends on the detectors temperature. This effect is called *annealing*.

The naive reason behind the annealing is that, since interstitials and vacancies have very high mobility in the silicon lattice, they can recombine, giving back a perfect crystal. More subtle effects depend on the stability of the defects complexes. It is worth notice that all defects complexes are stable up to a certain activation energy or temperature called "annealing temperature". Through thermal motion the defects complexes may evolve into other semi-stable structures with different electrical properties. These different properties may not always be beneficial in terms of detector performances. If that would have been the case, it would have been sufficient to heat periodically the detectors to bring back to low values the leakage current. On the contrary, it has been observed that over long periods of time the leakage current raises again. This phenomenon is called *reverse annealing* and it is explained through the modification of initially inactive defects complexes into active ones. High temperatures accelerate the reverse annealing while low temperatures (typically below $0°C$) can reduce it or completely suppress it.

As it will be shown in the next section, the temperature at which the detectors in the SCT will have to operate, have been carefully studied to obtain the maximum benefit from the annealing reducing the harmful effect of the reverse annealing.

7.2 Thermal Specification for the SCT

The thermal specifications of the SCT endcap modules [92] are based on certain assumptions about the operation of the LHC and about the characteristics of the silicon detectors to be used in the SCT. The main concerns driving the specifications are related to the total particle flux through the SCT and the maximal leakage current of the detectors caused by that flux.

The total particle flux through the SCT has been estimated with Monte Carlo simulations. The radiation damage in the silicon bulk depends on the energy and type of the particles produces in the *pp* collisions. However, since the bulk damage is mainly due to the interaction of recoiling silicon atoms with the rest of the lattice, it is possible to rescale the radiation damage from one radiation type to another, obtaining an estimate independent from the type of the primary radiation. The quantity used to quantify the radiation damage is the non ionizing energy loss (NIEL) and it is commonly normalized to the NIEL of 1 MeV neutrons. The effect of the different type of radiation is then usually parametrized with a corrective multiplicative constant called "hardness factor" κ defined as:

$$\Phi_{eq} = \kappa \cdot \Phi$$

where Φ is the fluence of a particle specie and Φ_{eq} is the equivalent fluence of 1 MeV neutrons.

The simulated particle flux in the forward SCT reaches its maximum on the inner modules for the disk closer to the interaction point (see figure 7.1) where it is predicted to be $1.8 \cdot 10^{14}$ 1 MeV neutrons/cm^2 after 10 years of data taking, with an uncertainty of $\pm 50\%$.

To estimate the expected leakage current of the silicon a sample of forward SCT detectors have been used. A procedure has been developed to simulate the environmental conditions that they will have to sustain in the ten years of data taking, including a realistic scenario describing the periods of operation (cold detectors) and the periods of maintenance (warm detectors) of the SCT.

The detectors were irradiated at the CERN PS irradiation facility with 24 GeV protons up to a fluence of $3.0 \cdot 10^{14}$ protons/cm^2, to obtain the same radiation damage that they will be subjected to in ten years of ATLAS data taking.

After irradiation, the detectors have then been kept for 7 days at 25°C , to simulate the integrated time where the detector will have to be warmed up for maintenance,
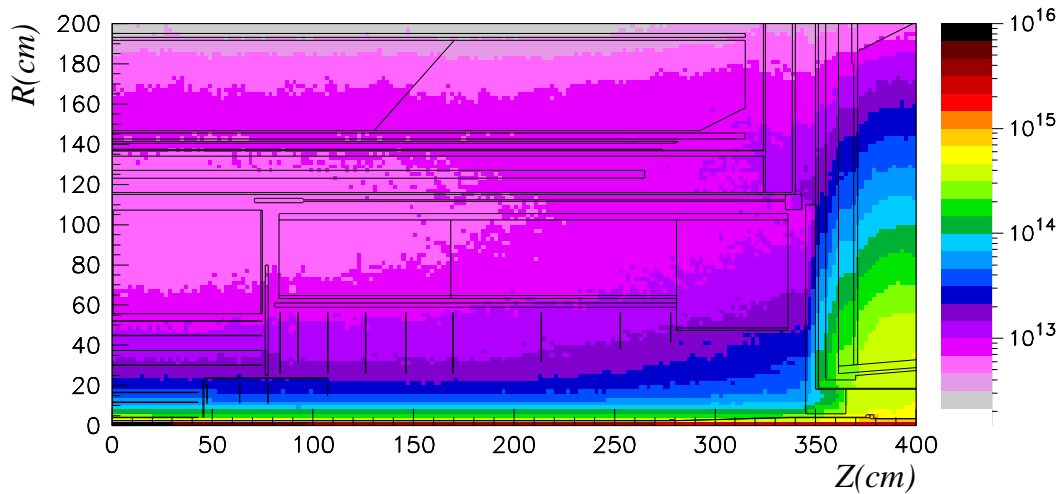
Figure 7.1: *Fluence in the inner detector cavity in units of 1 MeV equivalent per cm^2*

being annealed.

The maximum leakage current on the pre-series detectors is measured to be $0.402 \cdot 10^{-6}$ A/mm^2 at 460 V and at a temperature of 0°C . The value of 460 V is the maximum expected bias voltage on the detectors [92], while the temperature of 0°C , given the current temperature dependence, is just a convenient reference point. The corresponding maximal power density that the detectors will experience is 185 μW/mm^2 at 0°C .

The detectors operating temperature has to be chosen to minimize the harmful effects of reverse annealing. A shallow optimum value has been found at about -7°C , where the leakage current is also significantly reduced.

To keep a temperature of -7°C on the detectors it is necessary to understand the heat sources and sinks in the SCT.

The most significant heat load on the modules comes from the readout electronics housed on the electrical hybrid.

The maximum total power dissipated by the hybrid has been estimated to be 6.76 W. The value considered for the thermal performance studies has been conservatively chosen to be 7 W.

The SCT will operate in a thermal enclosure filled with nitrogen at atmospheric pressure to avoid condensation. To estimate the heat load on each module it has been necessary to study the convection patterns inside the enclosure [93]. The convective heat transfer process has been studied with both fluid dynamics simulations and with

measurements on a thermal mock up. These studies had to rely on a simplified geometry of the system and on few assumptions related to the temperature patterns (boundary conditions) of the modules. The detectors are large and thin layers of silicon, that makes them good thermal exchanger. Being the environment and the hybrids warmer than the detectors, they act as heat sinks. The temperature differences between the detectors and the hybrids is a fundamental input to the studies of the convective pattern and it has been estimated, from preliminary studies on the module layout, to be about 22°C .

The results of the studies on the convective flow indicates that the heat transfer from the environment to the modules, is higher at the top of the disks for outer and middle modules, while for the inner modules the observed pattern is inverted. The upper limit on the power collected by each module has been estimated to be 0.8 W for outer and middle modules and 0.2 for the inner ones. These values also include a safe estimate of the additional heat load coming from the power tapes and thermal radiation.

The last specification on the thermal behaviour of the modules aims at avoiding the so called *thermal run-away*. The power dissipated by the detectors increases their temperature, so the leakage current increases and with it the power dissipation. If a proper cooling is not applied, the heat generated by the detectors leakage current and the heat load coming from other external sources, will drive the module in a thermally unstable condition, known as thermal run-away, where the detectors temperature and so their power consumption would diverge.

Since the thermal run-away represents a catastrophic failure of the module, that would oblige the ATLAS crew to switch it off, it is necessary to set severe specifications on the cooling design of each module. For this reason it has been decided that the module have to be able to sustain 30% more than their maximal power consumption before reaching the thermal run-away.

Based on the previous considerations, we can summarize the module thermal specifications [92] as:

- when the module is dissipating 7 W on the hybrid, 185 $\mu W/\text{mm}^2$ at 0°C on the detectors and is subjected to the environment heat load, the detectors have to be cooler than -7°C

- when the power on the hybrid is 7 W and the module is subjected to the environmental heat load, the thermal run-away must not occur at power densities on the detectors below 240 $\mu W/\text{mm}^2$ at 0°C .

The first specification aims at getting the most favorable annealing conditions, the second set a strict limit on the thermal runaway.

In chapter 8 we will show how a proper module design can satisfy this strict requirements.

7.2.1 Module Electrical Specification and Performance

The electrical performance of a module is the combination of the electrical performance of the silicon detectors, the ASICs and the hybrid. In the final period of the module development, the detectors and ASICs performance were already considered satisfactory to proceed to the series production, while the hybrid was going through the last steps of the R&D.

The design of the hybrid is extremely challenging because it has to distribute the high voltage to the detectors, as well as the low voltage, the clock and the other digital signals to the ASICs. For instance, a possible source of noise could be a pick up of the 40 MHz clock signal from HV detectors bias. Another important issue concerns the grounding. Being the binary readout based on a fixed discriminator threshold, any grounding fluctuation at the hybrid level, would offset the entire module threshold's reference, faking a signal on all the channels at the same time (this effect is called common mode noise).

The performance any detector has to be optimized in terms of two basic quantities: signal and noise.

Given the binary read-out of the ABCD3T chip, the noise is commonly defined in terms of occupancy. The noise occupancy is defined, at a fixed threshold, as the number of firing strips when no signal (from charged particles or internally generated) is present. A high occupancy is problematic in terms of pattern recognition because it increases the wrong hit combinations when reconstructing a track and so the number of fake tracks. It is also problematic for the data transmission, because it increases the amount of data to be transferred. The specification on the maximum acceptable noise occupancy has been studied with simulations [87] and set to 5×10^{-4} at the expected operating threshold of 1 fC.

The signal in the detectors is generated by the electric field induced by the charge deposited in the silicon, drifting in the electric field of the strips. The most probable value of the charge deposited by a minimum ionizing particle in the SCT silicon detectors (285 μm) is 3.6 fC, corresponding to 22,500 electrons. An important figure of merit for a detector is the signal to noise ratio. In order to estimate the signal to noise ratio of a detector is necessary to express the noise coherently in terms of electrons, or Equivalent Noise Charge (ENC). This is done assuming a gaussian noise centered at zero and writing the ENC as the standard deviation of the gaussian distribution in units of the electron charge. The specification of a noise occupancy below 5×10^{-4} implies a threshold at 3.3 σ. Setting the 3.3σ threshold to the expected

operating value of 1 fC, implies an ENC of 0.3 fC or 1900 electrons, resulting in a signal to noise ratio of about 12.

About 20 K5 modules and eight KB modules have been produced and used to validate their electrical performance ([88], [89]). All the K5 and KB modules of this small prototype productions performed within specifications.

The modules will have to operate for 10 years of expected ATLAS data taking. In this period both the detectors and the readout chips will suffer damages from the received radiation.

Five K5 modules and one KB module out of this batches have been irradiated at the 24 GeV proton beam of the CERN-PS irradiation facility to simulate radiation damage that they will experience during the expected ten years of ATLAS data taking. After irradiation the K5 modules showed a noise occupancy ranging between 27×10^{-4} and 160×10^{-4}, with an ENC noise between 2140 and 2430. These values are above the specification. In order to reach the specification values it would be necessary to raise the discriminator threshold to 1.2 fC.

The KB modules showed a noise occupancy of 40×10^{-4} and a noise of 1980 ENC. Also in this case the values are above specification. Nevertheless the measurements were affected by large common mode noise generated by an inappropriate grounding scheme of the test-setup. No conclusive studies were performed to establish the source of the ground failure.

An higher threshold reduces the noise but it also reduces the signal detection efficiency. The SCT specification on the single track efficiency is set to 99%. To quantify the hit efficiency of the modules we used the test beamsetup at the SPS-H8 beamline [78]. In the test beam the SCT modules were mounted between two telescopes, (old silicon modules with known performance) and triggered by scintillators. The single track efficiency is measured as the number of times where the SCT module finds a hit corresponding to a telescope track (in a given fiducial volume) divided by the total number of telescope tracks.

At the nominal threshold of 1 fC all the non irradiated K5 and KB modules tested on the pion beam exceed an efficiency of 99%

No test beam data are available for the irradiated KB module. For the K5 irradiated modules the efficiency remains above 99% up to a threshold of about 1.2 fC, where the noise occupancy is above the specification of 5×10^{-4}.

Combining the noise occupancy with the efficiency requirements, the range of operability of the irradiated K5 module is reduced to a narrow window around 1.2 fC, see figure 7.2
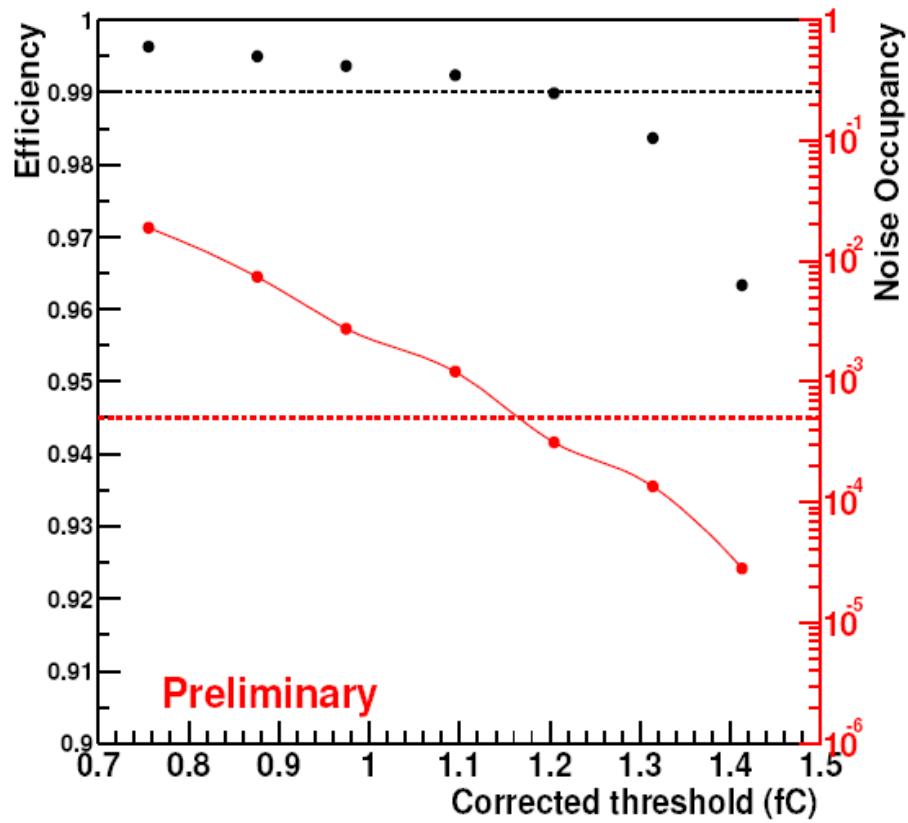
Figure 7.2: *The plot shows the efficiency (black dots) and the noise occupancy (red dots) as a function of the applied threshold. The horizontal lines represent the specifications of trigger efficiency greater than 99% and noise occupancy lower than 5×10^{-4}.*

Chapter 8

Module Thermal Design

"Provando e riprovando."
Galileo Galilei

The design of a fully functional hybrid, which performs to the stringent SCT thermal and electrical requirements described in the previous chapter, is complicated by the complexity and the sensitivity of the readout electronics and it is therefore a major technical challenge, which can result in many time consuming prototyping cycles.

Before achieving the final design (called "K5") several design-prototype iterations has been necessary. Pushed by the early success of the barrel hybrid, a backup layout (called "KB") capable of integrating the barrel hybrid on the end-cap geometry, has been developed.

The layouts were validated through a small prototype production and both performed according to the SCT electrical and thermal specifications. Finally, the baseline solution has been adopted for series production.

In the following we will summarize the fundamental criteria driving the conception of the thermal-mechanical design of the SCT forward modules. Then the development of the KB design and its thermal performance validation through finite element analysis (FEA) and measurements on a prototype module will be presented. Finally, the validation of the thermal performance of the baseline K5 design has been performed through measurements on a prototype module, using the same procedures developed for the KB.

8.1   Basic Thermal-Mechanical Module Design Considerations

The thermal-mechanical design of the modules is the outcome of an optimization process that looks for the best compromise between thermal performance, mechanical solidity and the least possible amount of material in the tracker.

The heat in each module is produced by the electronics housed on the hybrid and by the silicon detectors. The typical temperature of the hybrid is several degrees above the detectors temperatures, hence the detectors will collect some of the heat dissipated by the hybrid. The main goal of the thermal design is to keep the detectors and hybrid thermal paths (the path from the point where the heat is generated to the point where it is removed) well separated, trying to avoid possible thermal cross talks.

At the same time it is necessary to keep the module mechanically solid. Each module has to have a rigid structure to resist the unavoidable thermal stress during maintenance, and the even more dramatic circumstances of a cooling incident, without any relevant distortion. Moreover a solid design will allow a safe handling during module production and installation.

The solidity of the module has to be compromised with the requirements on the amount of materials in the SCT. The material in the tracker influence the multiple scattering of the particles traversing it, hence its tracking performance. To limit this effect special attention has to be paid to reduce the amount of material of each module and of the necessary infrastructures (cables, pipes, etc...) on the disks.

Given the different geometries of the hybrids, the KB and K5 modules have been designed implementing different solutions to cope with the previous requirements. Details and performance of the different designs will be analysed in the respective sections.

8.2   The KB module

The KB module design [94] has been developed using thermal finite element analysis (FEA) simulations. We studied the outer module configuration because it is the longer module and it has the longer detector thermal path and so it is the most critical in terms of thermal performance. When the thermal finite element analysis (FEA) of the module showed that the design performed within specifications, a prototype module has been built and tested. Thermal simulations have been compared with the measurements and finally used to extrapolate the behaviour of the module in different cooling scenarios.
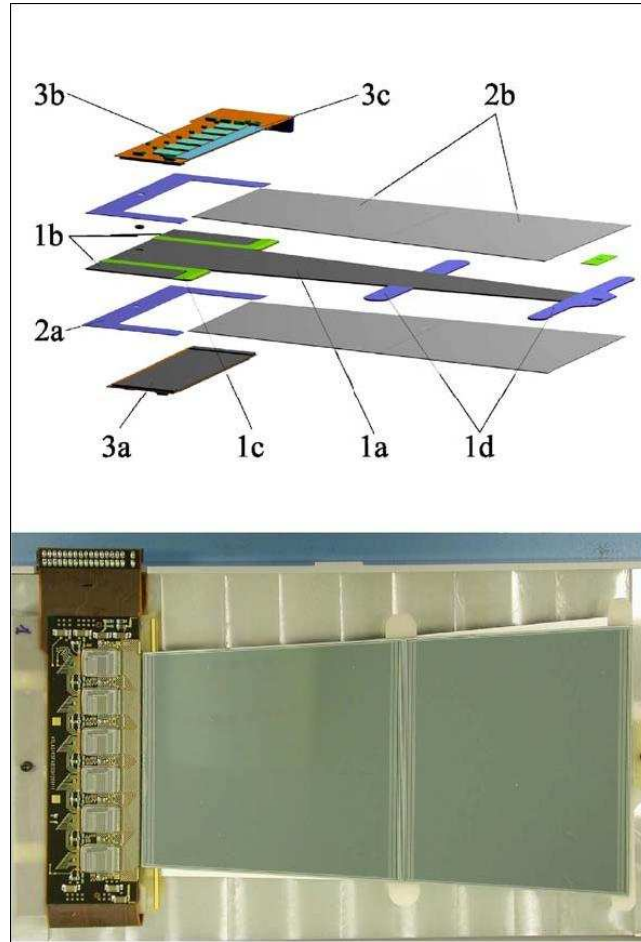
Figure 8.1: *Top: exploded view of the KB design. (1a) is the central TPG spine, (1b) are two TPG inserts, (1c) "L-shaped" isolation, (1d) AlN supports, (2a) AlN facings, (2b) microstrip detectors, (3a) is the carbon-carbon hybrid support, (3b) hybrid, (3c) readout chips. Bottom: picture of a module from the small prototype production.*

8.2.1 Thermal design concept

The main challenge of the KB design has been to use a single cooling point for each module. The reason behind this choice has been to avoid a second cooling circuit on the disk thus reducing the overall amount of material in the SCT. As already noticed, the detectors and hybrid thermal paths have to be decoupled to avoid that the warmer hybrid dissipates part of its heat on the detectors. This concept, becomes more delicate when the heat paths have to reach the same cooling point. After several iterations the module design converged to the one shown in figure 8.1.

The mechanical details of the KB design can be found in [77], here we will summarize the main aspects related to the thermal performance.

The KB module consists of three component groups: the central "spine", which provides cooling for the detectors and hybrid as well as serving as a structural support; the detectors which are glued to the spine; and the electronics hybrid which is also glued to the spine. The module is mounted and cooled at the rear end behind the hybrid. The spine consists of a long central piece of high-quality Thermal Pyrolithic Graphite (TPG [95]) (part 1a), below the detector and hybrid, and two small pieces of TPG (part 1b), in the area where the hybrid is attached to the spine. The TPG pieces provide the main cooling to the detectors (part 1a) and hybrid (part 1b) through their excellent heat conductivity in longitudinal direction. The central TPG (1a) carries the heat from the detectors to the cooling contact and it is wedge shaped to have less thermal resistance. The small TPG pieces (1b) remove the heat from the hybrid and conduct it to the cooling contact. The central TPG is separated from the smaller TPG pieces by two "L"-shaped parts of thermoplast Polyetheretherketon (PEEK) (part 1c). They thermally separate the central TPG from the hybrid TPG pieces and also serve as structural reinforcement between the spine and detectors. At the far detector end, the detector edges are supported by pieces of AlN ceramic (parts 1d). The central spine pieces are sandwiched at the cooling and mounting point by two "U"-shaped pieces of AlN (parts 2a). Their function is to serve as the main cooling contact and mounting surface of the module. The hybrid consists of the Kapton flex circuit (part 3b), which is laminated to two carbon-carbon bridges (part 3a), one for the front and one for the rear side of the module. The carbon-carbon bridge reaches over the central spine by leaving a 0.8mm air gap between the bridge and the center TPG piece. This air gap minimizes the unwanted heat transfer from the hybrid to the center TPG and detectors. The bridge feet are glued to the forward extensions of the AlN facings (2a). The heat dissipated by the chip is conducted from the bridge through the AlN facing into the small TPG pieces.

The thermal design of a module has to take into account the design the cooling block where the module will be mounted. The cooling block is a crucial component of the design because it represents the interface between the module and the cooling fluid. A picture of the cooling block is shown in figure 8.2. The cooling block keeps down to the cooling fluid the separation of the detectors and hybrid thermal paths. The block is divided in three thermally conductive pieces separated by two isolation insertions. The lateral conductive pieces are in correspondence with the lateral TPG piece (1b) bringing the power generated by the hybrid to the cooling fluid. The central conductive piece corresponds to the central TPG piece (1a) of the detectors cooling path.

The isolant pieces in between the conductive ones keep separations of the thermal paths.
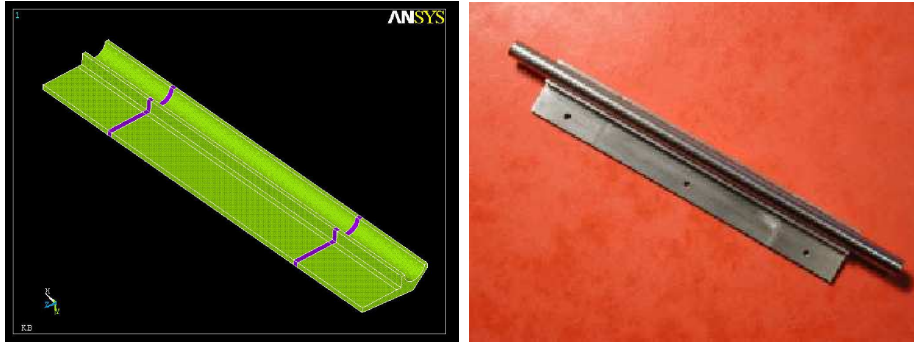
Figure 8.2: *Left: drawing of the KB cooling block; in yellow the thermal conductive aluminum pieces, in violet the isolating ones. Right: the realization of the cooling block with the CuNi cooling pipe mounted on it.*

A common issue about all block designs is the coupling of the different parts of the block through the cooling pipe and the solder layer. Since the solder has high thermal conductivity, to reduce the coupling across the different parts of the block, its thickness is reduced to $\sim 100~\mu$m . The material chosen for the pipe is CuNi, a low thermal conductivity metal alloy ($\sim$29 W/mK) but, to keep a reasonably low radial thermal resistance the thickness of the pipe has been reduced to $\sim$70μm .

8.2.2   Thermal Simulations: an FEA Model

The thermal simulations of the KB modules have been performed using ANSYS (version 5.7.1). ANSYS is a commercial general purpose finite element analysis package that allows 3D simulations [96]

The detectors are modeled with 3D thermal-electrical elements. The ANSYS package allows to describe the electrical resistivity of the material as a function of the temperature. It is thus possible to include the leakage current temperature dependence in the model. With this peculiarity it is possible to simulate the heat generation due to the leakage current in the detectors and analyze the thermal runaway point.

The KB module has an adiabatic surface corresponding to its symmetry plane. Taking advantage of this symmetry it is sufficient to simulate half of the module, reducing significantly the number of finite elements, and so the required computational time, see figure 8.3.

Each module component has been included in the FEA model, as well as all the glue layers. The hybrid and chips are replaced in this study with a single volume generating 3.5 W per side. The description of the temperature distribution on the hybrid is then not very accurate, but it gives enough detail to study the cross talk between the hybrid and the detectors thermal paths. The cooling block is fully simulated in the FEA model.

The description of the interface between the coolant and the cooling pipe is particularly delicate because it requires good knowledge of the heat transfer coefficient (HTC) of the coolant through that surface. The FEA model will be used to compare the measured thermal map of the module with the simulated one.

The cooling system foreseen for the SCT is based on an evaporative cycle, while the measurements of the module cooling performance will be performed using a monophase liquid coolant. Instead of measuring the HTC for this not final configuration, in the simulations we will set a fixed "effective" cooling temperature on the inner wall of the cooling pipe, that will be tuned on the measurements.

In a second step we will use the FEA model to predict the thermal map of the module with the evaporative cooling system that will be used for the SCT, for which a set of HTC measurements were performed [97].

The finite elements subdivision (mesh) of the module, shown in figure 8.3, and its stability (temperature independence from the finite elements size) has been accurately verified.

The FEA were used to find the optimal materials and geometry configuration. To validate the FEA results and gain confidence on the proposed design, a prototype module has been assembled and irradiated to recreate the high leakage current conditions.

In the following section we will show the thermal measurements performed on the prototype module and the comparison with the FEA results. After that the
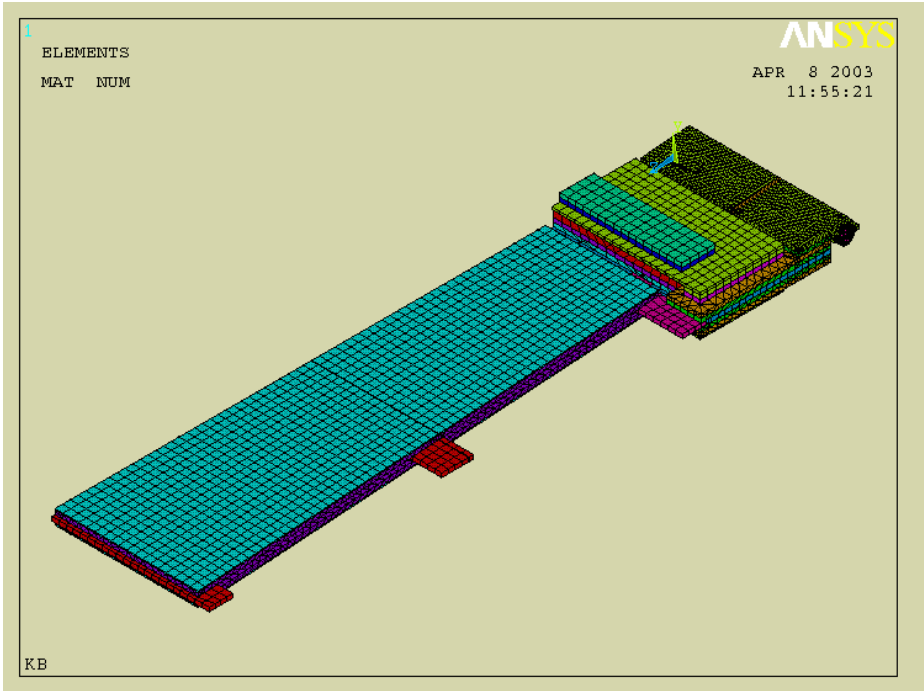
Figure 8.3: *KB FEA model, showing the finite elements subdivision.*

FEA model will be used to predict the KB thermal performance in different cooling scenarios.

8.2.3   Thermal Measurements

Setup description

The setup used for the thermal measurements aims at emulating in laboratory the environment where the module will have to operate. The relevant conditions to be controlled are the coolant temperature and the effect of convection and radiation on the detectors surface.

The thermal measurements were performed on an irradiated and annealed module.

The results we are going to report for the measured thermal performance have to be considered as conservative with respect to several aspects. First, the thermal measurements are performed with a module and a cooling block where, for practical reasons, vetronite has been used instead of PEEK. The higher thermal conductivity of the vetronite with respect to the PEEK will increase the coupling between the detectors and hybrid thermal paths. Second, for this first prototype the cooling pipe has been glued instead of soldered onto the cooling block; thus the thermal resistance of the block is much higher than the real one. And third the measurements are performed with a chiller circulating a monophase liquid coolant (water and ethanol mixture) that has an HTC much lower than the C_3F_8 used in the evaporative cycle foreseen in the SCT. The exact value of the HTC of the mixture used in this setup with the cooling pipe is anyhow not known.

The convection and radiation conditions present in the experiment are difficult to emulate. Instead of trying to recreate the convection and radiation heat loads, we tried to eliminated them, aiming at creating a situation easy to be compared with simulations. When the FEA will correctly represent the measured values, the additional environmental heat loads effect will be studied adding them in the FEA model. In our tests the module is operating in flushing nitrogen atmosphere to avoid condensation (the relative humidity has been kept below 10% at any atmosphere temperature). The module was installed in a dedicated test box (see figure 8.4) placed in a climate chamber. This feature allows to regulate the temperature of the box walls and, through an heat exchanger placed into the climate chamber, the temperature of the atmosphere in the box. Tuning the temperature of the climate chamber to the temperature of the detectors allows to reduce drastically the convection and radiation heat load on the detectors surface, leading to a situation easy to compare with simulations.[1]

The module has been kept electrically fully operative all over the measurements. This means that high voltage was applied on the detectors and the readout electronics was powered and exercised via the dedicated SCT-DAQ readout software.

---

[1]To remove any contribution from the atmosphere it would be necessary to test the module in vacuum but, due to practical reasons, this has not been possible.
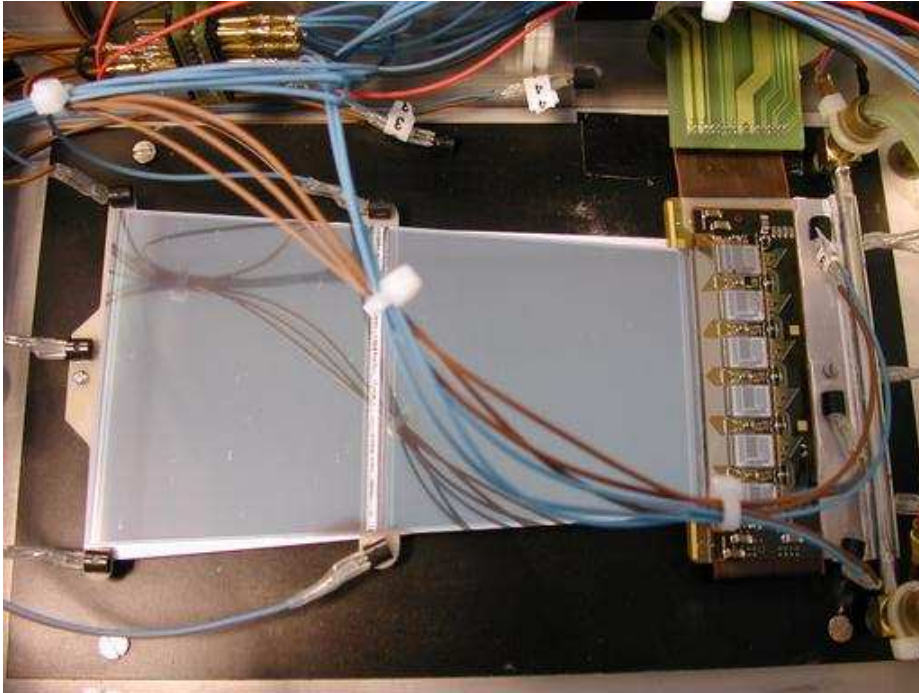
Figure 8.4: *Module mounted in the dedicated box with sensors glued at several location.*

Sensors Calibration

The module and environment temperatures are measured with digital sensors (DS1820 [98]) glued at several critical points, see figure 8.4. Five sensors are mounted on the AlN supports of the detectors, three on the "U"-shaped AlN facings at the module rear end, three on the cooling block, two on the box walls, one monitoring the atmosphere in the box, one on the cooling inlet and one at the cooling outlet. We decided not to glue the sensors onto the silicon detector surface, to avoid possible damages that would lead to a modification of the current density and so to a modification of the temperature distribution.

To read out the sensors we developed a dedicated LabView interface.

While an ideal sensor can read the temperature of the surface at which is thermally grounded, regardless of the environment conditions surrounding it, none of the real sensors allow this feature. To overcome this inconvenient we developed a specific procedure consisting in a two steps calibration.

First, the sensors are thermally grounded to a large block of aluminum placed in a climate chamber. Setting the block at different temperatures allows to check the linear response of the sensors over a wide range of temperatures. The sensors appear to have an excellent linearity in the range of interest between -25°C and +25°C (see

figure 8.5).
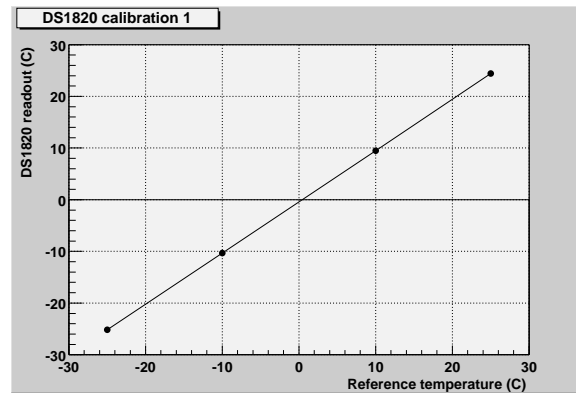
Figure 8.5: *Temperature values measured with a typical DS1820, plotted against the reference temperature.*

In a second step a measurement of the influence of the atmosphere temperature on the sensors read out is performed. The sensors are glued in their final position on the module and in the box. The chiller temperature is set to a fixed low value (about -20°C) and the atmosphere temperature is varied from -20°C up to a about +30°C . Since no power is injected in the module the temperature of the inlet, outlet, cooling block and facings are in very good approximation at the same temperature of the coolant, while the detectors, due to their geometry, change their temperature during this operation. It is possible to observe from figure 8.6 that the measured value of the DS sensors varies sensibly increasing the atmosphere temperature. The measured temperature, the real surface temperature and the atmosphere temperature can be related in the following way:

$$T_{read} = T_{surface} + k(T_{atm} - T_{surface}) \tag{8.1}$$

where k is the slope fitted from the previous plot 8.6. From this equation it is possible to work out the real temperature of the surface:

$$T_{surface} = (T_{read} - k \cdot T_{atm})/(1 - k)$$

The sensors glued onto the AlN supports of the detectors cannot be treated in the same way, because the detectors, contrary to the facings that are close to the cooling block, will change their temperature, following the atmosphere conditions, invalidating the calibration procedure. For this reason a different approach has been developed to avoid the environment bias on the sensors readout. Anytime a power
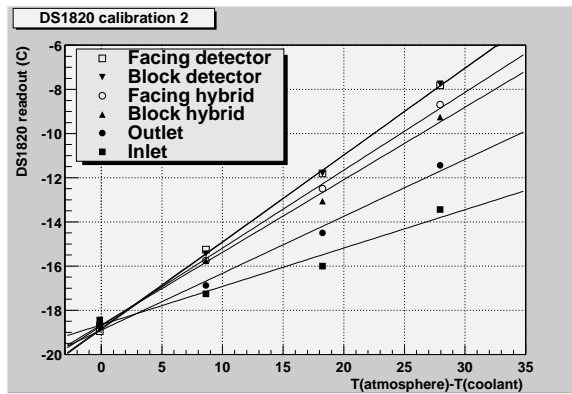
Figure 8.6: *Influence of the atmosphere temperature on the sensor readout value. In the plot the temperature read with the DS sensors is plotted against the temperature difference between the atmosphere and the real surface temperature assumed to be equal to the coolant temperature.*

density (bias voltage) is set on the detectors, the thermal equilibrium between the detectors and the environment has to be reached. Stepping through thermal equilibrium states, the effect of the environment on the temperature measurements is canceled. This is however a lengthy procedure because at each modification of the environment temperature the leakage current will change and with it the detectors temperature. The environment temperature tuning may takes few iterations before converging to equilibrium.

Measurements Results

Different runs at different coolant temperatures have been taken. A first run at -13°C
has been performed tuning the temperature of the atmosphere to the temperature of
the detectors at each point.
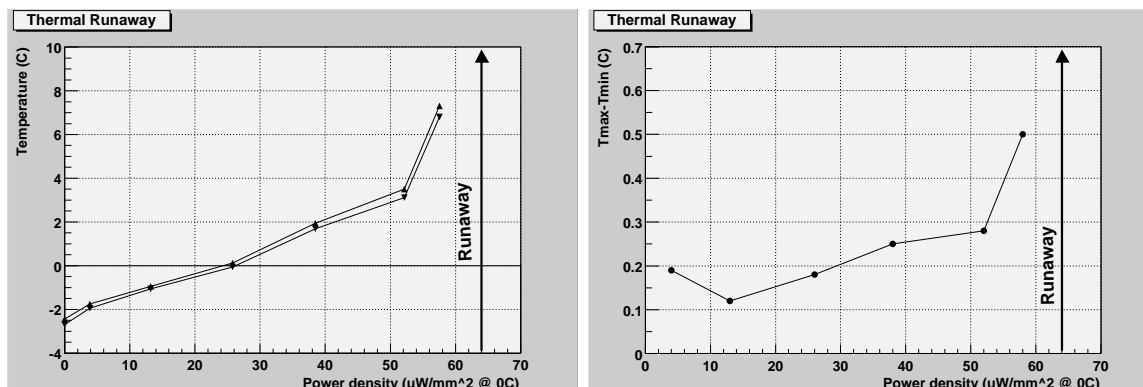
Figure 8.7: *LEFT: Runaway plot done with a coolant temperature of -13°C . With
down triangles the coolest temperature measured on the wings, with up triangles the
warmest one; RIGHT: Difference between the warmest and coolest temperature mea-
sured on the detectors.*

It is common to represent these measurements with "run-away plots" as the one
in figure 8.7. In the run-away plots the maximum and minimum detectors temper-
ature are plotted against the power normalized to 0°C . In our case the maximum
and minimum detector's temperature are replaced with the maximum and minimum
temperatures measured on the detector supports. Normalizing the detector power
density to a fixed temperature (conventionally chosen to be 0°C) allows to see the
point where the module reach the unstable condition of the thermal run-away as a
vertical asymptote. In the same figure, the same phenomenon is also shown from a
different point of view. When the module is operating in stable cooling conditions
the variation of temperature across the detectors is negligible; when it approaches the
runaway point, the corners of the detectors (as well as the AlN supports) with longer
thermal path will run warmer.

At a coolant temperature of -13°C the thermal run-away appears above
$65\mu W/mm^2$ at 0°C . We decided not to reach the exact run-away point, not to damage
the module. Instead we will compare the measured points with the FEA and use the
latter to estimate the true run-away point.

A second run has been performed to test the stability of the module in conditions
similar to the ones expected in the SCT environment. In the real experiment the
temperature of the nitrogen atmosphere far from the convectional plume is predicted

to be around -7°C with large variations between different module positions on the disk. Considering a coolant temperature of -23°C the temperature difference between coolant and atmosphere will be around 16°C . Keeping the same temperature difference when the coolant temperature is at -18°C leads to a nitrogen temperature of -2°C . In this run the atmosphere is maintained at -2°C all over the scan.

Figure 8.8 shows the thermal run-away plot in these conditions. The highest power density reached (160 $\mu W/\text{mm}^2$ at 0°C) has been obtained biasing the detectors at 460 V, the highest expected voltage when running the SCT after 10 years of data taking and the module still operates stably.
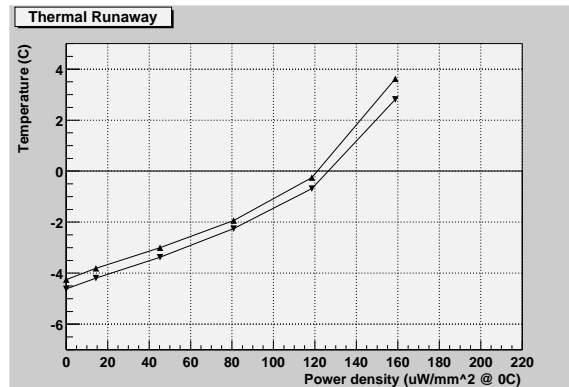
Figure 8.8: *Runaway plot done with a coolant temperature of -18° C and a fixed atmosphere temperature of -2° C . With down triangles the coolest temperature measured on the wings, with up triangles the warmest one.*

8.2.4 Simulations and Measurements: Comparison and Predictions

The results coming from the simulations performed with the FEA model previously discussed has been compared with the measurements on the irradiated module.

As already said, the heat transfer coefficient of the monophase liquid coolant to the CuNi pipe is not available, so the coolant-pipe interface description used in the FEA has to be simplified, setting the inner wall of the cooling pipe to a fixed temperature.

Moreover, the prototype module used for the measurements differs from the final one with one respect: the two L-shaped pieces separating the detectors from the hybrid thermal paths, have been produced in vetronite instead of PEEK. Vetronite has a thermal conductivity higher by an order of magnitude with respect to PEEK. This create a larger thermal coupling between hybrid and detectors. The cooling block is also slightly different with respect to the final one. The cooling pipe has been glued on the block instead of been properly soldered and the material used to split the different portions of the block is again vetronite instead of PEEK.

Once these characteristics have been implemented in the simulations, only one parameter (the coolant temperature) has to be tuned to reproduce the measured situation. With the chiller set to a nominal coolant temperature of -13°C , the measured inlet temperature in the box was about -10°C and the value used in the simulations has been tuned to -8.5°C . In figure 8.9 the measured temperatures have been superimposed to the simulated thermal map taken at a power density of 58 $\mu W/\mathrm{mm}^2$ at 0°C .

There is good agreement between the values measured on the detectors and the simulated ones. The agreement is worse on the hybrid because of the extreme simplification adopted.

Once the coolant temperature has been tuned, the model was used to predict the detectors temperature at different power densities. Figure 8.10 shows that the agreement is within a degree down to $4\mu W/\mathrm{mm}^2$ at 0°C .

The runaway point extracted from the simulations in these conditions is above $75\mu W/\mathrm{mm}^2$ at 0°C .

The FEA model can now be used as a tool to investigate the thermal performance in the SCT expected cooling conditions. The materials in the model for the module and the block are changed to the one foreseen in the experiment: PEEK instead of vetronite and solder instead of glue on the cooling block. The fixed temperature on the pipe inner wall is substituted to the heat transfer coefficient description of the coolant-pipe interface. The measured heat transfer coefficient [97] is about 3000 W/m²K.

In figure 8.11 we show the runaway plot obtained fixing the coolant temperature at -20°C and three values of the heat transfer coefficient have been considered around
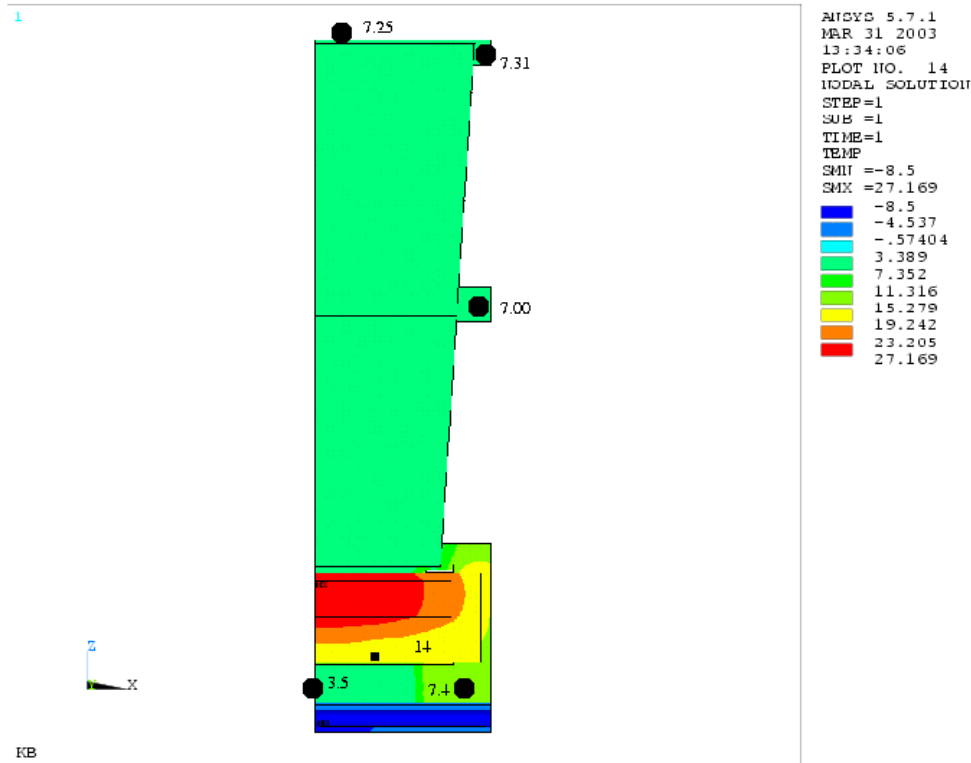
Figure 8.9: *Thermal map obtained with $58\mu W/mm^2$ at $0^\circ C$ fixing the pipe inner wall temperature to $-8.5^\circ C$. The black dots represent the measured temperatures.*

the expected 3000 W/m^{2}K. The runaway point is around $400\mu W/mm^2$ at 0°C considering an heat transfer coefficient of 3000 W/m^{2}K, but the module is still within the specification with an heat transfer coefficient of 2000 W/m^{2}K.

To simulate the heat load of 0.2 W per detector coming from convection and emission radiation, it has been decided to generate that extra-power in the detectors volumes. The results are reported in figure 8.12. The module is still within the specifications with -20°C coolant temperature and an heat transfer coefficient of 3000 W/m^{2}K, but it would be out of specifications if the heat transfer coefficient is reduced to 2000 W/m^{2}K. The coolant temperature needed to meet the specification if the HTC is 2000 W/m^{2}K is -22°C while it can be raised up to -18°C if the HTC is 4000 W/m^{2}K, as shown in figure 8.13

In figure 8.14 the thermal map expected with a coolant temperature of -20°C and an HTC of 3000 W/m^{2}K is shown.

In these conditions the temperature differences between different parts of the
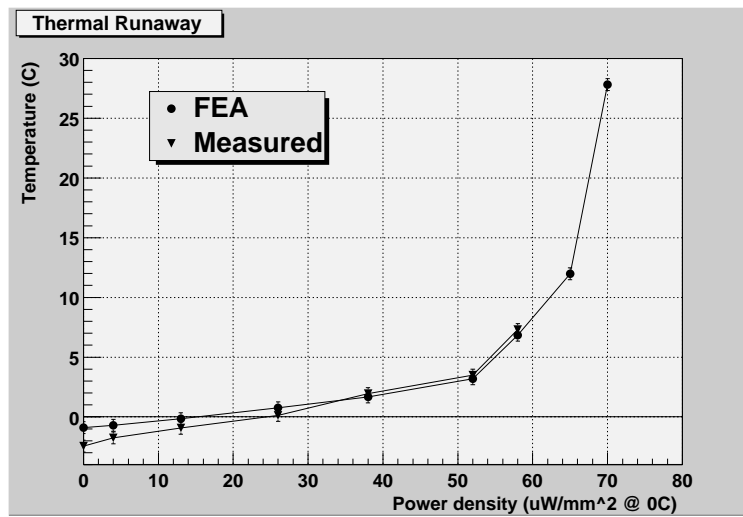
Figure 8.10: *Comparison between the simulated (dots) and the measured (triangles) runaway curves. (Maximal temperature of the detectors versus the detectors power density normalized to $0^\circ C$).*

detectors are listed in table 8.2.4.

ΔT	
coolant - max detector	11
coolant - max hybrid	27
max hybrid - max det	16

Table 8.1: *Temperature differences as predicted by the FEA with a power density of $185\mu W/mm^2$ at $0^\circ C$, coolant temperature = $-20^\circ C$, HTC = 3000 W/m^2K and including an heat load of 0.2 W per detector simulating the heat load coming from convection and emission radiation in the SCT.*
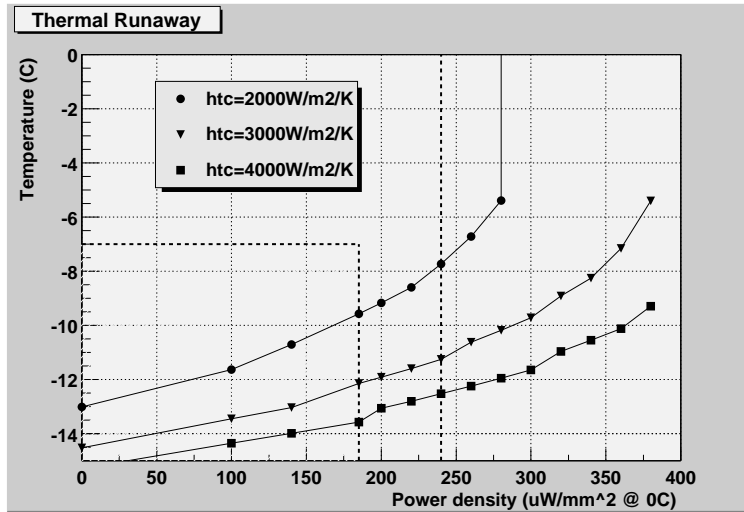
Figure 8.11: *Runaway plot using a coolant temperature of -20° C for different heat transfer coefficients. (Maximal temperature of the detectors versus the detectors power density normalized to 0° C). The dashed lines indicate the specifications: the detectors have to be cooler than -7° C up to 185μW/mm² at 0° C and the runaway must not occur below 240μW/mm² at 0° C .*

Figure 8.12: *Runaway plot using a coolant temperature of -20° C for different heat transfer coefficients when the heat load of 0.2W per detector coming from convection and emission radiation is simulated. (Maximal temperature of the detectors versus the detectors power density normalized to 0° C). The dashed lines indicate the specifications: the detectors have to be cooler than -7° C up to 185μW/mm² at 0° C and the runaway must not occur below 240μW/mm² at 0° C .*

Figure 8.13: *Runaway plots obtained tuning the coolant temperature in order to meet the specifications for different heat transfer coefficients. The heat load of 0.2W per detector coming from convection is simulated. The dashed lines indicate the specifications: the detectors have to be cooler than $-7°C$ up to $185\mu W/mm^2$ at $0°C$ and the runaway must not occur below $240\mu W/mm^2$ at $0°C$.*
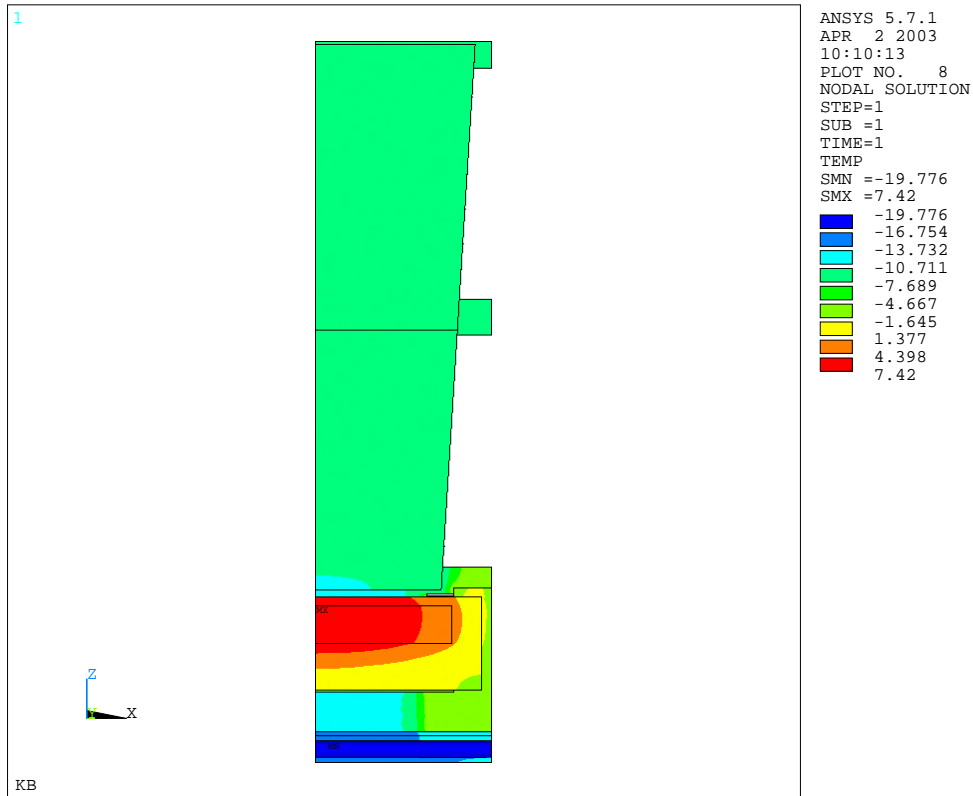
Figure 8.14: *Thermal map obtained with a power density of $185\mu W/mm^2$ at $0^\circ C$, coolant temperature = $-20^\circ C$, heat transfer coefficient = $3000\ W/m^2 K$ and including an heat load of 0.2 W per detector simulating the heat load coming from convection and emission radiation in the SCT.*

8.3   The K5 Module

The baseline project K5 was already finalized when we developed the KB design. Nevertheless the K5 design was relying only on simulations and measurements on dummy modules. Since we developed all the necessary infrastructures to perform the measurements on the a fully functional KB prototype module, we modified the existing setup to accommodate also the K5 layout. In this section we will describe the K5 thermal mechanical design and the thermal run-away measurements performed on the module [99].

8.3.1   Thermal design

The K5 module design is shown in figure 8.15. The main structure of the K5 module is similar to the one of the KB, with the central spine providing cooling for the detectors and serving as structural support, the detectors glued on the spine and the electronics hybrid connected to the detectors at one end of the module. The hybrid is glued on a carbon-carbon substrate providing the cooling. The modules are mounted on a cooling block located between the hybrid and the detectors in thermal contact with the carbon-carbon substrate of the hybrid and the TPG spine. The outer and middle module configurations, take advantage also of a second cooling block on the other side of the detectors with respect to the main cooling block to increase the cooling on the detectors.

As for the KB the goal of the thermal design is to keep the detectors and hybrid thermal paths separated, to avoid that the heat from the warmer hybrid leaks to the detectors. The two thermal paths join at the main cooling block that represents a critical aspect of the design. A picture of the main cooling block can be found in figure 8.16.

Different block designs have been proposed and tested. In the final one the separation of the heat paths is implemented with a piece of low thermal conductivity material (PEEK) fused in between two pieces of carbon-carbon.

A common issue about all block designs (already presented in the KB block description) is the coupling of the two halves of the block through the underlying pipe and solder layer. Since the solder has high thermal conductivity, to reduce the coupling across the two sides of the block, its thickness is reduced to $\sim 100~\mu\mathrm{m}$. The material chosen for the pipe is CuNi as for the KB, $\sim 70\mu\mathrm{m}$ thick.

The inner module, which does not take advantage of a second cooling block at the detectors end, represents the most critical layout in terms of thermal performance, and for this reason this will be the one used to validate the K5 design.

The two cooling points strategy for the detectors, in the outer and middle modules configurations, however presents a risk. If a considerable coupling is present at
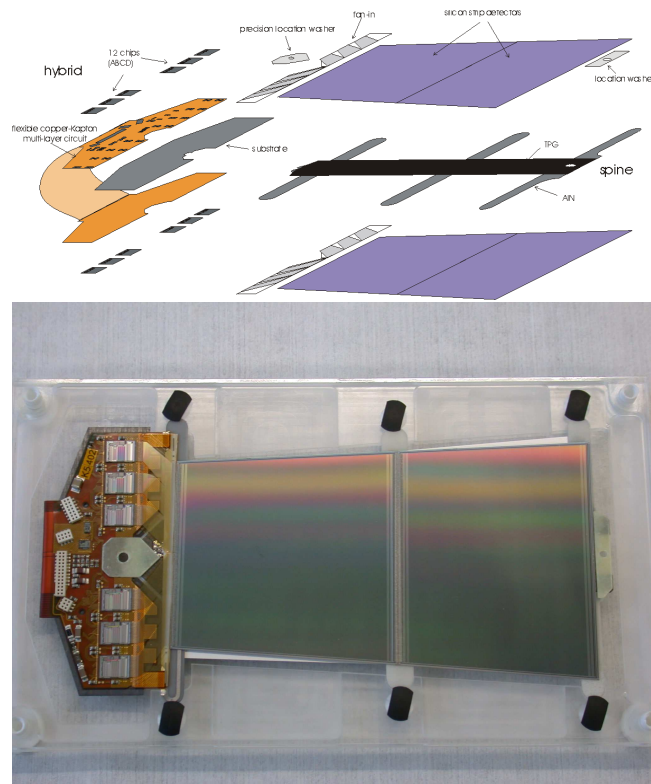
Figure 8.15: *Top: exploded view of the K5 outer module design; Bottom: picture of a K5 module from the prototype production*

the main cooling block, a dangerous thermal path is created from the warm hybrid through the main cooling block and through the detectors, to the second cooling block. This aspect has been carefully studied with simulations. The validation of the thermal design of the outer and middle module configurations, thought proposed has not been possible due to practical reasons.

8.3.2 Thermal measurements

The aim of the thermal measurement on the K5 module is to verify that it is safe against thermal run-away when operated at the nominal cooling temperature of -22°C estimated for the final evaporative cooling rig [100].

The module used for this test has been irradiated at the CERN-PS 24 GeV proton beam up to the fluence of $1.5\,10^{14}$ protons/cm^2, annealed at 25°C for one week and then stored in a freezer at about -20 °C . During the various measurements and shipping to different laboratories it is estimated that it remained at room temperature for an additional period of about 3 weeks. The lower fluence ($1.5\,10^{14}$ instead of

Figure 8.16: *Picture of a prototype cooling block*

the nominal $3.0\,10^{14}$ protons/cm^2) was requested to perform electrical tests at an intermediate irradiation level. This will be corrected to the nominal one through an analytic rescaling.

Setup Description

As for the KB, the module has been placed in a dedicated test box and operated in flushing nitrogen atmosphere to avoid condensation on the detectors. The test box has been installed in a climate chamber. The nitrogen flowing in the box was cooled via an heat exchanger mounted in the climate chamber.

The module and environment temperatures are measured with several DS1820 [98] glued in different critical points (see figures 8.17 and 8.18) and readout with the same dedicated LabView interface developed for the KB. All temperature sensors have been calibrated following the same procedure detailed in the KB section.

The environment load on the temperature sensors glued on the AlN detectors support has been reduced tuning the temperature of the box walls and the nitrogen atmosphere to the temperature of the detectors supports.

The cooling block we used was a prototype of the final one with the PEEK insertion to separate the detector and hybrid thermal paths. The block was soldered on a CuNi pipe and connected to a monophase liquid coolant circuit.

The module has been kept electrically fully operational all over the measurements. This means that high voltage was applied on the detectors and the readout electronics was powered and exercised via the SCT-DAQ.

Measurements results

The runaway point has been approached with a coolant temperature of -5°C . At any variation of the detector bias (power density) the thermal equilibrium between
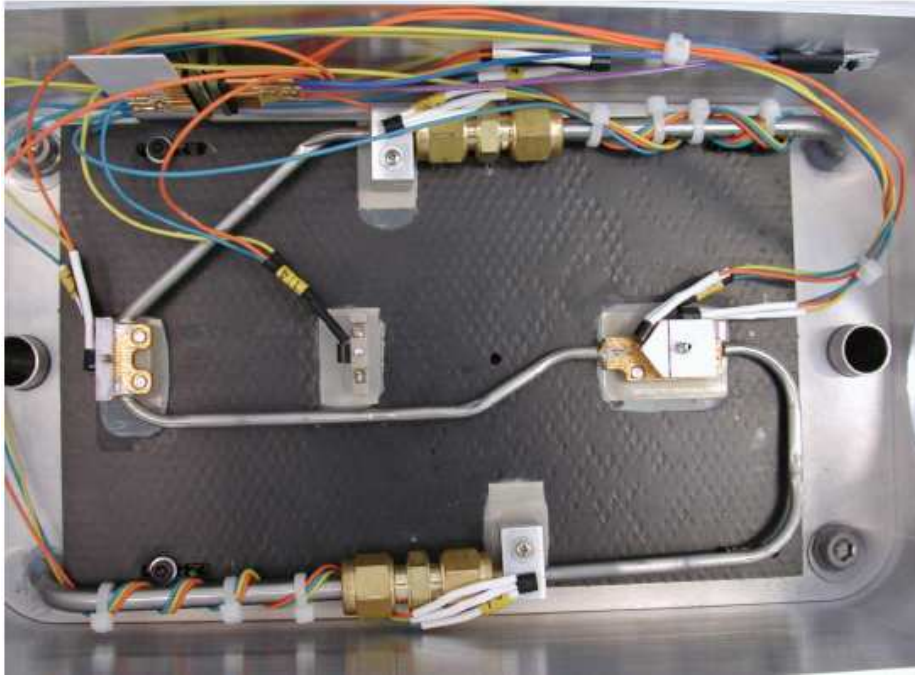
Figure 8.17: *Thermal box used for the k5 thermal measurements equipped with DS1820 sensors. The relative humidity sensor (HIH3605) is also visible in the upper right corner.*

detectors and environment has been reached with an opportune tuning of the climate chamber temperature.

In figure 8.19, the corresponding run-away plot is shown. The runaway curve is reaching the expected asymptote at a power density above 80 $\mu W/mm^2$ at 0°C .

This value cannot be compared directly with the values set in the thermal specifications since the operating temperature is much warmer than the one expected in the experiment and the heat transfer coefficient of the monophase liquid is lower than the one of the evaporative system

Instead of using FEA simulations, as we did for the KB, we rescaled the measurements to the expected cooling temperature, using an analytical method. The results will have anyway to be considered as conservative in that the HTC of the monophase liquid coolant is much lower than the one measured for the C_3F_8.

The rescaling method takes advantage of the temperature dependence of the detectors power density and it embraces part of the power dissipation as effective radiation damage. It is possible to formulate the problem in the following way.

Let's assume a detector dissipates a power $\mathscr{P}$ at a given temperature (and bias). As already observed in chapter 7 the temperature dependence of the leakage current
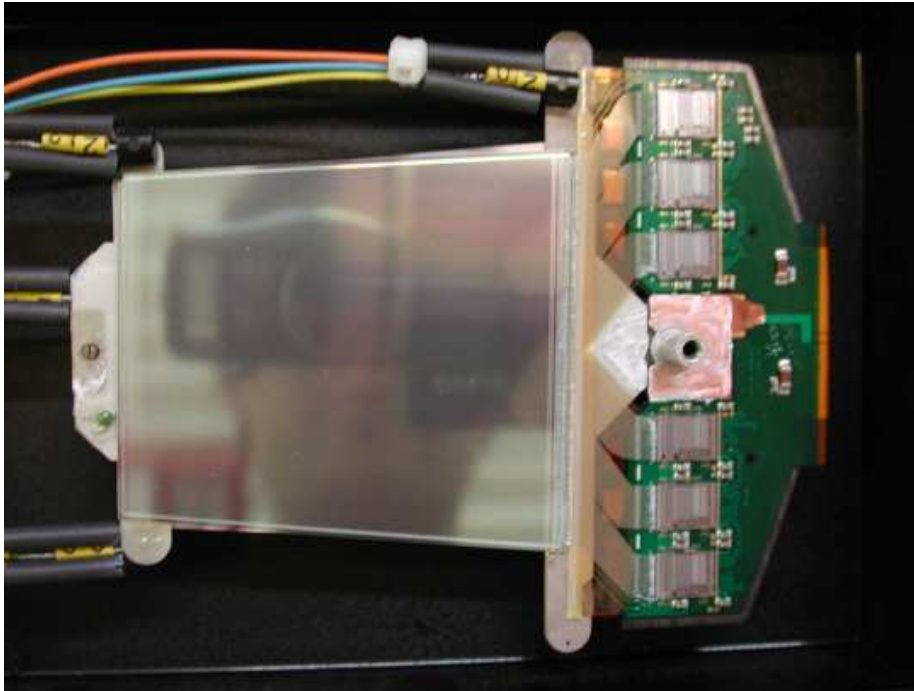
Figure 8.18: *DS1820 positions on the module. The module is upside-down showing the surface in contact with the cooling block.*

can be described to a good approximation by:

$$I(T) = I(T_0) \cdot 2^{\frac{T-T_0}{7}}$$

We can then write the power density of the detectors at the temperature T as:

$$\mathscr{P} = P(T) = P(0) \cdot 2^{\frac{T}{7}}$$

where $P(0)$ describe the effective radiation damage at $0°C$, and the other term describes the temperature dependence. The same power density can be obtained from a detector with higher radiation damage at a lower temperature. If we reduce the temperature of the detectors to $T' = T - \Delta T$ we can write:

$$\mathscr{P} = P'(0) \cdot 2^{\frac{T-\Delta T}{7}}$$

where $P'(0)$ is the new radiation damage that the detector would need, to dissipate the same power $\mathscr{P}$ at a lower temperature T'. Therefore we can rescale the detectors power density increasing the radiation damage and at the same time lowering the
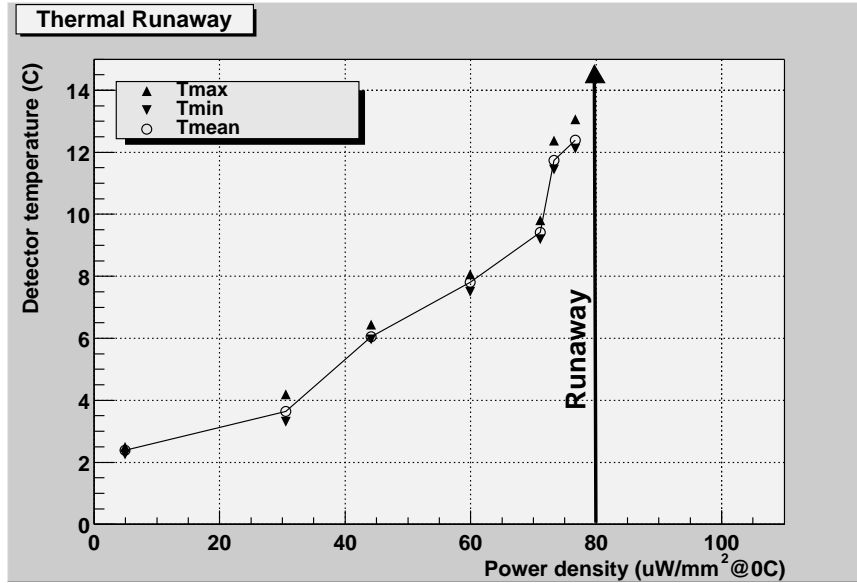
Figure 8.19: *Measured thermal runaway plot.*

detectors temperature. The new radiation damage can be written as:

$$P'(0) = P(0) \cdot 2^{\frac{\Delta T}{7}}$$

The run-away measurement has been performed at a coolant temperature of -5°C , and the run-away appeared at about $80\mu W/\text{mm}^2$ at 0°C . With the previous formulas we can estimate the measured power densities to different coolant temperatures. Figure 8.20 shows the measured run-away plot and the rescaled values at a coolant temperature of -22°C . The run-away point is well above the thermal run-away specification value.

The other thermal specification required for the SCT modules, demands the detector temperatures, at a power density of $185\mu W/\text{mm}^2$ at 0°C , to be below -7°C . The plot in figure 8.20 shows that the detectors temperature is at about -12°C when the power density is $185\mu W/\text{mm}^2$ at 0°C . This value however does not take into account the heat load coming from the environment that has been intentionally made negligible during the measurements. To estimate the expected detectors temperature with the environment heat load we refer to the analysis made in [101]. It is estimated that the thermal resistance of the detectors thermal path in the inner module configuration (defined as the detectors temperature increase per watt injected) is 4.5 K/W. So expecting an heat load of 0.4 W on the module we should expect an increase of about 2 °C . The expected temperature at $185\mu W/\text{mm}^2$ at 0°C is expected to be at about -8 °C , well within specifications.
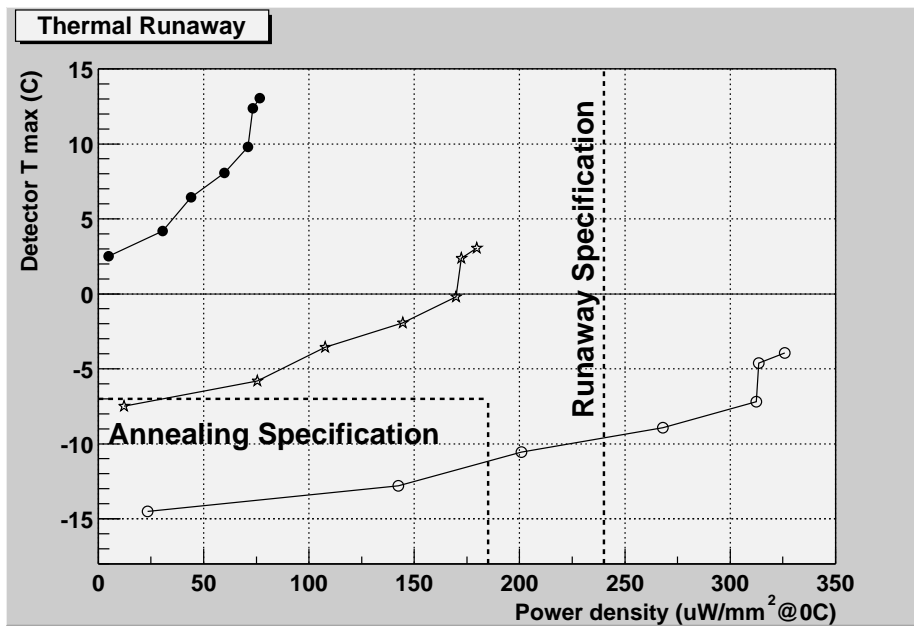
Figure 8.20: *Rescaled thermal runaway plot to different coolant temperatures: black dots (measured) Tcool=-5°C , stars Tcool =-15°C , white dots Tcool=-22°C*

8.4 Conclusions

Two module designs for the SCT end-caps have been validated; the baseline layout developed on the K5 hybrid and the backup layout (KB) developed on the barrel hybrid.

Both layouts have been produced in small prototype series and showed satisfactory electrical performance. However after irradiation, they both showed electrical noise outside specifications. For the K5 module it has been necessary to increase the discriminator threshold to 1.2 fC to fulfill the electrical noise specification. The irradiated KB module, on the other hand, was affected by large common mode noise caused by a non optimal grounding scheme of the setup. Once the common mode contribution to the noise was subtracted, the module performed within specification at the nominal threshold of 1.0 fC.

For the K5 module it has been possible to study the effect of the higher threshold on the single track efficiency in a test beam. We found that the irradiated K5 module performs within noise and hit efficiency specifications, in a narrow window around the discriminator threshold of 1.2 fC.

The KB and K5 thermal designs has been described. The design of the KB module, even using a single cooling point instead of the two used by the K5 module, showed thermal performance equivalent to the K5 ones.

Though an higher number of modules, irradiated at different fluences, would have been beneficial in the analysis of both electrical and thermal performance, the baseline K5 design, has been chosen for the final module production.

Appendix A

Test of the lifetime extraction method

A.0.1   Test of the method on Monte Carlo simulations

The proposed Monte Carlo based method has been developed to measure lifetimes in fully hadronic B decays, sculpted by the trigger and analysis cuts, and it has been first applied on $B \rightarrow D\pi$ decays. In this section we report the tests used to challenge the method on the $B_s \rightarrow D_s^- \pi^+$ mode.

The first test has been performed on Monte Carlo simulations, to check that the fitted lifetime is indeed compatible with the input value used to generate the Monte Carlo sample. We extracted the efficiency curve from a statistically independent Monte Carlo sample, and we developed an unbinned maximum likelihood fit on the proper decay time ct and the event by event σ_{ct} uncertainty. The results of the fit are reported in table A.1 and the fit projections are plotted in figure A.1.

Variable	$B_s \rightarrow D_s^- \pi^+$	Units
Generated Value	438	μm
Fitted Value	438.3 ± 3.2	μm
Sample Size	30000	events

Table A.1: *Results of the unbinned maximum likelihood fit on a high statistics Monte Carlo sample*
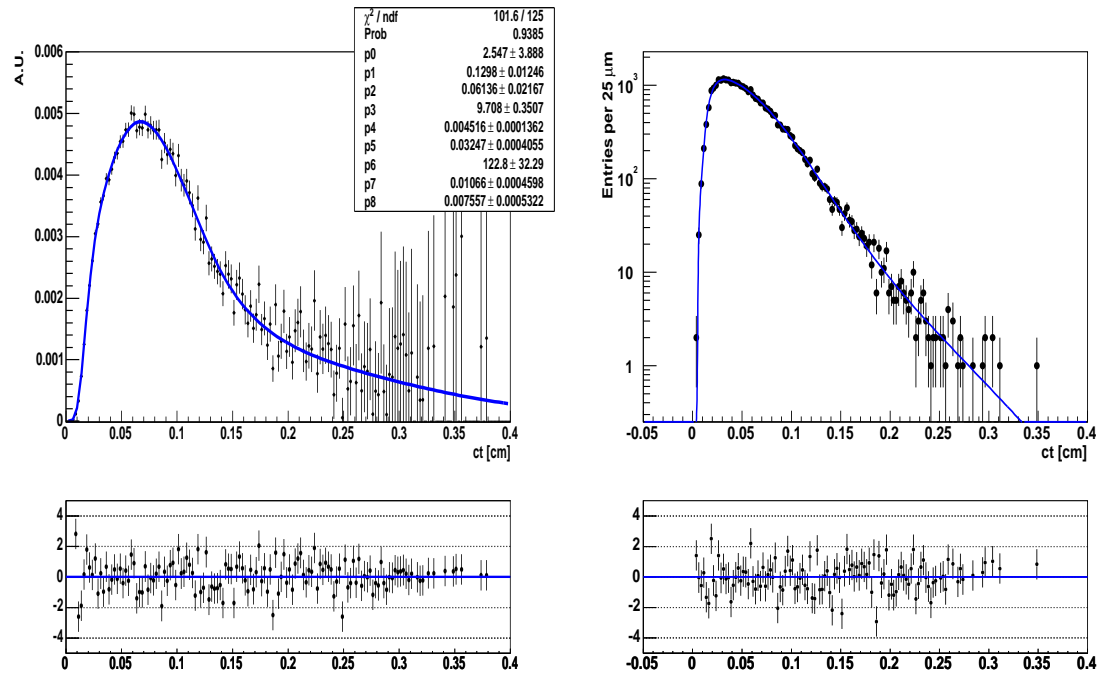
Figure A.1: *Monte Carlo simulations: (left) efficiency functions derived for the $B_s \rightarrow D_s^- \pi^+$ mode; (right) fit projection for the Monte Carlo signal only sample.*

The second test verifies the independence of the efficiency curves from the input lifetime of the Monte Carlo used to calculate it. This will allow to fit the lifetimes of different decays (having the same topology and kinematics, as $B_d \rightarrow D\pi$ and $B_s \rightarrow D_s\pi$ or $B_d \rightarrow \pi\pi$ and $B_s \rightarrow KK$) with the same efficiency curve, independently of the specific input lifetime of the Monte Carlo sample used to calculate it. To perform this test we generated several Monte Carlo samples differing only in the input lifetime. We then fitted the lifetime always using the same efficiency function calculated on the Monte Carlo produced with the input lifetime of $438\mu m$. Figure A.2 shows that the fitted lifetime are within the statistical error in good agreement with the lifetimes used as input to generate the sample, confirming that the efficiency function works on a broad range of lifetimes values.
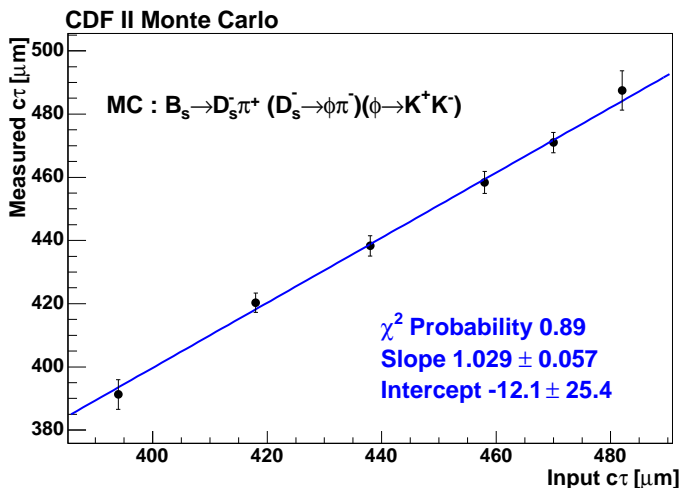
Figure A.2: *Correlation between the generated and fitted lifetimes values always using the efficiency function calculated on the Monte Carlo sample produced with a lifetime of* 438 μm .

A.0.2   Test of the method on an unbiased data sample

We performed a test of the proposed method on the high statistics $B^{\pm} \rightarrow J/\psi K^{\pm}$ sample, collected by a di-muon trigger, hence not affected by the sculpting effects of the TTT. Selecting a posteriori a sub-sample of events that pass the TTT requirements, it is possible to compare the lifetime measured before and after the TTT. The events selected for this test passed the list of cuts reported in table A.2.

An unbinned maximum likelihood fit has been performed using the mass and proper decay time information. The likelihood we used on the events before applying

Description	Cut Value
Muon Quality	≥ 3 axial SL with ≥ 5 hits in each
Muon Quality(CMU only)	$\chi^2_{CMU}(\mu^{\pm}) < 9.0$
Muon Quality	$p_T(\mu^{\pm}) > 1.5 \ GeV/c$
J/ψ mass window	$|m(\mu^+\mu^-) - M^{J/\psi}_{PDG}| < 80 \ MeV/c^2$
B Quality	$p_T^B > 5.5 \ GeV/c$
B Quality	$p_T^K > 1.6 \ GeV/c$
B Quality	$Prob(\chi^2) > 10^{-3}$

Table A.2: *Analysis cut applied to select the $B^{\pm} \to J/\psi K^{\pm}$ decay mode.*

the TTT is:

$$\mathcal{L}(m; \sigma_m; ct; \sigma_{ct}) = f_{sig}\mathcal{L}_{sig}(m; \sigma_m; ct; \sigma_{ct}) + (1 - f_{sig}) \cdot \mathcal{L}_{bkg}(m; \sigma_m; ct; \sigma_{ct})$$

where

$$\mathcal{L}_{sig}(m, \sigma_m, ct; \sigma_{ct}) = G(m; M; S_\mu \cdot \sigma_m) \cdot \mathcal{L}_{time}(ct; c\tau; S_{ct} \cdot \sigma_{ct})$$

$$\mathcal{L}_{bkg}(m; \sigma_m; ct; \sigma_{ct}) = \mathcal{M}_{bkg}(m; A) \cdot \mathcal{L}_{time}(ct; S_{ct} \cdot \sigma_{ct}; \lambda_-; \lambda_+; \lambda_{++})$$

In the signal part of the likelihood, G is a gaussian describing the mass peak and $\mathcal{L}_{time}$ is an exponential convoluted with a gaussian resolution function describing the proper decay time distribution. In the background term $\mathcal{M}_{bkg}(m; A)$ is a first order polynomial with slope A describing the mass distribution, while $\mathcal{T}_{bkg}$ is the sum of gaussian resolution function to describe the prompt J/ψ contribution, an exponential with negative lifetime λ_- for the misreconstructed events and two exponentials with positive lifetimes λ_+, λ_++ for the long-lived background. Two scale factors S_μ and S_{ct} have been used and left floating in the fit to properly take into account possible discrepancy in the mass and proper decay time resolutions. The fit results are reported in table A.3 and the fit projections are reported in figure A.3.

In order to simulate the TTT trigger, we selected a subsample of events requiring the events to pass the TTT trigger selection. Again we performed an unbinned maximum likelihood fit to extract the lifetime using the same likelihood function but changing the signal proper decay time pdf to:

$$T^{TTT}_{sig}(ct) = \frac{1}{c\tau}e^{-\frac{ct}{c\tau}} \otimes G(ct, 0, \sigma_{ct}) \cdot \epsilon(ct)$$
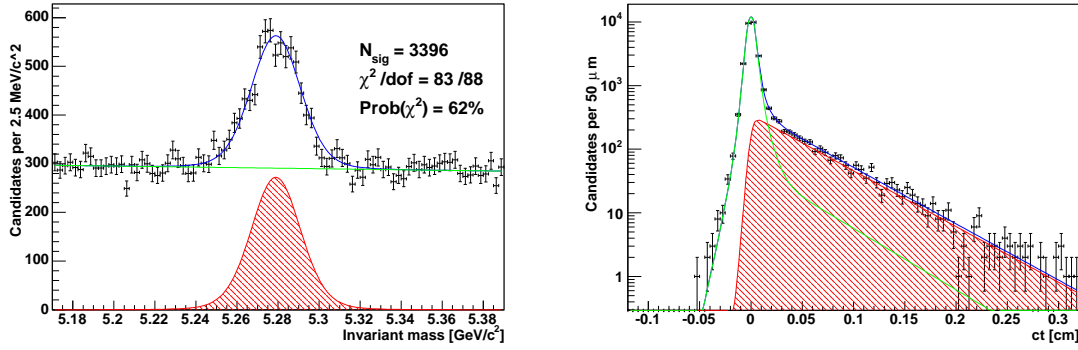
Figure A.3: *Projections on the mass and proper decay time variables of the unbinned maximum likelihood fit, performed on the di-muons triggered sample*

and the background one to :

$$T_{bkg}^{TTT} = \frac{1}{c\tau} e^{-\frac{ct}{c\tau_{bgk}}} \otimes G(ct, \mu_{bkg}, \sigma_{bkg})$$

Since the prompt J/ψ component is removed by the TTT trigger the scaling factor on the proper decay time resolution has been kept fixed to the value obtained in the previous fit. The fit results are reported in table A.3 and the fit projections are plotted in figure A.4.
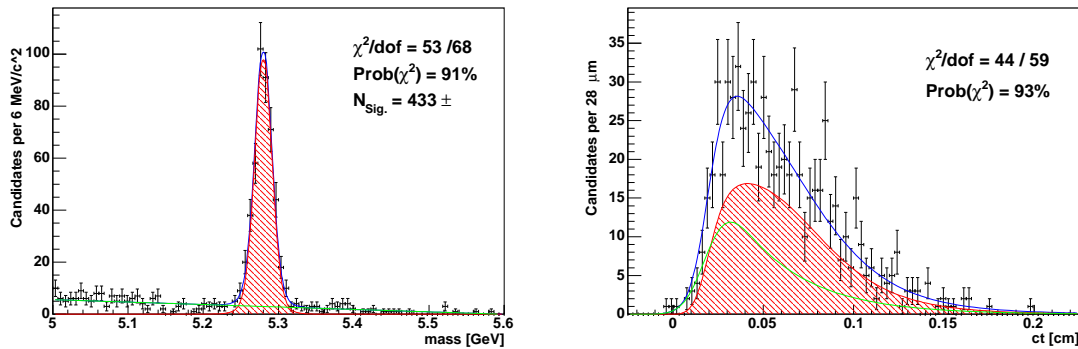
Figure A.4: *Projections on the mass and proper decay time variables of the unbinned maximum likelihood fit, performed on the TTT triggered sub-sample*

The lifetime value fitted on the sample triggered by the di-muon trigger and the one fitter on the sub-sample passing the TTT requirements are agreeing within

statistics (and with the world average).

This test provide also another piece of information on the developed fitting method. We observe that the statistical error on the lifetime does not scale with the root square of the number of events when passing from the di-muon to the TTT triggered sample. This because of the reduction in statistical power due to the smaller proper decay time window [61].

Another test that we can perform with this sample is comparing the efficiency curve calculated on Monte Carlo with the lower statistics one extracted from the sample itself. The two curves are overlaid in figure A.5 and a χ^2 test gives a probability of 52%, revealing a good agreement between the two distributions.
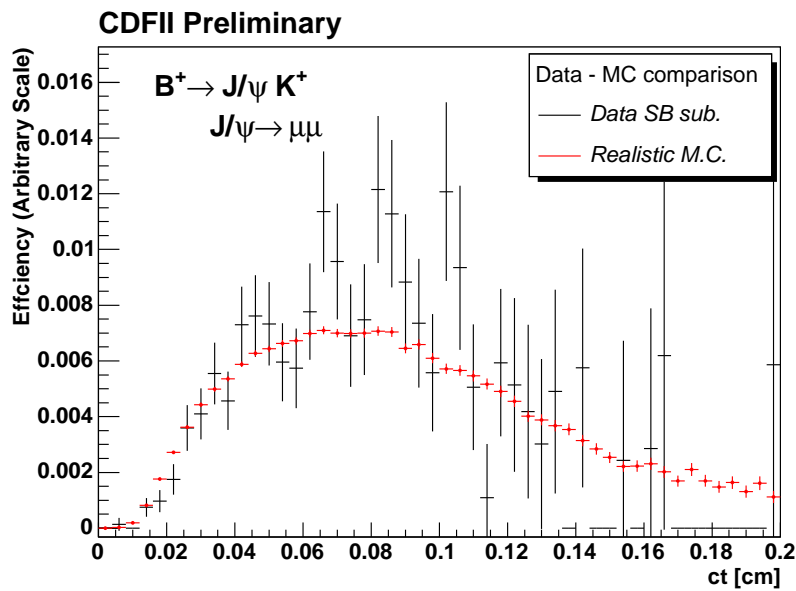
Figure A.5: *Efficiency curves calculated on Monte Carlo simulations and on $B^{\pm} \rightarrow J/\psi K^{\pm}$ sample*

Param.	Di-muon Trigger	TTT	Units
M	5278.93 ± 0.26	5279.80 ± 0.63	MeV/c^2
S_μ	1.556 ± 0.028	1.544 ± 0.028	
f_{sig}	0.1171 ± 0.0023	0.639 ± 0.021	
A	-0.85 ± 0.45	-5.64 ± 0.19	$(GeV/c^2)^{-1}$
$c\tau$	495.1 ± 9.7	523.4 ± 40.6	μm
S_{ct}	1.313 ± 0.011	1.313 FIXED	
N_{sig}	3396 ± 67	432 ± 14	
Background parameters (Dimuon Trigger)			
f_-	0.0341 ± 0.0062	-	
f_+	0.0099 ± 0.0078	-	
f_{++}	0.0183 ± 0.0022	-	
λ_-	55 ± 5	-	μm
λ_+	61 ± 5	-	μm
λ_{++}	450 ± 41	-	μm
Background parameters (TTT)			
μ_{bkg}	-	190 ± 19	μm
σ_{bkg}	-	97 ± 15	μm
$c\tau_{bkg}$	-	363 ± 32	μm

Table A.3: *Results of the unbinned maximum likelihood fit on the mass and proper decay time variables, performed on the di-muons triggered sample*

Appendix B

Templates

In this chapter we collect the $P(\alpha, p)$ templates for signal and background.

B.1   Signal

The $P(\alpha, p)$ distribution is taken for each of the four main $B^0 \to h^\pm h'^\mp$ decays from Monte Carlo simulations and fitted simultaneously in α and p with the following functional form:

$$P(\alpha, p) = \frac{1}{norm} e^{a_5\, p} \sum_{i=0}^{4} (a_i, p_i) \sum_{j=0}^{6} b_j \left(\alpha\, \frac{p-2}{p-4} \right)^{j}$$

where a_i, b_j coefficients depends on the specific decay mode.

- $B_d \rightarrow K^+\pi^-$

Parameter	value	Parameter	value
a_0	$-1.758 \cdot 10^{10}$	b_0	$6.848 \cdot 10^7$
a_1	$4.737 \cdot 10^9$	b_1	$1.777 \cdot 10^6$
a_2	$-3.591 \cdot 10^8$	b_2	$8.245 \cdot 10^7$
a_3	$9.533 \cdot 10^6$	b_3	$-1.158 \cdot 10^7$
a_4	221.183	b_4	$-1.303 \cdot 10^8$
a_5	-0.433	b_5	$1.111 \cdot 10^7$
		b_6	$-1.437 \cdot 10^7$

Monte Carlo
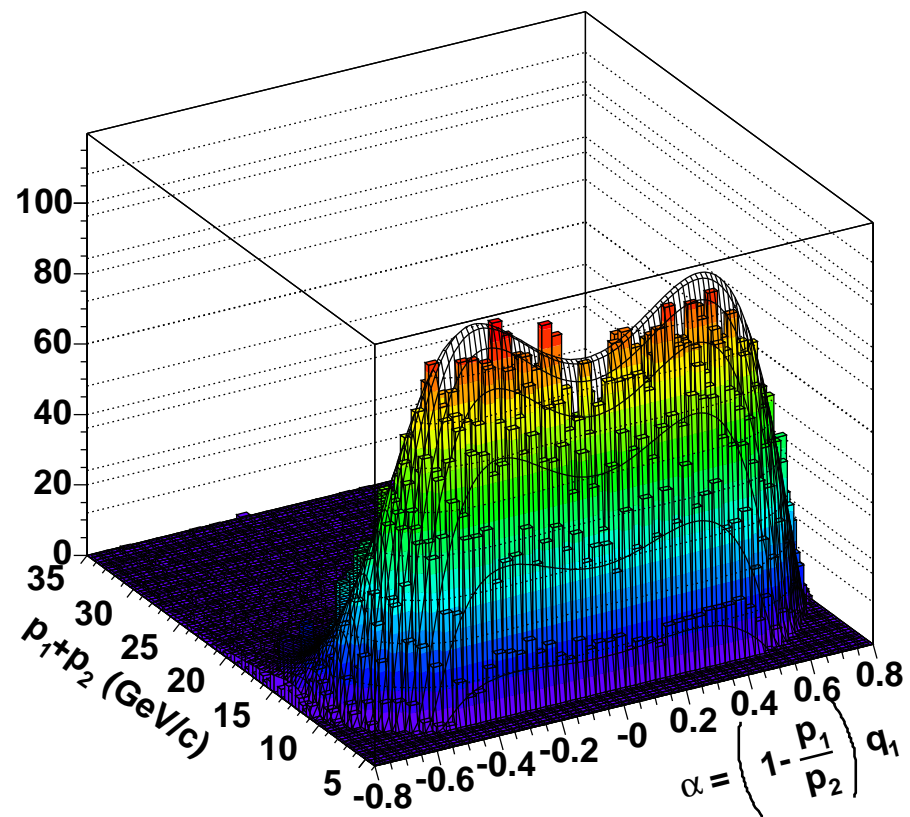
Figure B.1: $(\alpha, P(\pi_1) + P(\pi_2))$ distribution for the $B_d \rightarrow K^+\pi^-$ decay

Monte Carlo

Entries / 0.02

$$\alpha = \left(1 - \frac{p_1}{p_2}\right) q_1$$
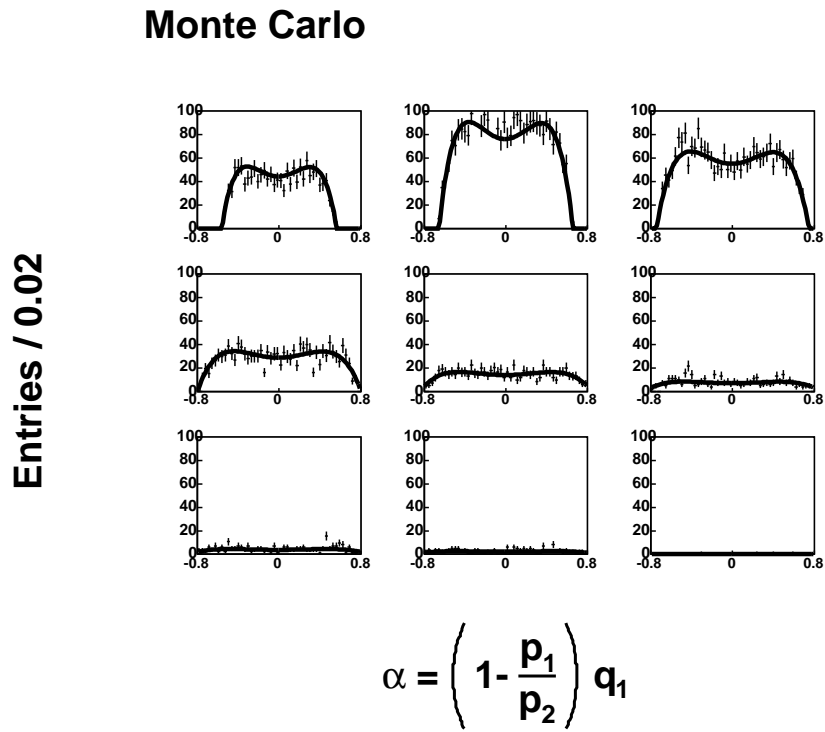
Figure B.2: $P(\pi_1) + P(\pi_2)$ sections of the $(\alpha, P(\pi_1) + P(\pi_2))$ distribution for the $B_d \to K^+\pi^-$ decay. The sections are taken at regular intervals of 0.096 in the range [-0.8,0.8]
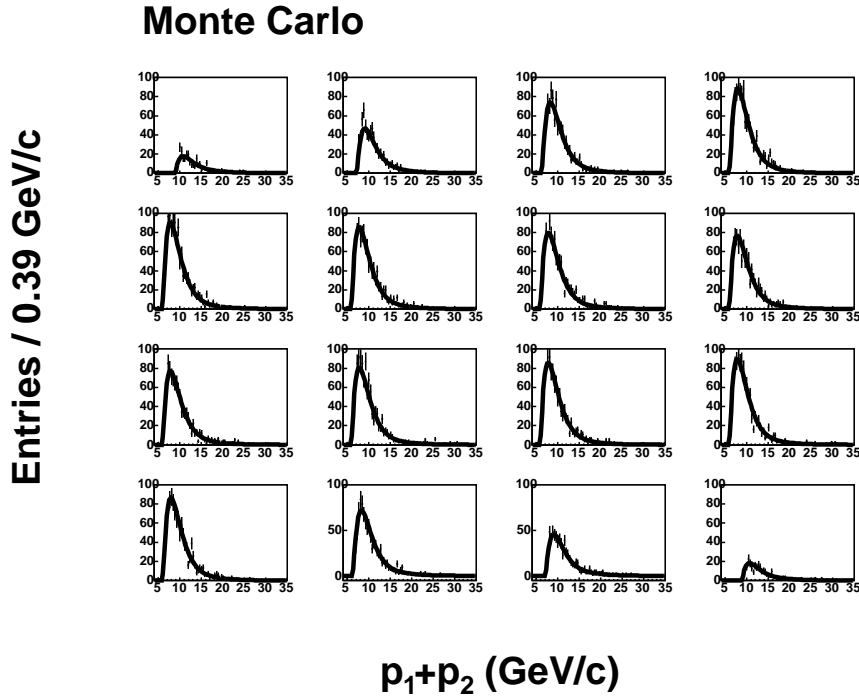
Figure B.3: α sections of the $(\alpha, P(\pi_1) + P(\pi_2))$ distribution distribution for the $B_d \to K^+\pi^-$ decay. The sections are taken at regular intervals of 1.94 GeV/c in the range [4.0,35.0] GeV/c

- $\bar{B}_d \to K^- \pi^+$

Parameter	value	Parameter	value
a_0	$-8.873 \cdot 10^7$	b_0	40.429
a_1	$2.384 \cdot 10^7$	b_1	0.190
a_2	$-1.802 \cdot 10^6$	b_2	48.488
a_3	48438.6	b_3	5.532
a_4	0.867	b_4	-79.440
a_5	-0.439	b_5	-4.912
		b_6	-4.720

Monte Carlo
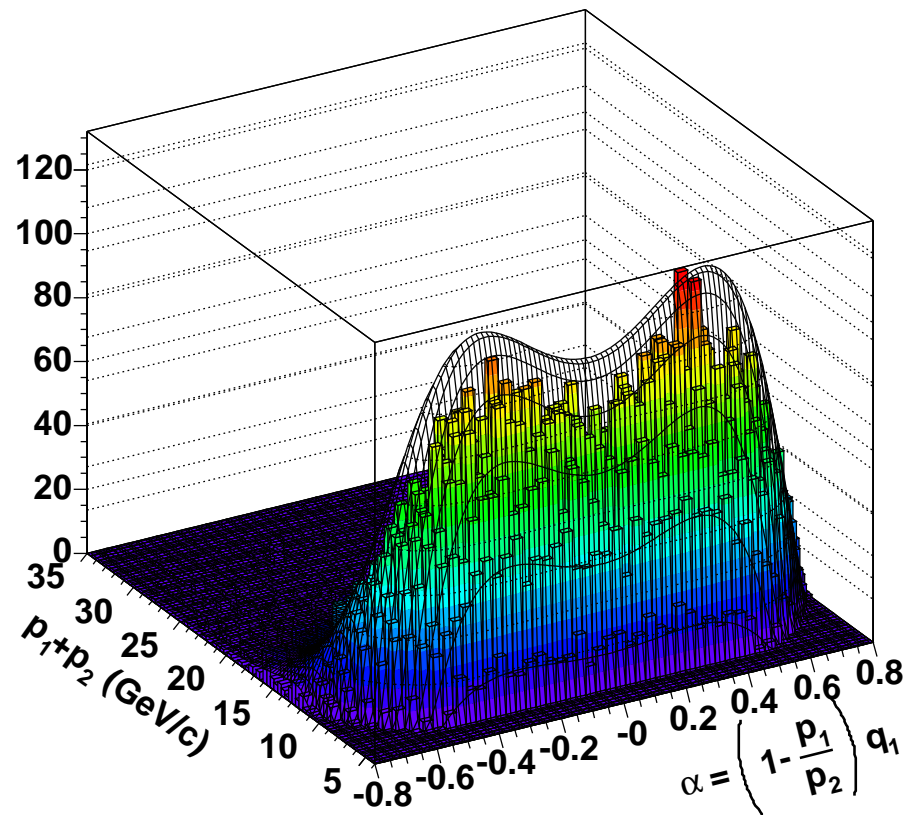
Figure B.4: $(\alpha, P(\pi_1) + P(\pi_2))$ *distribution for the* $\bar{B}_d \rightarrow K^- \pi^+$ *decay*

Monte Carlo


$$\alpha = \left(1 - \frac{p_1}{p_2} \right) q_1$$
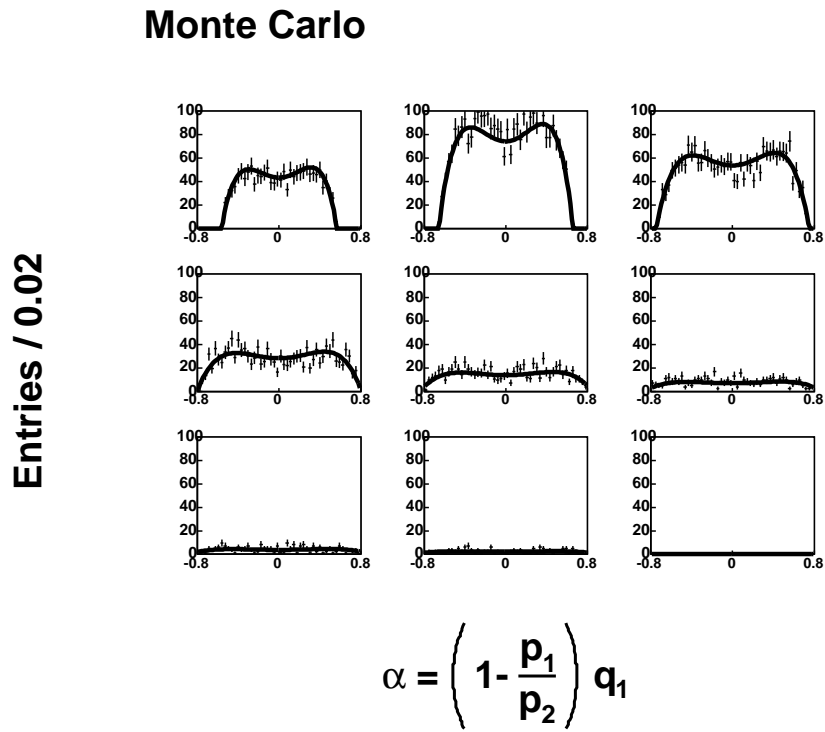
Figure B.5: $P(\pi_1) + P(\pi_2)$ sections of the $(\alpha, P(\pi_1) + P(\pi_2))$ distribution for the $\bar{B}_d \to K^- \pi^+$ decay. The sections are taken at regular intervals of 0.096 in the range [-0.8,0.8]

Monte Carlo
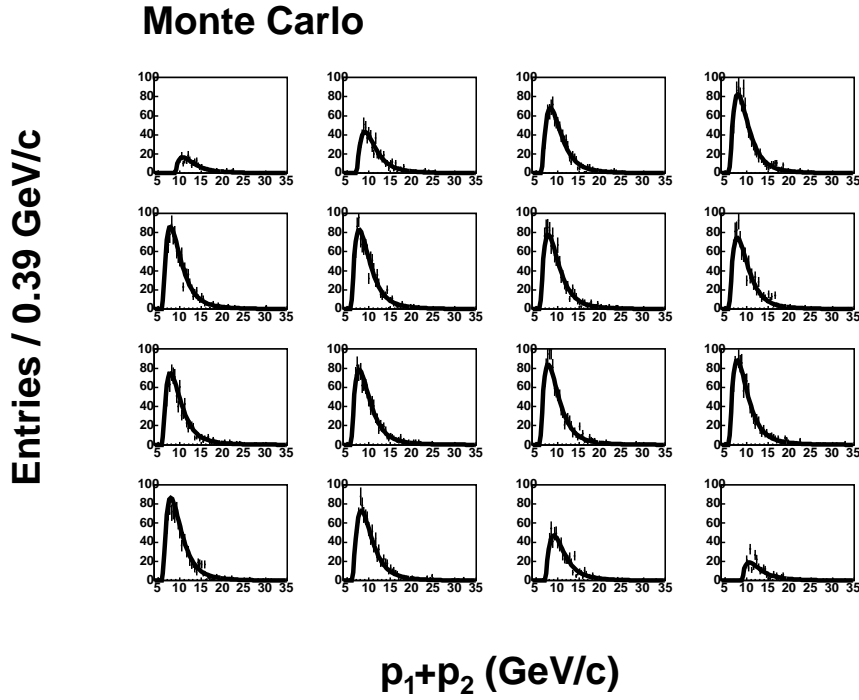
Figure B.6: α sections of the $(\alpha, P(\pi_1) + P(\pi_2))$ distribution distribution for the $\bar{B}_d \to K^- \pi^+$ decay. The sections are taken at regular intervals of 1.94 GeV/c in the range [4.0,35.0] GeV/c

- $B_d \rightarrow \pi^+\pi^-$

Parameter	value	Parameter	value
a_0	$-3.712 \cdot 10^9$	b_0	$1.828 \cdot 10^7$
a_1	$1.010 \cdot 10^9$	b_1	0
a_2	$-7.841 \cdot 10^7$	b_2	$2.223 \cdot 10^7$
a_3	$2.162 \cdot 10^6$	b_3	0
a_4	-0.387	b_4	$-3.583 \cdot 10^7$
a_5	-0.446	b_5	0
		b_6	$-2.466 \cdot 10^6$

Monte Carlo
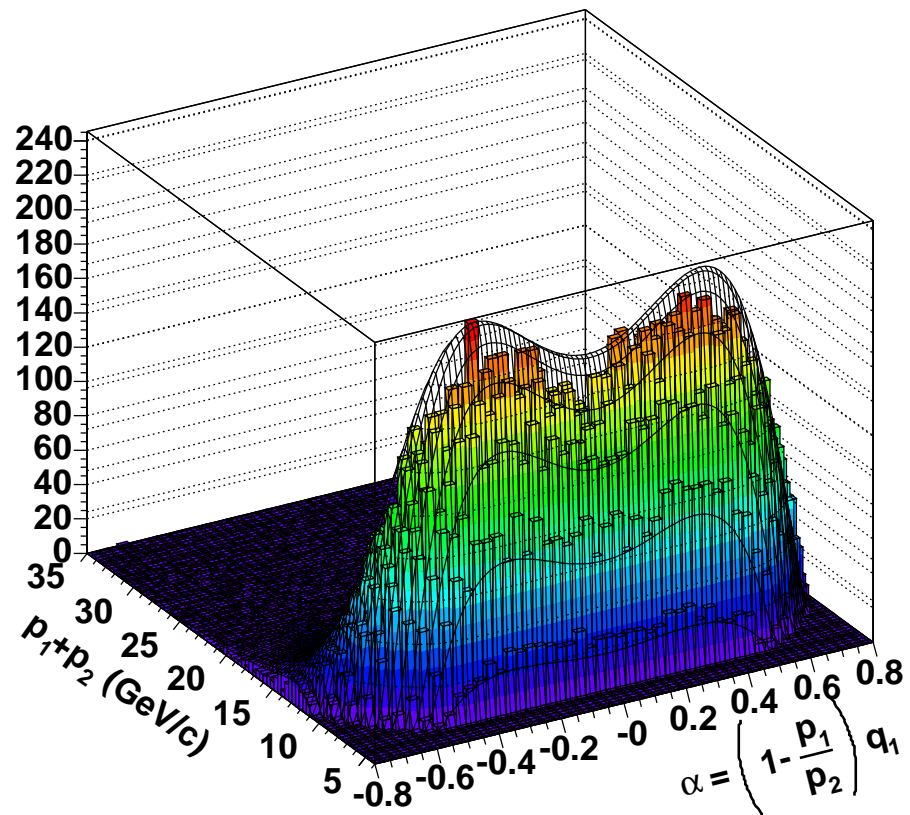
Figure B.7: $(\alpha, P(\pi_1) + P(\pi_2))$ *distribution for the* $B_d \to \pi^+\pi^-$ *decay*

**Monte Carlo**

$$\alpha = \left(1 - \frac{p_1}{p_2} \right) q_1$$
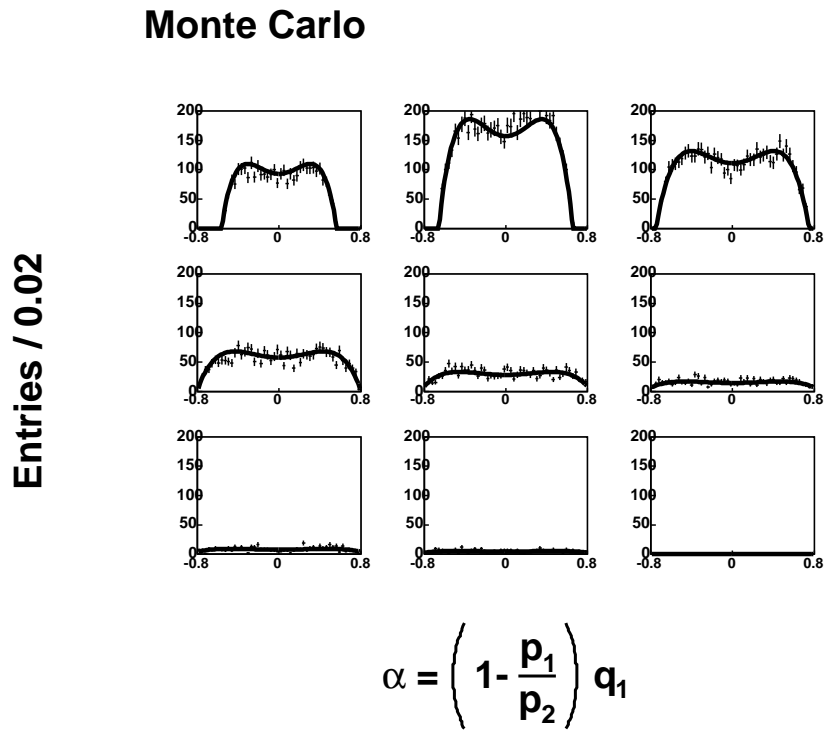
Figure B.8: $P(\pi_1) + P(\pi_2)$ sections of the $(\alpha, P(\pi_1) + P(\pi_2))$ distribution for the $B_d \to \pi^+\pi^-$ decay. The sections are taken at regular intervals of 0.096 in the range [-0.8,0.8]
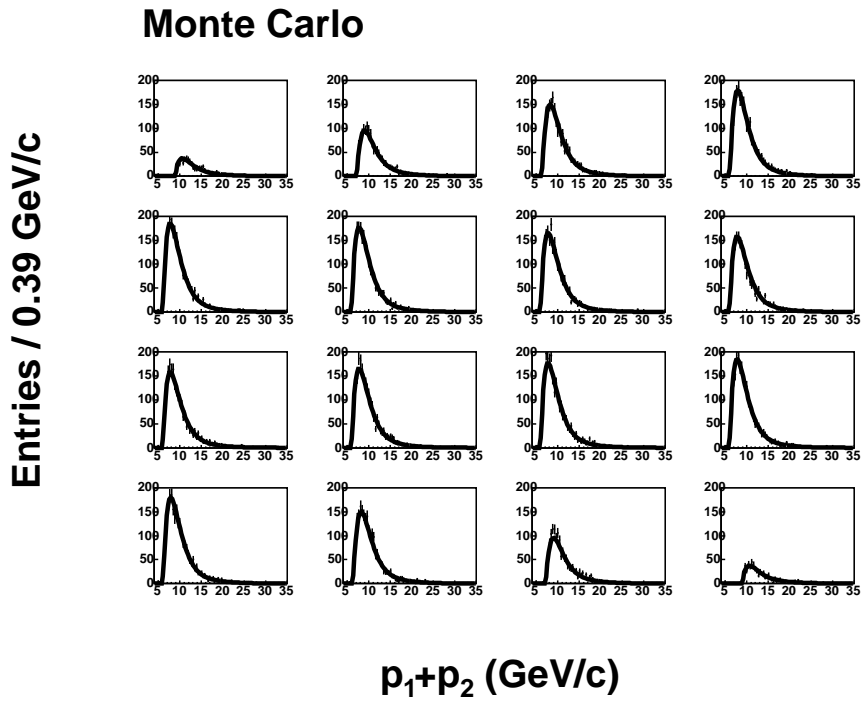
Figure B.9: α *sections of the* $(\alpha, P(\pi_1) + P(\pi_2))$ *distribution distribution for the* $B_d \rightarrow \pi^+\pi^-$ *decay. The sections are taken at regular intervals of 1.94 GeV/c in the range [4.0,35.0] GeV/c*

- $B_s \to K^+ K^-$

Parameter	value	Parameter	value
a_0	$-2.988 \cdot 10^9$	b_0	$2.973 \cdot 10^{-3}$
a_1	$8.037 \cdot 10^8$	b_1	0
a_2	$-6.111 \cdot 10^7$	b_2	$3.971 \cdot 10^{-3}$
a_3	$1.670 \cdot 10^6$	b_3	0
a_4	-23.808	b_4	$-6.945 \cdot 10^{-3}$
a_5	-0.438	b_5	0
		b_6	$3.338 \cdot 10^{-4}$
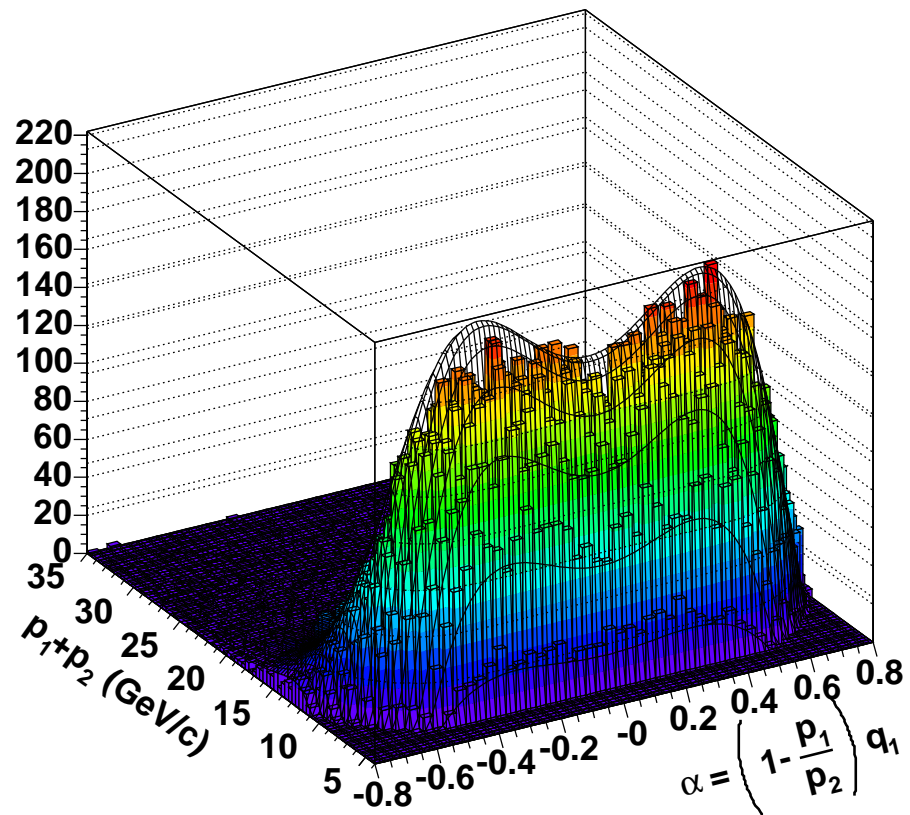
Figure B.10: $(\alpha, P(\pi_1) + P(\pi_2))$ distribution for the $B_s \rightarrow K^+ K^-$ decay

**Monte Carlo**

$$\alpha = \left(1 - \frac{p_1}{p_2}\right) q_1$$
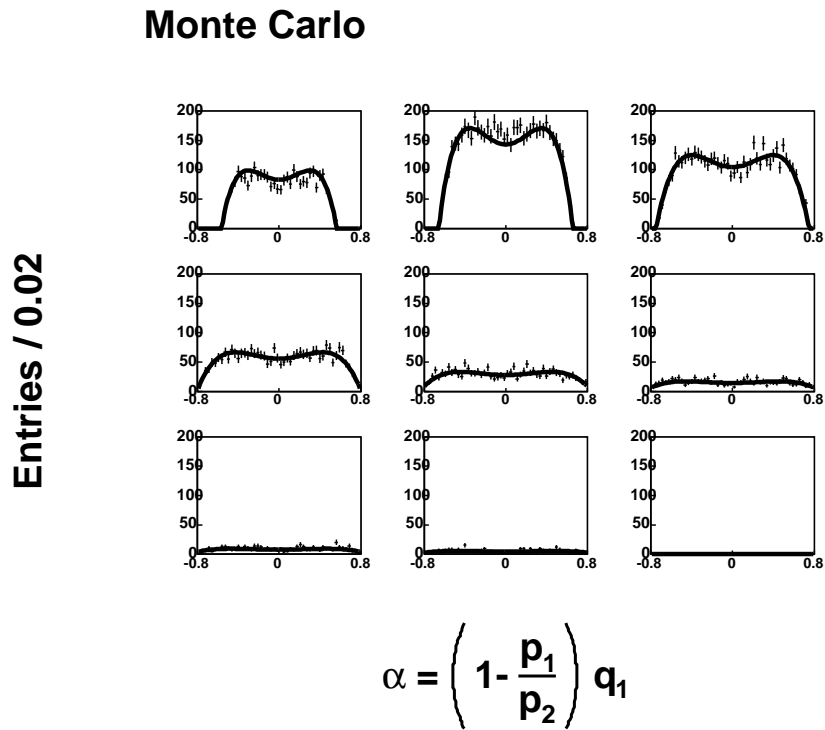
Figure B.11: $P(\pi_1) + P(\pi_2)$ *sections of the* $(\alpha, P(\pi_1) + P(\pi_2))$ *distribution for the* $B_s \to K^+ K^-$ *decay. The sections are taken at regular intervals of 0.096 in the range [-0.8,0.8]*

Figure B.12: α *sections of the* $(\alpha, P(\pi_1) + P(\pi_2))$ *distribution distribution for the* $B_s \rightarrow K^+ K^-$ *decay. The sections are taken at regular intervals of 1.94 GeV/c in the range [4.0,35.0] GeV/c*

- $B_s \rightarrow K^- \pi^+$
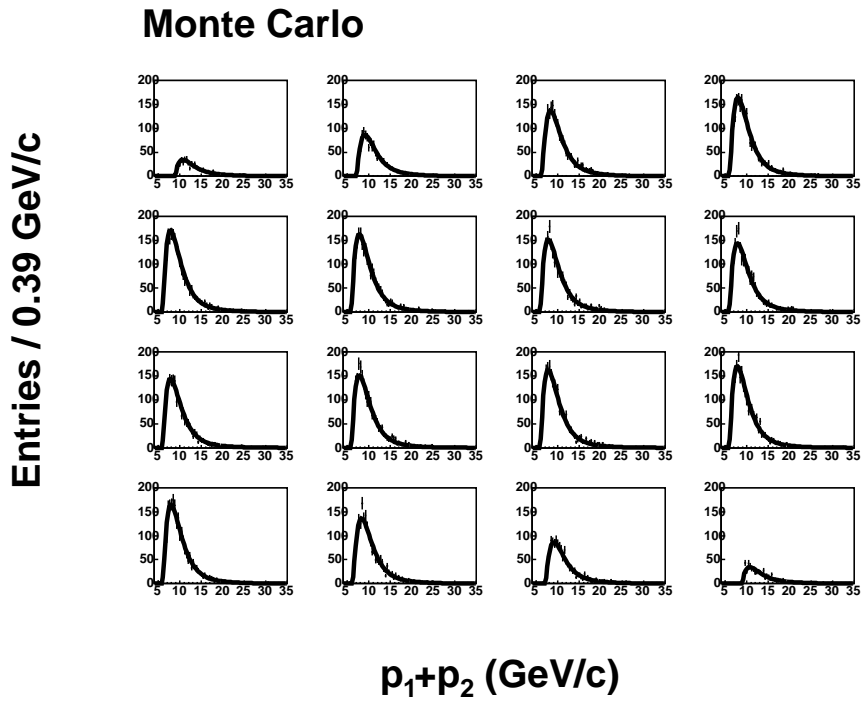
Parameter	value	Parameter	value
a_0	$-2.366 \cdot 10^{11}$	b_0	117240.0
a_1	$6.373 \cdot 10^{10}$	b_1	4649.44
a_2	$-4.857 \cdot 10^{9}$	b_2	129774
a_3	$1.323 \cdot 10^{8}$	b_3	10962.0
a_4	-1627.42	b_4	-191372.0
a_5	-0.4412	b_5	-12035.6
		b_6	-47005.5

Monte Carlo
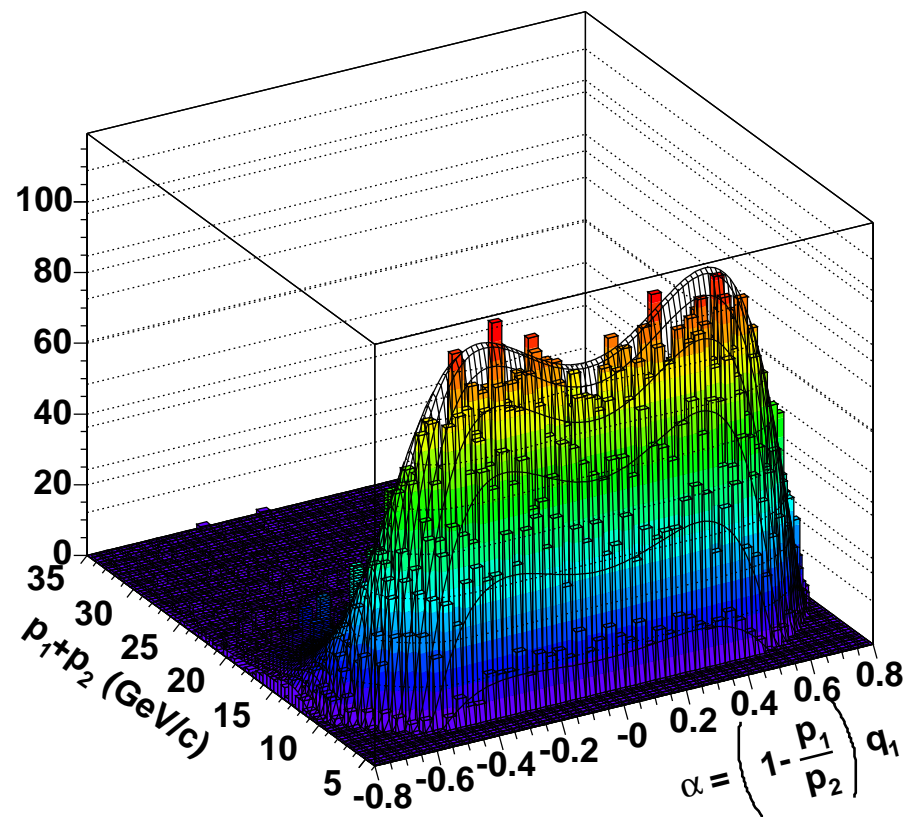
Figure B.13: $(\alpha, P(\pi_1) + P(\pi_2))$ distribution for the $B_s \to K^- \pi^+$ decay

Monte Carlo

$$\alpha = \left(1 - \frac{p_1}{p_2} \right) q_1$$
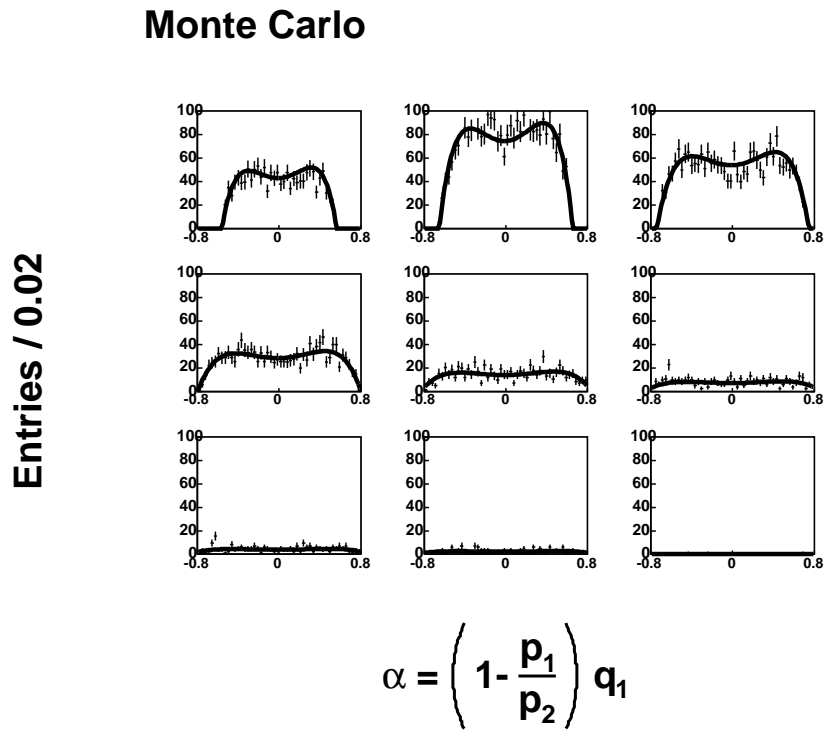
Figure B.14: $P(\pi_1) + P(\pi_2)$ sections of the $(\alpha, P(\pi_1) + P(\pi_2))$ distribution for the $B_s \to K^- \pi^+$ decay. The sections are taken at regular intervals of 0.096 in the range [-0.8,0.8]

Figure B.15: *α sections of the* $(\alpha, P(\pi_1) + P(\pi_2))$ *distribution distribution for the* $B_s \to K^- \pi^+$ *decay. The sections are taken at regular intervals of 1.94 GeV/c in the range [4.0,35.0] GeV/c*

- $\bar{B}_s \to K^+\pi^-$
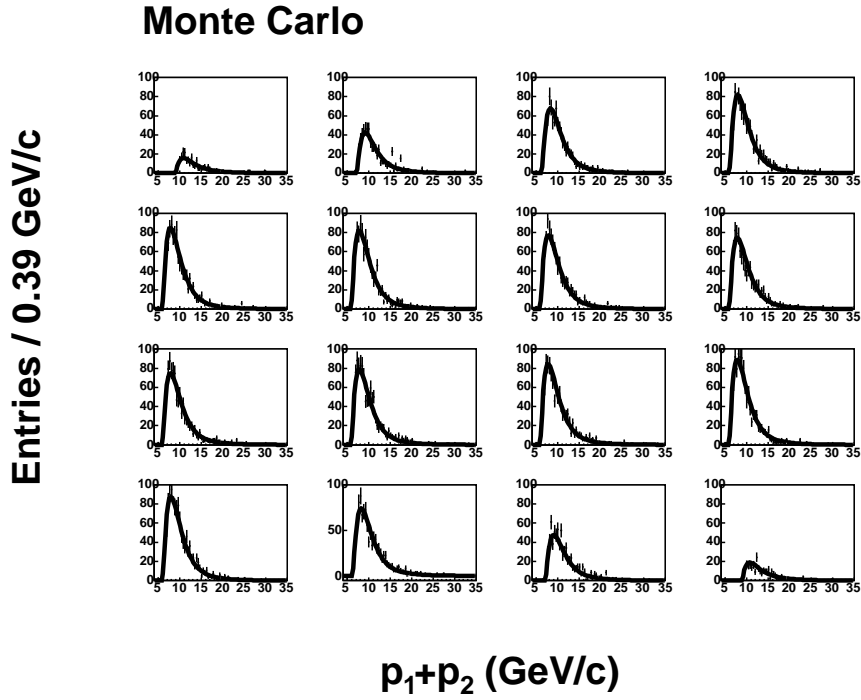
Parameter	value	Parameter	value
a_0	$-2.111 \cdot 10^{10}$	b_0	$1.799 \cdot 10^8$
a_1	$5.724 \cdot 10^9$	b_1	$-3.610 \cdot 10^6$
a_2	$-4.421 \cdot 10^8$	b_2	$2.329 \cdot 10^8$
a_3	$1.221 \cdot 10^7$	b_3	$7.758 \cdot 10^6$
a_4	-90.839	b_4	$-3.851 \cdot 10^8$
a_5	-0.443	b_5	$-3.382 \cdot 10^6$
		b_6	$-9.435 \cdot 10^6$
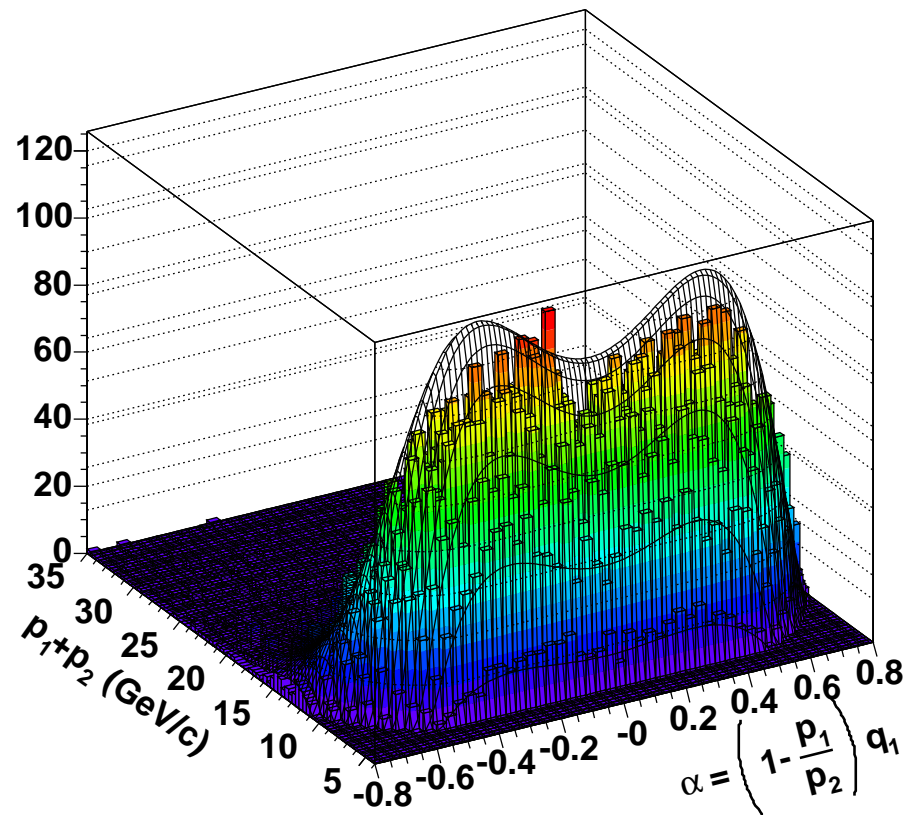
Figure B.16: $(\alpha, P(\pi_1) + P(\pi_2))$ distribution for the $\bar{B}_s \to K^+\pi^-$ decay

Monte Carlo

$$\alpha = \left(1 - \frac{p_1}{p_2} \right) q_1$$
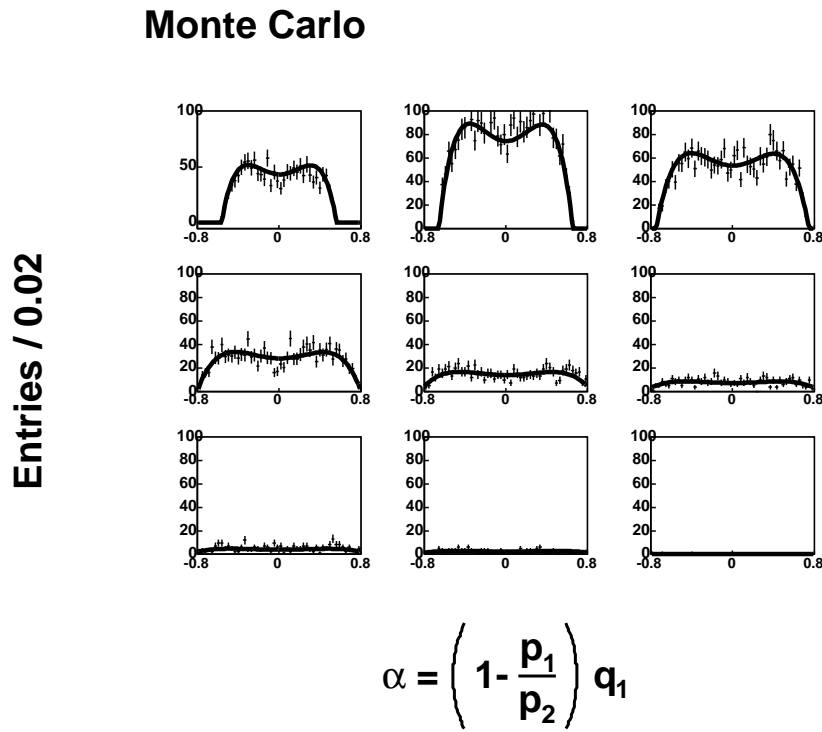
Figure B.17: $P(\pi_1) + P(\pi_2)$ *sections of the* $(\alpha, P(\pi_1) + P(\pi_2))$ *distribution for the* $\bar{B}_s \to K^+\pi^-$ *decay. The sections are taken at regular intervals of 0.096 in the range* *[-0.8,0.8]*
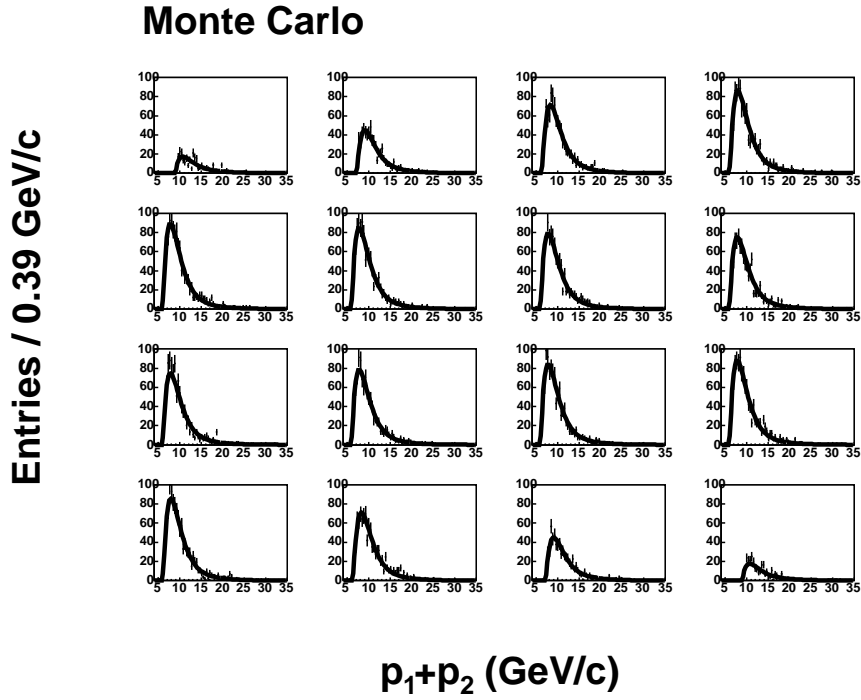
Figure B.18: α sections of the $(\alpha, P(\pi_1) + P(\pi_2))$ distribution distribution for the $\bar{B}_s \rightarrow K^+\pi^-$ decay. The sections are taken at regular intervals of 1.94 GeV/c in the range [4.0,35.0] GeV/c

B.2   Background

The $P'(\alpha, p)$ for the background is obtained fitting the bidimensional distribution of the variables (α, p) from data using the $B^0 \to h^\pm h'^\mp$ sidebands (chosen symmetrically around the $B^0 \to h^\pm h'^\mp$ mass peak at $[-7, -4]$ U $[+4, +7]$ standard deviations). The functional form used to fit the distribution is:

$$P'(\alpha, p) = \frac{1}{norm} \left[1 + \left(\frac{p - \lambda}{a} \right)^2 \right]^{-m} \exp \left[-\nu \tan^{-1} \left(\frac{p - \lambda}{a} \right) \right] \sum_{j=0}^{6} b_j \left(\alpha \, \frac{p - 2}{p - 4} \right)^j$$

- $\bar{B}_s \rightarrow K^+\pi^-$

Parameter	value	Parameter	value
$\lambda_b g$	5.233	b_0	$2.807\cdot10^{-2}$
$a_b g$	-0.405	b_1	0
$m_b g$	2.090	b_2	$5.165\cdot10^{-2}$
$\nu_b g$	20.749	b_3	0
		b_4	$-7.587\cdot10^{-2}$
		b_5	0
		b_6	$-2.148\cdot10^{-3}$
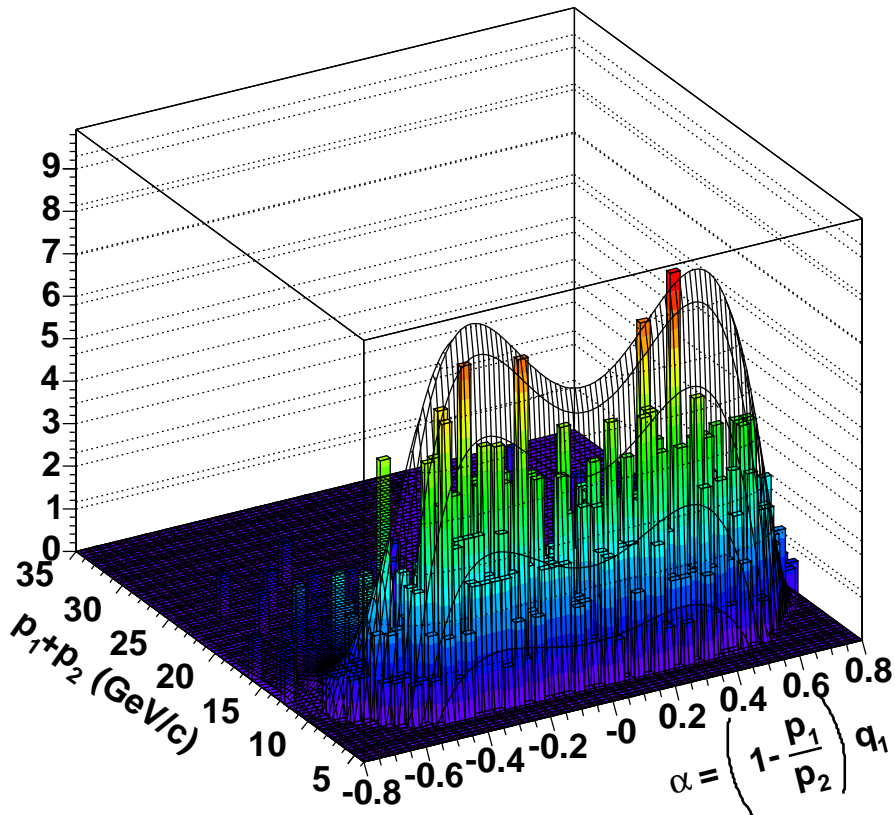
Figure B.19: $(\alpha, P(\pi_1) + P(\pi_2))$ *distribution for the background*
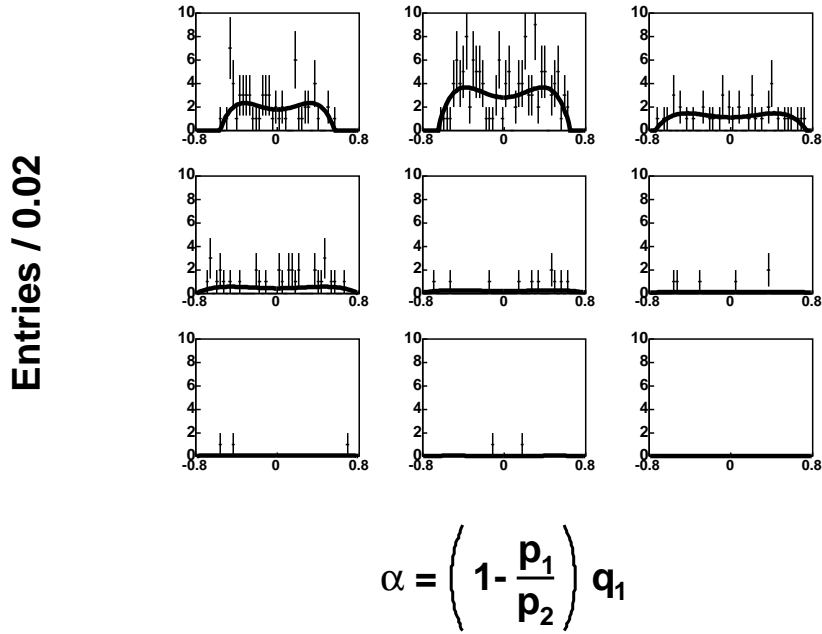
Figure B.20: $P(\pi_1) + P(\pi_2)$ *sections of the* $(\alpha, P(\pi_1) + P(\pi_2))$ *distribution for the background. The sections are taken at regular intervals of 0.096 in the range [-0.8,0.8]*
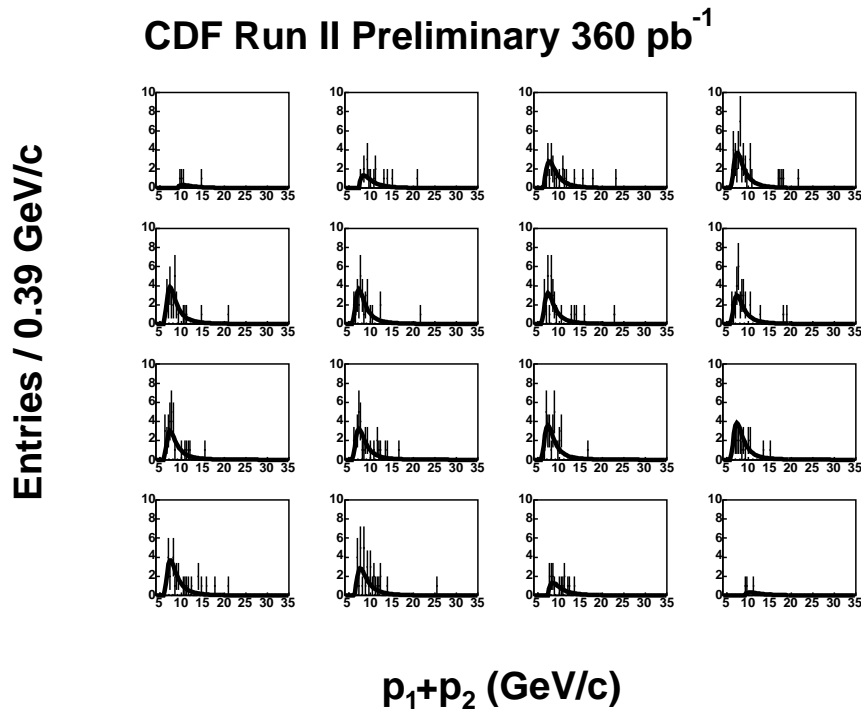
Figure B.21: α sections of the $(\alpha, P(\pi_1) + P(\pi_2))$ distribution distribution for the background. The sections are taken at regular intervals of 1.94 in the range [4.0,25.0] GeV/c GeV/c

Bibliography

[1] The LEP collaborations ALEPH, DELPHI, L3, OPAL, and the LEP Electroweak Working Group
   A Combination of Preliminary Electroweak Measurements and Constraints on the Standard Model
   http://arxiv.org/abs/hep-ph/0511027

[2] C. Quigg
   Beyond the standard model in many directions
   Lectures given at 2nd Latin American School of High-Energy Physics, San Miguel Regla, Mexico
   http://arxiv.org/abs/hep-ph/0404228

[3] C. Quigg
   Gauge Theories of the Strong, Weak and Electromagnetic Interactions,
   Benjamin-Cummings, Reading MA. (1983)

[4] P. Higgs
   Broken symmetries and the masses of gauge bosons
   Phys. Rev. Lett. 13, 508-509 (1964) P. Higgs
   Spontaneus symmetry breakdown without massless bosons
   Phys. Rev. 145, 1156-1163 (1966)

[5] M. Kobayashi and T. Maskawa
   CP violation i nthe renormalizable theory of weak interactions
   Progr. Theor. Phys. 49, 652-657 (1973)

[6] S. Glashow, J. Iliopoulos, L. Maiani
   Weak interactions with lepton-hadron symmetry
   Phys. Rev. D@ 1285-1292 (1970)

[7] C. Jarlskog.
   Commutator of the quark mass matrices in the standard electroweak

model and a measure of maximal CP non conservation
Phys. Rev. Lett. 55 1039-1042 (1985)

[8] S. Eidelman *et al.*
Particle Data Book
Phys. Lett. B 592, 1 (2004)

[9] L. Wolfenstein
Parametrization of the Kobayashi-Maskawa Matrix
Phys. Rev. Lett. 51 1945-1947 (1983)

[10] The BaBar collaboration
http://www-public.slac.stanford.edu/babar/

[11] The Belle collaboration
http://belle.kek.jp/

[12] The CDF collaboration
http://www-cdf.fnal.gov/

[13] The D0 collaboration
http://www-d0.fnal.gov/

[14] The UTfit Collaboration (M. Bona *et al.*)
The UTfit Collaboration Report on the Unitarity Triangle beyond the Standard Model: Spring 2006
http://arxiv.org/abs/hep-ph/hep-ph/0605213
http://utfit.roma1.infn.it/

[15] The CKMfitter Group (J. Charles et al.)
Eur. Phys. J. C41, 1-131 (2005)
http://ckmfitter.in2p3.fr

[16] M. Ciuchini, E. Franco, V. Lubicz, F. Mescia, C. Tarantino
Lifetime differences and CP violation parameters of neutral B-mesons at the next-to-leading order in QCD
JHEP - Journal of High Energy Physics 0308:031 (2003)

[17] Y. Grossman, Y. Nir and G. Raz
Constraning the Phase of $B_s - \bar{B}_s$ Mixing
http://arxiv.org/abs/hep-ph/0605028

[18] R. Fleischer
Flavour Physics and CP Violation
http://arxiv.org/abs/hep-ph/0405091

[19] K. Anikeev *at. al*
B Physics at the Tevatron: Run II and Beyond
http://arxiv.org/abs/hep-ph/0201971

[20] **Heavy Flavor Averaging Group (HFAG)**
http://www.slac.stanford.edu/xorg/hfag
http://arxiv.org/abs/hep-ex/0603003

[21] M. Beneke, G. Buchalla, A. Lenz and U. Nierste
CP asymmetries in flavor specific B decays beyond the leading logarithms
Phys. Lett. B576 173-183 (2003)

[22] The BaBar Collaboration
Limits on the lifetime difference of neutral B-mesons and on CP, T and CPT violation in $B^0 - \bar{B}^0 mixing$
SLAC-PUB-9696 (2003)

[23] The CDF Collaboration
Measurement of the $B_s - \bar{B}_s$ Oscillation Frequency
http://www-cdf.fnal.gov/physics/new/bottom/060406.blessed-Bsmix/

[24] The D0 Collaboration
Direct Limits on the B_s^0 Oscillation Frequency
http://arxiv.org/abs/hep-ph/0603029

[25] I. Dunietz, R. Fleischer and U. Nierste
In Pursuit of New Physics with B_s Decays
http://arxiv.org/abs/hep-ph/0012219

[26] Y. Grossman
The B_s width difference beyond the Standard Model
http://arxiv.org/abs/hep-ph/9603244

[27] Fermilab Beams Division
Run II Handbook
http://www-bdnew.fnal.gov/pbar/run2b/Documents/RunII_handbook.pdf

[28] Fermilab Beams Division
Linac Rookie Book
http://www-bdnew.fnal.gov/operations/rookie_books/Linac_PDF/Linac.html

[29] Fermilab Beams Division
Booster Rookie Book
http://www-bdnew.fnal.gov/operations/rookie_books/Booster_PDF/Booster_TOC.html

[30] Fermilab Beams Division
Main Injector Rookie Book
http://www-bdnew.fnal.gov/operations/rookie_books/Main_Injector_PDF/Main_Injector.html

[31] Fermilab Beams Division
Antiproton Source Rookie Book
http://www-bdnew.fnal.gov/operations/rookie_books/Pbar_PDF/Pbar.html

[32] Fermilab Beams Division
Recycler Design Report
FERMILAB-TM-1991
http://lss.fnal.gov/archive/test-tm/1000/fermilab-tm-1991.shtml

[33] Fermilab Beams Division
Tevatron Rookie Book
http://www-bdnew.fnal.gov/operations/rookie_books/Tevatron_PDF/TeV_Rookie_Book.htm

[34] The CDF Collaboration
The CDF II Detector Technical Design Report
FERMILAB-Pub-96/390-E
http://www-cdf.fnal.gov/upgrades/tdr/tdr.html

[35] C.S. Hill
Operational Experience and Performance of the CDFII Silicon Detector
FERMILAB-CONF-03-412-E, Jan 2004. 9pp.
Nucl. Instrum. Meth. A530:1-6, 2004

[36] A.Sill
CDF Run II Silicon Tracking Projects
Nucl. Instrum. Meth. A447:1-8, 2000

[37] A. Affolder *et al.*
Intermediate Silicon Layers Detector for the CDF Experiment
Nucl. Instrum. Meth. A453:84-88, 2000

[38] T. Affolder *et al*
et al. **COT Central Outer Tracker**
Nucl. Instrum. Meth. A526: 249, 2004

[39] C. Grozis *et al.*
A Time-Of-Flight Detector for CDF
Int. J.Mod. Phys. A16S1C:1119-1121, 2001

[40] Shin-Shan Yu *et al.*
COT dE/dx Measurement and Corrections
CDF/DOC/BOTTOM/PUBLIC/6361

[41] M. Donegà *et al.*
COT Track Based Calibrations for Summer Conferences 2004
http://www-cdf.fnal.gov/internal/physics/bottom/COTDEDX/COT_dedx_cali.html

[42] R. Snider *et al.*
TOF Reconstruction
http://www-cdf.fnal.gov/internal/upgrades/TOF/reconstruction/tof.html

[43] H.Frish *et al.*
Conceptual Design of a Deadtimeless Trigger for the CDF Trigger Upgrade
CDF/DOC/CDFR/2038, December 15, 1994.

[44] E.J. Thomson *et al.*
Online Track Processor for the CDF Upgrade
IEEE Transactions on Nuclear Science, vol.49, No.3, June 2002

[45] A. Bardi *et al.*
The CDF Online Silicon Vertex Tracker
FERMILAB-CONF-01-376-E, Dec 2001. 7pp.,
Published in Nucl.Instrum.Meth.A485:178-182,2002

[46] Y.S. Chung *et al.*
The Level-3 Trigger at the CDF Experiment at Tevatron Run II
IEEE 2004 (not yet published)

[47] M. Campanelli, E.Gerchtein
Calibration of the momentum scale for Kalman refitter using J/ψ events
CDF internal Note 6905 (2004).

[48] M.Feindt, S. Menzemer, K. Rinnert, P. Schemitz, A.Skiba
KalKalmanFitter. A Fast and Versatile Kalman Track-Fitter for CDF II
CDF internal Note 5388 (2000).

[49] S.Giagu *et al.*
The CharmMods/DFinder Reconstruction Package
CDF internal Note 6158 (2002).

[50] J. Marriner
Secondary vertex fit with mass and pointing constraints (CTVMFT)
CDF internal Note 1996 (1993).

[51] P. Sphicas
A $b\bar{b}$ Monte Carlo Generator
CDF internal Note 2655 (1994)

K. Anikeev *et al.*
Description of Bgenerator II
CDF internal Note 5092 (1999)

[52] P. Nason, S. Dawson, R.K. Ellis
The total cross-section for the production of heavy quarks in hadronic collisions
Nucl. Phys. B303:607, 1998.

[53] W. Bell, J.P. Fernandez, L. Flores, F. Wuerthwein, R.J. Tesarek
User Guide for EvtGen at CDF CDF internal Note 5618 (2003)

[54] R. Brun, F. Carminati
GEANT detector description and simulation tool
CERN Program Library Long Write-up W5013

[55] S. D'Auria *et al.*
CDF B Monte Carlo
http://www-cdf.fnal.gov/internal/physics/bottom/b-montecarlo/

[56] R.Carosi, M.Casarsa, P.Catastini, A.Cerri, M.A.Ciocci, S.D'Auria, S.Da Ronco, S.DeCecco, S.Donati, M.Donega', S.Giagu, D.Lucchesi, M.J.Morello, G.Punzi, M.Rescigno, G.Salamanna, P.Squillacioti, D.Tonelli, S.Torre
Branching Ratios and CP asymmetries in $B^0 \rightarrow h^{\pm}h'^{\mp}$ decays from $180pb^{-1}$
CDF internal Note 7066 (2004)

[57] M. Campanelli, R. Carosi, A. Ciocci, S. DaRonco, S. D'Auria, S. DeCecco, S. Donati, S. Giagu, D. Lucchesi, M. Morello, G. Punzi, M. Rescigno, F. Scuri, D. Tonelli, S. Torre

$B^0 \rightarrow h^{\pm} h'^{\mp}$ **signal extraction from the Two-Track Trigger data**
CDF internal Note 6356 (2003)

[58] W.J. Metzger*et al.*
Statistics Methods in Data Analysis
EHEF Nijmegen - Internal Publications: HEN-343

[59] M. Beneke, M. Neubert
QCD factorization for $B \rightarrow PP$ and $B \rightarrow PV$ decays
http://arxiv.org/abs/hep-ph/0308039

[60] H. Albrecht *et al.*
Search for hadronic $b \rightarrow u$ decays
Phys. Lett. B 241 (90) 278

[61] J. Rademacker *et al.*
**Reduction of statistical power per event due to upper lifetime cuts
in lifetime measurements**
http://arxiv.org/abs/hep-ex/0502042

[62] F. Abe *et al.*
**Measurement of b hadron masses in exclusive J/ψ decays with the
CDF detector**
http://arxiv.org/abs/hep-ex/0508022

[63] S. Yu *et al.*
COT dE/dx Measurement and Corrections
CDF internal Note 6361 (2003)

S. D'Auria*et al.*
Track-based calibration of the COT specific ionization
CDF internal Note 6932 (2004)

[64] S. Budroni *et al.*
**Measurement of direct CP asymmetry in $B_d \rightarrow K^+\pi^-$ decays in 355
pb^{-1} of Two-Track data**
CDF internal Note 8057 (2005)

[65] The CDF Bs mixing working group
B mesons lifetime determination in fully hadronic decays
CDF internal Note 7386 (2005)

[66] K. Anikeev *et al.*
B Meson Lifetime Measurements Using Exclusively Reconstructed Decays $B \to J/\psi X$
CDF internal Note 6266

[67] K. Anikeev *et al.*
Using Transversity Variable to Disentangle (C)P Eigenstates in $B_s \to J/\psi\phi$ and $B^0 \to J/\psi K^{*0}$
CDF internal Note 6266 (2004)

[68] P. Lukens *et al.*
Observation of the $B_c \to J/\psi\pi$ Decay
CDF internal Note 7881 (2005)

[69] M. Mangano, M. Cacciari: private communication

[70] G. Punzi
Comments on Likelihood fits with variable resolution
http://arxiv.org/abs/physics/0401045

[71] K. Hartkorn and H.G. Moser
A new method of measuring $\Delta(\Gamma)/\Gamma$ in the $B_s - bar B_s$ system.
Eur. Phys. J. C8 381 (1999)

[72] The D0 collaboration
Measurement of the Lifetime Difference in the B_s System
http://www-d0.fnal.gov/Run2Physics/WWW/results/prelim/B/B36/B36.pdf

[73] The D0 collaboration
Measurement of the Branching Ratio BR($B_s \to D_s^{(*)} D_s^{(*)}$) with the D0 Experiment
http://www-d0.fnal.gov/Run2Physics/WWW/results/prelim/B/B37/B37.pdf

[74] R. Van Kooten
B_s decays and B Leptonic Decays
http://arxiv.org/abs/hep-ex/0606005

[75] L. Feld *et al.*
SCT End-Cap Module Final Design Review Documents
http://atlas.web.cern.ch/Atlas/GROUPS/INNER_DETECTOR/SCT/ecmod/FDR.htm

[76] F. Campabadal *et al.*
**Design and performance of the ABCD3TA ASIC for readout of silicon
strip detectors in the ATLAS semiconductor tracker**
Nucl. Instrum. Meth. A552:292-328, 2005

[77] A.G. Clark *et al.*
**Design and test od a prototype silicon detector module for ATLAS
Semiconductor Tracker endcaps**
Nucl. Instrum. Meth. A538:265-280, 2005

[78] F. Campabadal *et al.*
Beam tests of ATLAS SCT silicon strip detector modules
Nucl. Instrum. Meth. A538:384-407 (2005)

[79] **LHC machine outreach**
http://lhc-machine-outreach.web.cern.ch/lhc-machine-outreach/

[80] The ATLAS Collaboration
ATLAS Detector and Physics Performance Technical Design Report
CERN/LHCC 99-14
http://atlas.web.cern.ch/Atlas/GROUPS/PHYSICS/TDR/access.html

[81] **Pixel Detector Technical Design Report**
CERN/LHCC 98-13
http://atlas.web.cern.ch/Atlas/GROUPS/INNER_DETECTOR/PIXELS/tdr.html

[82] **Inner Detector TDR**
CERN/LHCC/97-16, CERN/LHCC/97-17
http://atlas.web.cern.ch/Atlas/GROUPS/INNER_DETECTOR/TDR/tdr.html

[83] **Calorimeter Performance Technical Design Report**
CERN/LHCC 96-40
http://atlas.web.cern.ch/Atlas/TDR/caloperf/caloperf.html

[84] **Muon Spectrometer Technical Design Report**
CERN/LHCC 97-22
http://atlas.web.cern.ch/Atlas/GROUPS/MUON/TDR/Web/TDR_chapters.html

[85] **High-Level Trigger, Data Acquisition and Controls Technical Design
Report**
CERN/LHCC 2003-022
http://atlas-proj-hltdaqdcs-tdr.web.cern.ch/atlas-proj-hltdaqdcs-tdr/

[86] M. Dentan *et al.*
DMILL, a Mixed Analog-Digital Radiation-Hard Technology for High Energy Physics Electronics, RD29 Status Report
CERN/LHCC/97-15

[87] C. Lacasta *et al.*
Electrical Specifications and Expected Performance of the End-Cap Module
ATL-IS-EN-009

[88] M. Mangin Brinet *et al.*
Electrical Test Results from ATLAS-SCT End-Cap Modules
ATL-INDET-2003-004

[89] M. D'Onofrio *et al.*
Electrical Performance of ATLAS-SCT KB End-Cap Modules
ATL-INDET-2003-007

[90] G. Lutz
Semiconductor Radiation Detectors
Springer; 1 edition (November 1999)

[91] M. Moll **Radiation Damage in Silicon Particle Detectors**
http://mmoll.home.cern.ch/mmoll/thesis/

[92] Snow, S. *et al.*
Thermal and Mechanical Specifications and Expected Performance of the Forward SCT Module.
ATL-IS-EN-0007 (2002)

[93] F. Fowler
CFD Simulation of Convection Cooling in the ATLAS Forward Silicon Tracker
http://hepwww.rl.ac.uk/Atlas-SCT/engineering/ec_fdr/misc/convection_v2.pdf

I. Duerdoth*et al.*
Measurements of convection between the disks of the ATLAS SCT end cap
http://www.hep.man.ac.uk/atlas/TM/CONVECTION8.DOC

[94] M. Donegà *et al.*
Thermal Performance of the ATLAS-SCT KB Forward modules
ATL-INDET-2003-008

[95] Moore, A.V.*et al.*
Highly Oriented Pyrolitic Graphite and its Intercalation Compounds.
Chemistry and Physics of Carbon, v.17, pp233-304 (1981)

[96] **ANSYS**
http://www.ansys.com

[97] Snow, S. *et al.*
Recent results from evaporative cooling tests at RAL
http://www.hep.man.ac.uk/atlas/TM/RALtests.doc

[98] **DS1820 Temperature sensors**
http://http://www.maxim-ic.com/quick_view2.cfm/qv_pk/3021/

[99] A.G. Clark *et al.*
Thermal Performance of the ATLAS-SCT Forward Modules
ATL-INDET-2003-010

[100] **SCT evaporative cooling rig**
http://st-support-cooling-electronics.web.cern.ch/st-support-cooling-
electronics/default.htm

[101] Snow, S.*et al.*
Final results of thermal resistance measurements on K5-300 and K5-313
http://www.hep.man.ac.uk/atlas/TM/Thermal-resistance.doc

Acknowledgements